12-18-2013

Modulating Calcium Signaling by Protein Design and Analysis of Calcium Binding Proteins

You Zhuo
Georgia State University

Recommended Citation

Zhuo, You, "Modulating Calcium Signaling by Protein Design and Analysis of Calcium Binding Proteins." Dissertation, Georgia State University, 2013.
https://scholarworks.gsu.edu/chemistry_diss/84

MODULATING CALCIUM SIGNALING BY PROTEIN DESIGN AND ANALYSIS OF CALCIUM BINDING PROTEINS

by

YOU ZHUO

Under the Direction of Professor Jenny J. Yang

ABSTRACT

Transient change of cytosolic calcium level leads to physiological actions, which are modulated by the intracellular calcium stores, and gated by membrane calcium channels/pumps. To closely monitor calcium dynamics there is a pressing need to develop calcium sensors that are targeted to high calcium environment such as the ER/SR with relatively low binding affinity and fast kinetic properties to complement the current calcium indicator toolkits. In this dissertation, the development of fast red florescent calcium binding protein using the protein design is reported. The results show the calcium dependent fluorescence increase of mCherry mutant MCD1 (RapidER) and MCD15 (RapidER’) is able to monitor the ER calcium release in several cell lines responding to perturbations of extracellular calcium signaling. The specific targeting to the

ER membrane was achieved by fusing the ryanodine receptor 1 transmembrane domains for the spatio-temporal calcium imaging.

To understand the underlying mechanism of calcium binding induced fluorescence increase in the designed calcium sensor CatchER, the fluorescence lifetime of CatchER was determined in calcium free and bound forms using time resolved florescence spectroscopy. The results suggest that calcium binding inhibits the geminate quenching, resulting in a longer lifetime when the anionic form is indirectly excited at 395 nm. It is believed that such unique calcium-induced lifetime change can be applied to monitor calcium signaling in cell imaging.

NMR spectroscopy was used to investigate the protein-protein/ligand interaction in this dissertation. The residual dipolar coupling and T1, T2, NOE dynamic study were carried out to understand the binding mode of CaM and the N-terminal intracellular loop of connexin 43. The results show that both N and C terminal domains of Ca^{2+}-CaM contact with the peptide, leading to a partially unwound and bending central helix of CaM. The ligand binding induced conformational change was demonstrated by selectively labeled proteins including (1) extracellular domain of calcium sensing receptor and (2) the bacterial membrane protein SecA fragments C34 and N68.

INDEX WORDS: Protein design, Fluorescent proteins, mCherry, GFP, Homology modeling, Fluorescence lifetime, NMR, Calcium imaging, Targeting, Spatial-temporal calcium dynamics, Protein dynamics, Protein-ligand interaction

MODULATING CALCIUM SIGNALING BY PROTEIN DESIGN AND ANALYSIS OF CALCIUM BINDING PROTEINS

by

YOU ZHUO

A Dissertation Submitted in Partial Fulfillment of the Requirements for the Degree of

Doctor of Philosophy

in the College of Arts and Sciences

Georgia State University

2013

MODULATING CALCIUM SIGNALING BY PROTEIN DESIGN AND ANALYSIS OF CALCIUM BINDING PROTEINS

by

YOU ZHUO

Committee Chair: Jenny Yang

Committee: Aimin Liu

Donald Hamelberg

Electronic Version Approved:

Office of Graduate Studies

College of Arts and Sciences

Georgia State University

December 2013

DEDICATION

I lovingly dedicate this dissertation work to my family and friends. I want to thank my lovely parents Xingfu Zhuo and Ting Gao, who create such a joyful and healthy growing environment, and also help me to build a concrete knowledge background. They always support me, guide me through tough situation, and bring me happiness. I want to thank my dear husband, Chihwen Cheng, who supports me at each step of my Ph.D. life, helps me to build positive attitude, and gives me knowledgeable advice. I thank his unconditional love which always warms my heart, and his unique humor which brings me smile through unhappy moments.

I appreciate the support from my friends, Ziyue Chen, Bob Shih, Yunfeng Cheng, Fei Song, Chao Li, Danyang Li, Haidong Xue, He Gong, Leo Wu, Jesse Shin, Ivan Hsiao and Pitz Chen, as well as friends from my lab, Alice Zhang, Jina Qiao, Snow Liu, Johnny Chen, Jane Feng, and Julia Zou.

ACKNOWLEDGEMENTS

All the work in this dissertation was carried out under the direction of Prof. Jenny J. Yang. Her passion and enthusiasm at science inspires me all the way during the course of my research. In the journey of the Ph.D, her genuine concern and faith in me enables me to face and solve the difficult situations in both research and personal life. Her professional training provides me the solid scientific base and prepares me strong for the future career. I am especially grateful to her for continuously supporting my experiments and ideas, and helping me to express my research goals in writing.

I am fortunate indeed to have such knowledgeable committee members who gave me a lot of valuable suggestions and guidance and helped to make this a wonderful learning event for me. I would like to give my sincere thanks to our collaborators Dr.Osvaldo Delbono and Dr. Kyril Solntsev, who contributed to important and unique perspectives throughout the research development and analysis. Their advice and feedback have been more helpful than they may realize.

I want to express many thanks to my colleagues Dr. Yusheng Jiang, Dr. Shen Tang, Florence Reddish, Fantashia Demesheka, Dr. Michael Kirberger, Yunmei Lu, Ying Zhang, Dr. Yanyi Chen, Dr. Jingjuan Qiao, Dr. Bob Wohlhueter, Chen Zhang, Jie Feng, Juan Zou, Xueyun Liu, Mani Salarian and other members in Dr. Jenny Yang's lab. We worked together as a team and family, making the research vivid and colorful.

This work is supported by grants from National Institute of Health and Brain and Behavior Fellowship provided by Georgia State University. Finally, and most importantly, I would like to thank my parents and my husband, Chihwen Cheng, for their love, faith and encouragement while supporting my research work.

TABLE OF CONTENTS

ACKNOWLEDGEMENTS v

LIST OF TABLES x

LIST OF FIGURES xi

1 INTRODUCTION 1

1.1 Calcium signaling and its role in physiological functions 1

1.2 Calcium signaling and diseases 5

1.3 Development of calcium indicators 8

1.4 Fluorescent proteins 15

1.5 Structure, dynamics and function of Calmodulin (CaM) 17

1.6 Motivation of this dissertation and questions to be addressed 19

1.7 Overview of this dissertation 20

2 MATERIALS AND METHODS 22

2.1 Clone construction and PCR 22

2.2 Protein expression and purification 23

2.3 Determination of biophysical properties 25

2.4 Metal binding assays for designed calcium binding proteins 28

2.5 Kinetics study of calcium binding 32

2.6 Fluorescence lifetime measurement 34

2.7 Nuclear magnetic resonance spectroscopy ... 35

2.8 Computer assisted structure model building ... 38

2.9 Calcium response monitored by designed calcium binding proteins *in situ* 47

3 RATIONAL DESIGN AND EVALUATION OF CALCIUM BINDING FLUORESCENT PROTEINS ... 52

3.1 Introduction ... 52

3.2 Characterization of the biophysical properties of designed calcium binding proteins 56

3.3 Cell imaging and calcium response in situ ... 97

3.4 Discussion ... 107

3.5 Summary and conclusions ... 115

4 THE DYNAMIC AND STRUCTURAL ANALYSIS OF THE GREEN FLUORESCENT CALCIUM INDICATOR CATCHER ... 117

4.1 Introduction ... 117

4.2 Results and discussion ... 120

4.3 Summary and conclusions ... 143

5 THE FLUORESCENCE LIFETIME OF THE GREEN FLUORESCENT CALCIUM INDICATOR CATCHER ... 145

5.1 Introduction ... 145

5.2 Results ... 152

5.3 Discussion 163

5.4 Summary and conclusions 170

6 THE SPECIFIC TARGETING CATCHER TO THE CYTOSOLIC SIDE OF ENDOPLASMIC RETICULUM MEMBRANE 172

6.1 Introduction 172

6.2 Results 174

6.3 Discussion 193

6.4 Summary and conclusions 196

7 THE DYNAMIC STUDY OF THE COMPLEX OF CALMODULIN AND PEPTIDES 198

7.1 Introduction 198

7.2 Results and discussion 200

7.3 Summary and conclusions 209

8 NMR OF DIMETHYLATED LYSINE IN CALMODULIN AND CALCSIUM-SENSING RECEPTOR (CASR) 211

8.1 Conformational change of calcium sensing receptor extracellular domain (CaSR-ECD) induced by calcium and ligand binding 211

8.2 Lipid interaction induced conformational change of SecA fragments 221

8.3 Summary and conclusions 225

9 MAJOR DISCOVERIES AND SIGNIFICANCE 227

REFERENCES 231

APPENDICES 246

Appendix A Scripts for NMR data processing 246

Appendix B Protocols for NMR data processing 252

Appendix C Analysis of hydrogen bonds of MD simulation for CatchER 265

Appendix D Validation of Lys methylation using CaM.. 269

Appendix E Production of lentivirus.. 270

LIST OF TABLES

Table 1.1 The color distribution and binding affinity of GECIs. 11

Table 1.2 Kinetic parameters of recent major calcium indicators 14

Table 2.1 A list of the buffers utilized for the pH dependence measurements. 26

Table 2.2 Preparation of calcium standard for ICP-OES calibration 32

Table 2.3 Agonists and antagonists used for induce calcium change 50

Table 3.1 Variants and the corresponding mutation sites 62

Table 3.2 Biophysical properties of selected mCherry variants 75

Table 3.3 The dissociation constant and dynamic range of mCherry variants 82

Table 3.4 Calcium and terbium binding affinity calculated using different methods 94

Table 3.5 The electrostatic binding energy calculation 108

Table 4.1 The statistics of the cross peaks during the Gd^{3+} titration to CatchER. 124

Table 4.2 Summary of off rate and binding constants of resonance L42, L44 and T153. 134

Table 5.1 Values of the time constants (τ_i) and normalized (to 1) pre-exponential factors (A_i) 157

Table 5.2 Hydrogen bond analysis in the chromophore environment by MD simulation 161

Table 6.1 Data summary of CatchER with different tags in calcium imaging 195

Table 7.1 The RDC fitting of CaM-Cx43np to different CaM-peptide complex 204

LIST OF FIGURES

Figure 1.1. The time scale of the calcium channels in the intracellular membranes. 5

Figure 1.2. The representative organic calcium dyes. 8

Figure 1.3. The cartoon structure of GECIs. 10

Figure 1.4. Crystal structure comparison of mCherry and GFP. 16

Figure 3.1. Structural analysis and design of calcium binding sites on mCherry. 58

Figure 3.2. Predication of calcium binding to the modeled red fluorescent proteins. 61

Figure 3.3. Purification of MCD15 from BL21 (DE3) transformed with pET28a. 64

Figure 3.4. Comparison of SDS-PAGE pattern of MCD15 purified from different *E.coli*. strains. 65

Figure 3.5. Removal of cleaved peptides by size exclusion chromatography (SEC). 67

Figure 3.6. UV-vis spectra of MCD1 supplemented with denaturants. 68

Figure 3.7. Typsin digestion of MCD1. 69

Figure 3.8. The film of western blot for mCherry variants MCD1, MCD14, MCD15 and the wild type. 70

Figure 3.9. The representative optical and fluorescence spectra of mCherry derivatives. 71

Figure 3.10. The UV-vis and fluorescence spectra of mCherry and MCD1 at different concentrations. 73

Figure 3.11. The fluorescence lifetime of MCD1, MCD14 and MCD15 in the absence and presence of Ca^{2+}. 74

Figure 3.12. pH profile and pK_a determination. 76

Figure 3.13. The 3D plot of the ratio of $[Ca^{2+}]_{it}$/ $[Ca^{2+}]_{free}$ as a function of [P]t and $[Ca^{2+}]_{free}$. 78

Figure 3.14. Equilibrium-dialysis assay for calcium dissociation constant determination. 80

Figure 3.15. The curve fitting for K_d of (A) MCD1 and (B) mcEE. 82

Figure 3.16. The salt-dependent K_d determination. 84

Figure 3.17. Tb^{3+}-FRET titration of mCherry and its variants. 87

Figure 3.18. The calculated distance between ion and the chromophore. 90

Figure 3.19. Metal and nucleotides selectivity of MCD1. 91

Figure 3.20. Kinetics analysis of association of Ca^{2+} with MCD1. 93

Figure 3.21. The stacked 1D proton NMR spectra of calcium titration to MCD1 at 37°C. 96

Figure 3.22. HSQC spectra of MCD14 at 25 ℃ and 40 ℃. 96

Figure 3.23. The overlaid ^1H-^{15}N-HSQC spectra of calcium-free (blue) and loaded (red) MCD14. 97

Figure 3.24. The confocal image of ER-tagged MCD1 expressed in C2C12 cells. 98

Figure 3.25. Comparison of MCD1x responding to ionomycin. 99

Figure 3.26. Calcium dynamics monitored by MCD15-transfected HEK293. 101

Figure 3.27. Calcium dynamics monitored by MCD15-transfected BHK cells. 102

Figure 3.28. Calcium dynamics monitored by MCD15-transfected HeLa cells. 102

Figure 3.29. Calcium dynamics monitored by MCD15-transfected C2C12 cells. 103

Figure 3.30. Comparison of MCD15 responding to 4-cmc and CPA induced Ca^{2+} release from ER. 103

Figure 3.31. Calibration for MCD15 expressed in HEK 293 cells. 105

Figure 3.32. *In situ* calibration for MCD15er transfected in BHK, HeLa and C2C12 cells. 106

Figure 3.33. Comparison of the electrostatic surface between (left) MCD1 and (Right) CatchER. 108

Figure 4.1. The ^1H-^{15}N HSQC spectra overlay of CatchER in different buffer solutions. 120

Figure 4.2. The ^1H-^{15}N HSQC spectra overlay of CatchER with (Cyan) and without (Red) Gd^{3+}. 121

Figure 4.3. The ^{15}N-^1H HSQC spectra of Gd^{3+} titration to CatchER. 122

Figure 4.4. The histograms of the chemical shift change in Gd^{3+} titration. 122

Figure 4.5. Mapping residues affected by Gd^{3+} PRE in the calcium loaded CatchER crystal structure... 124

Figure 4.6. Comparison of the ratio R2/R1 of apo and holo CatchER. 126

Figure 4.7. Comparison of the ratio NOE_{on}/NOE_{off} of apo and holo CatchER. 127

Figure 4.8. Comparison of the simulated S2 value calculated by Modelfree 4.0 of holo (red, solid) and apo (black, dash) CatchER. 128

Figure 4.9. The flexible and rigid regions in the crystal structure of Ca^{2+}-CatchER. 129

Figure 4.10. Titration of calcium for CatchER monitored by ^1H-^{15}N HSQC. 133

Figure 4.11. The RMDS and RMSF of 20-ns MD simulation. 138

Figure 4.12. The snapshots of CatchER during 20-ns MD simulation. 140

Figure 4.13. The dihedral angle between the chromophore imidazolinone and tyrosine phenol. 142

Figure 5.1. The crystal structure of apo (PDB ID: 4L1I)) and holo CatchER (PDB ID: 4L12). 150

Figure 5.2. The pH profile of the absorbance of CatchER. 153

Figure 5.3. The emission spectra of CatchER in the pH cocktail buffer at different pH. 154

Figure 5.4. CatchER fluorescence decay at pH 5.0, 7.6 and 9.6. 155

Figure 5.5. The decay of CatchER at pH 7.4. 156

Figure 5.6. Fluorescence decay traces of apo-CatchER (dash line) and CatchER supplemented with 10 mM Ca^{2+} (Holo, solid line) in H_2O (black) and D_2O (grey). 157

Figure 5.7. The UV/optical and fluorescence spectra of CatchER in H_2O (black) and D_2O (grey), in the absence (dash line) and presence of Ca^{2+} (solid line). 158

Figure 5.8. The normalized fluorescence emission spectra of apo (dash line) and holo CatchER (solid line) in H_2O (left) and D_2O (right). 159

Figure 5.9**.** The comparison of crystal structures of (A) apo-CatchER (PDB ID: 4L1I), (B) Ca^{2+}-CatchER (PDB ID: 4L12), (C) GFP (PDB ID: 2WUR) and (D) EGFP (PDB ID: 4EUL). 162

Figure 6.1. Construct of ER-anchoring CatchER. 176

Figure 6.2. Induced differentiation of C2C12 myoblasts. 177

Figure 6.3. The confocal images of targeted CatchER in non-differentiated C2C12 myoblasts. 179

Figure 6.4. The confocal images of targeted CatchER in non-differentiated C2C12 myoblasts. 180

Figure 6.5. CatFKBP responding to drugs in (A) non-differentiated and (B) induced differentiated C2C12 cells. 183

Figure 6.6. The calcium imaging of CatZ5 transfected to (A) C2C12 myoblasts and (B) differentiated C2C12 cells. 186

Figure 6.7. The calcium imaging of CateZ5 transfected (A) C2C12 myoblasts and (B) differentiated C2C12 cells. 188

Figure 6.8. The calcium imaging of CatLeZ5 transfected non-differentiated C2C12 myotubules. 190

Figure 6.9. The calcium imaging of Z10Cat transfected to (A) C2C12 myoblasts and (B) differentiated C2C12 cells. 192

Figure 7.1. The binding modes of CaM and peptide complex. 199

Figure 7.2. The cartoon of connexin 43 topology and predicted CaM binding sites. 201

Figure 7.3. The ^{15}N-HSQC of holo-CaM interacted with the peptide Cx43np. 203

Figure 7.4. The dynamics analysis of CaM-Cx43np complex by T1, T2 and NOE. 207

Figure 7.5. The ^{1}H-^{15}N HSQC spectra comparison of apo-CaM (Blue), holo-CaM (purple), apoCaM-pRYR1975-1999 (green) and the tested CaM-pRYR1975-1999 (Red). 209

Figure 8.1. ^{1}H-^{15}N HSQC spectra of calcium titration of ^{15}N-Phe selectively labeled CaSR-ECD. 215

Figure 8.2. The^{1}H-^{13}C HMQC spectra of [^{13}C-dimethylated-Lys]-CaSR-ECD expressed in HEK293 cells. 216

Figure 8.3. The ^{1}H-^{15}N HSQC spectrum of the bacterial expressed CaSR-ECD. 217

Figure 8.4. The 1D proton and STD spectra of CaSR-ECD titration with L-Phe and GSH. 219

Figure 8.5. The STD spectra comparison between Ca2+ free and loaded CaSR-ECD. 220

Figure 8.6. The structure analysis of SecA. 223

Figure 8.7**.** NMR study of selectively labeled SecA fragment N68 and C34. 225

1 INTRODUCTION

1.1 Calcium signaling and its role in physiological functions

Ca^{2+} plays an indispensable role in physiology and biochemistry of organisms. With a tight systemic regulation by hormones, calcium levels in the blood and soft tissues must be maintained in a very narrow concentration range for normal physiological functioning. Calcium signaling is originated from the steep concentration gradients across membranes, including plasma membrane, the membranes of the endoplastic reticulum (ER), mitochondria (1), lysosome (2), and other organelles. The extracellular calcium concentration is maintained at 1-2 mM, while hundreds of nanomollar in the cytoplasm.

Calcium-sensing receptor (CaR), first cloned and characterized by Brown and colleagues (3), senses the change in extracellular fluid Ca^{2+} concentration, and regulates the releasing of hormones like PTH and calcitonin to control calcium homeostasis. Ca^{2+} concentration in cytoplasm is approximately at the level of 10^{-7} M, while in the organelles it is higher up to 10^{-4}-10^{-3} M. The intracellular calcium concentration is regulated by ion channels in those membranes. For example, when cells are activated, calcium influx into cells through plasma calcium channels like voltage-gated calcium channel in the excitable cells, and the plasma membrane Ca^{2+} ATPase (PMCA) can transport calcium out of cells; smooth endoplasmic reticular Ca^{2+} ATPase transporters (SERCA) transports calcium into the ER lumen and the ryanodine receptor (RyR) and inositol 1,4,5-trisphosphate receptor (IP_3R) can release calcium from ER, resulting in a calcium transient in cytosol (4).

Calcium signals come from transient rises of the cytoplasmic Ca^{2+} concentration, which mediates the constriction and relaxation of blood vessels, nerve impulse transmission, muscle contraction, cell-cycle progression, lymphocyte activation, and the secretion of hormones(5-7). Several calcium binding proteins are involved in signaling pathways, called calcium signaling proteins, such as calmodulin, S100 proteins, protein kinase C, and C2 domains(4). ER, as the primary intracellular Ca^{2+} store, can produce intrinsic Ca^{2+} release and propagation of Ca^{2+} oscillations(8-10), where the concentration is only known to be in the micromolar level so far. In excitatory Ca^{2+} signaling, the voltage change, extra- or intracellular ligand binding will trigger the plasma membrane ion channels to open. The initial increase in Ca^{2+} concentration will lead to more release from the ER, primarily through RyR, which is called calcium induced calcium release (CICR) in the cardiac myocytes. ATP, ionomycin, histamine, caffeine and glutamine, *etc.* will activate the Ca^{2+} receptors and pumps located in ER, such as IP_3R and RyR, to release Ca^{2+} from ER into cytoplasm(11-13). In the non-excitable cells, the first depletion of Ca^{2+} in the ER will activates the Stim/Orai complex formation and cause store operated calcium influx (SOC). Also, SOC refills Ca^{2+} into the ER from extracellular environment via both the plasma and the ER membrane channels(14). The alternation of cellular Ca^{2+} concentration activates intracellular Ca^{2+} sensing proteins, transmitter-gated and voltage-gated ion channels, gap junction channels, further regulating numerous cellular events and cell-to-cell signaling.

1.1.1 *Calcium signaling network*

Calcium signaling is a network involving organelles inside a cell. The endoplasmic reticulum (ER) is the major calcium storage and the source of intracellular calcium transients. Mitochondria, Golgi, lysosome are also recognized as the intracellular calcium stores and conduct corresponding calcium signaling via the activity of membrane calcium channels. Those calcium storages and the channels function together to regulate a physiological dynamic event. On the other hand, increasing evidences support that calcium signaling is temporal and spatial to prevent excess responses.

In addition to be a calcium storage, the ER is the factory to synthesize proteins and responsible for post-translational modification, and protein trafficking. A misfolded protein is first recognized by the ER and induces ER stress, which in turn initiates the unfolded protein response (UPR) to relieve the stress. It is important to maintain the normal resting calcium level in ER to ensure correct function of those ER proteins like ER chaperones(15). Many proteins in the ER share the feature of calcium binding with low affinity and high capacity such as calreticulin and calsequestrin. The former one serves as one of the ER chaperones and plays a very important role in the folding and loading of MHC class I molecules. Calsequestrin is a calcium buffer protein in the ER lumen with > 40 calcium binding sites and regulates the activity of ryanodine receptor (RyR) with association of junctin and triadin. Briefly, when calcium sites are occupied, calsequestrin has a conformational change from ransom coil to helices, dissociates with junctin and triadin and activate RyR.

Calcium influx across mitochondria is closely related to the membrane potential, and controls the mitochondria energy production. Intramitochondrial calcium can activate enzymes coupled to the Krebs cycle. Moreover, calcium uptake can modulate the intracellular calcium signaling, regulate mitochondrial motility and morphology, and induce cell death. The calcium channel in the mitochondrial outer membrane is called voltage-dependent anion channels (VDAC), which is permeable to free calcium and may have a role in the crosstalk between the ER and the mitochondria(16). In the inner membrane of mitochondria, the inward calcium channel includes mitochondrial calcium uniporter (MCU), mitochondrial RyR, the rapid mode of mitochondrial Ca^{2+} uptake (RAM). Mitochondrial Na^{+}-Ca^{2+} exchanger (mNCX) is one of the major outward calcium channels(17). ER-mitochondrial coupling provides the local calcium signaling and plays an important role in the early phases of ER stress(18) and apoptosis(19). Several calcium channels are thought to play roles in the ER-mitochondrial interface, and the hot spots of high calcium level were found to enable the efficient calcium transfer(20); however, the details still remain unclear.

1.1.2 *Kinetics of the ER related calcium channels*

The ER controls the intracellular calcium signaling by regulating the activities of its membrane calcium channels. As shown in Figure 1.1, the kinetics of those channels plays a central role to modulate the calcium-dependent physiological events such as excitation-contraction coupling (ECC). Dihydropyridine receptor (DHPR) and ryanodine receptor (RyR) are two primary proteins involved in the early stage of ECC, which are different in cardiac and skeletal myocytes. In skeletal muscle, four DHPR resemble together and physically contacts with RyR1. Membrane depolarization induced conformational change of DHPR triggers opening of RyR1 and hence the calcium influx via DHPR is not required for the skeletal muscle cells. While, in cardiac muscle, calcium influx due to the activation of DHPR is essential for the later opening of RyR2, called calcium induced calcium release (CICR). The mean open time of DHPR is around 0.5 ms and the time constant of activation of RyR is about 0.6 ms (21). The activity of RyR is biphasically modulated by Ca^{2+} concentration. The onset has a time constant of ~1 ms and the deactivation time constant is about 2-5 ms. The duration of a single action potential is 2-5 ms for the skeletal muscle, 100-400 ms for cardiac muscle and <1 ms for nerve(21).

IP_3R is another calcium release channel in ER membrane. Like RyR, IP_3R's activity is also dependent on calcium concentration and exhibits a bell shape. Moreover, the activation of this channel requires binding of IP_3, which is one of the cleavage products of phosphatidylinositol 4,5 bisphosphate (PIP2) by phospholipase C (PLC). The activity of IP_3R is more complex than RyR. At least two opening states are engaged in the channel's activity. The fast one has a time constant <10 ms and the slow component has a time constant more than 200 ms (22).

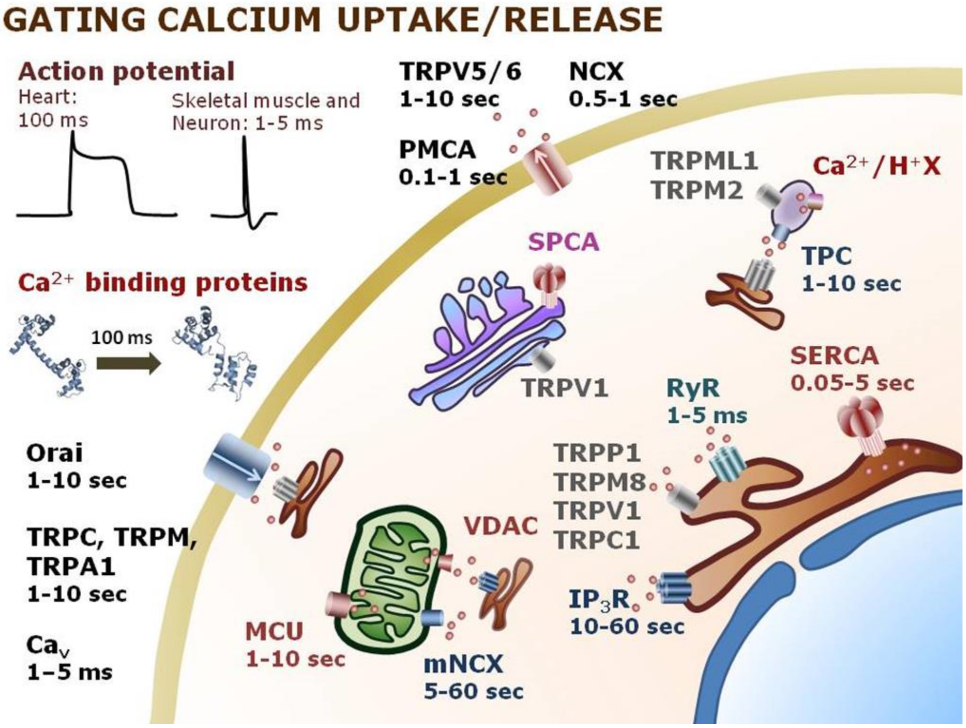

Figure 1.1. The time scale of the calcium channels in the intracellular membranes.

1.2 Calcium signaling and diseases

Ca^{2+} signaling is important for homeostatic handling of cardiovascular functions. The activation of cardiac myocytes requires the addition of ~100 μM Ca^{2+} in cytosol, for which the Ca^{2+} source is the sarcoplasmic reticulum (SR)(23). The cardiac ryanodine receptor (RyR2), IP_3R and SERCA2a are three pivotal channels for the Ca^{2+} mobilization from SR to cytosol during this agonist-induced process. Dysfunction of these proteins has been proved to be the leading cause of heart failure with increasing evidence collected both from animals and humans (24, 25). The prolonged increase of the cytosolic Ca^{2+} level in cardiac myocytes will result in downregulation of Ca^{2+} signaling proteins in cardiac hypertrophy, leading to defects of muscle contraction and relaxation and ultimately heart failure (26). Alzheimer's disease (AD) is the worldwide aged disease that is characterized as extensive synaptic and neuronal loss. Although the cause of AD still remains unclear, abnormal expression level of calcium signaling proteins has been found from animal models and postmortem brain samples. The increased Ca^{2+} level in neuron cells due to the extensive release of calcium ion from the ER triggers a series of signaling process and affects the synaptic stability and neuronal health(27).

1.2.1 *Calcium signaling and apoptosis*

One of the calcium signaling pathways is related to apoptosis. Calcium overload in the ER will lead to the crosstalk between the ER and mitochondria. Mitochondria can uptake calcium directly from the ER and the increased accumulation of calcium is a trigger for the release of cytochrome C to cytosol where it can activate initiator caspase-9 and executioner caspase-3 and lead to apoptosis (28, 29). Also, ER stress can lead to the sustained calcium accumulation in mitrochondrial matrix, triggering permeability transition, dissipation of the electrochemical potential, matrix swelling, relocalization of Bax to mitochondria, and release of cytrochrome C (30). There is a cytochrome C independent pathway to induce apoptosis, which is the calpain-induced apoptosis in ER. Calpain is a calcium-dependent cysteine protease, which activates caspase-12 localized in the ER, leading to the subsequent activation of caspase-9. Tharpsigargin induced apoptosis was independent of cytochome C and thus probably was induced by calpain(29).

It has been reported that Bcl-2 can form complex with IP_3R and disrupt its normal function by dephospharylation of IP_3R, which in turn blocks the apoptosis signal (31). Rong and the coworkers also showed evidence that the BH4 domain of Bcl-2 interacted with IP_3R to inhibit the channel open so as to block the calcium induced apoptosis (32). There is a big debate in the relationship between Bcl-2 and the ER calcium content (33, 34). In the previous study, people found that Bcl-2 decreases the ER free calcium content (35, 36). Sano and co-workers recently found that the passive Ca^{2+} leaking from the ER caused by BI-1, which can be rescued by over-expression of SERCA or treatment of SERCA activators (37). This result also built the linkage between the mitochondrial bioenergetics and autophagy. However, using some ER calcium indicators with lower calcium binding affinity than the calcium dyes, some groups found that Bcl-2 can increase the ER calcium content (38).

1.2.2 *Calcium signaling and Alzheimer's Disease (AD)*

The hallmark of AD is the excessive production of β-amyloid (Aβ) and its massive accumulation in amyloid plaque. Aβ monomer can not activate calcium influx and even may play a role in protecting mature neurons against excitotoxic death (39, 40). Misfolding of Aβ results in oligomerization and it's the major cause of the final product amyloid plaque. However, more and more evidence showed that the plaque may not be primarily responsible for the neurological deficits. It has been further proposed that the plaque may contribute to the removal of small toxic soluble species(41, 42). The Aβ oligomer of 2-50 peptides is soluble and has been characterized as the most toxic forms and the small intermediate potently disrupts cellular calcium homeostatsis (40, 43). The Aβ oligomer can impair the normal function of endogeneous plasmaluminal ion channels, disrupt the membrane integrity and form the cation pore(44). The consequences of those effects are the unregulated calcium flux, which is the major factor underlying Aβ toxicity. In normal neuron cells, protective and pathogenic calcium cascades exist together and can be triggered sequentially. For example, excess calcium first activates NFκB-like anti-apoptotic factors and then the increased intracellular calcium through Aβ mediated mechanisms leads to mitochondrial calcium overload and causes apoptosis. Calcium dysfunction can cause the apoptosis, synaptic degeneration, and excitotoxicity. On the other hand, due to the correlation between the calcium homeostasis and AD, some drugs are expected to rescue abnormal calcium signaling (45, 46).

1.3 Development of calcium indicators

1.3.1 *Organic calcium dyes*

Calcium sensor has been emerged to study cardiac and neuronal processes. There are two major classes of current calcium sensors. The first one is the small organic molecules, which has been developed by Roger Tsien and others (Figure 1.2). They are evolved from single-wavelength intensity change to ratiometric signal change (47-49). These sensors exhibit the great signal dynamic range (30-50 fold) upon binding Ca^{2+} and a broad range of binding affinity. However, the major limitation of their application in living cells is that they cannot be targeted to specific subcellular organelles due to the non-specific membrane permeability (50). Therefore, the precise cytological localization cannot be guaranteed. It is also difficult to load these sensors into denser or thicker tissues, hindering further research with animals and humans.

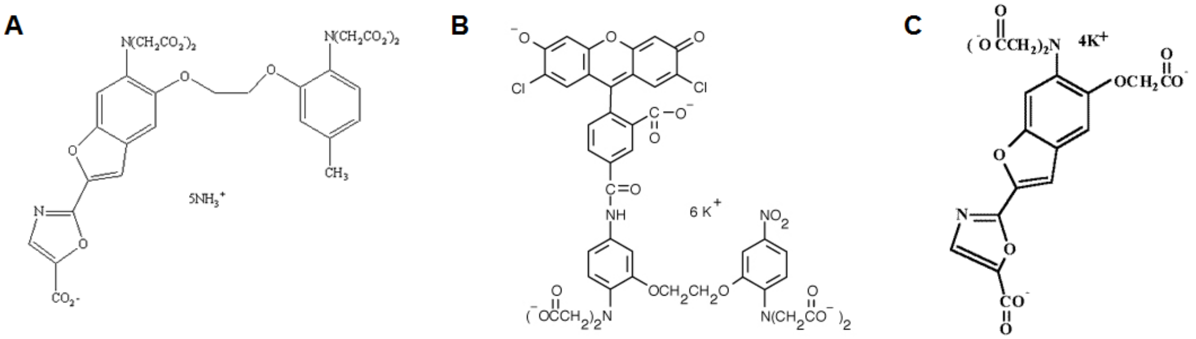

Figure 1.2. The representative organic calcium dyes.
(A) Fura-2 AM, (B) Calcium Green 1-5N, (C) Mag-fura-2.

1.3.2 *Genetically encoded calcium indicators (GECIs)*

The second class is the protein-based Ca^{2+} sensors. Aequorin, a bioluminescent calcium sensor, was originally isolated from luminescent jellyfish and other marine organisms. It generates luminescence as a result of Ca^{2+}-induced conformational change in the presence of its prosthetic group, coelenterazine. The major advantage of aequorin over other indicators is that luminescence does not rely on any optical excitation, eliminating the interference from autofluorescence(51). The primary limitation of aequorin is that luminescence results from oxidation of the prosthetic group coelenterazine after binding three Ca^{2+} so that continuous addition of coelenterazine into the media is required (52), which obstacles its application in real-time detection.

Genetically encoded calcium sensors has been rapidly developed in the last decade, including the calmodulin-based sensor(53-55) and the troponin-based sensor (e.g. TN0-L15, TN-XXL(56)) (Figure 1.3 and Table 1.1). The fluorescent resonance energy transfer (FRET)-based Ca^{2+} sensors are designed based on the significant spectral overlap of the donor emission spectrum and the acceptor excitation spectrum. Calcium concentration change triggers a radiometric change of the spectra and the background noise can be reduced. The FRET pair is linked by the native CaM or some active Ca^{2+} binding domain, which will get close to each other upon the Ca^{2+} binding-induced conformational change of CaM. The representative FRET-based genetically calcium sensors are GCamp series, Yellow Cameleon (YC series)(57-60) and pericam(61). The early generation of these sensors suffered the photobleaching, pH instability, low expression level in cells, and low reproducibility, *etc.*(62). Some of these problems have being gradually solved through various modifications of these sensors and even the dynamic range has been increased up to 100 fold (55). However, there are several drawbacks of this kind of sensors remained to be removed. Specifically they are the bulky size (more than 60 kDa), high requirement of microscopy facility (dual excitation and emission wavelengths), narrow Ca^{2+} binding affinity range (almost the same as native CaM), and the risk of perturbing cellular Ca^{2+} signaling and non-specific binding to other small peptides by the functional group CaM or its variants. In contrast, Nakai, Miyawaki and colleagues developed a single fluorescent protein-based Ca^{2+} probe, who fused M13 fragment and CaM in N- and C-terminals of the circular permutated EGFP and EYFP (cpEGFP and cpEYFP), respectively(61, 63-65). However, its cooperative Ca^{2+} binding feature due to the four EF-hand motifs of CaM limits the application in quantitative measurement.

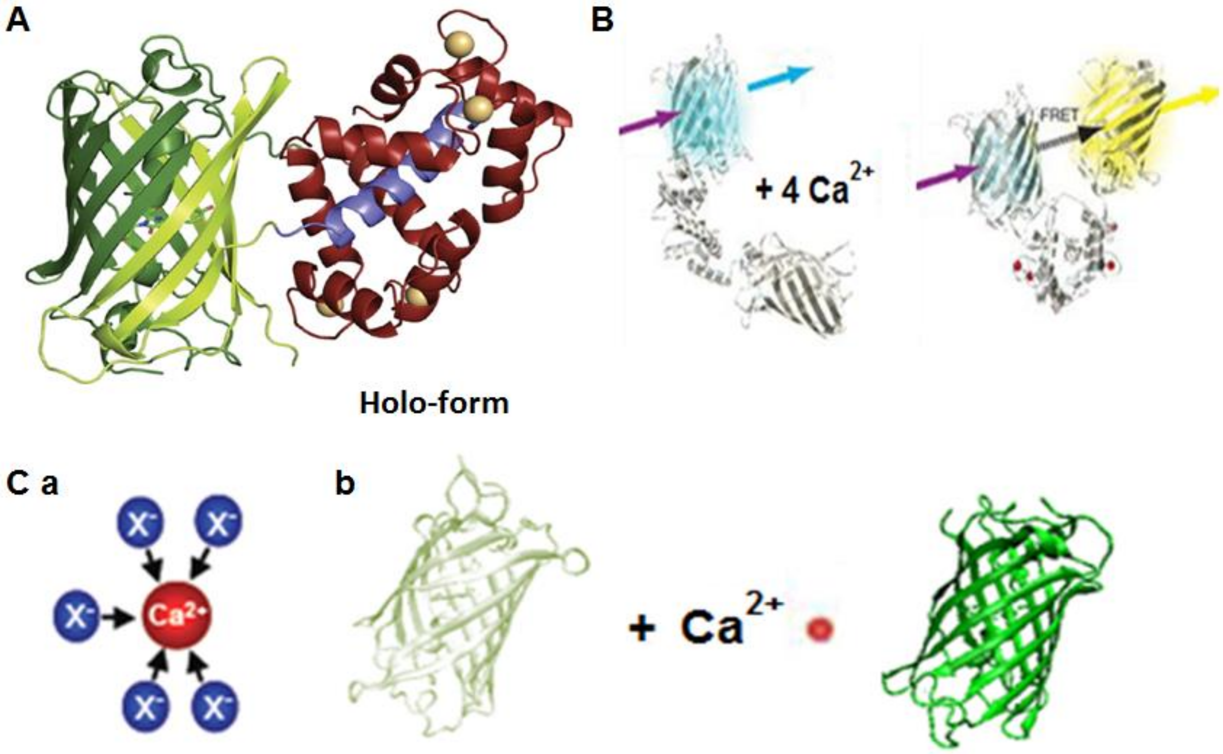

Figure 1.3. The cartoon structure of GECIs.
(A) the calcium loaded form of GCaMP-2 (PDB ID: 3EK8). (B) The calcium induced conformational change of FRET-based Cameleons. (C) The calcium binding geometry (a) and calcium induced fluorescence enhancement (PDB ID: 4L12) (b).

CatchER (Calcium sensor for detecting high concentration in the ER) is an EGFP-based calcium sensor with fluorescence change at a single wavelength that developed in Yang lab (66). The feature of CatchER is the fast kinetics and the low affinity to calcium (K_d = ~180 μM). It was successfully used to monitor the SR calcium release in mouse flexor digitorum brevis (FDB). Compared to D1ER, another calcium sensor derived from cameleon with a low calcium binding affinity (K_d = ~60 μM) (38), CatchER exhibits a better fidelity and faster off-rate. D4cpv-calsequestrin was reported by Sztretye in 2011 to be a new ratiometric calcium indicator targeted to the skeletal muscle SR (18) (19). The dissociation constant was 222 μM and its dynamic change of 2.5 had a big improvement over comparable sensors.

Table 1.1 The color distribution and binding affinity of GECIs.

Subcellular compartment	CYAN	GREEN	Yellow	RED
Intracellular (0.1-1 μM)	B-GECO (K_d=0.2-0.5 μM)	GCaMP (K_d=0.5 μM) G-GECO (K_d=0.6-1.2 μM)	Flash pericam (K_d=0.7 μM)	R-GECO (K_d=0.5 μM)
	YC3.6 (K_d=0.3 μM) TN-XXL (K_d=0.8 μM)			
Golgi	YC3.3 (K_d=4.4 μM)			
Lysosome				
Mitochondria/ Nuclear envelope (1-10 μM)	Cameleon-2 (K_d=0.07; 11 μM); YC4.6 (K_d=0.06, 14.4 μM);		Ratiometric pericam (K_d=1.7 μM); Camgaroo -2 (K_d=5.3 μM);	
ER/SR (0.2-1 mM)	D1ER (K_d=0.8, 60 μM); Cameleon-4 (K_d=0.083, 700 μM)	CatchER (K_d= 190 μM)		

1.3.3 *Calcium binding kinetics of current calcium indicators*

Understanding calcium signaling was advanced by the development of calcium dyes and genetically encoded calcium indicators (GECIs) (50, 67-72). Organic calcium dyes are often used to monitor calcium transients in the cytosol because the K_d is in the magnitude of hundreds of nanomollar. However, the detection of $\Delta[Ca^{2+}]$ induced by a train of high frequency, especially the rapid release from the ER store, is largely limited by the availability of calcium indicators.

It has been reported that it is not suitable for the calcium dye Oregon Green BAPTA 1 to detect the calcium transients upon action potential stimulation of more than 50 Hz because the slow decay (k_{off}=2.6 s^{-1}) results in the accumulation of signals (67, 73-75).

The low affinity calcium dyes, with their low affinity and rapid off rate, such as Fluo-5N (76-78), Mag-Fluo-4 (79), Calcium-green-5N (80, 81) were used to monitor calcium change in internal calcium stores including the mitochondria and the endoplasmic reticulum (82-84). However, the reported kinetics and the amount of calcium concentration change during EC coupling in skeletal and cardiac muscle cells as well as neurons were largely varied. For example, it was reported a broad range from 3.3 to 8.0 ms of the calcium release presented by the full duration at half-maximum (FDHM) at room temperature from the mouse fast-twitch fibers upon the action potential (85-88). Such variations are likely a result of limitations associated with calcium dyes, including the spatial localization of dyes, binding affinity, and kinetics (k_{on} and k_{off})(71, 89).

The development of genetically encoded indicators (GECI), such as GCaMP, GECO, TN and Cameleon series, enables to probe spatial-temporal cellular events and cell signaling in real time (19, 54, 60, 90-97). GECI are composed with a fluorescent protein moiety and native cytosolic calcium trigger proteins (CBPs) such as calmodulin (CaM) or troponin C (TnC) that are used to sense calcium concentration change and calcium-induced global conformational rearrangement. Each CaM or TnC binds four calcium ions cooperatively with a strong calcium binding affinity (K_d=10^{-7} M) and calcium binding on rates in the magnitude of 10^7 $M^{-1}s^{-1}$ that enable them to sense the immediate [Ca^{2+}] rise in the cytosol (98-101). Meanwhile, these GECIs have slow dissociation rate around 0.1-10 s^{-1} likely due to the cooperativity associated with multiple calcium binding sites and multiple layers of conformational change (102, 103). Their slow kinetics of signal decay hampers their applications in probing physiological fast calcium transient especially in the neuron and skeletal muscle cells (56, 91, 104). Further efforts to reduce the calcium binding affinities in Cameleon D1ER results in a multiple K_ds around 0.8 and 60 μM and the off rate around 256 s^{-1} (38). Such sensor, however, was not able to capture the calcium release from SR upon the stimulation in the mouse FDB fibers (105, 106). In addition, the risks of interference to the normal physiological pathways would be considered due to the interaction between the native calcium binding proteins with their target proteins.

To fulfill the unmet need of a fast calcium indicator required for monitoring calcium releases in high concentrations such as the ER/SR and not incorporating native calcium binding proteins, we developed a calcium sensor called CatchER without using the native calcium binding domain (66). CatchER was created by designing a calcium binding site into a single enhanced green fluorescent protein (EGFP). The binding stoichiometry is 1:1 and the K_d is 0.18 mM *in vitro* and 0.8 mM calibrated *in situ* allowing measurement of basal calcium in different cell lines and their changes in response to different drugs. Compared to Cameleon D1ER, CatchER exhibits faster kinetics, allowing it to catch the SR calcium change in the skeletal muscle cells (107). To date, however, there is no sensors available for measuring calcium responses at the red wavelength region with an advantage of better tissue penetration to complement the green sensors developed by us and others (66). In the Chapter 3, we reported the achievement of designing calcium binding protein MCD1 (RapidER) using a red florescent protein mCherry by integrating key factors for calcium binding kinetics and metal induced optical property change. We show that the designed red calcium binding sensor MCD1 (RapidER), on the surface of mCherry, is able to report calcium concentration by fluorescence in the range of 10^{-4}-10^{-3} M with an unprecedented dissociation rate in the magnitude of 10^3 s^{-1}. Our finding reveals essential factors needed for future design of fast calcium binding proteins, fulfilling a pressing need for monitoring calcium dynamics in fast biological processes. Table 1.2 summarizes the kinetic data of recent applied calcium indicators, and includes two calcium sensors developed by Yang's lab.

Table 1.2 Kinetic parameters of recent major calcium indicators.

GECI/Dye	Rise time constant	Decay time constant	k_{on} (M^{-1} s^{-1})	k_{off} (s^{-1})
GCaMP2[a]	14 ms	75 ms		13
GCaMP2[c]	0.63s	0.38s		2.6
TN-XL[a]	240 ms	430 ms		2.3
TN-XXL[f]	1.04 s	0.88 s		1.1
D1ER[b]			3.6×10^6	256
YC3.3[c]	1.41s	1.05s		12
YC3.6[c]	0.82s	0.73s		1.4
YC2.6[c]		5.24s		0.2
D3cpv[c]	0.68s	1.96s		0.5
TN-L15[c]	0.81s	1.49s		0.7
TN-XL[c]	0.59s	0.20s		5
GCaMP1.6[c]	1.38s	0.45s		2.2
CatchER		1.44 ms	~3.89×10^6	~700
RapidER		0.33 ms	>2.5×10^7	>2100
OGB-1[c]	0.24s	0.38s		2.6
Fluo-4[e]			6.0×10^8	210
Calcium Green-5N[d]			4.0×10^8	9259
Mag-Fura-2[d]			7.5×10^8	26760
Fluo-5F[e]			3.0×10^8	300

[a] McCombs, Methods, 2008, data collected *in vitro*.
[b] Palmer, PNAS, 2004, data collected *in vitro*.
[c] Hendel, J Neurosic, 2008, data collected *in vivo*.
[d] T-jump 1997
[e] Scott,R. J. Neurosci. 2006
[f] Mank M. Nat. Meth. 2008, 40 Hz AP (0.2-0.4 nA for 10 ms) in 2s

1.4 Fluorescent proteins

1.4.1 *mCherry, a red fluorescent protein originated from coral*

mCherry is a bright monomeric red fluorescent protein derived from DsRed, which was isolated from *Discosoma sp.*(108-110). mCherry has a cylindrical beta-can structure folded by eleven β-strands connected with main chain hydrogen bonds (Figure 1.4 A and C), belonging to the GFP super-family. The fluorophore is formed by autocatalytic cyclization of residues M66, Y67 and G68 and is buried inside the beta-can. The complex hydrogen-bond network between Met-Tyr-Gly triad and its neighboring residues produces the distinguished fluorescence, which exhibits an emission wavelength at 587 nm that can be excited at 610 nm. Unlike GFP (Figure 1.4 B and D), the chromophore conjugated system in mCherry is extended to the backbone of the residue Phe in the N-terminal of the chromophore Met so as to generate a bigger π-system than GFP. The lower energy results in the red shifted spectrum. Compared to GFP that have been widely expressed in established cell lines, primary cells and transgenic animals for the targeting imaging or detection of specific molecule, mCherry takes the advantages of its longer wavelength, pH tolerance and shorter maturation time. Long wavelength is preferred in molecular imaging studies of living subjects since it causes less photo damage to cells, less auto-fluorescence background and better tissue penetration (111).

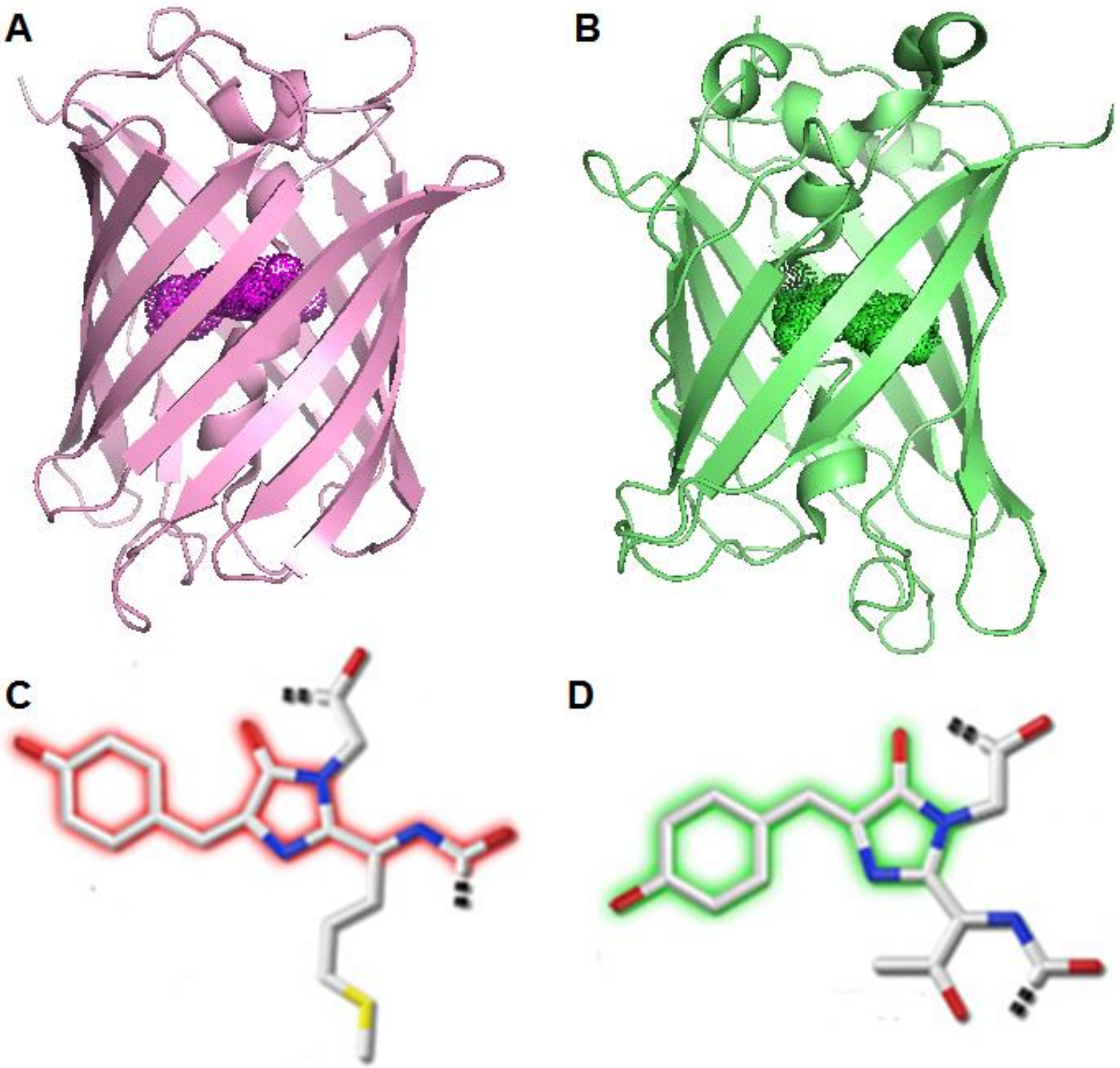

Figure 1.4. Crystal structure comparison of mCherry and GFP.
(A) The cartoon structure of mCherry (PDB ID: 2H5Q) and (B) The cartoon structure of GFP (PDB ID: 2WUR) with the chromophore presented in dots. The conjugated system are highlighted in the chromophores of mCherry (C) and GFP (D).

EGFP is derived from wild type GFP in 1995 with F64L and S65T, where S65T was first mutated by Tsien(112) to improve the spectral properties such as increasing fluorescence, photostability and shift the major exciation peak to 488 nm while maintaining the emission maxima. F64L was mutated by Thastrup based on S65T mutant to increase its folding efficiency at 37 ℃.

1.4.2 *cp-mKate, a far red fluorescent protein*

The mKate was first reported by Chudakov group in 2007, which is far-red fluorescent protein originated from sea anemone *Entacmaea quadricolor*, named eqFP578 (113). Chudakov and colleagues developed the protein TurboRFP featured with fast maturation, pH-stability and high brightness based on eqFP578, and further developed Katushka and its monomer mKate. The Stoke's shift of mKate is enlarged with the excitation and emission at 588 and 635 nm compared to mCherry (excited at 578 and emitted at 610 nm), as well as the quantum yield (φ=0.33). The extinction coefficient was 45 mM^{-1} cm^{-1}, and the brightness is around 45% of EGFP. The pKa of mKate (6.0) is greater than mCherry (3.5), suggesting that the chromophore is more protonated than mCherry at normal physiological condition (pH 7.2). There is no sign of aggregation formed when expressing mKate in mammalian cells so far. The crystal structure of mKate at different pH revealed the different isoforms of the chromophore. The *trans* form favors acidic environment and is dimmer than the *cis* form which is dominant at higher pH (71, 114). There is a light-induced *cis-trans* isomerization observed when irradiated by the green light.

The second generation of mKate is named mKate2, which was also reported by Chudakov's group (115). By mutions of V49A, M152T and K239R, its biophysical properties were enhanced. The quantum yield and the extinction coefficient were increased by 30% and 100%, respectively, resulting in the increase of the brightness of 300%. In addition, the pK_a was decreased to as low as 5.4.

1.5 Structure, dynamics and function of Calmodulin (CaM)

Calmodulin (CaM) is a ubiquitous, calcium binding protein which can be found in eukaryotic cells, to regulate a variety of physiological events. The genetic evolution of calmodulin shows it is a highly conserved protein, and calcium binding proteins found in high G+C Gram-positive bacteria appear high similarity with eukaryotic calmodulin, suggesting the evolutionary prototyping of EF-hand containing calcium binding proteins (116). The mammalian CaM has four EF-hand calcium binding motifs evenly distributed in two terminal domains. The calcium binding affinity of C-domain is 10-fold higher than that of N-domain (117, 118), in the range of 1-10 μM. The association and dissociation rate of calcium binding to the isolated CaM terminal domains were reported by several groups (119) including Baylay and the co-workers using ^{43}Ca NMR spectroscopy (100), Martin (120), Black (121) and Johnson (122) using stopped-flow. The dissociation rate (500-1000 s^{-1}) of N-domain is approximately 100-fold higher than that of C-domain (2-10 s^{-1}).

The cooperative binding of calcium ions at each domain induces global conformational rearrangement of CaM, which in turn binds the target protein to regulate a variety of physiological events. CaM adopts different conformations when interacts with the targets including enzymes and Ca^{2+}-activated channels (123). In addition, the domain motion can be independent for both two and function separately. For example, the activation and inhibition bifunctional regulation of CaM was found in the voltage-gated Ca^{2+}-channel $Ca_v2.1$, where Ca^{2+}-loaded CaM C-domain activate the channel while the N-domain occupied by Ca^{2+} due to increased intracellular [Ca^{2+}] inhibits the channel activity (124).

The structure of Ca^{2+}-free CaM was first solved by NMR due to lack of the well-folded rigid structure (125). The interaction between CaM and its target peptide, their dynamic properties and the binding mode is widely investigated by NMR spectroscopy, including the paramagnetic relaxation enhancement, residual dipolar coupling and T1/T2/NOE. The binding mode of

CaM plays essential role in modulating the conformational change and activity of the target protein, which will be discussed in Chapter 7.

1.6 Motivation of this dissertation and questions to be addressed

In the past decades, the Yang lab has been taking effort to understand the features of calcium binding and design the calcium binding site in the non-calcium binding proteins. The previous member revised the calcium binding sites in the protein database and pulled out the features. The tools of calcium binding site prediction were developed. Starting with CD2, we successfully added the calcium binding site and modulate the binding affinity. As accumulated experience and knowledge, the first GFP-based calcium indicator targeted in high calcium environment called EGFP-G1 was generated. To increase the dynamic range and the protein folding, continuous attempt was taken and one of the second generation of sensor s called CatchER, with dramatically increased dynamic range and kinetic property, was developed and applied in investigating the SR calcium change in collaboration with Dr. Osvaldo Delbono. Motivated by the need to expand the spectral window of calcium sensors for high calcium environment, and reduce the fluorescence dependence on physiological pH change, I desired to generate a class of red fluorescent protein-based calcium indicators.

Our challenges in this study are (1) to maintain the fluorescence while introducing the calcium binding ability; (2) to enlarge the dynamic range upon binding calcium; (3) to emerge the ratiometric change instead of the single wavelength change to avoid the background noise; (4) to modify the K_d to make it suitable for different cells.

The long term goal of the project is to design fluorescent calcium sensors and apply it to discover the calcium-dependent physiological functions and also to detect the relevant diseases. Quantitative real-time monitor of Ca^{2+} concentration in particular physiological microenvironment such as the endoplasmic reticulum (ER)/sarcoplasmic reticulum (SR) and interspace between adjacent cells is essential for exploring the mechanism of Ca^{2+}-dependent signaling processes. The idea of current reported genetically encoded Ca^{2+} sensors is based on natural Ca^{2+} binding proteins, calmodulin, which is limited due to the perturbation and interference of functional Ca^{2+} signaling (54, 126-128) and the bulky size of the fusion protein causes potential problems like maturation time, expression level and aggregation. Also, the natural high binding affinity (K_d ranged from nanomolar to micromollar) of calmodulin restricts their application for detecting the fluctuation of Ca^{2+} concentration in most calcium-related biological activities where the calcium level is approximately hundreds of nanomollar. To overcome these limitations, my purpose is to design Ca^{2+} biosensors by engineering a single Ca^{2+} binding site into monomeric fluorescent protein and target it to a specific subcellular location for spatial-temporal detection of calcium dyanmics.

To achieve the goal, several questions need to be answered in this dissertation: 1) what is the criteria to select fluorescent proteins to mount the calcium binding site? 2) How to control the calcium binding affinity? 3) How to improve the metal selectivity? 4) How to investigate and control the calcium binding induced conformational change? 5) How to correlate the calcium binding induced conformational change with fluorescence change? 8) What can be learned from the existing calcium indicators like CatchER? 7) How to select the tag for a specific targeting? 8) How to combine the structure, dynamics and function study of proteins?

1.7 Overview of this dissertation

To address the pressing needs for a red-shifted calcium indicator in high calcium subcellular environment and questions discussed above, in this Ph.D. dissertation, I have developed a class of red fluorescent calcium binding proteins, MCD1 series, by protein engineering.

Chapter 2 includes the experimental methods and protocols that we used for the dissertation.

Chapter 3 describes the rationales for design a class of calcium binding sites in the red fluorescent protein mCherry. The effort in cloning, expression, purification, optical, biophysical and conformational characterization, metal binding and *in situ* evaluation of MCD1 variants will be reported.

Chapter 4 reveals the structure and dynamics of CatchER in absence and presence of calcium by NMR and molecular dynamics simulation.

Chapter 5 reports the calcium effect on the ground and excited-state prototropic properties of CatchER.

Chapter 6 reports the screening of the ER membrane anchoring sequence, and the cellular localization, as well as the performance of calcium sensing *in situ* of the tagged CatchER.

Chapter 7 reports the dynamic interaction of calmodulin and its target peptides through the residual dipolar coupling and T1, T2, NOE by using NMR spectroscopy.

Chapter 8 introduces two case studies of investigating the conformational change of large proteins involved protein-ligand interactions by NMR incorporating selective labeling method.

In Appendix A and B, I organized the established protocols and scripts to analyze the NMR data, including calculation and fitting of the dynamics parameter by T1, T2 and NOE, analysis of RDC, and measurement of the hydrodynamic radius. Appendix C records the detailed hydrogen bond analysis by AMBER-PTRAJ (Chapter 4). Appendix D showed the method validation for the lysine methylation and the methyl signal detection by ^{1}H-^{13}C HMQC. Appendix E documented the protocol to produce lentivirus.

2 MATERIALS AND METHODS

2.1 Clone construction and PCR

2.1.1 *Materials and supplies*

Pfu DNA polymerase and the *E. coli.* strain XL-10 Gold were purchased from Stratagene. KOD hot start PCR kit (Novagen) was purchased from EMD Millipore. The *E. coli.* strain DH5α, the plasmid vector pCDNA3.1(+), was purchased from Invitrogen. All the restriction enzymes, T4 DNA ligase, and T4 polynucleotide kinase (PNK) were purchased from New England Biolabs. The rapid DNA ligase kit was purchased from Roche. The plasmid pRSETb encoding mCherry was obtained from Dr. Roger Tsien from University of California at San Diego. The plasmid pRSETa encoding cp-mKate was obtained from Dr. Michael Kotlikoff at Cornell University. Primers were ordered from Integrated DNA Technologies. DNA sequencing for all clones was carried out by GENEWIZ Inc.. The restriction enzyme cleavage was checked using the web server Web Cutter (http://rna.lundberg.gu.se/cutter2/). The plasmid extraction was carried out using the QIAGEN mini-prep and maxi-prep kits.

2.1.2 *Approaches*

mCherry or cp-mKate variants with designed binding sites were created by site-specific mutagenesis using *Pfu* DNA polymerase. The grafting method was used to insert a Ca^{2+} binding motif or replace a segment of DNA, for example, to substitute an original loop with a Ca^{2+} binding motif. The primers were designed by limiting the melting temperature T_m of the annealed fragments in the range of 55-65 °C, not longer than 45 base pairs (bps) and the GC content less than 70%. T_m was calculated using the salt-adjusted equation (Equation 2.1).

$$Tm = 81.5 + 16.6 \times (\log_{10}([Na^{+}] + [K^{+}]) + 0.41 \times (\%GC) - 675 / N$$ Equation 2.1

mCherry subcloned to pRSETb was consisted of a His-tag, a T7 phage gene 10 leader enhancing the expression of foreign DNA in E. coli., the enterokinase (EK) cleavage site and the mCherry gene in order from 5' to 3' end. The BamHI restriction site was inserted right after the EK cleavage site and *EcoRI* site was located after the stop codon. For mammalian expression, the DNA encoding the designed proteins was subcloned to pCDNA3.1(+) vector by inserting the *BamHI*/*EcoRI* double digested DNA from the pRSETb vector. The mCherry DNA was sub-cloned to pET28α for bacterial expression as well using the same double digestion method. To target the proteins in endoplasmic reticulum (ER) lumen, ER retention sequence KDEL was fused to the C-terminal before the stop codon and ER targeting sequence of calreticulin MLLSVPLLLGLLGLAAAD was inserted to the N-terminal after *SacI* recognition site of pCDNA3.1(+) and before the *BamHI* site.

2.2 Protein expression and purification

2.2.1 *Materials and supplies*

The granulated LB broth miller media, yeast extract, tryptone, agar were purchased from EMD Millipore. The *E. coli.* strains BL21(DE3), BL21 (DE3) PlysS and Rosetta gami DE3 PlysS were obtained from Novagen for protein expression. The polyclonal anti-DsRed antibody was purchased from Clontech. The isotopic labeled $^{15}NH_4Cl$ was purchased from Cambridge Isotope Laboratories Inc.. The FPLC system (AKTA prime and AKTA FPLC), the Ni-chelating Hi-Trap column, the ion exchange Q and SP column, the gel filtration Superdex-75 column and the hydrophobic interaction HIC column, were purchased from GE Healthcare.

2.2.2 *Approaches*

For 1 liter media, 25 g LB broth medium was used and pH was adjusted to 7.0, followed by autoclave at 121 ℃, 15 MPa for 15 min. *E.coli.* strain BL21(DE3) was screened to express wild type EGFP and its variants, wild type mCherry, MCD1 and its derivatives, while BL21(DE3) PlysS was selected to express MCD2 and its derivatives. mCherry and its variants were fused into pRSETb with resistance of ampicillin; EGFP and its variants were fused to pET28b with resistance of kanamycin. Bacteria with the desired plasmid were precultured in 10 ml LB media containing the particular antibiotics (100 μg/ml ampicilin for pRSETb and 30 μg/ml kanamycin for pET28b) overnight at 225 rpm, 37 ℃. The preculture was mixed with 1 L fresh LB media containing antibiotics and the culture was continued to be incubated at 37 ℃, 225 rpm until OD600 reached 0.5-0.6. At this point, 200 μl IPTG (1 M stock) was added to induce expression and the temperature was lowered to 25 ℃. The protein was expressed for overnight. To express proteins in Rosetta gami (DE3) PlysS, the temperature was adjusted to be 30 ℃ after mixing the 10 ml preculture to the 1 L media pre-warmed at 37 ℃, allowing the bacteria to adopt the temperature change before IPTG induction.

The cell pellets were harvested by centrifugation at 5,000 g at 4 ℃ for 10 min. Extraction buffer (20 mM Tris, 100 mM NaCl, 0.1% Triton X-100, pH 8.0) was added to resuspend the pellets. Both French Press (1240 CELL DIS) and sonication (Brenson Sonifier 450) were used to break the cells. For French Press, 20 mL extraction buffer was used for 1 L culture and 1000 psi was applied to break cells according to the manufactory manual. For sonication, 10 ml extraction buffer was used for 1 L culture and the instrument was set as output control at 6, duty cycle at 80% and 30 pulses for one cycle. 6 cycles were applied and the interval between two cycles was 5 min. Centrifugation at 17,000 rpm at 4 ℃ for 30 min was applied to separate the cell debris and the soluble parts. The protein solution was filtered using 0.45 μm membrane (Millipore) and loaded to 5 ml Hi-Trap column charged with Ni^{2+}. FPLC was chosen to purify the protein of interest using AKTA prime. Before loading the protein, the column was charged with 0.1 M $NiSO_4$ and equilibrated with Buffer A (50 mM phosphate, 250 mM NaCl, pH 7.4). The pump B was washed by Buffer B (50 mM phosphate, 250 mM NaCl, 0.5 M imidazol, pH 7.4). Protein with His-Tag was bound to column while other nonbound fragments were washed away by 300 ml Buffer A. An additional wash step was done with 10 ml 10% Buffer B. A gradient of 10-100% Buffer B was applied to elute the bound protein. The purity of fractions was determined by SDS-PAGE. The additional purification steps were required if the SDS-PAGE gels showing the existence of other proteins. The Mono-Q column and gel filtration Superdex-75 column were used to remove impurities. The purified fractions were collected and dialyzed in 2 L buffer of 10 mM Tris (pH 7.4) three times. The dialyzed protein was then concentrated and stored at -20 ℃ or used for experiments.

2.3 Determination of biophysical properties

2.3.1 *pK_a measurement*

To measure the chromophore pK_a of mCherry variants, separate samples were made at each pH to be measured and the absorbance and fluorescence of the samples were examined. Various buffers were utilized to maintain the pH at each desired value, which are listed in table 2. The protein concentration was ~10 μM for each mutant. The samples were allowed to equilibrate overnight at 4^oC. For UV-vis spectra, a baseline was run for each pH with the appropriate buffer before the sample at that pH was measured. The absorbance was measured from 700 nm to 220 nm so all protein peaks would be included. The fluorescence was measured with the excitation at

587 nm, and the emission spectra were collected from 595 to 700 nm while the excitation scan was done by fixing emission maxima at 610 nm and spectra was from 450 to 600 nm. The sample at pH 9 was measured first so the slit widths could be set for optimal intensity, and the samples were measured with decreasing pH. The pH was calculated after the spectra were acquired using Equation 2.2.

$$Y = \frac{Y_{\min} \times 10^{-pH} + Y_{\max} \times 10^{-pKa}}{10^{-pH} + 10^{-pka}}) \qquad \text{Equation 2.2}$$

Table 2.1 A list of the buffers utilized for the pH dependence measurements.

Buffer	**pH**
0.5 M Sodium Acetate (CH3COONa)	2.0
10 mM Sodium Acetate (CH3COONa)	3.0, 4.0, 4.5
10 mM MES (2-Morpholinoethanesulfonic acid)	5.0, 5.5, 6.0
10 mM PIPES (1,4-Piperazinediethanesulfonic acid)	6.5, 7.0
10 mM Tris [Tris (hydroxymethyl) aminomethane]	7.4, 8.0, 9.0

2.3.2 *Extinction coefficient of mCherry and its variants*

The molar extinction coefficient (ϵ) of a protein at 280 nm depends almost exclusively on the number of aromatic residues, particularly tryptophan, and can be estimated from the sequence of amino acids. If the extinction coefficient is known, it can be used to determine the concentration of a protein in solution based on the Beer’s law. All proteins contribute to absorbance at 280 nm. Here we concern about dimerization and cleavage of mCherry according to the SDS-PAGE results. In order to calculate the extinction coefficient of the chromophore, the extinction coefficient of alkali denatured chromophore was used as a reference(58, 109). The chromophore at pH 13 has the same extinction coefficient and the absorbance maxima shifts to around 455 nm as long as the chromophore is the same. Aliquot of 10 M NaOH was added to the sample to reach pH 13 and the spectrum was taken immediately. Equation 2.3 was used to calculate the extinction coefficient.

$$\varepsilon_{587nm} = \varepsilon_{455nm}(\frac{A_{587nm}}{A_{455nm}}) \qquad \text{Equation 2.3}$$

In the equation 3, ε is the extinction coefficient; A is the absorbance. $\varepsilon_{587\text{ nm}}$ and $A_{587\text{ nm}}$ were obtained from the mCherry and its variants at pH 7.4, while $\varepsilon_{455\text{ nm}}$ and $A_{455\text{ nm}}$ were from the proteins at pH 13.0, which in principle is the same for all variants.

2.3.3 *Quantum yield and brightness of mCherry and its variants*

The quantum yield (Φ) of a protein is defined as the number of photons emitted as fluorescence, divided by the number of excited states that were produced in the excitation (129) (130). In other words, it is the fluorescent light emitted by the protein divided by the absorbance of light of the protein. A quantum yield ratio of zero value means no fluorescence, while a quantum yield ratio of 1 means 100% fluorescence. As described by equation 2.4, we can determine the quantum yield for mCherry proteins by measuring the emitted fluorescent intensities at 610nm and the absorbance of the chromophore at 586 nm at different protein concentrations. In this work, we will used mCherry WT as a control to calculate quantum yield of other variants. By calculating both the molar extinction coefficient and quantum yield of a specific variant, we can obtain the brightness of that protein by using Equation 2.5, which is the product of the two values. Brightness is defined as a visual perception in which a source appears to emit or reflect a given amount of light. In other words, brightness is the perception elicited by the luminance of a visual target (58, 129) (130).

Ultraviolet and visible (UV-vis) absorption spectra of mCherry and its variants were determined with a Shimadzu UV-1601 spectrophotometer (Shimadzu). A fluorescence spectrophotometer (Photon Technology International, Inc.) was used to monitor the fluorescence property with a 10 mm path length quartz cell at room temperature. The fluorescence emission spectra were collected in the region of 595-750 nm when excited at 587 nm; likewise, the excitation spectra were measured in the region of 400 -600 nm when emitted at 610 nm. The quantum yield and brightness of all mCherry variants were calculated using Equations 2.4 and 2.5.

$$\varphi_P = \varphi_r \left(\frac{F_P}{A_P}\right) / \left(\frac{F_r}{A_r}\right) \qquad \text{Equation 2.4}$$

$$B = \varphi \times \varepsilon \qquad \text{Equation 2.5}$$

In Equation 2.4, φ is the quantum yield of the protein of interest; F/A is the slope of the fluorescence intensity as a function of the absorbance; the subscript P indicates the protein of interest and r indicates the reference protein, which is the wild type mCherry in this work.

2.4 Metal binding assays for designed calcium binding proteins

2.4.1 *Dissociation constant (K_d) determination*

Calcium was titrated to the protein sample to trigger the increase of fluorescence until the fluorescence intensity reach maximum. The commercial standard calcium chloride solution of 100 mM was used for titration. For each sensor, triplication of calcium titration was carried out. For CatchER, protein samples of concentration of 2 µM, 10 µM and 20 µM were tested to verify that K_d is protein concentration independent. For mCherry, 5µM and 10 µM protein was used. The K_d was calculated using Equations 2.6 and 2.7(131).

$$f = \frac{F - F_{\min}}{F_{\max} - F_{\min}} = \frac{[P]_T + [Ca^{2+}]_T + K_d - \sqrt{([P]_T + [Ca^{2+}]_T + K_d)^2 - 4[P]_T[Ca^{2+}]_T}}{2[P]_T} \qquad \text{Equation 2.6}$$

$$\frac{\Delta F}{F_{\min}} = \frac{F - F_{\min}}{F_{\min}} = \frac{a \times [Ca^{2+}]}{(K_d + [Ca^{2+}])} \qquad \text{Equation 2.7}$$

Here, F is the fluorescence intensity read from the fluorimeter; F_{max} and F_{min} are the highest and lowest fluorescence intensity reading in an individual experiment; $[P]_T$ and $[Ca^{2+}]_T$ are the total concentration of protein and calcium; a is the dynamic range of fluorescence change.

2.4.2 *Calcium binding using Tb^{3+} as a probe*

To further prove the calcium binding to mCherry-based calcium sensors, Tb^{3+}-FRET was applied. Titration was monitored by fluorescence spectrophotometer (Photon Technology International, Inc.) with excitation at 282 nm and emission in the range of 500-570 nm. To avoid precipitation due to the formation of $Tb(OH)_3$, pH was maintained at 6.5 using 20 mM PIPES. KCl with a final concentration of 10 mM was supplemented to minimize non-specific metal binding. Tb^{3+} stock was prepared in the same buffer with a final concentration of 10 mM and 100 mM. Protein concentration was approximately 6 μM to ensure the amount of the donor for FRET, and minimize the precipitation as well.

2.4.3 *Metal selectivity*

Selectivity of a calcium sensor against other physiological metals and small molecules is an important criterion. The physiological metals such as Mg^{2+}, Zn^{2+}, Cu^{2+}, Na^+ and K^+, and small molecules such as ATP, GTP, ADP and GDP were added to the sensor pre-loaded with 1 mM Ca^{2+}. The optical properties was monitored by both UV-vis and fluorescence spectrophotometer. The concentrations of each competitor were as least 5 times as much as those of the free form in the physiological conditions.

2.4.4 *Equilibrium dialysis assay*

2.4.4.1 Simulation of equilibrium-dialysis assay

The purpose of the dialysis equilibration is to verify the direct binding of calcium to the protein. The protein filled into the dialysis bag was dialyzed against 10 mM Tris-HCl buffer containing calcium at certain concentration. When reaching the equilibrium state, since protein binds to calcium, the total calcium inside the dialysis bag is more than that of the same volume of the buffer outside the bag. The difference can be detected by ICP-OES. This method can verify the ligand binding even the binding is weak, for example, in the magnitude of 10^{-3} M. The scheme 1 shows the typical 1:1 binding reaction.

$$Ca^{2+}P \xrightarrow{K_d} Ca^{2+} + P \qquad \text{Scheme 2.1}$$

In the equilibrium state, there is:

$$\begin{aligned}
&P_{free} = P_t - Ca^{2+}P \\
&Ca^{2+}P = Ca^{2+}{}_{it} - Ca^{2+}{}_{free} \\
&K_d = \frac{Ca^{2+}{}_{free} \times P_{free}}{Ca^{2+}P} \\
&P_{free} = \frac{K_d \times P_t}{K_d + Ca^{2+}{}_{free}} \\
&\frac{Ca^{2+}{}_{it}}{Ca^{2+}{}_{free}} = \frac{Ca^{2+}{}_{free} + P_t - \dfrac{K_d \times P_t}{K_d + Ca^{2+}{}_{free}}}{Ca^{2+}{}_{free}}
\end{aligned} \qquad \text{Equation 2.8}$$

To achieve the optimal result, the simulation was run by MatLab based on Equation 2.8. Assuming the K_d value is 0.5 μM and the unit for both protein and calcium is μM, the Matlab m file as below:

```
clear all
close all
clc

[x,y] = meshgrid(0:5:1000);
z=(x+y-x*500./(500+y))./y;

meshz(x,y,z);
xlabel('P_t');
ylabel('Ca_(71)');
zlabel('Ca_(132)/Ca_(58)');
```

2.4.4.2 Total metal measurement using ICP-OES

The equilibrium-dialysis assay was conducted to illustrate the binding constant of mCherry variants. The positive (α-lactalbumin) and negative (w.t.-mCherry and buffer) control was used to validate this method. According to a simulation of this experiment, to obtain the large ratio of $[Ca^{2+}]_{bag}$ to $[Ca^{2+}]_{out}$, the concentrated protein and small calcium will be used. For this experiment, 5 ml 30 μM protein in 10 mM Tris, pH 7.4 was dialyzed against 1.6 L buffer containing 15 μM Ca^{2+} 10 mM Tris, pH 7.4 for 48 h at 4 ℃. The sample inside and outside the dialysis bag were collected and analyzed using ICP-OES. To obtain Well-folded mCherry variants concentration was determined by UV at 587 nm and total protein concentration was determined using extinction coefficient at 280 nm.

The standard calcium solution was prepared by commercial calcium standard (0.1 M VWR) and the ultra-pure water supplemented with 2 % HNO_3 as Table 2.2 below. The internal standard is 1 g/ml YCl_3, prepared in 2% HNO_3. The calcium concentration was monitored by the following wavelength in nm: 396.847, 317.933, 219.779, 370.602, 643.907, 220.861 and 373.690. The $[Y^{3+}]$ is monitored by 360.074 and 371.029 nm.

Table 2.2 Preparation of calcium standard for ICP-OES calibration

Ca^{2+} ([a]ppm)	Ca^{2+} (µM)	Total volume (ml)	Add [d]blank (ml)	Take out blank (µl)	[b]Ca^{2+} stock 1 (µl)	Final HNO_3
10	250	15	15.00	37.50	37.5	2.00
4	100	15	15.00	15.00	15	2.00
3	75	15	15.00	11.25	11.25	2.00
2	50	15	15.00	7.50	7.5	2.00
1	25	15	15.00	3.75	3.75	2.00

Ca^{2+} (ppm)	Ca^{2+} (µM)	Total volume (ml)	Add blank (ml)	Take out blank (µl)	[c]Ca^{2+} stock 2 (µl)	Final HNO_3
0.5	12.5	15	15.00	37.50	37.5	2.00
0.3	7.5	15	15.00	22.50	22.5	2.00
0.1	2.5	15	15.00	7.50	7.5	2.00
0.05	1.25	15	15.00	3.75	3.75	2.00
0	0	15	15.00	0.00	0	2.00

[a]1 ppm = 1 µg/ml; [b]Ca^{2+} stock 1=100 mM (Std. from VWR); [c]Ca^{2+} stock 2=5 mM prepared by 2% HNO_3 in ultra-pure water; [d]HNO_3 final=2%, prepared using 70% HNO_3 diluted by ultra-pure water.

2.5 Kinetics study of calcium binding

Stopped-flow kinetic measurement were performed on a Hi-Tech SF-61 stopped-flow spectrofluorimeter equipped with the mercury-Xe lamp (10 mm path length, dead time of 2 ms) with a 1:1 (v/v) ratio of the protein sensor and calcium at 20 °C. Fluorescence emission changes associated with binding of calcium to the protein were determined by mixing calcium in the range of 1/5 K_d - 5K_d and 10 mM Tris buffer, pH 7.4 with excitation at 587 nm and a long-pass 600 nm filter. Florescence changes associated with dissociation of calcium from the protein were measured upon mixing the protein pre-loaded with calcium of the concentration equal to K_d and EGTA of 10-fold equivalent protein concentration in the same buffer. Generally, six duplicate measurements were carried out for each point, and the last three were fitted to obtain the observed rate, k_{obs}, by fitting of the stopped-flow traces according to the single-exponential function shown in Equation 2.9.

For MCD15, which has K_d at 0.5 mM, the final [Ca^{2+}] are: 100, 200, 300, 500, 900, 1300, 2500 µM. Calcium solutions will be prepared as: 200, 400, 600, 1000, 1800, 2600, 5000 µM. To obtain a high S/N ratio, the fluorescence intensity is required to be high. Also, the lowest calcium concentration should be at least 5 times higher than the protein concentration to fulfill the assumption that [Ca^{2+}] >> [Protein]. As a result, the final protein concentrations were 10 and 20 µM. MCD15 purified from pET28α in *E. coli.* BL21 (DE3) was used for the kinetics study. The lowest (buffer) and highest signal (protein mixed with calcium of the highest concentration) will be taken first to figure out the dynamic range, and the instrument setting will be adjusted to enhance the dynamic range.

$$
\begin{aligned}
&F = F_0 + amp[1 - \exp(-k_{obs} \times t)] \\
&F = F_\infty - amp \times \exp(-k_{obs} \times t) \\
&amp = F_\infty - F_0 \\
&k_{obs} = k_{on} \times [Ca^{2+}] + k_{off} \qquad \text{Equation 2.9} \\
&K_d = \frac{k_{off}}{k_{on}} \\
&k_{obs} \times \tau = \ln 2
\end{aligned}
$$

Here, F is the fluorescence intensity reading from the fluorimeter; F_0 is the initial fluorescence intensity, which is the lowest one as well; F_∞ is the fluorescence maximum; amp is the amplitude of the fluorescence; k_{obs} is the observed rate constant, which is obtained by exponential fitting the fluorescence time course; k_{on} and k_{off} are the on and off rate of calcium binding; τ is the observed lifetime of calcium dissociation.

2.6 Fluorescence lifetime measurement

2.6.1 *Sample preparation*

Proteins used for the lifetime measurement were expressed by *E.coli*. BL21 (DE3) Gold and purified using the Ni^{2+} charged prepacked Hi-Trap column and the size exclusion column packed with Superdex-75 (GE Healthcare). The concentrated pure protein in 10 mM Tris, pH 7.4, were lyophilized and dissolved by in H_2O and D_2O (95% D). The final pH and pD were checked and adjusted to 7.4 and 7.8, respectively. To obtain the optimal signal in lifetime measurements, the absorbance spectra were collected and the protein concentration was adjusted to get the peak height maximum at 395 nm in the range of 0.2-0.3. The final concentration of 10 mM Ca^{2+} was supplemented to obtain the calcium-loaded CatchER.

2.6.2 *Lifetime measurements*

The fluorimeter was equipped with two lasers, 372 nm and 467 nm. Both wavelengths were applied to excite the neutral and anionic forms of CatchER. The monitored emission wavelengths are 440 nm for the neutral form, 510 nm for the anionic form. The 1024 data points were collected for the set of excitation at 372 nm and emission at 440 nm in 5 ns and 20 ns separately, with steps of 0.004883 ns and 0.019531 ns, respectively. For the sets of emission at 510 nm, 1024 data points were collected in 20 ns and 50 ns, with steps of 0.019531 ns and 0.04883 ns, respectively. All measurements were carried out at 25 ℃.

2.6.3 *Data analysis*

The instrument response function was taken into account and deconvoluted using the program FFIT developed by Tkachenko (Equation 2.10). The time course of fluorescence decay was fitted using exponential equation (Equation 2.11). The artificial components were ignored, which was recognized as the negative amplitude reflecting the initial fluorescence rise prior to decay, the component with lifetime smaller than 10 ps and greater than 15 ns. The valid fitting fulfilled the conditions of chi-square in the range of 0.9-1.3 and the residuals in the range of ±4. The average lifetime was calculated as Equation 2.12 for each fitting.

$$F_i(t) = \int I(x+t+s_i)\, f_i(x)dx \qquad \text{Equation 2.10}$$

$$f_i(t) = A_{i0} + \sum A_{ij} \exp(-t/\tau_j) \qquad \text{Equation 2.11}$$

$$\tau_{ave} = \sum\left(\frac{A_i}{\sum A_i}\tau_i\right) \qquad \text{Equation 2.12}$$

Here, $F_i(t)$ is the fluorescence intensity at any given time t; I is the instrumental response function; $f_i(x)$ is the real fluorescence of the chromophore/protein at the time x; A is the amplitude of the background fluorescence; τ_i is the lifetime of the component i.

2.7 Nuclear magnetic resonance spectroscopy

The molecule dynamics can be roughly classified by the time scale. The molecule tumbling is ranged in pico-sec to nano-sec. The molecule internal motion is from pico-sec to micro-sec. The molecule diffusion is relatively slow, in the range of milli-sec to sec. The chemical reaction or exchange has a larger range, from sub-micro-sec to sec.

2.7.1 *Protein dynamics study by T1, T2, and Nuclear Overhauser Effect (NOE)*

The molecule tumbling ranged in pico-sec to nano-sec motion can be studied by collecting T1, T2 relaxation and internal ratio of NOE values. From R1, R2 and NOE, the dynamic parameters like J(0), $J(\omega_N)$, $J(0.87\omega_H)$, the order parameter S^2, correlation time $\boldsymbol{\tau}_c$ and exchange rate R_{ex} can be obtained by reduced spectral density function mapping. The greater internal motion can be reflected by decrease of J(0) and J(ω_N) and increase of J(0.87ω_H). The chemical exchange is reflected by significantly increased J(0). S^2 is the square of the generalized order parameter characterizing the amplitude of the internal motion, which can be used to justify the degree of the internal motion, ranged in 0-1. If S^2=1, you will stay in the same orientation at any time, meaning that this residue is completely rigid. The correlation time is the measure of how fast a molecule tumbling in the liquid, or the rate of molecule motion, which is different from the isotropic rotational correlation time τ_m. The exchange rate R_{ex} is a function of exchange rates, populations and chemical shifts of different conformations. See the protocol of the data processing in Appendix A.1.

2.7.2 *Residual dipolar coupling (RDC)*

RDC originates from the anisotropic component of the dipolar interaction, which is dependent on the angle between an internuclear vector and the magnetic field. When a molecule orients uniformly as it does in normal solution, RDCs average to zero and are not observable. If it is dissolved in a dilute liquid crystalline medium or other orienting medium, it becomes partially aligned and the dipolar couplings are not completely averaged to zero. This leads to a small contribution to the splitting of NMR signals. The angular dependence of these contributions provides the structural information. RDCs can be used to validate protein structures, to refine structures to improve quality, and to provide constraints as a part of an initial structure determination. RDCs can also be used to determine the rotational symmetry axis of oligomers and this information can be used to properly orient the positions of subunits within an oligomeric complex.

HSQC-TROSY pairs provide one way of measuring RDCs. The procedure is applicable to proteins of small and moderate size (10-30 kDa). The measurements are easily visualized as displacements of peaks in 2D frequency domain spectra. The HSQC member of the pair gives a single peak at the center of the four peaks expected in a fully coupled HSQC experiment. The TROSY member gives only the sharpest component. The offset in either H or N direction is one half (J). Transfer all assignments (or cross peak labels) from a reference isotropic HSQC spectrum to TROSY and HSQC spectra obtained under both isotropic and aligned conditions. Transferring assignments is usually straightforward because the positions of cross-peaks in the aligned HSQC spectrum usually change little with addition of an alignment medium; if they do change, there is often a constant offset for all peaks due to changes in the lock resonance. Corresponding peaks for TROSY assignments are diagonally displaced (down and to the right) by 38-58 Hz. The isotropic coupling (J) is calculated from the difference in Hz between the ^{15}N dimension of isotropic HSQC and TROSY spectra (the offset is one half (J), so the final value needs to be multiply by 2). Similarly, the aligned coupling (J+D) is calculated from differences in peak positions for the aligned HSQC and TROSY spectra. The Hz values of the corresponding peaks can be subtracted to calculate the RDC values.

The J-modulation is another way to measure RDC. J-modulation is a kind of intrinsic interconvertion of in-phase and anti-phase magnetization, resulting in a combination of absorption and dispersive lineshapes which depends on the delay time envolved. An array of the delay is applied to obtain a series of 2D spectra. The max delay should be bigger than 3/(2J) to make sure the modulation curve crosses zero at least twice. The coupling constant J is obtained by curve fitting using Equation 2.13.

$$f(x) = c * (-a + \cos(3.14159 * 2 * j * x)) * \exp(-2 * x/t) \qquad \text{Equation 2.13}$$

where f(x) is the intensity and x is the delay time, t is the T2 relaxation time, j is the coupling constant of one-bond N-H in Hz, a is the variable accounting for the imperfection of pi pulses during the experiment, and c is the initial intensity of the peak. See the protocol of the data processing in Appendix B.

2.7.3 *Molecular hydrodynamic radius*

The pulsed-field-gradient NMR can be used to calculate the hydrodynamic radius by Stokes-Einstein equation, where the diffusion coefficient is inversely proportional to hydrodynamic radius. In this experiment, the temperature and the solvent viscosity affect the measurement of diffusion coefficient. The internal standard, e.g., a small molecule, can be added. So there is $R_{ref}*D_{ref}=R_{pro}*D_{pro}$. A series of 40 spectra is collected with the strength of the diffusion gradient varying between 5-100% of the max gradient level. See protocol in Appendices A and B.

2.8 Computer assisted structure model building

2.8.1 *Using delphi to create the electrostatic potential map*

Delphi is used to calculate the electrostatic potential in and around macromolecules(133). The chromophore is not a standard amino acid, which is necessary to have one more step to create the atomic radii and charge files for the chromophore manually, which are shown below:

mc-cro.crg

```
! united atom amber charges for chromophore of mCherry
CE    CH6      0.007
N1    CH6     -0.520
CG1   CH6      0.090
CB1   CH6      0.037
SD    CH6     -0.025
```

```
CA1   CH6      0.137
C1    CH6      0.526
N2    CH6      -0.277
OH    CH6      -0.368
CD2   CH6      -0.035
CE2   CH6      0.100
CZ    CH6      -0.121
CE1   CH6      0.100
CD1   CH6      -0.035
CG2   CH6      -0.001
CB2   CH6      0.022
CA2   CH6      0.245
C2    CH6      0.526
O2    CH6      -0.500
N3    CH6      -0.194
CA3   CH6      0.246
C3    CH6      0.526
O3    CH6      -0.500
```

mc-cro.siz

```
N1    CH6   1.5
CE    CH6   1.7
SD    CH6   1.85
CG1   CH6   2.0
```

```
CB1   CH6   2.0
CA1   CH6   2.0
C1    CH6   1.7
N2    CH6   1.5
OH    CH6   1.4
CD2   CH6   1.7
CE2   CH6   1.7
CZ    CH6   1.7
CE1   CH6   1.7
CD1   CH6   1.7
CG2   CH6   1.7
CB2   CH6   2.0
CA2   CH6   1.7
C2    CH6   1.7
O2    CH6   1.4
N3    CH6   1.5
CA3   CH6   2.0
C3    CH6   1.7
O3    CH6   1.4
```

The parameter file (fort.10) is the one to allow Delphi to configure the library, the protein and the environment conditions. The size and charge files (For) and the protein (pdb) are required. Other parameters, like grid size and scale, salt concentration, dielectric constant, *etc.*, should be defined by users. One example of the parameter file (fort.10) for running Delphi shows below:

```
gsize=150                    #grid size
scale=2.0                    #lattice spacing in number of Angstrom
in(pdb,file="2h5q.pdb")      #input pdb file
in(siz,file="parseres-mc.siz    #input atomic radii library
in(crg,file="parseres-mc.crg")   #input atomic charge library
indi=2.0                     #dielectric constant inside
exdi=80.0                    #dielectric constant outside
prbrad=1.4                   #radius (in A) of the water probe mol
salt=0.02                    #salt concentration
bndcon=2                     #2-Debue-Huckel potential of the equ. dipole
maxc=0.0001                  #potential max change threshold
linit=800                    #linear iterations
out(modpdb,file="2h5q_delphi.pdb") # output modified pdb
out(phi,file="2h5q.phi",format=2)  # output electrostatic density map
energy(s,c,g)                # write out energy
```

Users have four choices for boundary conditions (bndcon): potential zero; Debue-Huckel potential of the equivalent dipole to the molecular charge distribution; focusing from a previous phi-map calculation; Debue-Huckel potential of all charges (coulombic). The flag of MAXC is suggested to be defined by the DELPHI MANUAL, which is the convergence threshold value based on root mean square change of potential. A low maximum change in the potential is a sign for a good convergence, for example, 0.001 [kT/e]. The iteration (linit) needs to be sufficient to allow the final maximum change less than the maxc value defined. Energy output can be written in grid (g), salvation (s), coulombic (c), analytical surface (as) and analytical grid (ag).

2.8.2 *Using Modeller to build the structure model*

Modeller is a tool used to build a structural model based on a given template, which is suitable for building the model of mCherry variants. Modeller is written by Python, which can be run either in the Python shell or under prompt with the script. The template is necessary for the model construct. In our case, the template is the wild type mCherry. The variants were aligned with the w.t. mCherry. The alignment file (*.ali) was generated by Modeller, which was used for building models. The scripts for alignment and model building are shown below:

```
 from modeller import *
env = environ()
aln = alignment(env)
mdl = model(env, file='mcwt', model_segment=('FIRST:A','LAST:A'))
aln.append_model(mdl, align_codes='mcwt', atom_files='mcwt.pdb')
aln.append(file='variant.ali', align_codes='variant')
aln.align2d()
aln.write(file='v-wt.ali', alignment_format='PIR')
aln.write(file='v-wt.pap', alignment_format='PAP')
```

The script for running Modeller is:

```
from modeller import *
from modeller.automodel import *
env = environ()
```

```
a = automodel(env, alnfile='v-wt.ali',
              knowns='mcwt', sequence='variant',
              assess_methods=(assess.DOPE, assess.GA341))
a.starting_model = 1
a.ending_model = 5
a.make()
```

The number of models generated can be defined by user with the flag a.starting_model and a.ending_model. The scoring methods of DOPE and GA341 were used in this model building. DOPE (discrete optimized protein energy) model score is designed for selecting the best structure by the satisfaction of global spatial restrains from a collection of models built by Modeller (134). DOPE is derived from an atomic distance-dependent statistical potential from a sample of native structures independent on any adjustable parameters, which uses the noninteracting atoms in a homogeneous sphere as the reference state. As a result, it accounts for the finite and spherical shape of the native structure. GA341 is the scoring function based on the compactness of the model, a combined statistical potential z-score and the percentage sequence identity of the alignment (135).

The program was run under the cmd in Windows XP by typing the command:

```
>mod9v8 aln.py
>mod9v8 model.py
```

2.8.3 *Using AutoDOCK-VINA to dock calcium ion to designed calcium binding proteins*

AutoDOCK-VINA is used to predict the interaction between a ligand and a protein. VINA is the newest version of Autodock, which improves the performance of the old version and keep the algorithm. The format of input file of both ligand and protein should be pdbqt, which can be generated by Autodock Tools or MGL Tools (The Scripps Research Institute). The polar hydrogens should be added first and charge will be assigned and written into the pdbqt file. This input file, including the coordinates and the partial charge of each atom, will be generated automatically when choosing the macromolecule in the menu of Grid. The grid size and positions can be set in the Grid Box, which is required for VINA.

To run VINA, the configuration file named **conf.txt** should be written by the user. The input receptor (protein) and ligand pdbqt files are directed, as well as the grid information. One example as:

```
receptor = MC_P1-min.pdbqt
ligand = ca.pdbqt
center_x = 40.819
center_y = 18.051
center_z = 13.987
size_x = 48
size_y = 54
size_z = 50
exhaustiveness = 8
```

The center_x/y/z and size_x/y/z are the parameters of the grid box, which is read from the MGL Tools. Under cmd, go to the directory of all pdbqt files, and type:

```
“\Program Files\The Scripps Research Institute\Vina\vina.exe” –config conf.txt –log log.txt
```

2.8.4 *Molecular dynamic simulation of CatchER*

2.8.4.1 Preparation of the chromophore using GAUSSIAN and RESP

RESP (Restrained Electrostatic Potential) charge derivation is used for assign partial charges for a “new” molecule. It is a crucial step in the molecular dynamics simulation based on AMBER and CHARMM force fields. To obtain the partial charges by this method, quantum chemistry calculation is first applied to optimize the molecule to output a stable minimized structure and subsequently to calculate a molecular electrostatic potential (MEP) in a three-dimensional grid which is generated by GAUSSIAN or GAMESS. RESP program is then used to fit an atom-centered charge to MEP.

Here, R.E.D. (RESP ESP charge Derive) program was used for derive RESP charges for the chromophore. In the R.E.D. program, two steps of the quantum chemistry calculation and the final charge fitting are integrated and no format conversion is required. This program is executed under LINUX platform. The initial input file of the chromophore in PDB format is directly extracted from the mCherry structure (PDB ID: 2H5Q). Then Ante_R.E.D. program will generate five files for further quantum calculation, including P2N file (.p2n), PDB output (.pdb), GAMESS input file (.inp), GAUSSIAN input file (.com), and the file containing atom connectives (.txt).

The command is:

```
perl Ante_RED.pl cro.pdb > Ante_RED.log
```

GAUSSIAN03 was used for the quantum chemistry calculation to generate the input file for RESP fitting:

```
g03 < cro.com > cro-Gaussian.log
```

However, the frequency job in this the QM output file can not be recognized by the following program, so it has to be removed before running RESP fitting (containing "Frequencies"). And the filenames of the p2N and GAUSSIAN output should be changed to Mol_red1.p2n and Mol_red1.log, respectively. Since the chromophore is the non-standard residue in the middle of the peptide, so some charge restriction should be defined, like the peptide backbone N, C, H and O. In this case, charges for N, C and H will be defined and one remark will be added into the P2N file :

```
REMARKS
……
```

Finally, the RESP charge is fit by the command:

```
perl RED-vIII.4.pl > RED-vIII.log
```

2.8.4.2 Structure minimization and MD simulation by AMBER

AMBER package includes several programs for molecular simulation. In the study of mCherry variants, AMBER is used for energy minimization and simulation. AMBER requires users to prepare the pdb files for minimization. Sometimes the protein pdb files are involved in non-standard amino acids. In these cases, AMBER does not recognize it and ignores it, like the chromophore in GFP and mCherry. If we want AMBER to take account for them, the specific parameter files have to be created. Antechamber is one of the tools in AMBER package, which is used to deal with the small organic molecules. tLeap can further generate the files of the complex of protein and ligand ready for Sander. Protein pdb file should be checked first to avoid the unexpected errors and all hydrogen should be removed at this step. The chromophore pdb file is prepared by extracting the chromophore from the mCherry directly. Antechamber is used to generate the amber preparation input file in the format of prepi and the bond parameter file in the format of frcmod. tLeap is used to generate the library of the chromophore, cro.lib, which is further used for building the SANDER input files of the complex (topology and coordinates). All the scripts and commands are shown in Appendix A.2.

2.9 Calcium response monitored by designed calcium binding proteins *in situ*

2.9.1 *Materials and supplies*

Dulbecco's modified Eagle's medium (DMEM) and Hank's balanced salt solution (HBSS) were purchased from Sigma Chemical Co.. Fetal bovine serum (FBS), Opti-MEM reduced serum media, and lipofectamine 2000 were purchased from Invitrogen. FuGENE HD Transfection reagent was purchased from Roche. All media and buffer was filtered using the filter unit from Millipore.

The SERCA pump inhibitor Cyclopiazonic acid (CPA) and Thapsigargin, the cell membrane permeabilizer digitonin, the IP_3R agonist Histamine and IP_3, the Ryanodine receptor agonists 4-Chloro-m-cresol (4-cmc) and caffeine, the calcium ionophore ionomycin, as well as the solvent DMSO, were purchased from Sigma.

2.9.2 *Cell culture and DNA transfection*

HEK293 and C2C12 cells were grown on 100 mm culture dishes or glass cover slips (0.5-1.0 $\times 10^6$ cells/dish) in 35 mm culture dishes in DMEM with high glucose for HEK293 and C2C12 with 44 mM $NaHCO_3$ (pH 7.2) and supplemented with 10% (v/v) fetal bovine serum (FBS), 100 units/mL penicillin, and 0.1 mg/ml streptomycin (Pen/Strep) at 37 ℃ with 5% CO_2 in a humidified incubation chamber. The cells were seeded and grown overnight before transient transfection with Ca^{2+} sensor plasmid constructs.

Plasmid DNA used for transfection was harvested from transformed *E. coli* (DH5α) using a QIAGEN Miniprep protocol (Qiagen). Each of the mCherry variants was individually and transiently transfected into cells with FuGENE HD Transfection reagent or lipofectamine 2000 and serum-free Opti-MEM per the manufacturer's instructions. The plasmid DNA (1.5 μg) with a ratio of DNA to transfection reagent at 1:2 -1:3 (μg/μl) was generally used in a typical transfection. The cells were then grown for 2 days in a humidified chamber with 5% CO_2 at 37 ℃ before fluorescence microscope imaging. For C2C12 cell line, incubation at 30 ℃ was favored.

2.9.3 *Cell imaging of calcium calibration and response*

Calibration protocol described by Aldebaran Hofer was used as a standard one here for the mCherry-based calcium sensors targeted to ER lumen(83). Mag-Fura-2 AM, which was recognized to be accumulated in ER, was used for comparison. A variety of drugs, e.g. , 4-Chloro-m-cresol (4cmc), Cyclopiazonic acid (CPA), Inositol-1,4,5-trisphosphate (IP_3), Thapsigargin and Adenosine-5'-triphosphate (ATP), were applied to cells to either activate the calcium channels such as ryanodine receptor (RyR) and Inositol trisphosphate receptor (IP_3R) to release ER calcium or inhibit sacroplasmic reticulum Ca^{2+}-*ATPase (*SERCA) pump to reload calcium into

ER. Thus, the calcium concentration in ER decreased when treating cells with these drugs. Table 2.3 summarizes the effect of these drugs on the various calcium channels.

Table 2.3 Agonists and antagonists used for induce calcium change

Agents	Stock Conc.	Buffer	Target	Anticipated effect	
				$[Ca^{2+}]_{ER}$	$[Ca^{2+}]_{cyt}$
ATP	100 mM	Steril H_2O	IP_3R	Decrase	Increase
Caffeine	40 mM	Steril H_2O	RyR	Decrase	Increase
Histamine	50 mM	Steril H_2O	IP_3R	Decrase	Increase
Thapsigargin	1 mM	DMSO	SERCA	Decrase	Increase
Ionomycin	5 mM	DMSO	IP_3R and Membrane	Decrase and cell death	Increase
Digitonin	25 mg/ml	Steril H_2O	Membrane	Cell death	
4cmc	20 mM	Steril H_2O	RyR	Decrase	Increase
CPA	50 mM	DMSO	SERCA	Decrase	Increase
IP_3	10 mM	DMSO	IP_3R	Decrase	Increase

The standard Ringer's buffer was prepared using 1xstock buffer (145 mM NaCl, 2.5 mM K_2HPO_4, 1 mM $MgCl_2$, 1.8 mM $CaCl_2$, 10 mM HEPES, pH 7.2) with supplement of 10 mM glucose before use. The intracellular buffer was prepared as 125 mM KCl, 25 mM NaCl, 10 mM HEPES, 0.2 mM $MgCl_2$, 200 µM $CaCl_2$, 500 µM EGTA to give a final free $[Ca^{2+}]$ of approximately 100 nM and the addition of 0.5 mM Na_2ATP before use; pH was adjusted to be 7.25. KCl solution was prepared as 125 mM KCl, 25 mM NaCl, 10 mM HEPES, 0.2 mM $MgCl_2$, pH 7.25, which was used for calibration together with the calcium stock (1 M $CaCl_2$) and Nitrilotriacetic acid (NTA) stock (1 M). *To ca*librate calcium indicators targeted in the ER, the membrane is necessary to be permeabilized by digitonin at a final concentration of 25 µg/mL in the intracellular buffer. Calcium buffers were prepared to obtain the low calcium concentration in micromollar level. The calcium-NTA buffers for in situ calibration as calculated by the computer program (MAXC) developed by Chris Patton (Stanford University)(136, 137).

2.9.4 *Production of lentivirus encoding CatchER*

The lentivirus is a kind of defected virus, which can infect cells and tissues. The 3rd generation of lentivirus is composed with 3 plasmids, (1) pCMVΔR8.92 encoding HIV-1 Gag/Pol and Tat gene which is essential for replication of wild type HIV-1, (2) pLP/VSVG Vesicular Stomatitis Virus Envelope Protein, supplying the helper functions as well as structural and replication proteins. It is a heterologous coat protein other than native HIV envelope protein, (3) pFUGW containing gene of interest flanked with two LTR sequences. The helper lacks the packaging sequence and genes encoding some essential accessory proteins which are required for HIV to create a replicative competent lentivirus (RCL) are deleted. Ideally, since the vector plasmid lacks any of the other structural genes, it cannot form a replicative competent virus in the host cell.

The HEK293FT contains SV40 large T-antigen, which is commonly used for virus expression. The cells were cultured with 5 ml DMEM high glucose medium in 100 mm dish at 37 ℃ under 5% CO_2. Cells were split to maintain certain density twice a week. At the day before transfection with three plasmids, the cells was divided and keep it around 10^7 in a dish. Three plasmids (pFUGW, pΔR8.92 and pVSV-G) were mixed as the ratio of 2:1.5:1in 0.5 ml OPTI medium. A ratio of 2 µl lipofectamin-2000:1 µg DNA will be applied. For a 100-mm dish, 10 µg pFUGW is required. The DNA solution (22.5 µg in total) was completely mixed with the 45 µl Lipofectamin-2000 pre-diluted in 500 µl OPTI medium, and equilibrated for 20 min. The mixture will be added and culture for 48 – 72 h. The medium was collected and be centrifuged at 5000 rpm for 5 min. The supernatant was collected and filtered by 0.45 µm membrane to remove cells. The lentivirus in the medium will be enriched by ultracentrifigation at 27,000 rpm for 2 h with SW-40 Ti rotor. The pellet was resolved in a small amount of sterile PBS buffer. The detailed protocol was in Appendix E.

3 RATIONAL DESIGN AND EVALUATION OF CALCIUM BINDING FLUORESCENT PROTEINS

3.1 Introduction

Calcium ion has been widely known as the secondary messenger, which is associated with calmodulin, calbindin, calcineurin and other calcium binding proteins in a variety of organs and tissues, to mediate muscle contraction, heart beating, neurotransmitter release, and gene expression (Figure 1.1) (4, 5, 138-140). As the first messenger, via the calcium sensing receptor or group 1 metabotropic glutamate receptors, it controls calcium homeostasis in organs such as parathyroid gland, liver, kidney, blood vessels, as well as axon and dendrite outgrowth in nervous system (141-145). Calcium signaling is determined by the amplitude and kinetics of calcium transients, which is contributed by the activation and kinetics of calcium pumps, channels and the buffer proteins. Those calcium binding proteins including calcium channels sophistically control the spatial-temporal calcium gradient and transient, resulting in different physiological signal transduction.

Calcium (Ca^{2+}) transients originate from the calcium concentration gradients across biological membranes and are determined by the calcium binding affinity and kinetics of calcium channels/pumps as well as intracellular calcium binding proteins. The spatial-temporal calcium concentration change results in different physiological signal transduction, including muscle contraction, heartbeat, neurotransmitter release, gene expression, etc. (4, 5, 138, 139, 141). The time scale of calcium signaling varies from milliseconds to minutes. The fast calcium signaling, especially associated with action potentials usually occurs with a rapid local calcium rise (milliseconds) due to the calcium influx via the membrane voltage gated calcium channel and the calcium release from the internal stores, for example, the excitation-contraction coupling (EC coupling) in muscle cells and the neuron-transmitter release in neuron cells (21, 139, 146-155). On other hand, the slower calcium signaling usually happens in cellular events such as immune response, which can last minutes and even hours (7). In those slow calcium signaling pathways, the calcium transient is controlled by several factors and second messengers like DAG, IP3 and ATP, involving more complicated regulation mechanisms (156).

To accurately monitor the calcium transients in terms of the kinetics, amplitude, and duration, calcium indicators/sensors are required to have several key properties. It is necessary to match the dissociation equilibrium constant (K_d) of calcium indicators to the resting calcium concentration of the sub-cellular compartment. On the other hand, to detect fast action potential related calcium release from internal calcium pools such as the endoplasmic reticulum/sarcoplasmic reticulum (ER/SR) in skeletal muscle and neuronal cells, calcium binding affinity in the range of 0.1-1.0 mM and a calcium dissociation rate greater than 200 s^{-1} is necessary (considered the time constant range of action potential is 1-5 ms).

Understanding calcium signaling was advanced by the development of calcium dyes and genetically encoded calcium indicators (GECIs) (50, 67-72). High-affinity organic calcium dyes are often used to monitor calcium transients in the cytosol because the K_d is in the magnitude of hundreds of nanomollar. However, the detection of $\Delta[Ca^{2+}]$ induced by a train of high frequency, especially the rapid release from the ER store, is largely limited by the availability of calcium indicators. It has been reported that it is not suitable for the calcium dye Oregon Green BAPTA 1 to detect the calcium transients upon action potential stimulation of more than 50 Hz because the slow decay (k_{off}=2.6 s^{-1}) results in the accumulation of signals (67, 73-75).

The low affinity calcium dyes, with their low affinity and rapid off rate, such as Fluo-5N (76-78), Mag-Fluo-4 (79), Calcium-green-5N (80, 81) were used to monitor calcium change in internal calcium stores including the mitochondria and the endoplasmic reticulum (82-84). However, the reported kinetics and the amount of calcium concentration change during EC coupling in skeletal and cardiac muscle cells as well as neurons were largely varied. For example, it was reported a broad range from 3.3 to 8.0 ms of the calcium release presented by the full duration at half-maximum (FDHM) at room temperature from the mouse fast-twitch fibers upon the action potential (85-88). Such variations are likely a result of limitations associated with calcium dyes, including the spatial localization of dyes, binding affinity, and kinetics (k_{on} and k_{off}) (71, 89).

The development of genetically encoded indicators (GECI), such as GCaMP, GECO, TN and Cameleon series, enables to probe spatial-temporal cellular events and cell signaling in real time (19, 54, 60, 90-97). GECI are composed with a fluorescent protein moiety and native cytosolic calcium trigger proteins (CBPs) such as calmodulin (CaM) or troponin C (TnC) that are used to sense calcium concentration change and calcium-induced global conformational rearrangement. Each CaM or TnC binds four calcium ions cooperatively with a strong calcium binding affinity (K_d=10^{-7} M) and calcium binding on rates in the magnitude of 10^7 $M^{-1}s^{-1}$ that enable them to sense the immediate [Ca^{2+}] rise in the cytosol (98-101). Meanwhile, these GECIs have slow dissociation rate around 0.1-10 s^{-1} likely due to the cooperativity associated with multiple calcium binding sites and multiple layers of conformational change (102, 103). Their slow kinetics of signal decay hampers their applications in probing physiological fast calcium transient especially in the neuron and skeletal muscle cells (56, 91, 104). Further efforts to reduce the calcium binding affinities in Cameleon D1ER results in a multiple K_ds around 0.8 and 60 μM and the off rate around 256 s^{-1} (38). Such sensor, however, was not able to capture the calcium release from SR upon the stimulation in the mouse FDB fibers (105, 106).

The statistical analysis of calcium binding geometry and charged residue preference has been study by our group (66, 157, 158). The classic calcium binding pocket is consisted with 6-7 oxygen atoms, and forms a bipyramidal shape, resulting in the high calcium binding affinity and selectivity. To obtain different calcium binding capability, alternation of the classic calcium binding rule was allowed. For example, to lower the calcium binding affinity, the geometry would be modified to form 3/4 or 1/2 shell of the classical bipyramidal; the negatively charged residues could be replaced by the neutral glutamine or asparagine and the non-polar amino acids; the glutamate and aspartic acid could be substituted with each other to change the side chain length.

To fulfill the unmet need of a fast calcium indicator required for monitoring calcium releases in high concentrations such as the ER/SR, we reported a calcium sensor called CatchER without using the native calcium binding domain (66). CatchER was created by designing a calcium binding site into a single enhanced green fluorescent protein (EGFP). The binding stoichiometry is 1:1 and the K_d is 0.18 mM in vitro and 0.8 mM calibrated *in situ* allowing measurement of basal calcium in different cell lines and their changes in response to different drugs. Compared to Cameleon D1ER, CatchER exhibits faster kinetics, allowing it to catch the SR calcium change in the skeletal muscle cells (107). To date, however, there is no sensors available for measuring calcium responses at the red wavelength region with an advantage of better tissue penetration to complement the green sensors developed by us and others (66). In this chapter, we report the achievement of designing calcium binding protein RapidER using a red florescent protein mCherry by integrating key factors for calcium binding kinetics and metal induced optical property change. We show that the designed red calcium binding sensor RapidER, on the surface of mCherry, is able to report calcium concentration by fluorescence in the range of 10^{-4}-10^{-3}

M with an unprecedented dissociation rate in the magnitude of 10^3 s^{-1}. Our finding reveals essential factors needed for future design of fast calcium binding proteins, fulfilling a pressing need for monitoring calcium dynamics in fast biological processes.

3.2 Characterization of the biophysical properties of designed calcium binding proteins

3.2.1 *Structural analysis and design of calcium binding site on the red fluorescent proteins*

Calcium binding site candidates were searched on the available crystal structure of mCherry(159). The chromophore environment was first mapped out to locate the residues involved in the chromophore hydrogen-bonding network. Figure 3.1 shows the mCherry chromophore environment in the crystal structure 2H5Q, and the potential hydrogen bonds were depicted using dash lines. At neutral pH, mCherry chromophore is deprotonated since pK_a of mCherry is not more than 4 (109). Direct hydrogen bonds were found between the chromophore tyrosyl and the side chain hydroxyl of Ser146 and Gln163 side chain amide group. The side chain of Ser146 has double conformer, and the H-bond to the chromophore can be formed by either of them. Through Ser146, the chromophore was indirectly hydrogen bonded to Ile197 and Glu144. A hydrogen bond network was consisted of the imine nitrogen of the chromophore imidazolinone, Glu215, Gln42, Ser69-Lys70, the carbonyl of the chromophore imidazolinone, Arg95 and Gln64. The H-bond interaction can be also observed between the side chain amide of Gln213 and the thioether sulfur of the chromophore. Among the residues mentioned above, only the residue Glu144 interacts with the chromophore through its main chain, while others form H-bonds through their polar side chain. Those surrounding residues assist to mount the chromophore inside the β-barrel.

The potential calcium binding site can be created by constructing an area of high negative potential formed by the side chains of glutamate and aspartate (Figure 3.1.Bc). Unlike EF-hand motif, in which the calcium binding coordinators are carbonyl or carboxyl from both the main chain and side chain located in the loop, the main chain coordinator is avoided since the hydrogen bonding between the β-strands is essential for the barrel architecture. Therefore, the residues with the side chain pointing outwards and adjacent or close to the residues involved in the electrostatic interaction with the chromophore are taken into account for the candidates of the calcium binding ligands as the first step screening. The following screening was carried out to look for the residues or stretches which are relatively flexible, estimated by the B-factor of the pdb file (Figure 3.1(Bb)). There is the assumption that the less constrained residues are not important as much as the rigid ones for maintaining the fluorescence.

The Cα geometry of several EF-hand motifs (both Ca^{2+}-loaded and Ca^{2+}-free forms) was analyzed and compared to our previous designed binding sites. We found that: (1) all the classic EF-hand motifs appear to have 5 residues for calcium binding; (2) the distribution of Cα forms a trigonal bipyramidal -like geometry, in which a near-planar was formed by four Cα and the fifth one hangs up; (3) the distance between any two of Cα located in the “plane” is approximately 6 angstrom and the longest distance is between the hanging Cα and one of Cα in the “plane”; (4) calcium atom is surrounded by these five residues while the positions of five Cα are not changed significantly upon calcium binding. Compared to this, the hanging residue was not included in our previous design, which probably is the reason for the low binding affinity. Since the positions of Cα will not be changed much upon calcium binding, and the geometry of Cα was conserved to some extent, the Cα can be a good potential sign to define a calcium binding pocket.

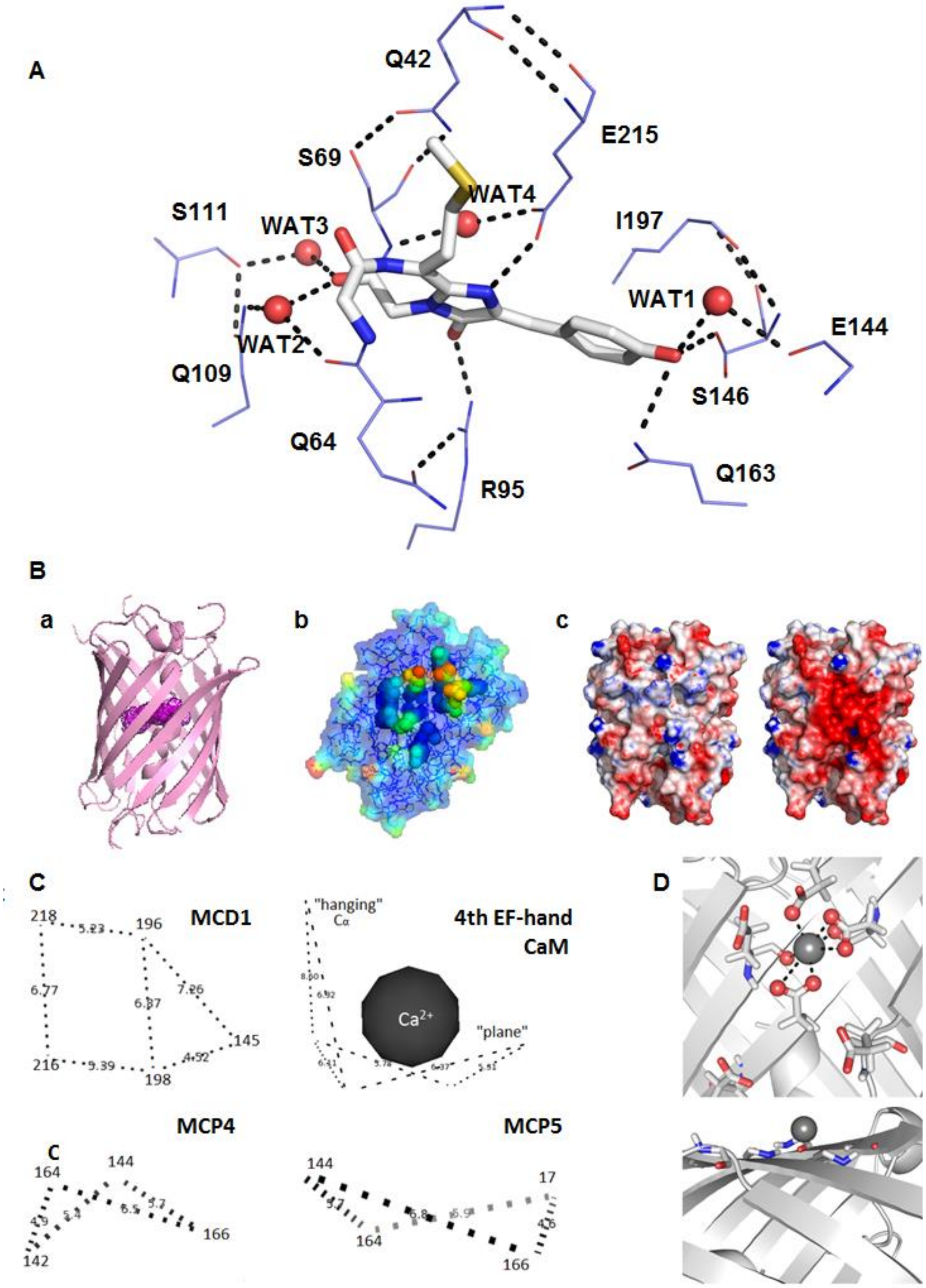

Figure 3.1. Structural analysis and design of calcium binding sites on mCherry.
(A) The mCherry chromophore environment (PDB ID: 2H5Q). The chromophore was shown in the stick mode. The dash line indicate the hydrogen bond and the cut-off distance for the H-bond is 3.5 Å; (B) a: the overall mCherry structure in cartoon; b: the B-factor map and the electrostatic density map of the wild type mCherry, showing the most flexible area colored with red and blue indicating the most rigid area; c: the electro-density map change from wild type mCherry to MCD1 (RapidER). (C) the Cα geometry of MCD1, MCP4 and EF-hand motifs of calmodulin (PDB ID: 3CLN); the dash line together with the number in the middle indicate the distance between two Cα, and the residue number is labeled at the point of Cα for all variants.(D) The oxygen geometry (top) and backbone (bottom) of modeled MCD1.

Have taken all together, residues 145, 196, 198, 216 and 218 were selected for the first calcium binding site MCD1x. The residue 145 is next to Glu144 and Ser146, both of which connect to the chromophore. Residues 196 and 198 are next to Ile197 and residue 216 is next to Glu215. The glutamate and aspartate were shuffled in these five positions to generate a series of mutants. The positive potential provided by the residue Arg220 may have negative effect on calcium locating to this binding site, which was also be substituted by glutamate. The second binding site, MCD2x, includes the residues 144, 198, 200, 214 and 216. Similarly, these positions are close the chromophore environment residues and partially overlapped with the first site. The third site MCD3 (MCP6), including 92, 94, 108 and 110, was selected, which locates in the opposite side of the first and second potential calcium binding sites. The first and second calcium binding site candidates are mainly focused to alter the electrostatic hindrance in the chromophore tyrosyl, while the third one is aimed to influence the chromophore imidazolinone imine nitrogen.

Considered the Cα geometry, the forth site was designed in the loop region close to the chromophore, including Glu144, as shown in Figure 3.1C. The Cα geometry of Glu144, Arg164, Lys166 and Gly142, and Glu144, Arg164, Lys166 and His172, was similar with and even more convex than what can be seen in EF-hand motif without the hanging residue. His172, in which the nitrogen of imidazol ring was only 2.6 Å away from the carboxyl oxygen of Glu144, was mutated to Glu to further perturb the hydrogen bonding between them. The hydrogen bond between Arg164 and Asp174 was disturbed in both mcEE and MCP4, resulting in the alternation of the local electrostatic property and further lower the interaction between the strands β7 and β8.

Instead of locating the calcium binding site on the convex surface of beta-can by site mutagenesis, the grafting approach was used to insert a calcium binding motif into the fluorescent protein. Unlike the direct calcium binding to the fluorescent protein, introduction of another binding domain requires the corresponding conformational change upon calcium binding which will in turn to modify the chromophore environment so as to affect the spectral properties. The loop region near chromophore (140-147) was chosen to be the first potential binding pocket, where the non-negatively charged residues were replaced for glutamate acid, or the loop was substituted with the second EF-hand motif of calbindin D9K (TLDELFEELDKNG-DGEVSFEEFQVLVKKI) or loop (DKNGDGE). There was evidence showing the calcium binding to this specific loop triggers the conformational change (Dr. Yanyi Chen's unpublished data), which may alter the original chromophore environment and the fluorescence.

These design strategies were first modeled using the MODELLER, AUTODOCK-Vina and the calcium binding prediction program MUG (160). Figure 3.2 shows the wild type mCherry, the modeled structures of the designed calcium binding proteins and predicted calcium binding sites. Four cp-mKate variants, 149-148, 154-153, 168-167 and 189-188, were used as the templates of the new constructs (161). These four cp-mKate showed the shoulder around 350-500 nm in the optical spectra and reduced brightness compared to mKate. The stable chromophore environment was affected and open possibilities to manage the chromophore environment by mutagenesis. The designed calcium binding pocket is in the equivalent position of CatchER and MCD1 (also as RapidER). Table 3.1 summarizes the variants created for the calcium sensor screening.

The electrostatic repulsion in the binding site due to these negatively charged residues weakens the hydrogen-binding network among the beta sheets, which will increase the solvent accessibility and thus increase the fluorescence quench by solvent. Ca^{2+} binding results in charge neutralization in this area, further leading to recovery of the natural stable scaffold structure. The designed binding site was considered to maintain the native folding of the fluorophore to avoid the perturbation of the fluorescent activity.

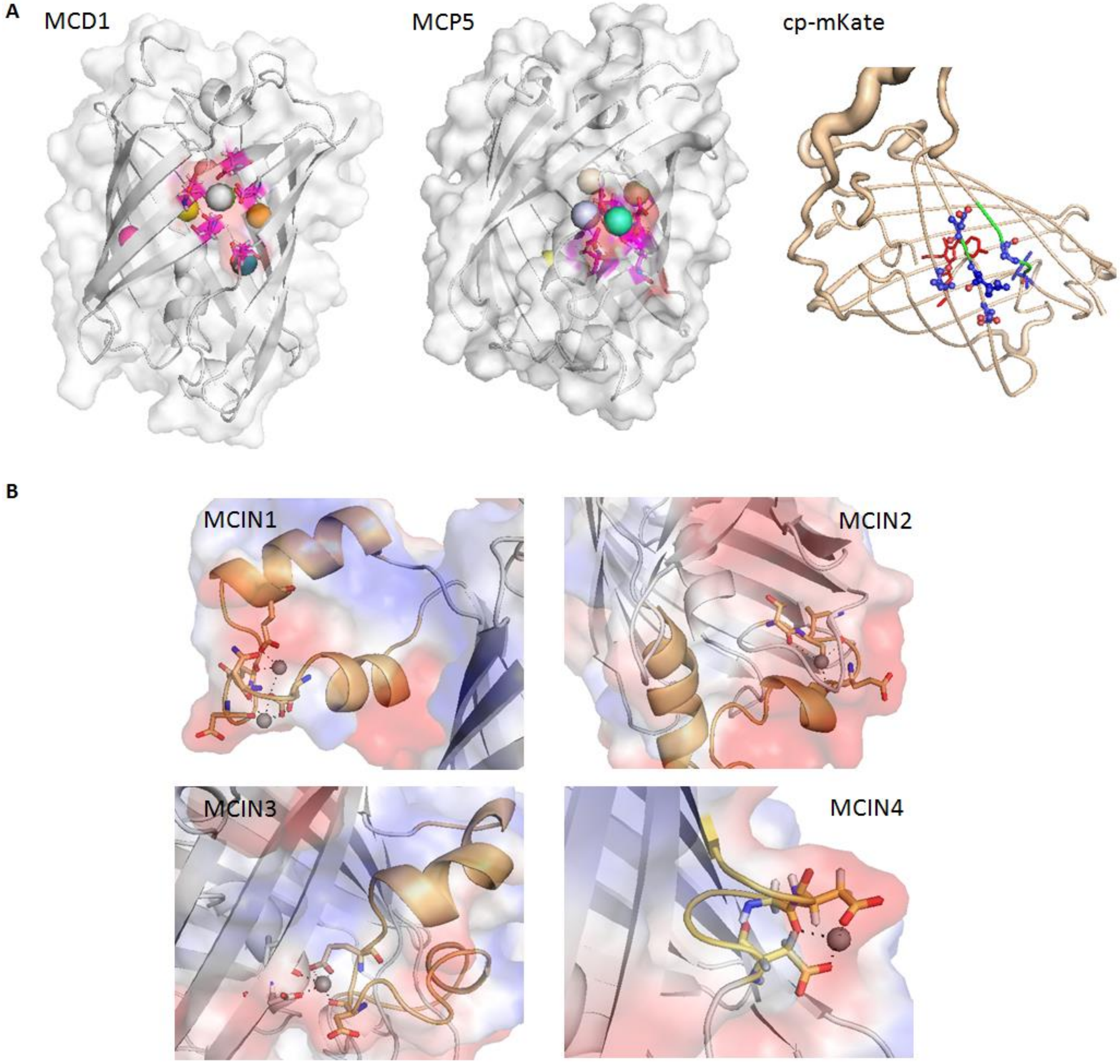

Figure 3.2. Predication of calcium binding to the modeled red fluorescent proteins.
(A) The models of MCD1 (also as “RapidER”) and MCP5 and cp-mKate. The model structures MCD1 and MCP5 was applied with energy minimization by AMBER9. VINA can find the designed binding site. The cartoon structure of cp-mKate-168-167 (PDB ID: 3RWA) was shown and the mutation sites are depicted, which is in the equivalent position as CatchER and MCD1. (B) The initial models of MCIN1, 2, 3 and 4 were built by Modeller. VINA was used to dock calcium. Calcium ion was placed into the expected pocket.

Table 3.1 Variants and the corresponding mutation sites

Position	Design Strategy	Clones	Mutation/Insertion
Pocket 1	To influence the hydrogen bonds formed between the chromophore tyrosyl and WAT1-E144 backbone, S146 side chain. (Figure 3.1). Modification around MCD1 is to modify the Ca^{2+} binding affinity and the optical properties.	MCD1	A145E/N196D/K198D/R216E
		MCD14	MCD1+R220E
		MCD14Y	197Y+MCD14
		MCD14YS	197Y/199S+MCD14
		MCD15	MCD14 + D198E
		MCD16	MCD14 + S147D
		MCD17	MCD14 + I197T/K198E/L199S/D200A
		MCD18	MCD14 + K198E/D200A
		MCD19	MCD1 + D198E
		MCD110	MCD15 + L199S
		MCD111	MCD15+D196E
		MCD112	MCD1+E220Q
Pocket 2	To influence the hydrogen bonds formed between the chromophore tyrosyl and WAT1-E144 backbone. (Figure 3.1)	MCD2	K198D/Y214E/R216E
		MCD22	K196E/Y214E/R216E
		MCD23	MCD2 + D200E
		MCD24	MCD2 + D200Q
		MCD25	MCD2 + D200N
		MCD26	MCD2 + E216D
Pocket 3	To influence the hydrogen bonds formed between the chromophore tyrosyl and Q163 side chain. (Figure 3.1)	mcEE	R164E/K166E
		mcP4	G142E/R164E/K166E
		mcP5	R164E/K166E/H172E
Pocket 4	To influence the hydrogen bonds formed between the chromophore and Q109 and R95. (Figure 3.1)	mcP6	K92E/T108E
Pocket 5	To insert the EF-hand away from the chromophore.	MCIN1	153^154 (Insertion is between residue 153 and 154.Same as below)
Pocket 6	To insert the EF-hand near the chromophore tyrosyl.	MCIN2	135V^142G
		MCIN3	142G^147S
		MCIN4	143W^147S
mKate	To mount the calcium binding site in cp-mKate in the corresponding location as MCD1 and Catch-ER.	cp-mKate_149-148 cp-mKate_168-167 cp-mKate_189-188 cp-mKate_154-153	Corresponding to mKate A142E/R198E/V216E

3.2.2 *Expression and purification*

Protein folding was dependent on the *E. coli.* strains and affected by the vectors. Although the SDS-PAGE showed the band at the expected position, the protein lost its color if expressed in the inappropriate combination of the vector and the cell strain. mCherry variants with mutations at the first binding site MCD1x encoded in pRSETb vector were expressed by *E. coli.* BL21 (DE3); while MCD2x encoded in pRSETb were expressed in BL21 (DE3) PlysS strain. The gene encoding mCherry and its variants was released from pRSETb and inserted to the vector pET28α which is used for EGFP and its variants expression. The new construct was transformed into BL21 (DE3) and after overnight expression at 25 ℃, the red color culture was observed from the broth. Cell was broken by sonication and after purified by HiTrap chelating column, the gel showed a lot of other bands although the abundance was the protein of interest (Figure 3.3 C and D). The precipitates can be observed when titrating calcium to the protein purified by the affinity column, resulting in the light scattering when recording the optical spectrum (Figure 3.3E). After further purification using Mono-Q column and desalting column (Figure 3.3 A and B), the impurities was reduced as shown in Figure 3.3 D and F, and no precipitates formed during calcium titration.

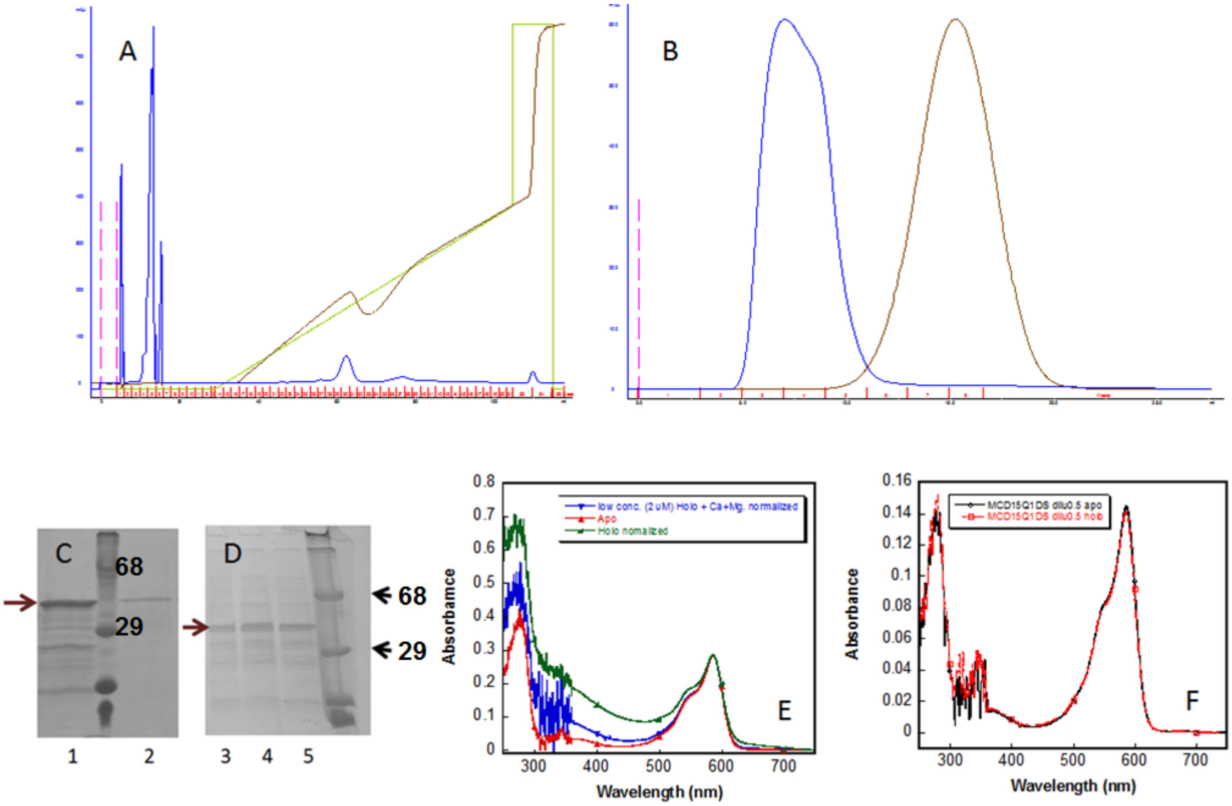

Figure 3.3. Purification of MCD15 from BL21 (DE3) transformed with pET28a.
(A) The trace of MCD15 eluted from Mono-Q column. (B) The trace of desalting MCD15 using Sephdex-75 (GE Healthcare). (C and D) lane 1: the protein purified from Ni-chelating column; lane 2: the supernatant of the MCD15 sample titrated with calcium after spin; lane 3-5: precipitates of the MCD15 samples titrated with calcium after spin. (E) The optical spectra of the apo MCD15 purified by only the affinity column and the one with calcium. (F) The optical spectra of the apo-MCD15 purified by the affinity, Q and desalting columns and the one with calcium.

Alternatively, the vector pRSETb was transformed to Rosetta gami (DE3) PlysS for expression. Before IPTG induction, the temperature was lowered to 30 ℃. After the protein expression at 30 ℃ for overnight, bacteria were harvested and the total soluble protein was extracted by sonication and centrifugation. The total protein was loaded to Ni^{2+} column (HiTrap chelating column, GE Healthcare) and the fractions from HiTrap chelating column were collected and the gel showed in the Figure 3.4A was very clean compared to the one purified from pET28α (Figure 3.4B). But the amount of the cleaved bands is more than that from pET28α. Compared to the previous purification, the percentage of cleaved bands was reduced, but the impurity increased using the pET28α construct and the yield was lower. Rosetta gami (DE3) PlysS transformed with pRSETb is able to produce protein with a satisfactory yield and also less purification steps will be adopted since the purity of the protein after Ni^{2+} affinity column is high.

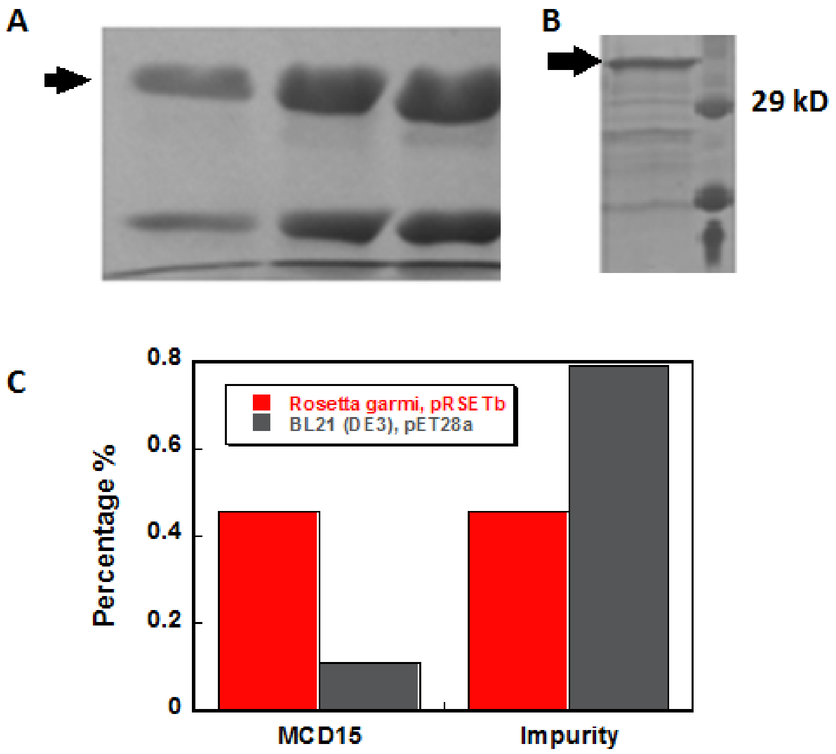

Figure 3.4. Comparison of SDS-PAGE pattern of MCD15 purified from different *E.coli*. strains. (A) Different fractions of FPLC purification for protein produced by Rosetta gami (DE3) PlysS, showing the full length protein and the cleaved peptides. (B) The protein expressed in *E.coli*. BL21 (DE3) encoding pET28a and purified from Ni-chelating column; bands other than cleaved peptides can be observed. (C) The intensity analysis by ImageJ showed the abundance of MCD15 in the total purified protein in the gels A and B.

3.2.2.1 Separation of cleaved peptides

The cleaved peptides could make the quantitative analysis complicated, although only the active form of chromophore was taken into account when all experiments were conducted. As a result, attempts were done to obtain the pure full length protein. Considered the size difference, size exclusion chromatography (SEC) was applied and the resulting trace was shown in Figure 3.5A. Only one symmetric peak was observed, indicating it failed to separate the cleaved peptides. The native PAGE shown in Figure 3.5C and D suggesting that the cleaved peptides were tightly associated with each other as an intact protein or with the full length protein.

To remove the tightly associated cleaved peptides from MCD1 purified from Rosetta gami pLysS (DE3) with Ni-chelating column, denaturants such as urea and SDS was added to the elution buffer. MCD1 exhibits surprising conformational stability since it cannot be denatured by even 8 M urea. As shown in Figure 3.6A, optical spectra do not change in either 8 M urea or 1% (w/v) SDS, compared with the one in the storage buffer (10 mM Tris, pH7.4). The SEC then was applied and buffer supplemented with 2 M and 8 M urea was used for elution. As shown in Figure 3.5B, 2 M urea elution resulted in two peaks. The SDS-PAGE and native PAGE in the Figure 3.5B inset have the similar pattern in Figure 3.5A and 3D, indicating that it was not able to remove the cleaved peptides. Similarly, elution with 8 M urea cannot separate the cleaved peptides from the full length protein as shown in Figure 3.5E and 3.5F. Getting together, the associated cleaved peptides are not able to be isolated by 8 M urea. However, the major fraction of 8 M urea SEC for MCD1 shows a ratio of absorbance at 280 nm to the one at 587 nm more close to reference (110), compared to MCD1 before SEC, which demonstrated that SEC with elution of 8 M urea removed the peptide involving inactive chromophore as shown in Figure 3.6B.

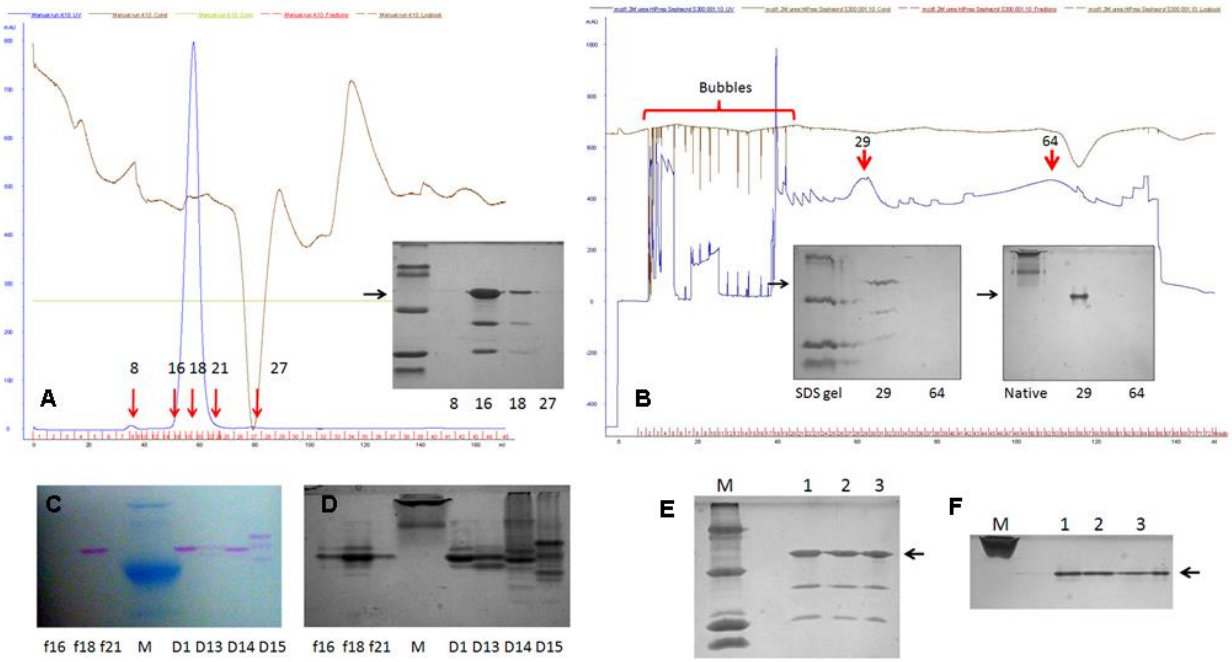

Figure 3.5. Removal of cleaved peptides by size exclusion chromatography (SEC).
(A) SEC traces for MCD1, which was eluted by 10 mM Tris, pH 7.4. The blue trace indicates UV intensity at 280 nm and the brown one indicates the conductance. The inset shows the SDS-PAGE of fractions as labeled. (C and D) The native gel of SEC fractions of MCD1, MCD1 before SEC, MCD13, MCD14 and MCD15, before (C) and after (D) coomassie staining. (B) SEC trace for MCD1, which was eluted by the buffer containing 2 M urea and 10 mM Tris, pH 7.4. The sharp peaks with the red blankets was resulted by air trapped in the column. And one major and one minor peaks were obtained. The insets show the SDS-PAGE of fractions as labeled. (E) SDS-PAGE of MCD1. lane 1: the major peak of SEC with elution of 2 M urea; lane 2: the major peak of SEC with elution of 8 M urea; lane 3: MCD1 before SEC. The loaded proteins are at the same level of active chromophore, checked by UV-vis spectra (data not shown). (F) the native gel of the same samples as (E).

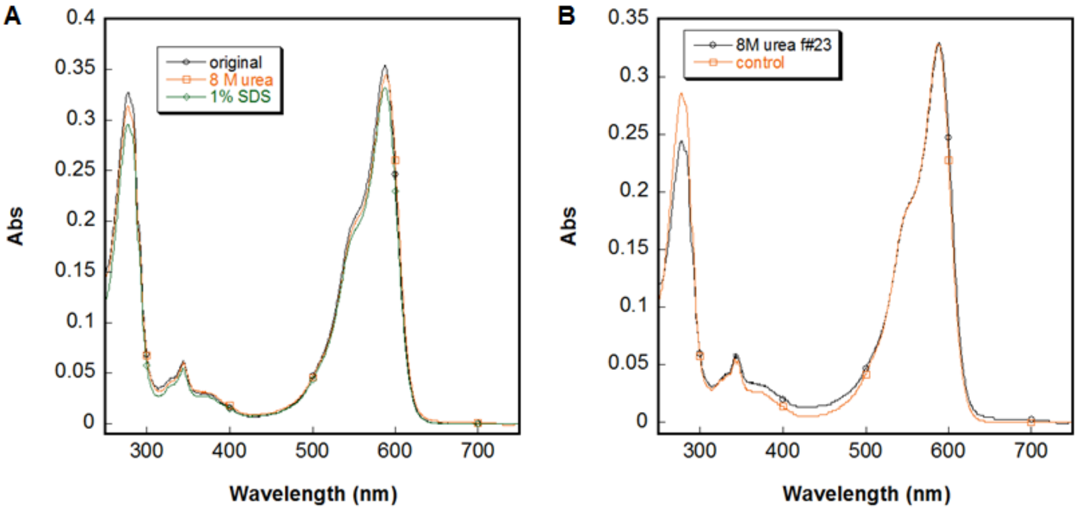

Figure 3.6. UV-vis spectra of MCD1 supplemented with denaturants.
(A) Comparison of the UV-vis spectra of the MCD1 in storage buffer containing 10 mM Tris, pH7.4 with MCD1 of the same concentration in 8 M urea and 1% (w/v) SDS. (B) Comparison of the UV-vis spectra of MCD1 before loaded to gel filtration column and the fraction 23 of SEC with 8 M urea. The spectra was normalized to the same concentration of active chromophore that results in a peak at 587 nm.

Trypsin was suspected to be the enzyme which digested the full length mCherry and caused the tightly associated peptides. To understand that, trypsin digestion was carried out. As shown in Figure 3.7A, at the first 5 min of digestion, the optical property was not altered and in the following 30 min, the fluorescence intensity decreased, suggesting that the active chromophore was reduced. The cleavage pattern of MCD1 was shown in the SDS-PAGE gel in Figure 3.7B, where the full length protein was totally cut and five bands (30 kDa, 29.5 kDa, 19 kDa, 15 kDa and 9.5 kDa) can be observed in the lane loaded with MCD1 digested for 16 h. At the end of the reaction, the lowest band (9.5 kDa) showing up in the control was fragmentized by trypsin, while the second band (19 kDa) remained the same. The difference of the SDS-PAGE patterns means the trypsin is not the enzyme resulting in the cleavage issue of mCherry and its variants. Here, the fluorescence intensity increased back at the time points of 35 min and 2 h was probably due to the fluctuation of the instrument.

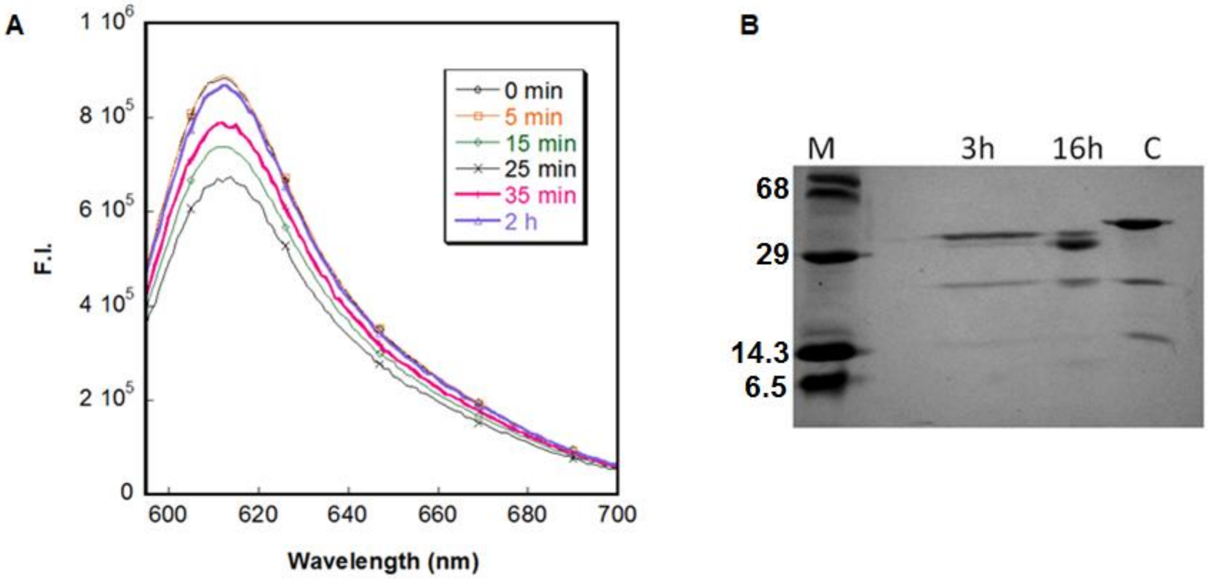

Figure 3.7. Typsin digestion of MCD1.
(A) The fluorescence spectra of the trypsin-digested MCD1 at different time points. Trypsin with a final concentration of 500 nM was added to 10 µM MCD1 in 10 mM Tris, 20 mM $CaCl_2$, pH 7.4. The reaction was incubated at 37 ℃. (B) The SDS-PAGE for the digested product at 3 h, 16 h and MCD1 before digestion as a control.

3.2.2.2 Western blot of mCherry variants in cell lysate

It is important to understand whether the cleavage issue exists in mammalian cells, which can be revealed by Western blot. The HEK-293 cells were collected after 48 hr transfection of mCherry variants. The protein concentration was determined by BioRad protein assay. The polyclonal anti-DsRed antibody (Clontech) and alkaline phosphatase conjugated with chemiluminescent substrate were used for detection of protein of interest. The developed Western-blot film was shown in Figure 3.8, clearly showing that no cleavage bands were observed in mCherry variants expressed in HEK-293 cells except the wild type mCherry. The band intensity was analyzed by ImageJ, and normalized to the wild type mCherry. The expression level of the variants was approximately 50% of the wild type, although MCD1 showed the relatively more expression.

The minor band in the wild type mCherry sample probably resulted from the non-specific interaction with the polyclonal DsRed antibody.

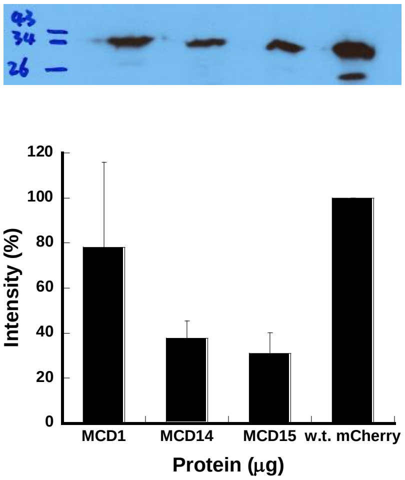

Figure 3.8. The film of western blot for mCherry variants MCD1, MCD14, MCD15 and the wild type. For each protein, 20 μg total protein was added to each well. The SDS-gel was electro-transformed to PVSF membrane at 21 V, 4°C for 16 h. The exposure time was 1 min.

3.2.3 *Spectral properties of designed calcium binding proteins*

Figure 3.9 shows the representative UV/visible and fluorescence spectra of the mCherry variants, which were used to evaluate the correct protein folding and determine their optical properties. All the fluorescent mCherry derivatives showed the similar optical spectra. MCD14Y, MCD14YS, mcIN2, mcIN3, mcIN4 and all cp-mKate mutants lost the red color and the excitation/emission spectra was blue-shifted to λ_{ex}=350 nm/λ_{em}=430 nm. For mutants maintaining red color, there was no difference in the wavelength of peak maxima (587 nm) and line shape compared to the wild type mCherry. The fluorescence spectra showed no shift as well, in which the protein was maximally excited at 587 nm and emitted at 610 nm. The consistency of the spectral property demonstrated that introducing negatively charged residues on the β-barrel surface did not affect the chromophore conjugated system. For those showing no color, it was suggested that opening of the middle of the β-sheet either broke the chromophore environment or affected the self-catalysis of the cyclic tri-amino acid formation and protein folding. However, these mutants may fold better in the mammalian system so they can be expressed in HEK-293 cells and the study of the expression level as well as optical properties could be continued in the future.

The fluorescence intensity was increased when adding calcium to MCD1 and MCD2 series (Figure 3.9B), while it remained no change for others. For the protein mcP4 expressed in HEK 293 cells, the protein folded and the fluorescence was detected although it did not show any color in the bacterial expressing product. Even though, the fluorescence was too dim for the further study. Compared to mcEE and mcP5, the mutation G142E was harsh for the protein folding, especially in *E. coli.*.

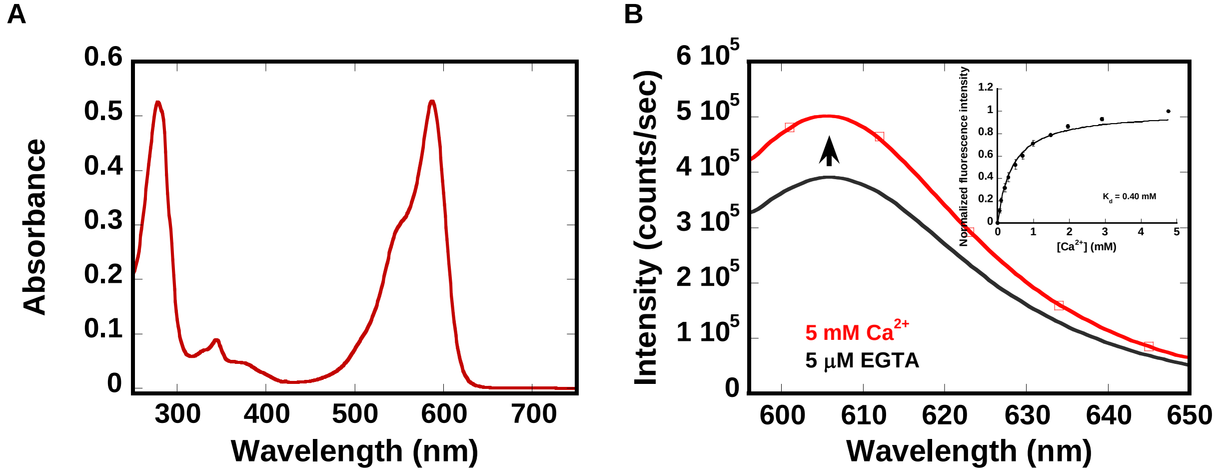

Figure 3.9. The representative optical and fluorescence spectra of mCherry derivatives.
(A) The UV/visible spectra of MCD1. (B) The fluorescence spectra of holo (red)- and apo (black)-MCD1.

3.2.4 *Biophysical properties of mCherry variants sensing calcium*

3.2.4.1 Extinction coefficient, quantum yield and fluorescence lifetime

Due to the cleavage of both wild type and mutated proteins, the alkali denaturation assay was used for determination of extinction coefficient (110). Taken MCD1 as an example, Figure 3.10 showed the linear relationship between the absorbance at 587 nm at pH 7.4 and absorbance at 455 nm at pH 13.0 using different concentrations of protein, as well as the fluorescence and the absorbance. Here, the extinction coefficient and quantum yield of the wild type mCherry at neutral pH condition are known as 72,000 M^{-1} cm^{-1} and 0.22, respectively. The unchanged extinction coefficient at 455 nm at pH 13.0 was determined using the wild type mCherry ε_{587nm} as the reference. Equations for the calculation were described in **Materials and Methods 2.3.2 and 2.3.3**. The results were summarized in Table 3.2. Figure 3.10 showed the representative spectra of MCD1 and the wild type mCherry collected for determining the extinction coefficient and quantum yield.

The decrease in both quantum yield and extinction coefficient of was more or less observed in all mutants, leading to less brightness than the wild type. For all mutants, calcium binding does not change the extinction coefficient. The MCD1 and derivatives showed higher quantum yield in the presence of calcium, but not in mcEE, mcP5 and mcIN1. It was assumed that the designed binding site caused the concentrated local negative potential and in turn diminished the packing of the β-barrel by electrostatic repulsion force. Although the chromophore itself was not directly affected, the protein matrix providing the electrostatic restriction and steric hindrance was changed and quenched the fluorescence. Calcium binding recovers the fluorescence by neutralizing the strong negatively charged area on the β sheets and reducing the repulsion force.

The fluorescence lifetime (Figure 3.11) was measured in the absence and presence of calcium for MCD1, MCD14 and MCD15. Compared to the wild type, whose lifetime was reported as 1.46 ns (162), the mutation of MCD1 and MCD14 increased the fluorescence lifetime, and MCD15 was similar as the wild type. In agreement with the quantum yield calculation, the increase of lifetime was observed upon calcium addition although it is not significant.

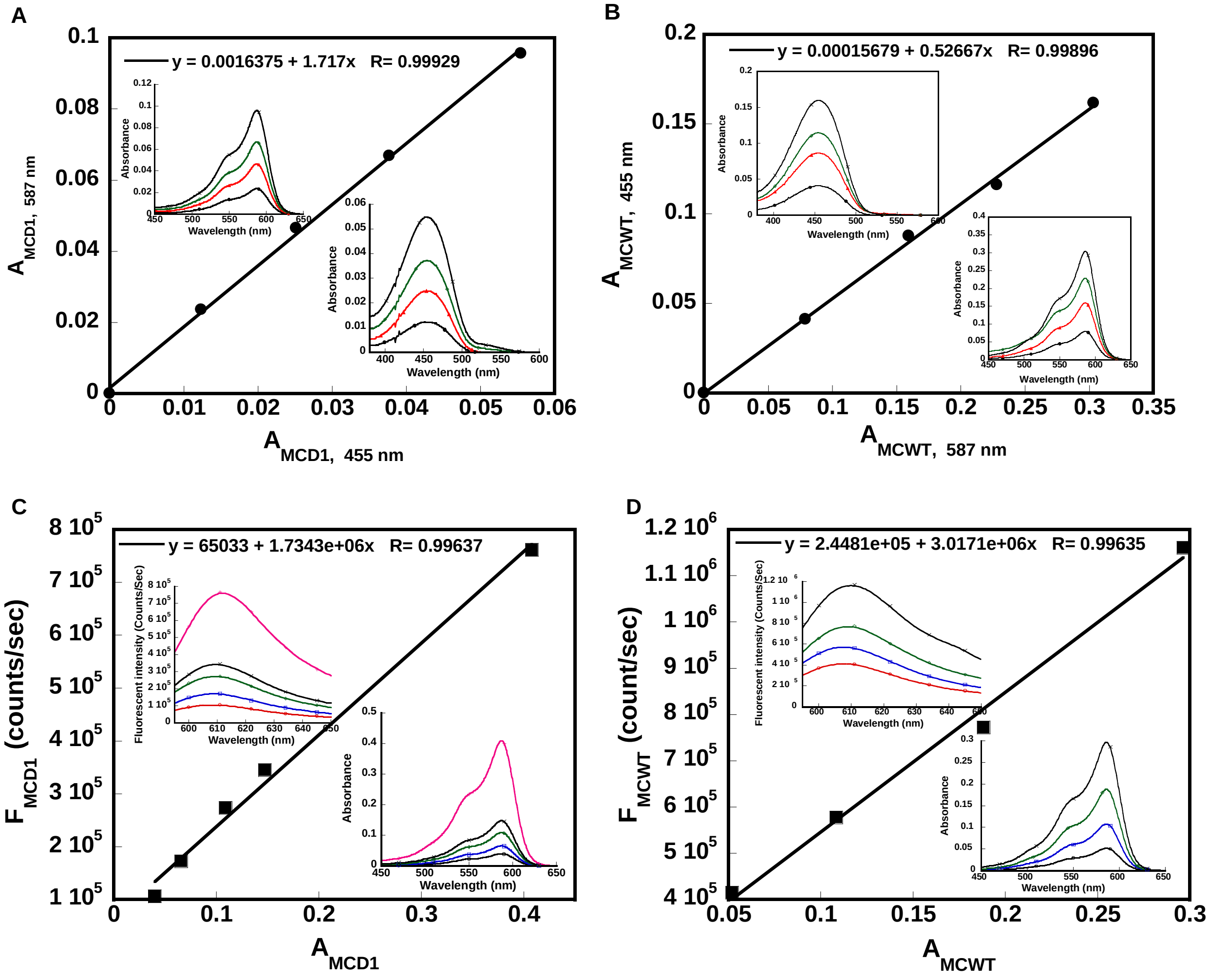

Figure 3.10. The UV-vis and fluorescence spectra of mCherry and MCD1 at different concentrations. The absorbance maxima at 587 nm in UV-vis spectra. The fluorescence emission spectra were collected by setting the excitation wavelength 587 nm and emission from 590 – 700 nm. The protein was prepared in 10 mM Tris, pH 7.4. All experiments were carried out at room temperature.The fluorescence intensity maxima at 610 nm of each sample were plotted. The data was linearly fitted using KaleidaGraph.

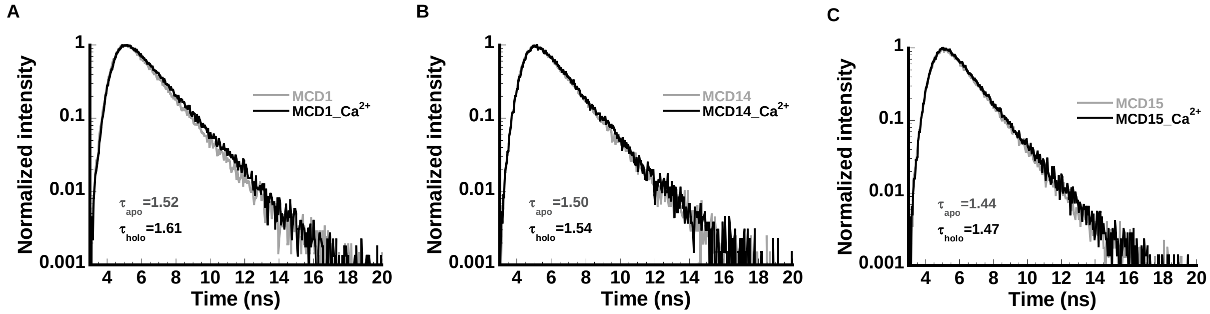

Figure 3.11. The fluorescence lifetime of MCD1, MCD14 and MCD15 in the absence and presence of Ca^{2+}.
The protein was prepared in 10 mM Tris, pH 7.4. The excitation wavelength was 590 nm and emission was at 610 nm.

3.2.4.2 pH profile and pK_a determination

To obtain the pK_a of the mCherry mutants, proteins were incubated in buffer at various pH (Table 2.1) overnight at 4 ℃ and saturated in presence of 1 mM EGTA or 5 mM Ca^{2+}. Data from the optical, excitation and emission spectra were collected (Figure 3.12 C and D) and fitted with Equation 2.2. The average value was listed in Table 3.2. The chromophore of the wild type mCherry and mutants listed in Table 3.2 was colorless when pH<3. The pH profile and curve fitting of the wild type mCherry was measured as control and the pK_a was consistent with the reported one (110). In the cases of MCD1 and mcIN1, introducing negatively charged residues acidified the protein to some extent and resulted in the lower pK_a. However, the proteins MCD14 and MCD15 have one more negative charge substitution than MCD1, showing the same pK_a as the wild type, even around 1 unit higher than MCD1, indicating the chromophore pK_a was independent of the surface charge number. For MCD1, adding calcium resulted in a higher pK_a value, suggesting a less population of deprotonated chromophore was expected at neutral pH. Calcium binding did not shift pK_a of MCD14, MCD15, mcEE, mcP5 and mcIN1 significantly. In general, the chromophore was sensitive to the pH from 3 to 6, which was resulted from the perturbation of the charge balance near the chromophore microenvironment and the electronic repulsion would enlarge the solvent accessibility surface of chromophore.

As shown in Figure 3.12A, the effect of pH ($\Delta F/F_{min}$) on the fluorescence intensity was greater in MCD14, compared with the wild type. Calcium binding even enhanced the influence. MCD1 and MCD15 showed the similar performance. Binding of calcium sensitizes the chromophore to pH change, implying that the binding indirectly alters the chromophore environment. Generally for all mCherry-based calcium sensors, the pK_a of the apo form is lower than its holo-form and smaller than 5. In the physiological range of most organelles other than lysosome and endosome where pH was lower than 6, those sensors are valid to reflect the calcium change without the interference of pH.

Table 3.2 Biophysical properties of selected mCherry variants

Proteins	ε_{587} (mM^{-1} cm^{-1})	Quantum yield Φ		Average lifetime (ns)		Brightness		pK_a	
	Apo/Holo	Apo	Holo	Apo	Holo	Apo	Holo	Apo	Holo
MCD1	64	0.17	0.24	1.52	1.61	0.11	0.15	3.6	5.0
MCD14	67	0.20	0.22	1.50	1.54	0.13	0.15	4.4	4.8
MCD15	65	0.21	0.24	1.44	1.47	0.14	0.16	4.4	4.6
mcEE	58	0.18				0.14		4.3	
mcP5	69	0.18				0.12		-----	
mcIN1	68	0.21				0.14		4.0	
w.t.MC	72	0.22		1.46		0.16		4.3	

(1) The standard deviation was not shown because they were smaller than 0.01.
(2) All experiments were taken at room temperature and in 10 mM Tris, pH 7.4.

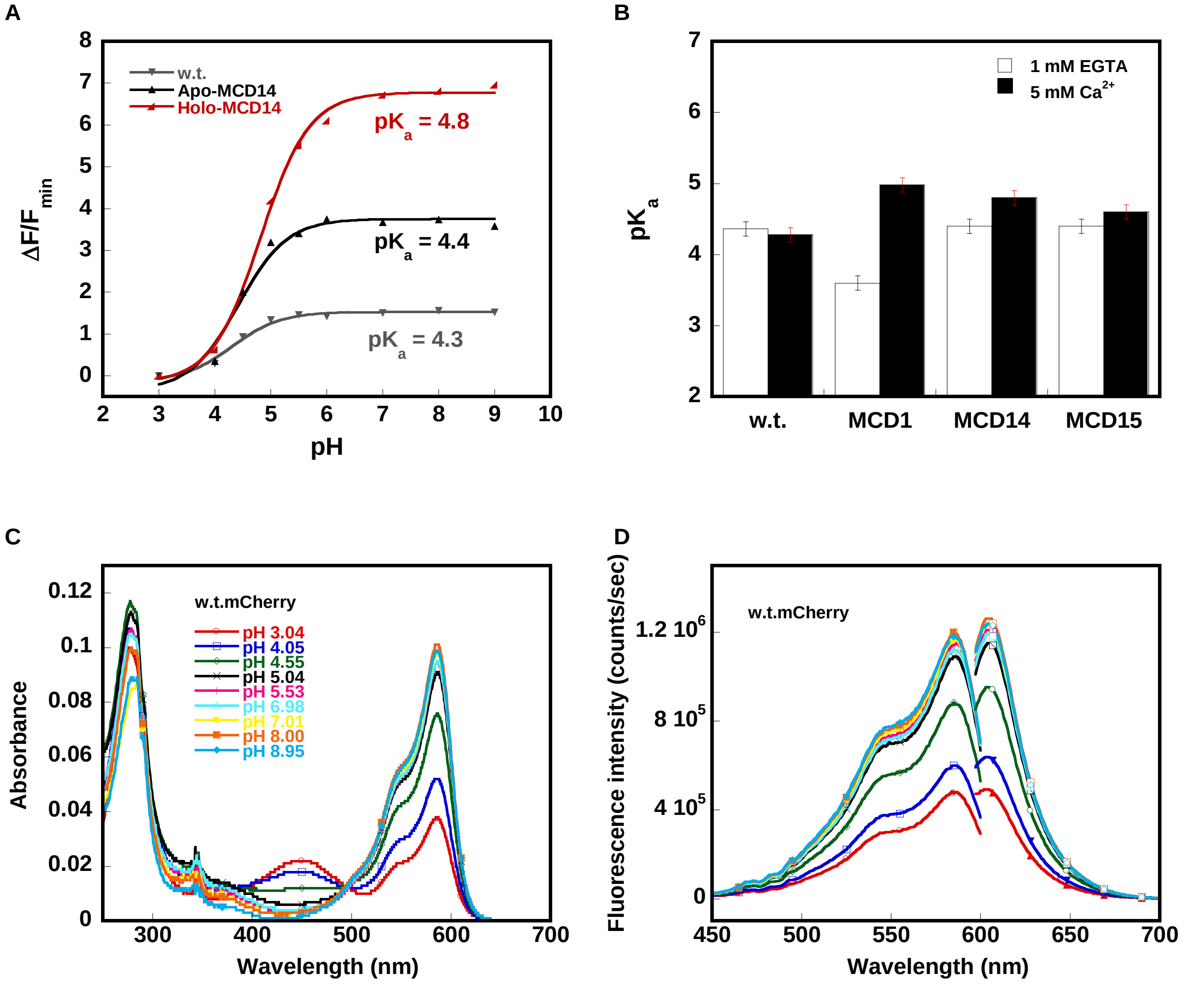

Figure 3.12. pH profile and pK_a determination.
(A) The representative pH profile of 10 mM wild type mCherry and MCD14 in the absence and presence of calcium. (B) Summary of pKa of mCherry variants. The proteins was incubated in buffers at different pH as described in methods. Ca^{2+} with a final concentration of 5 mM was supplemented as the holo form and EGTA with a final concentration of 1 mM was added to chelate the free calcium in buffers as the apo form. The pKa value was obtained by fitting the curve using Equation 2.2. (C) The UV/visible spectra and (D) the fluorescence excitation/emission (587/610 nm) spectra of the wild type mCherry. The spectra for other mutants were similar as those of the wild type.

3.2.5 *Equilibrium-dialysis assay using ICP-OES to detect calcium amount*

3.2.5.1 The simulation of the equilibrium-dialysis assay

To obtain an optimal result, the simulation of the dialysis-equilibrium binding assay was conducted. The variants in this simulation are the free calcium concentration at the equilibrium state and the total protein input. The readout of ICP-OES (Inductively coupled plasma optical emission spectrometry) is the value of the total calcium concentration, which is the sum of the free calcium concentration and calcium ($[Ca^{2+}]_{free}$) concentration in the dialysis bag ($[Ca^{2+}]_{it}$). The dissociation constant was determined by the calcium titration. There are two assumptions here. One is that the initial calcium concentration in the buffer is equal to the free calcium concentration in the buffer at the equilibrium state, which is indicated by $[Ca^{2+}]_{free}$. This is assumption was made when the buffer's volume is much larger (>2000 times) than the protein's volume, and the K_d is in the sub-μM to mM level. The other assumption is that the protein is in the calcium-free form.

Figure 3.13 shows the three-dimension plot, the ranges of both $[Ca^{2+}]_{free}$ and $[P]_t$ is 5 to 1000 μM, the ratio of $[Ca^{2+}]_{it}$/ $[Ca^{2+}]_{free}$ is represented by meshgrid. The red color indicates the high value. A high ratio is obtained by adding lower concentration of calcium in buffer and using higher concentration of protein inside the dialysis bag. From the plot, the highest ratio is 2.98, and the corresponding $[P]_t$ and $[Ca^{2+}]_{free}$ is 1 mM and 5 μM, respectively. However, 1 mM protein is less practical. Also, the contamination of the trace amount of calcium in ddH_2O is approximately 2 μM, determined by ICP-OES. As a result, the experiment can be conducted using 500 μl 100 μM protein and 10 μM calcium buffer, which will result in an expected ratio of 1.5 when K_d is 180 μM.

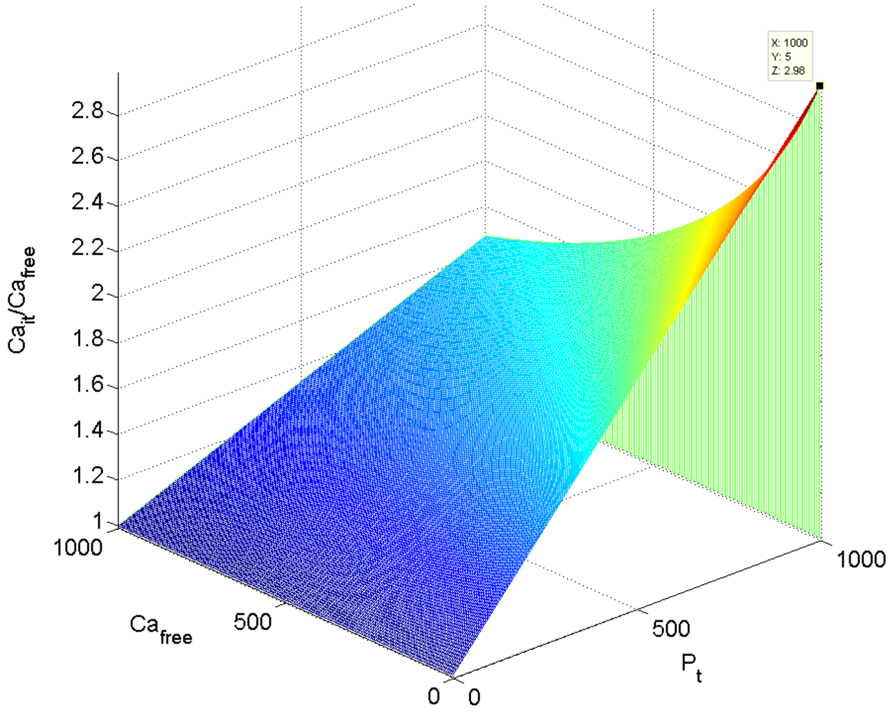

Figure 3.13. The 3D plot of the ratio of $[Ca^{2+}]_{it}$/ $[Ca^{2+}]_{free}$ as a function of [P]t and $[Ca^{2+}]_{free}$. The dissociation constant was set to be 0.5 mM. The highest point is [Cafree, Pt, Cait/Cafree] = [1000, 5, 2.98].

3.2.5.2 The equilibrium-dialysis assay

To determine the intrinsic calcium binding affinity of the protein, equilibrium-dialysis assay was applied. The equilibrium was reached after 48 h-long dialysis with stirring at 4°C. The UV spectra were record before and after dialysis for calculate the protein concentration in case of the possible volume change. The calcium standard, along with the solution inside and outside the dialysis bag collected after equilibrium reached was used to measure the total calcium concentration by ICP-OES. The ICP-OES is a technique for detecting the trace amount of metals. The temperature of argon plasma reaches approximately 8000 ℃ and thermally excites all elements. Each element emits light at its characteristic wavelengths, which is collected by spectrometer. Here, spectra of light at seven wavelengths (220.861, 219.779, 317.933, 370.602, 373.690, 396.847, 643.907 nm) emitted by calcium was collected and finally five of them were used since the dynamic range at 219.779 and 220.861 nm is too low (~300 for 3 ppm [Ca^{2+}] increase). The standard curves were fitted by linear equation. Calcium concentrations of different samples were back-calculated based on standard curves. Protein concentrations before and after dialysis did not significantly change.

The protein folding quality can be indicated by the ratio of A_{587}/A_{280} suggested that protein since the extinction coefficients at both 280 and 587 nm for all the variants are quite similar. The UV spectra implied that MCD14 and MCD15 were mixture of well-folded forms with active chromophore, which contribute to absorbance at 587 nm, and partially-unfolded protein lacking chromophore. Compared to MCD1 and the wild type, MCD14 and MCD15 had less fraction of folded protein. The cleavage issue of all mCherry protein was not taken into account because the previous studies have shown that the cleaved peptides associate with each other tightly (see Section **3.2.2.2**). One more negatively charged residue on MCD14 and MCD15 than MCD1 may cause the loosely packed β-barrel, which in turn affect the critical micro-environment for the formation of the chromophore. Proteins which did not successfully form chromophore may contribute to calcium binding with a different binding affinity, which caused the result reflecting only the general observed calcium binding affinity. Here, to simplify the problem, we assume that all the fractions have the same calcium binding capability. Therefore, the total protein concentration was used for calculation, which was determined using absorbance at 280 nm.

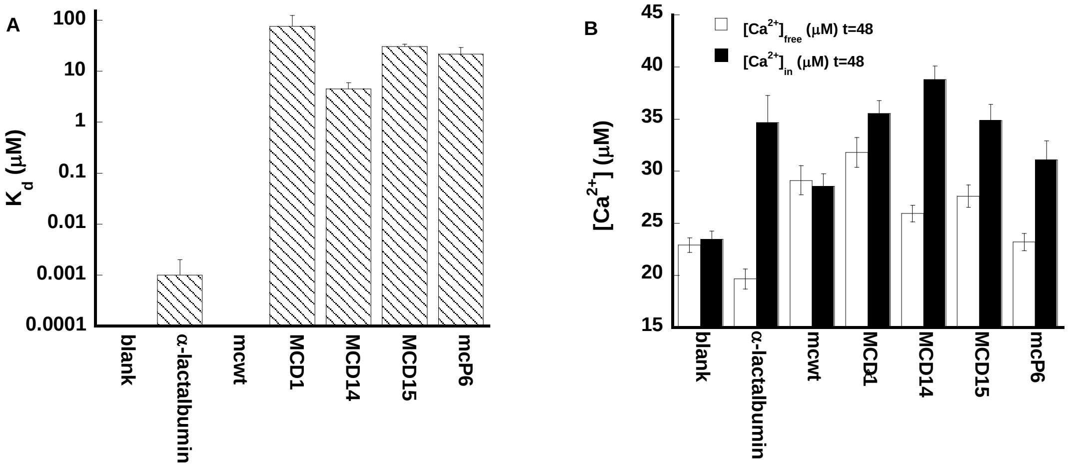

Figure 3.14. Equilibrium-dialysis assay for calcium dissociation constant determination.
(A) The calculated K_d. (B) The average of calculated calcium concentration. For comparison convenience, the calcium concentration was back-calculated assuming the protein concentration was the same. Using extinction coefficients ε_{280}=38.9 mM^{-1} cm^{-1}, the concentrations of total protein w.t.mCherry, MCD1, MCD14, MCD15 and mcP6 at equilibrium were 15 μM, 11 μM, 45 μM, 38 μM and 30 μM. The black bar indicates protein sample in the dialysis bag, and the white bar indicates the buffer samples which were collected outside the dialysis bags. All experiments were carried at 4°C and in 10 mM Tris, pH 7.4.

As shown in Figure 3.14B, in two negative controls, at equilibrium, calcium concentration inside or outside the dialysis bag appeared no significant difference. The calcium concentration inside the dialysis bag at equilibrium was even a little higher than that outside in the blank control, implying the non-specific adhesion of calcium on the dialysis bag. α-Lactalbumin served as the positive control, which showed great value of the ratio of $[Ca^{2+}]_{in}/[Ca^{2+}]_{buffer}$ at equilibrium. And the binding affinity is in the range nM, in agreement with the literature reported value. Both the negative and positive controls validate this approach.

The calculated K_d of mCherry variants were shown in Figure 3.14A. MCD14 appeared to have the highest calcium binding affinity (K_d=4.3 μM). MCD15 has only Glu-to-Asp mutation of MCD14, resulting in a 6-fold greater dissociation constant (29.4 μM). The binding affinity of MCD1, with two less formal charge around the designed calcium binding site, was 1/3 MCD15. mcP6, which had four formal charge designed to coordinate calcium ion, had no fluorescence change in addition of calcium, but the equilibrium-dialysis assay confirmed its calcium binding ability.

The K_d value calculated from this assay was generally larger than those calculated using either fluorometer or the stopped-flow spectrometer. The dissociation constants given by equilibrium-dialysis assay is 10% -50% of the values obtained using other methods. This is mainly accounted for the involvement of the total protein in the final calculation in the equilibrium-dialysis assay, while fluorescence is monitored in other methods, which was only contributed to the well-formed chromophore. In principle, the equilibrium-dialysis assay is more accurate for determination of binding constants for the pure protein. However, this assay can only provide the averaged value for the total protein including the isoform or unfolded protein.

3.2.6 *Calcium binding affinity of mCherry variants*

Calcium response was measured using the fluorometer by titrating Ca^{2+} to proteins in 10 mM Tris buffer (pH7.4). The data was fitted using Equation 2.6 and 2.7 assuming the binding stoichiometry was 1:1 (131), as shown in Figure 3.15. For MCD1, although it seemed to have another binding phase beyond 1 mM calcium, MCD1 was 90% saturated in the presence of ~1 mM calcium (Figure 3.15A). Except MCD1, other calcium sensor did not show the “second phase” during titration. One more mutation of MCD1/R220E, MCD14, facilitated the calcium binding and increase the binding affinity. However, with the same charge distribution as MCD14, MCD15 had lower calcium binding affinity. Compared to MCD14, the Glu-to Asp substitution in MCD15 changed the side chain length of one expected calcium coordinator, resulting in only 20% of the calcium binding affinity. The mutation 197Y of MCD14, which was designed for the aromatic stacking effect over the chromophore, showed the stronger binding affinity than MCD14. However, the protein was unstable at room temperature causing the color loss. mcEE was the intermediate product of the designed calcium binding pocket 4 (mcP4) and pocket 5 (mcP5). Upon calcium binding, the fluorescence intensity of mcEE decreased by 15% (Figure 3.15B). In the conditions of the intracellular buffer including 130 mM KCl and 1 mM Mg^{2+}, adding calcium showed no effect on fluorescence, which suggested mcEE can not be used in cell imaging. Table 3.3 summarized the dissociation constants of mCherry variants and CatchER measured in different buffers. The calcium-triggered increase of fluorescent intensity of MCD1 in high salt buffers indicates the possibility of its application in living cells.

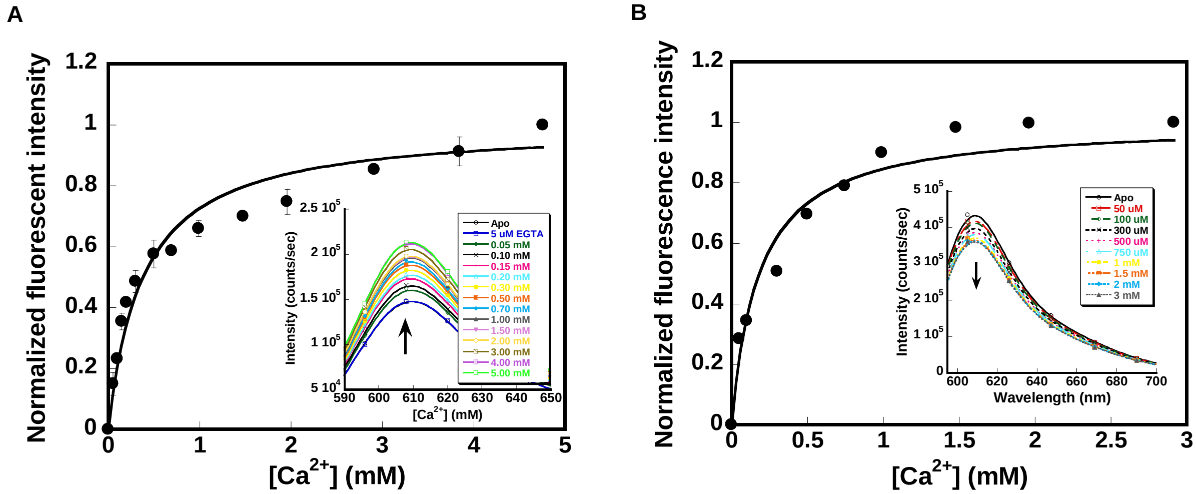

Figure 3.15. The curve fitting for K_d of (A) MCD1 and (B) mcEE.
The inset shows the fluorescence intensity change upon titrating calcium in the absence of salt. For MCD1, the data fitting from 0 to 5 mM Ca^{2+}, the K_d was calculated as 0.40 mM. For mcEE, the data fitting from 0 to 3.0 mM Ca^{2+}, where K_d was calculated as 0.18 mM. All experiments were carried out at room temperature and in 10 mM Tris, pH 7.4.

Table 3.3 The dissociation constant and dynamic range of mCherry variants

Sensors	Buffer/concentrations	Kd (mM)	Dynamic range
MCD1	10 mM Tris, pH 7.4	0.10 ± 0.03	1.40 ± 0.06
MCD2	10 mM Tris, pH 7.4	0.033 ± 0.003	1.14 ± 0.01
MCD23	10 mM Tris, pH 7.4	0.11 ± 0.01	1.18 ± 0.01
MCD14	10 mMTris, pH 7.4	0.085 ± 0.004	1.40 ± 0.01
MCD14Y	10 mMTris, pH 7.4	0.06 ± 0.01	1.33 ± 0.01
MCD15	10 mMTris, pH 7.4	0.48 ± 0.08	1.17 ± 0.01
mcEE	10 mMTris, pH 7.4	0.18 ± 0.02	1.13 ± 0.02
CatchER	10 mMTris, pH 7.4	0.33 ± 0.03	1.51 ± 0.03

Here, the dynamic range was defined by the ratio of the Ca^{2+}-saturated to the apo protein fluorescence (F_{max}/F_{min}) or the brightness ratio (B_{holo}/B_{apo}) (131). For the first site (MCD1x), among MCD1, MCD14, MCD15, the calcium-free form suppresses the fluorescence and calcium binding recover the fluorescence to the same level as wild type. For the second site (MCD2x), among MCD2, MCD23, the fluorescence can not reach the same level as wild type by calcium binding, although suppression of fluorescence by the pocket 2 variants was comparable with pocket 1. Steric hindrance reduces dynamic range but its effect was not in coincidence with binding affinity. Yang *et. al.* discussed the effect of calcium binding on the dynamic properties of the designed calcium binding pocket, and one conclusion was that the residues adjacent to the ligands play important role in the dynamic changes and even larger than the ligands themselves (163). In this aspect, residues 197 and 144 probably have bigger impact on the chromophore environment upon calcium binding. Also, the crystal structure analysis showed the disturbance of the chromophore by the corresponding position of 197 in holo-CatchER, compared to the apo-form.

The salt condition is a key determinant for the calcium binding affinity. In the [KCl] range of 0 – 0.5 M, both the calcium binding affinity and the fluorescence dynamic range decreases as increased [KCl] (Figure 3.16 A, B and C). The starting fluorescence intensity increased as increased KCl concentration while the end point of fluorescence intensity remained the same. In the presence of 0.5 M KCl, addition of calcium did not induce fluorescence intensity change. In the [KCl] range of 1.5 – 2.0 M, addition of calcium resulted in decrease of fluorescence intensity. The maximum decrease was about 10% for 1.0, 1.5 and 2.0 M KCl. The starting fluorescence intensity was the same for 1.0, 1.5 and 2.0 M KCl (Figure 3.16D). Such observation was similar as the KCl effect on Ca^{2+} binding to Calbindin D9K as well as small Ca^{2+} chelators EDTA and EGTA (164).

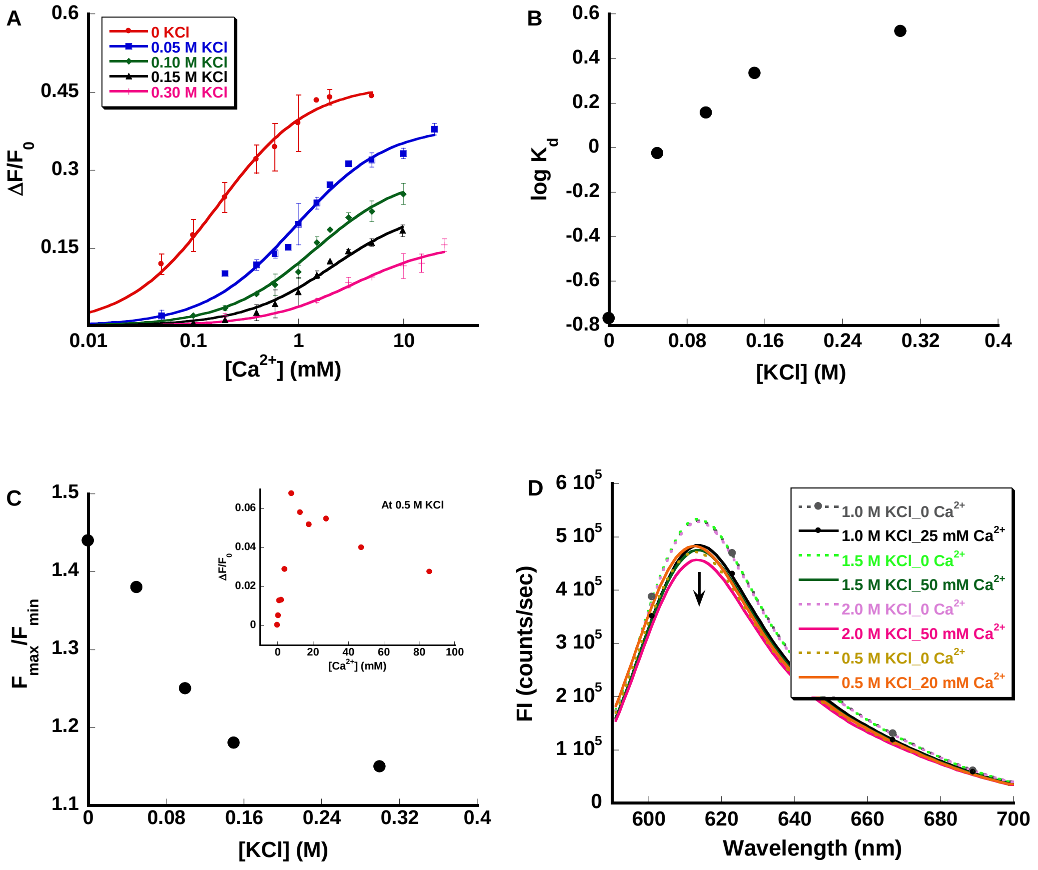

Figure 3.16. The salt-dependent K$_d$ determination.
(A) The fluorescence of calcium titration at different salt concentrations, 0, 0.05, 0.10, 0.15 and 0.30 M, as colored red, blue, green, black and pink. (B) The log K$_d$ plotted as a function of [KCl] (M); (C) The dynamic range of calcium response in the [KCl] range of 0-0.3 M, and the inset shows the ΔF/F$_0$ during calcium titration in the presence of 0.5 M KCl; (D) The fluorescence spectra of calcium free and loaded MCD1 in [KCl] range of 0.5-2.0 M.

3.2.7 *Tb^{3+}-tryptophan fluorescence resonance energy transfer (FRET)*

Tb^{3+} is the ion which has the similar effective ionic radius as Ca^{2+}, and the preference for oxygen as the coordinator (165). In addition, there is no restricted coordination number requirement for both ions. There is overlap between the emission spectrum of tryptophan and excitation spectrum of Tb^{3+}. One tryptophan Trp 143 was found around the designed calcium binding site, which is located in a short loop region in the middle of $\beta7$. Therefore, Tb^{3+}-FRET was applied to further verify calcium binding to the designed sensors. As shown in Figure 3.17, in comparison with wild type mCherry, all of these sensors exhibited the energy transfer after the addition of low concentration Tb^{3+} (< 100 μM) reflected by the significant increase of the peak at 545 nm, suggesting that Tb^{3+} was bound to the designed proteins. When Tb^{3+} was greater than 100 μM, precipitates was observed in wild type mCherry and the peak at 545 nm started growing due to the adherence of Tb^{3+} ion to the protein. This non-specific binding can also be found in the designed sensors after precipitates formed due to high concentration of Tb^{3+}. Before precipitates formed, a plateau can be observed during titrating Tb^{3+} to either MCD1 or MCD15. The dissociation constants can be fitted using the equation 5, and $K_{d,\ MCD1}$ and $K_{d,\ MCD15}$ were less than the value obtained by calcium titration due to the larger charge to ionic radius ratio of Tb^{3+}. MCD14 was precipitated by Tb^{3+} at >30 μM, and a linear relationship was found when $[Tb^{3+}]$ was in the range of 0-20 μM, suggesting a large K_d which was estimated to be greater than 100 μM. Surprisingly, MCD15 was able to tolerate higher concentration of Tb^{3+} up to 2 mM.

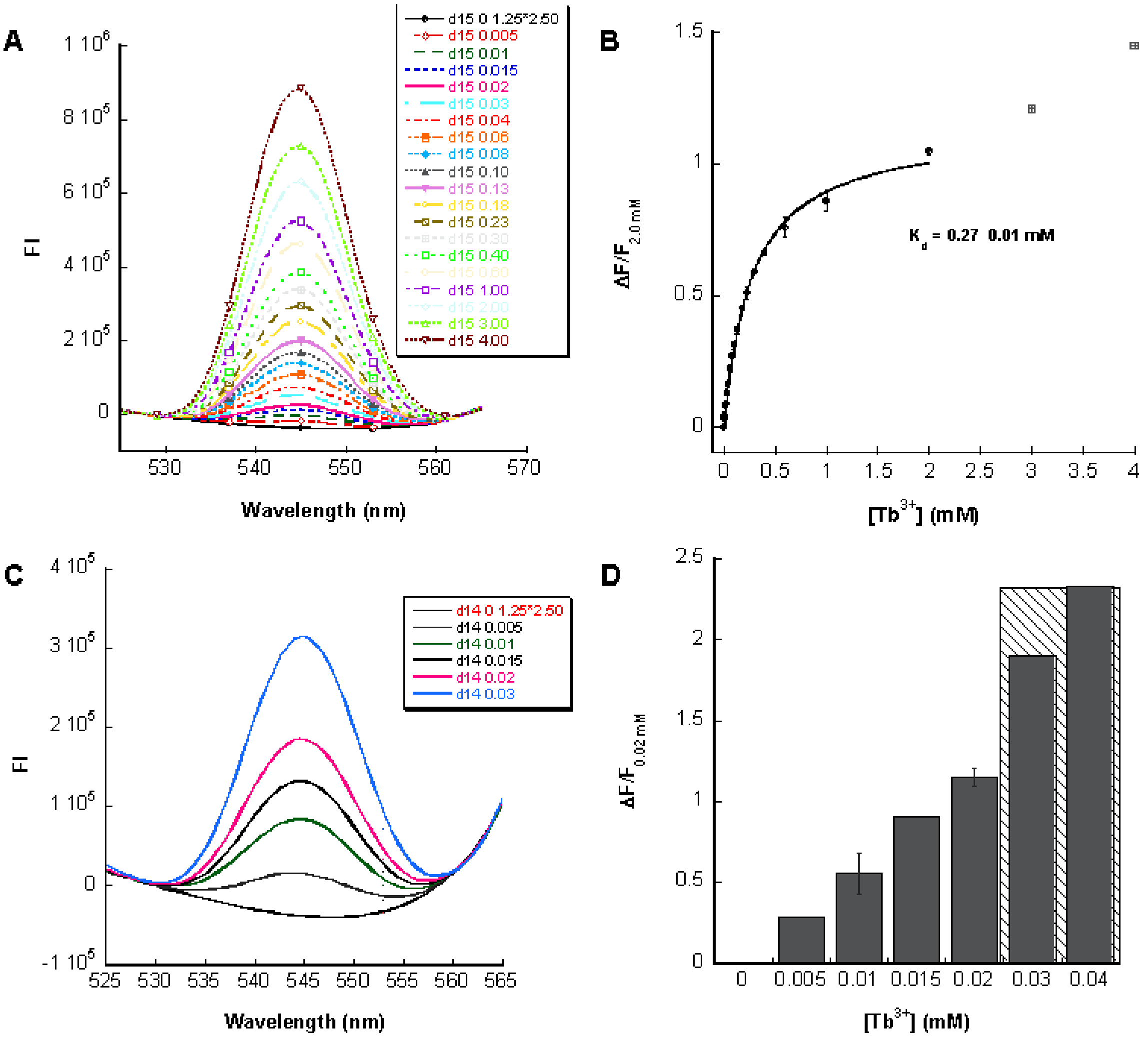
A
1 10^6
8 10^5
6 10^5
4 10^5
2 10^5
0
FI
530
540
550
560
570
Wavelength (nm)
d15 0 1.25*2.50
d15 0.005
d15 0.01
d15 0.015
d15 0.02
d15 0.03
d15 0.04
d15 0.06
d15 0.08
d15 0.10
d15 0.13
d15 0.18
d15 0.23
d15 0.30
d15 0.40
d15 0.60
d15 1.00
d15 2.00
d15 3.00
d15 4.00
B
1.5
1
0.5
0
ΔF/F2.0 mM
K d = 0.27 0.01 mM
0
0.5
1
1.5
2
2.5
3
3.5
4
[Tb3+] (mM)
C
4 10^5
3 10^5
2 10^5
1 10^5
0
-1 10^5
FI
525
530
535
540
545
550
555
560
565
Wavelength (nm)
d14 0 1.25*2.50
d14 0.005
d14 0.01
d14 0.015
d14 0.02
d14 0.03
D
2.5
2
1.5
1
0.5
0
ΔF/F0.02 mM
0
0.005
0.01
0.015
0.02
0.03
0.04
[Tb3+] (mM)

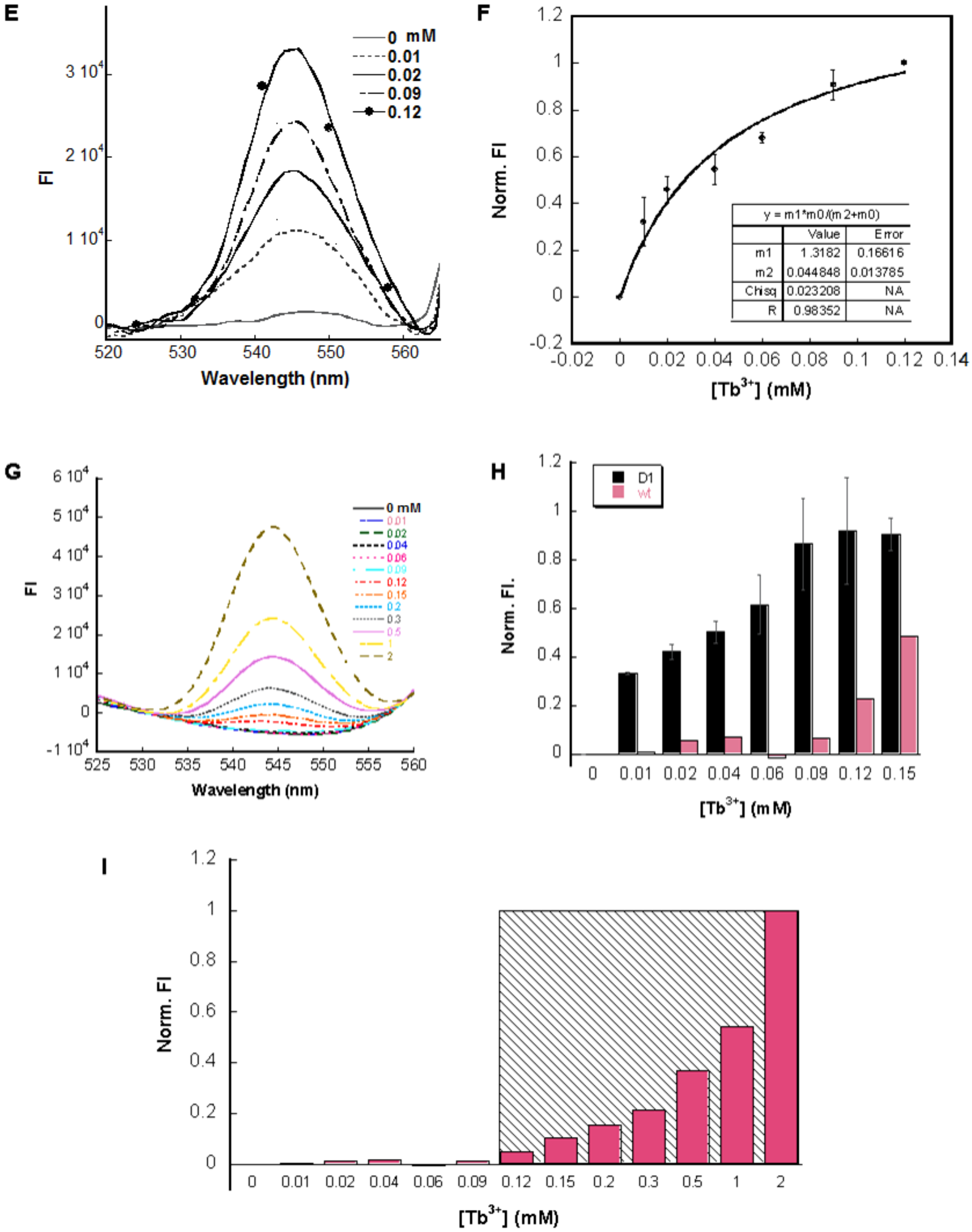

Figure 3.17. Tb^{3+}-FRET titration of mCherry and its variants.

Tb^{3+} stock (10 mM and 100 mM) was titrated into proteins with a final concentration of 5 µM in 10 mM PIPES, 10 mM KCl, pH 6.5. Panels A, C, E and G show the spectra at different concentrations of Tb^{3+} of MCD15, MCD14, MCD1 and w.t.-mCherry, respectively, which were record from 500 to 570 nm by fluorescence spectrophotometer with excitation at 282 nm. Panel B and F shows the titration curve of MCD15 and MCD1 fitted using Equation 2.6 and 2.7 and the dissociation constant was 0.27 ±0.01 mM and 0.04 ±0.01 mM, respectively. Panel D and I showed the fluorescence intensity of MCD14 and wt-mCherry at different concentrations of Tb^{3+}; the shadow indicates the precipitates. Panel H is the comparison of the fluorescence intensity of MCD1 (black) and wt-mCherry (pink) at low Tb^{3+} concentration. pH value was checked before and after titration.

Tb^{3+}-FRET suggests that Tb^{3+} mimicking Ca^{2+} accessed the designed calcium binding site. Among the sensors, the dynamic change of fluorescence intensity of MCD1 at 545 nm was smaller than MCD14 and MCD15, indicating a relatively lower energy transfer efficiency. The FRET efficiency is determined by the distance between the donor and acceptor. Hence, by increasing the negatively charged solvent accessible area with substitution of R220 with glutamic acid, the position of Ca^{2+} may shift in MCD14 and MCD15.

3.2.8 *Determine the distance between metal and chromophore using Tb^{3+} lifetime*

To understand the distance between the chromophore and calcium in MCD1/CatchER, we used the FRET efficiency to determine the distance between the FRET donor and acceptor. Terbium (Tb^{3+}) served as the energy donor, mimicking Ca^{2+} to be bound in the designed calcium binding spot. MCD1 served as energy acceptor, mimicking CatchER. MCD1ggg, of which the chromophore MYG was mutated to GGG, was the protein folded the same as MCD1 but was not fluorescent. Here, the actual donor was the Tb^{3+}-MCD1ggg because when Tb^{3+} binds to proteins, its lifetime may change as well as the quantum yield.

The relationship between the FRET efficiency and the lifetime of the donor with and without the acceptor was shown as Equation 3.1. The ratio of the distance between the acceptor and donor r to the critical distance R_0 was also related to the efficiency E. R_0 was determined by the quantum yield of the donor Φ, the refractive index n, the orientation factor κ and the spectral overlap degree between of the donor and acceptor J (Equation 3.2). In Equation 3.3, $F_D(\lambda)$ is the donor fluorescence intensity as a fraction of the total integrated intensity, and $\varepsilon_A(\lambda)$ was the acceptor absorbance spectrum normalized to its maximum molar extinction coefficient.

$$E = 1 - \frac{\tau_{DA}}{\tau_D} = \frac{1}{1 + (\frac{r}{R_0})^6} \quad \text{Equation 3.1}$$

$$R_0 = 0.2108 \times [\kappa^2 \Phi_D n^{-4} J]^{1/6} \quad \text{Equation 3.2}$$

$$J = \int F_D(\lambda) \varepsilon_A(\lambda) \lambda^4 d\lambda \quad \text{Equation 3.3}$$

Figure 3.18 illustrated that the lifetime of terbium was shorter when the acceptor chromophore was present. The FRET efficiency was 94% calculated using the Equation 3.1 and the ratio r/R_0 was 0.6. The critical distance was obtained following the protocol by Hink and Visser (166, 167). The quantum yield of the protein bound Tb^{3+} was 0.04 (168). The bandpass was 7 nm. So the calculated critical distance and the distance between the chromophore and Tb^{3+} ion was 29 Å and 17 Å, respectively. As shown in Figure 3.18B, the measured distance from Ca^{2+} to the chromophore was in the range of 11-17 Å, in agreement with the calculated one. It is conclusive that the calcium ion locates in the designed calcium binding site.

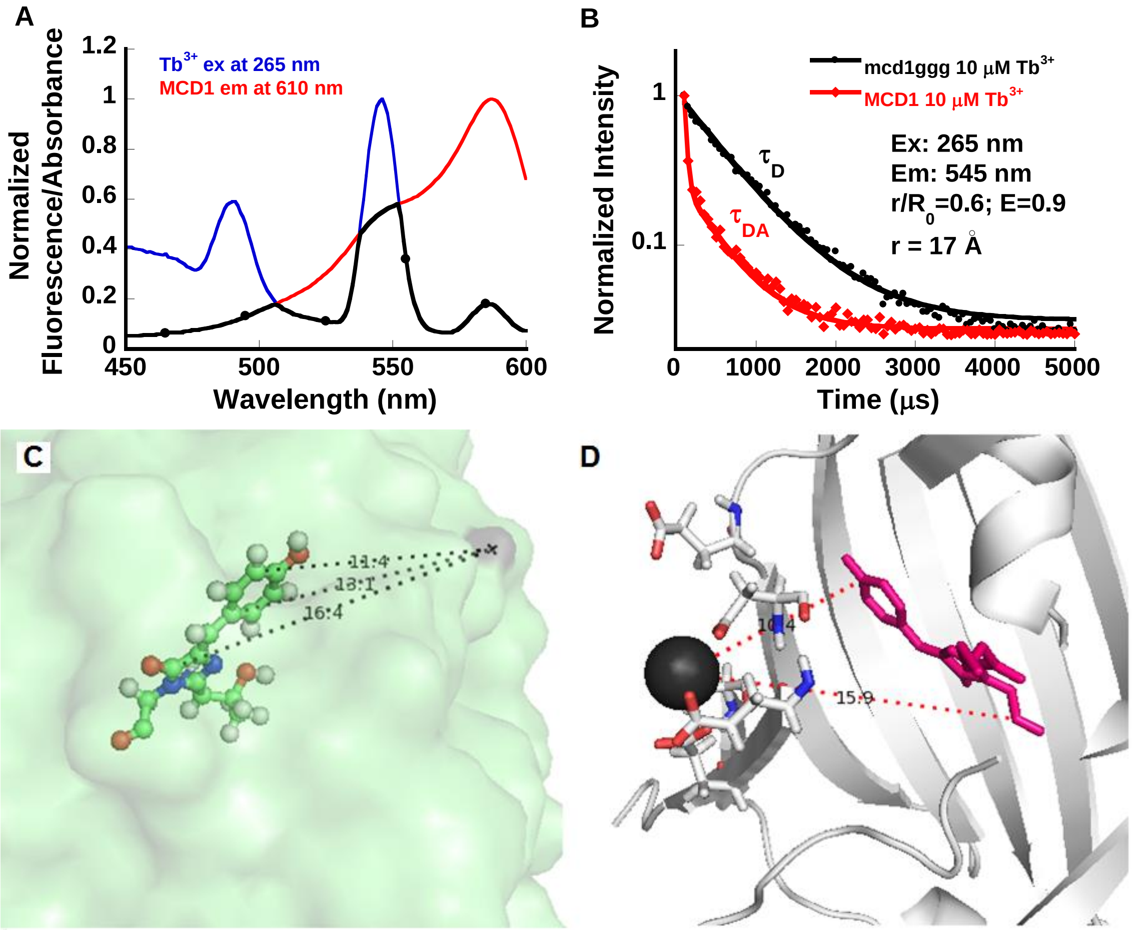

Figure 3.18. The calculated distance between ion and the chromophore.
(A) The spectra overlap between the emission of 10 mM Tb^{3+} and excitation of 10 μM MCD1 in 10 mM PIPES, pH 6.5. (B)The Tb^{3+} lifetime of the free form and in the FRET pair. The average lifetime was obtained by the double exponential fitting. (C) The distance of Ca^{2+}-CRO measured in the crystal structure of Ca^{2+}-CatchER. (D) The distance of Ca^{2+}-CRO measured in the model structure of Ca^{2+}-MCD1.

3.2.9 *Metal selectivity*

mCherry-based calcium sensors exhibit a good calcium selectivity over other metals in the physiological concentration. Figure 3.19 shows the fluorescence intensity of 10 μM MCD1 as a representative, in the present of 1 mM Ca^{2+} and 125 mM K^{+}, 25 mM Na^{+}, 5 μM Cu^{2+}, 5 μM Zn^{2+}, 1 mM Mg^{2+}, 0.2 mM ATP, 0.1 mM GTP and 0.1 mM GDP. The fluorescence intensity was not influenced by the tested metals and nucleotides other than copper ion. The fluorescence of mCherry variants can be quenched by Cu^{2+}. However, in the physiological condition, the free

[Cu^{2+}] is much less and close to zero. Thus, Cu^{2+} quench effect can be ignored when it is applied to the living cells.

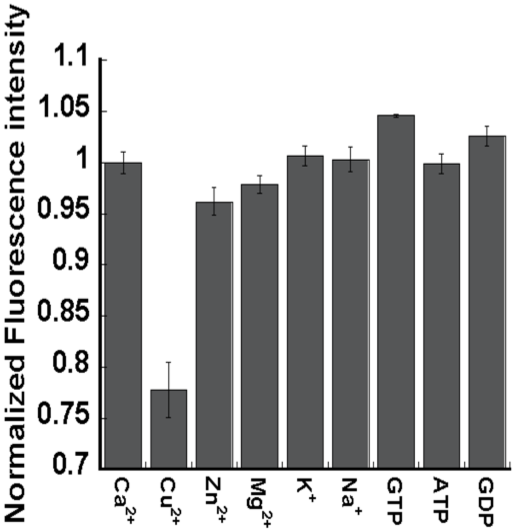

Figure 3.19. Metal and nucleotides selectivity of MCD1.
All metals and small molecules were added to 5 μM MCD1 pre-loaded with 1 mM Ca^{2+} in 10 mM Tris, pH7.4. The excitation was at 587 nm and emission was collected from 590-700 nm.

In addition, the detailed analysis of the metal selectivity will be performed to obtain the binding affinity of Mg^{2+}, Zn^{2+}, Gd^{3+} and Fe^{2+} by calcium titration monitored by both fluorescence and equilibrium-dialysis-ICP assay. The information is essential for the design of the specific metal binding sites in the future.

3.2.10 *Kinetics study of calcium binding to MCD1*

The kinetics of calcium binding is essential for a calcium indicator. The value of k_{on} and k_{off} reflect the binding on-rate and off-rate. An ideal biosensor is required to have the fast on- and off-rate so as to be able the capture a whole biological event. MCD15 purified from pET28α in *E. coli.* BL21 (DE3) was used for the kinetics study. The calcium binding kinetics was monitored by the stopped-flow fluorimeter equipped with the mercury-Xe lamp. The intensity was first calibrated by the samples with the lowest and the highest fluorescence and scaled to 0-100%. The fluorescence dye x-Rhod 5F was used to optimize instrument conditions including to determine the fluorescence intensity has linear relationship with the concentration.

Before experiments, the fluorescence intensity was calibrated using the calcium saturated x-Rhod-5F (Invitrogen) to make sure the linear relationship between the fluorescence and concentration (Figure 3.20D). In Figure 3.20A, mixing MCD1 with different concentrations of calcium solutions resulted in the rapid increase of the fluorescence signal. However, the binding process was totally lost in the dead time. There is less likelihood to fit k_{obs} at even the lowest calcium concentration applied. Similarly, the off rate was too fast to be captured. As shown in Figure 3.20B, the overlaid stopped-flow traces indicated that the fluorescence signal fell back to the basal level upon EGTA chelating Ca^{2+}. Considered the 2 ms dead time of this instrument, four half lifetime was finished. k_{off} can be estimated to be at least 1.9×10^3 s^{-1}. Assuming calcium binding to MCD1 follows the simple 1:1 binding mode, k_{on} can be estimated to be at least 2.72×10^7 $M^{-1}s^{-1}$ according to Equation 2.9. The dissociation constant was fitted using the amplitudes, which was consistent with the K_d value independently determined by the calcium titration monitored by a spectrofluorometer with the error in an acceptable range. As the positive control (Figure 3.20C), the off rate of x-Rhod-5F was determined by mixing 2 μM x-Rhod-5F preloaded with 5 μM calcium with 10 mM EGTA. The process of calcium dissociation from the dye was lost in the dead time and only the plateau was observed. Similarly, the off rate of x-Rhod-5F was estimated to be at least 2.1×10^3 s^{-1}. For more accurate determination, T-jump may be applied; however, the present data suggested that the fast response of MCD1 to calcium enable it to detect most physiological events.

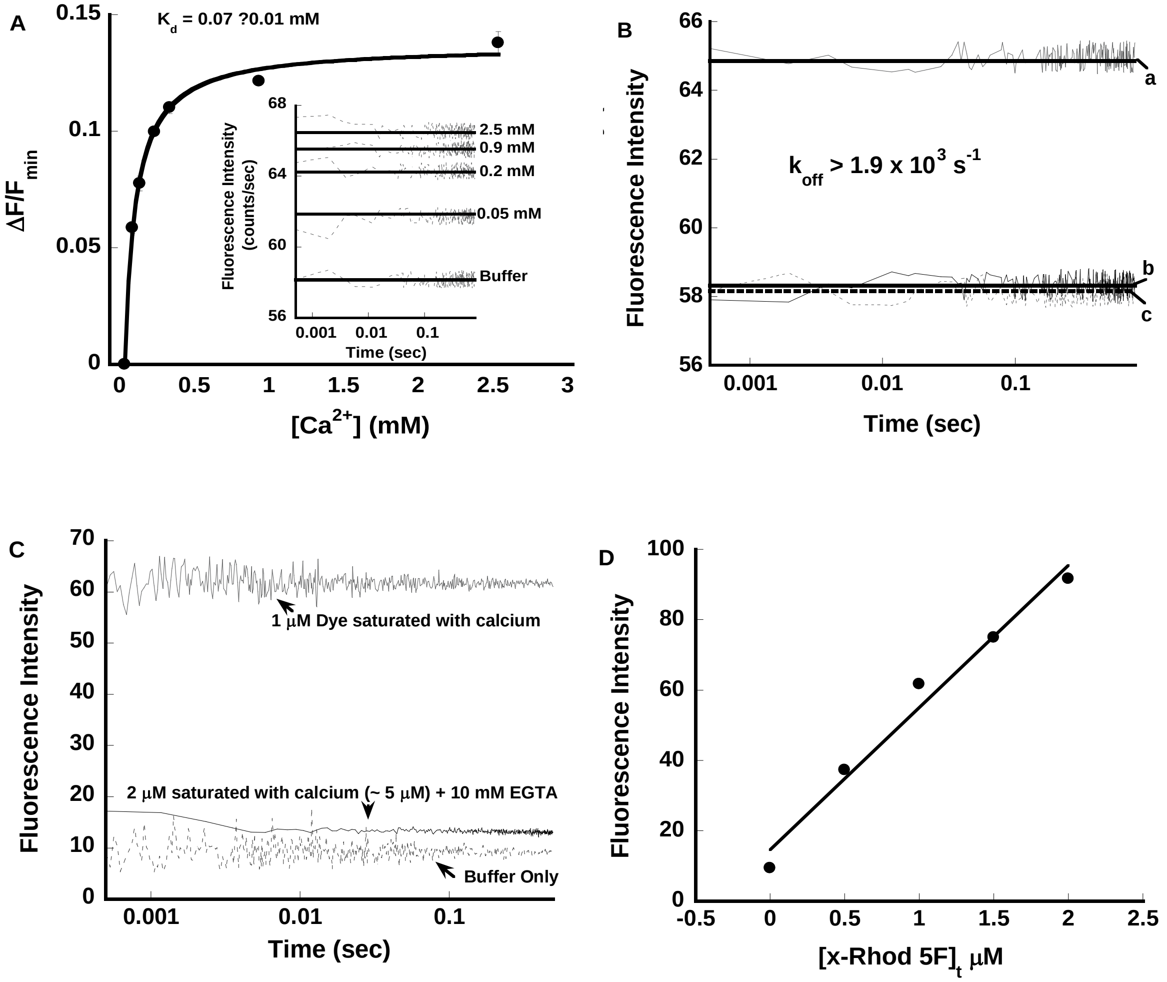

Figure 3.20. Kinetics analysis of association of Ca^{2+} with MCD1.

(A) The amplitude of the fluorescence increase observed in the panel A as a function of calcium concentration. Inset shows the stopped-flow traces of fluorescence increase upon rapid mixing of MCD1 at a final concentration of 10 μM with Ca^{2+} at different concentrations. (B) The stopped-flow traces of the fluorescence change upon (a) mixing of 20 μM MCD1 with 0.6 mM Ca^{2+}, (b) mixing of 20 μM MCD1 preloaded with 0.6 mM Ca^{2+} with 10 mM EGTA and (c) mixing of 20 μM MCD1 with buffer. (C) The stopped-flow traces of calcium-saturated x-Rhod-5F mixing with 10 mM EGTA. (D) The intensity calibration for the stropped-flow fluorescence spectrometer using x-Rhod-5F.

Table 3.4 Calcium and terbium binding affinity calculated using different methods

MCDx	Ca^{2+}(mM)			Tb^{3+} (mM)[d]
	Titration[a]	Stopped-flow[b]	Eq.-Dialysis[c]	
MCD1	0.10±0.03	0.07±0.01	0.07±0.04	0.04±0.01
MCD14	0.08±0.01	NA	0.004±0.001	NA
MCD15	0.47±0.12	NA	0.03±0.01	0.27±0.01

[a] The proteins were excited at 587 nm and the maximum fluorescence emission intensity at 610 nm was used for calculation.

[b] The excitation/emission was set as 587/610nm, respectively. The average fluorescence intensity at the plateau was used for calculation.

[c] The average value was obtained from five Ca^{2+} signature emission wavelengths: 317.933, 370.602, 373.690, 396.847, 643.907 nm.

[d] The experiment was carried out at 10 mM PIPES, pH 6.5, 10 mM KCl. The excitation was at 350 nm and the emission was collected from 420-600 nm.

3.2.11 *NMR spectroscopy*

To understand the structural change upon calcium binding in mCherry variants, NMR was set up for 1D and 2D analysis. ^{15}N labeled MCD14 was expressed and purified as described before. Here, all fid data was collected using Varian INOVA 600 MHz spectrometer at the departmental facilities. The 1D H-NMR of MCD1 and MCD14 was acquired using water gate pulse sequence. The 2D ^{1}H-^{15}N spectra of MCD14 was acquired using gNhsqc pulse sequence. Before running sample, D_2O of the final concentration of 10% (v/v) was added. Pulse-field gradient diffusion experiment was run using MCD1 sample. One more run should be carried out using lysozyme as the standard in the same condition to obtain the hydrodynamic radius. 1D spectra of calcium titration were taken using MCD1 sample to find the saturation point. There was no significant change upon calcium titrated MCD1 as shown in Figure 3.21. When [Ca^{2+}] was higher than 2 mM, the peaks were not dispersed well. So holo-protein mentioned in this section means protein sample supplemented with 2 mM Ca^{2+}. Clearly, the 1D proton spectra were not enough to demonstrate whether the protein was saturated with calcium.

Temperature-dependent HSQC experiments were conducted at 25, 30, 35 and 40 ℃. The result shown in Figure 3.22 suggested that at higher temperature the spectrum was less crowded in the middle and peaks in general were sharper, which was resulted from the faster molecule tumbling. There were minor peaks observed near the major peaks, implying two conformations were in present in the protein sample.

The spectra overlay of calcium-free and loaded forms of MCD14 were shown in Figure 3.23, where the difference clearly indicated the partial structural change due to calcium binding. The overall peak intensity decreased upon adding 2 mM Ca^{2+}. Here, EGTA was not supplemented in the apo form, which may cause the disturbance of the trace amount of calcium and other metals. The chemical exchange of MCD14 was altered in addition of calcium, which is shown in the panel b, c and d as examples. In the panel a in Figure 3.23, the presence of calcium slowed down the rotational rate of the residue and stabilizes one state, which is indicated by the peak splitting. The residue Q69 in CatchER also exhibits the similar peak splitting induced by calcium binding. The inset d showed two effects of calcium binding, the chemical shift change and the peak splitting. The panel e showed the double peak merged to one upon adding calcium, suggesting the calcium binding induced the residue to rotate faster and becomes more flexible. If those residues experiencing chemical shift and line width change upon calcium addition could be assigned and understood, the insight will be gained that the molecular mechanism of calcium binding induced the fluorescence change. Although the assignment has not been done at this moment because of the difficulty to get the pure non-cleaved mCherry variants and the limited time, the calcium binding induced regional conformational change of mCherry variant MCD14 is confirmed by the NMR spectroscopy.

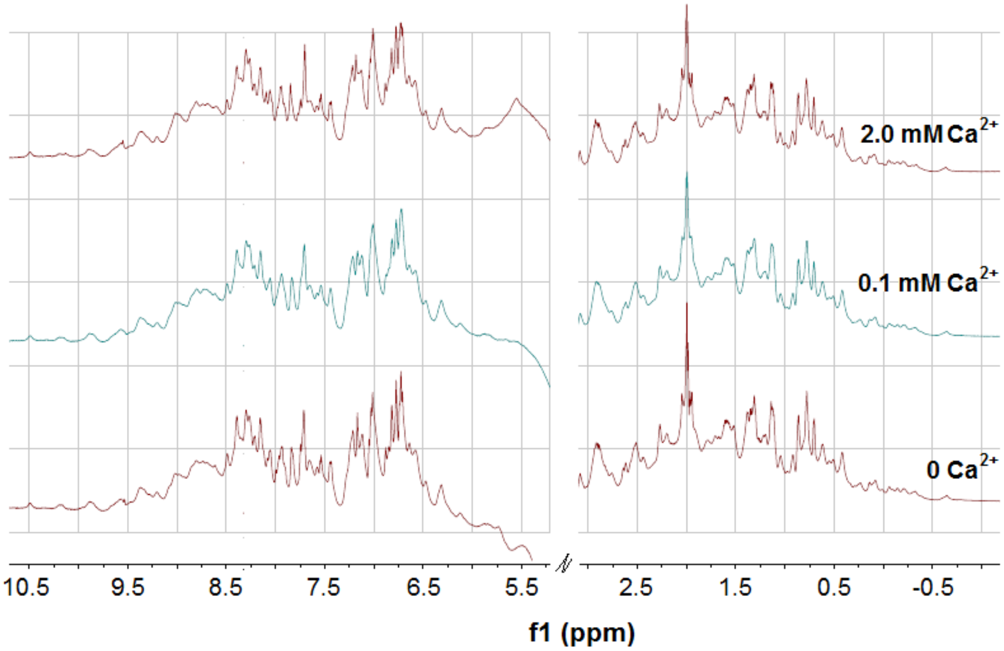

Figure 3.21. The stacked 1D proton NMR spectra of calcium titration to MCD1 at 37°C.
The top, the middle and the button ones were 100 µM MCD1 in buffer 10 mM Tris, pH 7.4, 10% D_2O, in addition of 2 mM, 100 µM, and 0 Ca^{2+} respectively.

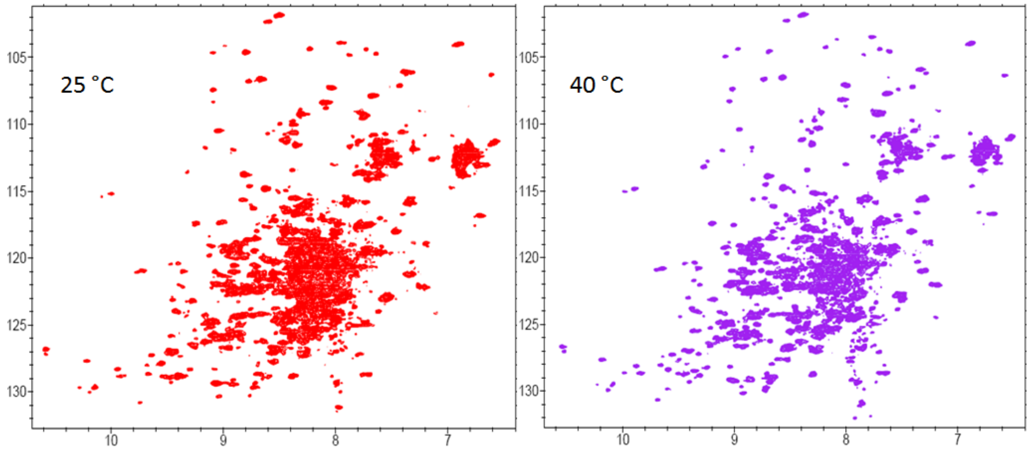

Figure 3.22. HSQC spectra of MCD14 at 25 ℃ and 40 ℃.
The experiment setting was the same except the temperature. The buffer was 10 mM Tris, pH 7.4. MCD14 concentration was 100 µM.

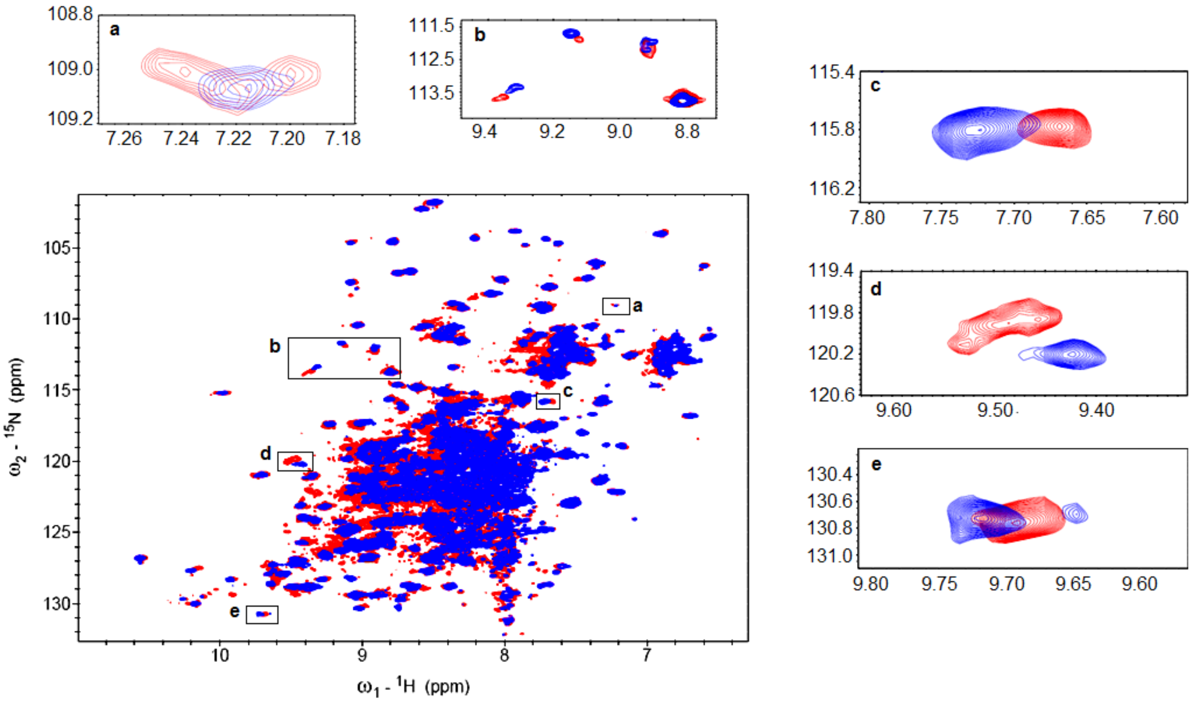

Figure 3.23. The overlaid ^{1}H-^{15}N-HSQC spectra of calcium-free (blue) and loaded (red) MCD14. The buffer was 10 mM Tris, pH 7.4. MCD14 concentration was 100 μM before adding calcium.

3.3 Cell imaging and calcium response in situ

3.3.1 *Drug response*

To evaluate the designed calcium binding proteins in high calcium environment *in situ*, the proteins were fused with the calreticulin ER tag in the N-terminal and the ER retention sequence KDEL in the C-terminal. The recombinant DNA was transfected to cells and express for 36-48 hours before calcium imaging. The reticulum-network was observed (Figure 3.24) around the DAPI-stained nucleus.

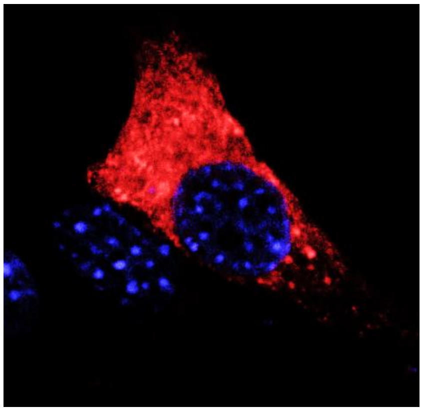

Figure 3.24. The confocal image of ER-tagged MCD1 expressed in C2C12 cells.
The blue color indicated the DAPI. The red color was the fluorescence produced by ER-tagged MCD1.

Four cell lines: HEK-293, BHK, HeLa, and C2C12 were used for validation. The cell imaging was collected from a LSM 510 laser confocal microscope (Carl Zeiss Inc., Thornwood, NY) using a 40 × oil immersion objective (Zeiss, Fluar, 1.30 n.a.). The whole cell is selected as the region of interest (ROI). The most common drugs, which are activators of ryanodine receptor (4-cmc), the inhibitor of SERCA pump (CPA) and the calcium ionophore (ionomycin), were applied and calcium response was monitored by the designed calcium binding proteins. The consequence of treatment of these drugs is calcium release from ER. The signal of ER-targeted calcium sensors is expected to be reduced upon adding these drugs.

Since ionomycin can form the calcium ionomycin salt and transport across the biological membranes, it is commonly used for equilibrium of intracellular and extracellular calcium. Appling ionomycin under the low calcium background leads to the calcium efflux out of the ER, which is not cell type dependent and thus used to test and calibrate the calcium dyes in all kinds of cell lines. However, the treatment of ionomycin is not physiologically significant. As shown in Figure 3.25A, C2C12 cells transfected with MCD1x were treated by ionomycin. The fluorescence intensity decreased once the ionomycin was added and it was recovered by changing the solution to Ringer's buffer containing 10 mM Ca^{2+}. MCD15 was saturated by ER calcium because the fluorescence intensity in the condition with high calcium did not differ from the one before any treatment. Figure 3.25B demonstrated the average fluorescence of MCD1x in the three phases of 0 Ca^{2+}, ionomycin and 10 mM Ca^{2+} in HEK 93 and C2C12 cells. It is clear that MCD15 has the largest fluorescence change. As a result, MCD15 was selected for the further tests by applying ER calcium channel activator and inhibitor.

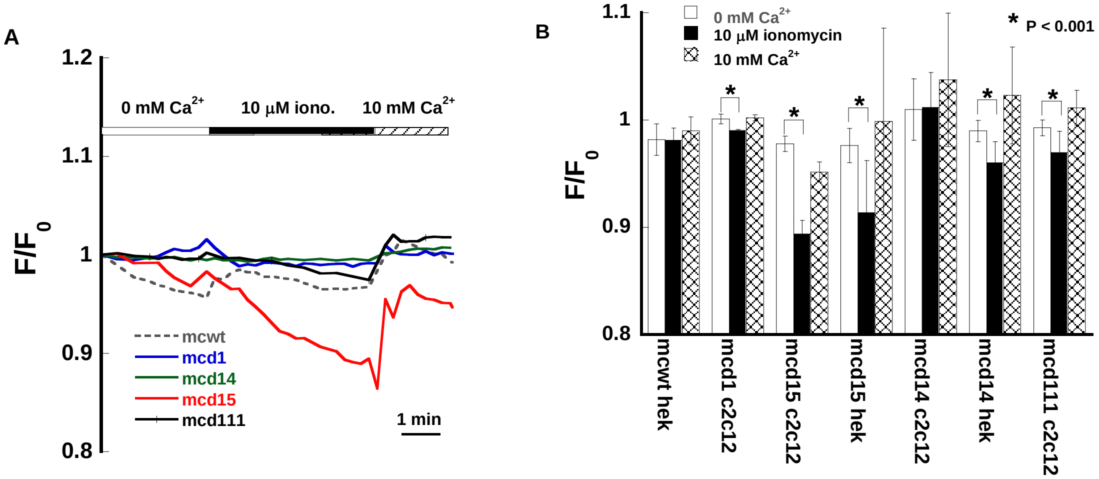

Figure 3.25. Comparison of MCD1x responding to ionomycin.
(A) The average fluorescence time traces of the MCD1x in the treatment of ionomycin. (B) The fluorescence intensity in the panel A of MCD1, MCD14, MCD15 and MCD111 in the treatment of ionomycin. The student test was applied to validate the difference between the un-treated and the ionomycin-treated states.

Treatments of all reagents mentioned above for all cell lines expressing MCD15 resulted in reduce of fluorescence intensity as expected. In HEK 293 cells, calcium release from ER triggered by ionomycin was monitored by MCD15er and Fura-2 simultaneously (Figure 3.26A). $[Ca^{2+}]_{ER}$ was decreasing upon addition of ionomycin, while $[Ca^{2+}]_{cyt}$ was increasing. Since no extracellular calcium was supplied, calcium was pumped out after the early stage of calcium accumulation in cytoplasma. When calcium was supplemented, both cytoplasmic and the ER $[Ca^{2+}]$ increased. Unlike cytosolic calcium, even if extracellular calcium was up to 10 mM, calcium in ER was only recovered to its resting level. Both the RyR and IP_3R agonists 4-cmc and histamine triggered fluorescence intensity decrease as calcium release (Figure 3.26E and F). Similar phenomenon of fluorescence change rising from the addition of reagents that induce calcium release from ER can be observed in BHK, HeLa and C2C12 cells expressing MCD15 as shown in Figure3.27-3.29.

The fluorescence change of MCD15 upon 4-cmc treatment was compared in Figure 3.30A, which was greater in C2C12 and HEK 293 cells than the other two. Even though, the maximum fluorescence change was only 6%, far away from the desired dynamic range for a qualified calcium indicator. The limitation is possible to be overcome by either further suppressing the quantum yield of the calcium-free form or enhancing the brightness of the calcium-loaded form. It would be promising to have such a red fluorescent protein with the property of calcium triggered-fluorescence enhancement.

Figure 3.26B shows the calcium dynamics in response to extracellular calcium change in the HEK cells cotransfected with MCD15 and CaR. The intracellular calcium was monitored by Fluo-4. The calcium oscillation was observed and meanwhile the fluorescence of MCD15 decreased, suggesting that $[Ca^{2+}]_{ER}$ decreased. CPA induced calcium release from the ER in HEK 293 showed no significant difference in the cells over-expressing CaR although there is 39% increase of the released calcium amount calculated in Figure 3.30B. The statistical significance was not obtained due to the limited amount of data collected.

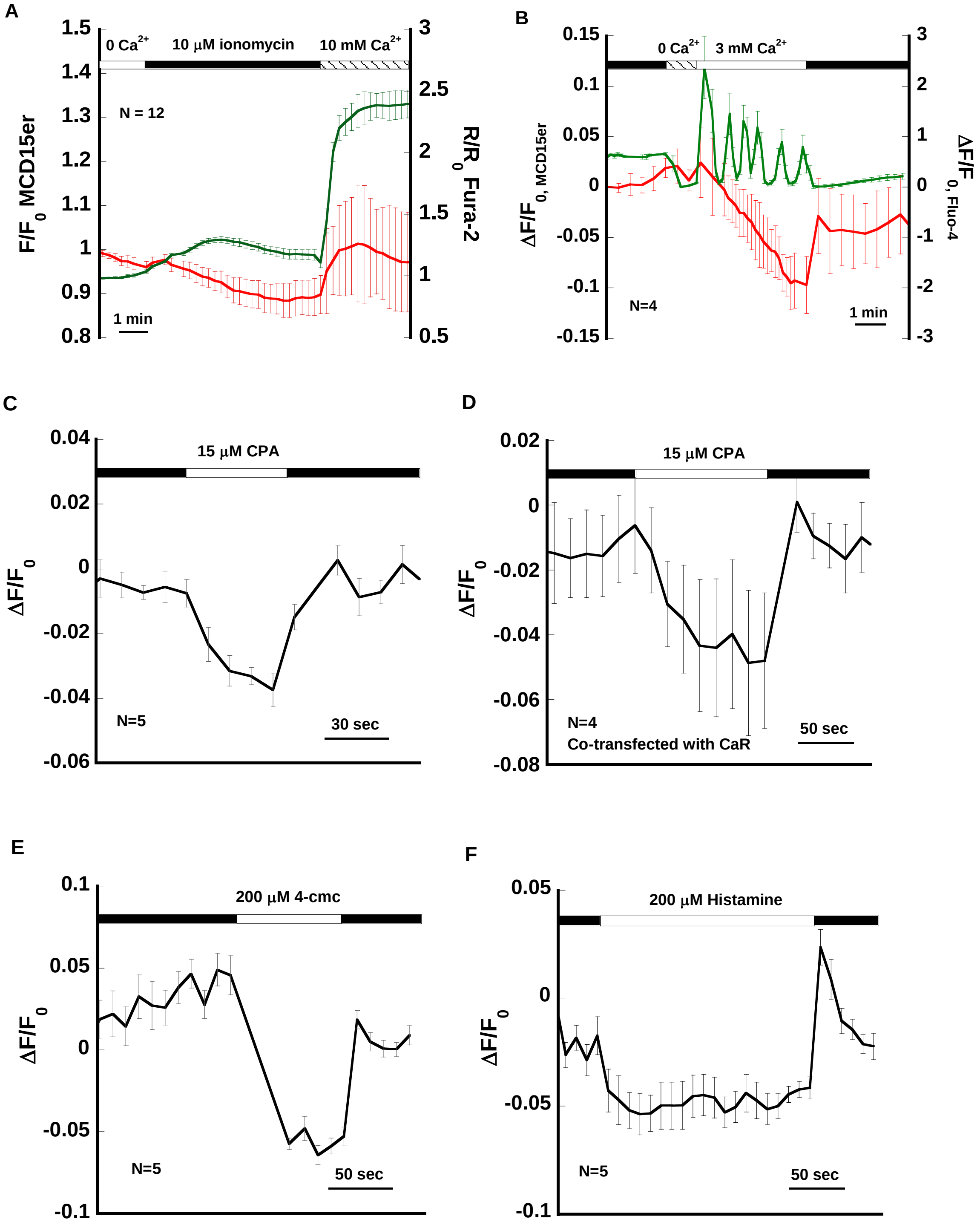

Figure 3.26. Calcium dynamics monitored by MCD15-transfected HEK293.
(A) The treatment of 10 μM ionomycin and 10 mM Ca^{2+}. The intracellular calcium was monitored by Fura-2. (B) The treatment of 3 mM extracellular calcium in the HEK 293 cell stably expressing CaR. The intracellular calcium was monitored by Fluo-4. (C) The treatment of 15 μM CPA, (D) Treatment of 15 μM CPA in the HEK 293 cell transiently transfected with CaR. (E) The treatment of 200 μM 4-cmc. (F) The treatment of 200 μM histamine.

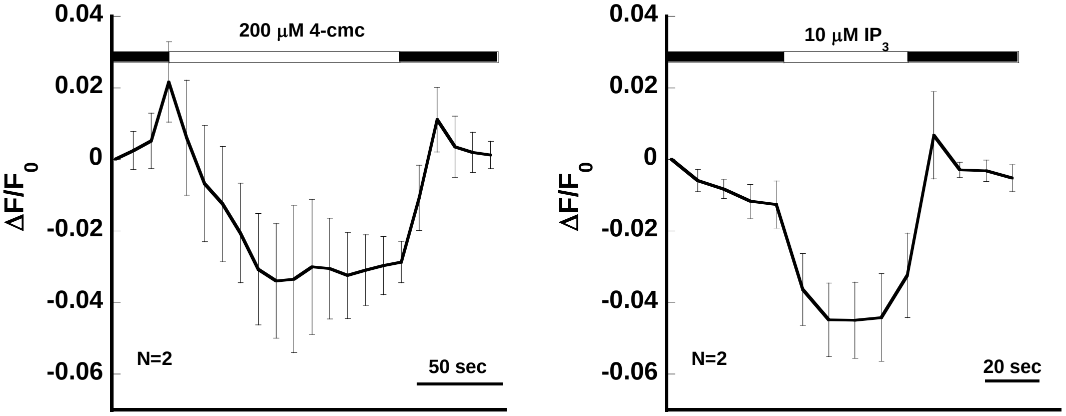

Figure 3.27. Calcium dynamics monitored by MCD15-transfected BHK cells.
The black bar indicates the cells were immersed in the standard Ringer's solution. The white bar showed the time course with addition of drugs. The number of cells for average was shown in N.

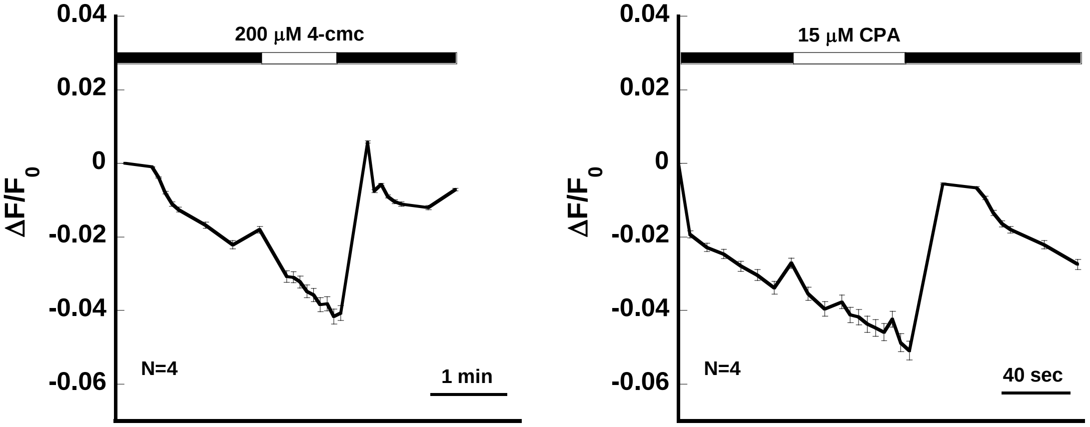

Figure 3.28. Calcium dynamics monitored by MCD15-transfected HeLa cells.
The black bar indicates the cells were immersed in the standard Ringer's solution. The white bar showed the time course with addition of drugs. The number of cells for average was shown in N.

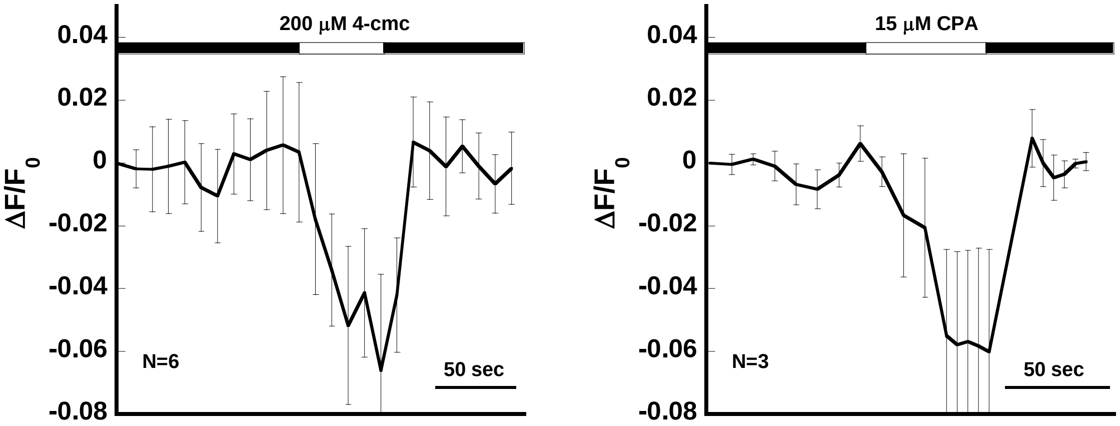

Figure 3.29. Calcium dynamics monitored by MCD15-transfected C2C12 cells.
The black bar indicates the cells were immersed in the standard Ringer's solution. The white bar showed the time course with addition of drugs. The number of cells for average was shown in N.

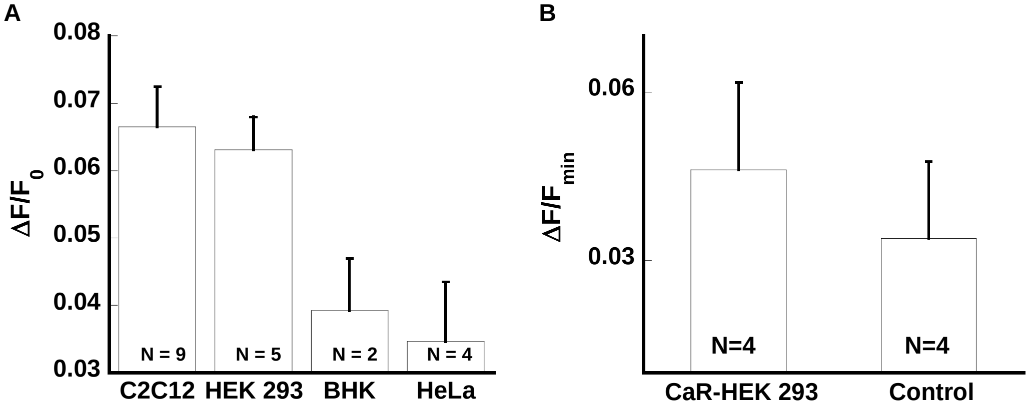

Figure 3.30. Comparison of MCD15 responding to 4-cmc and CPA induced Ca^{2+} release from ER.
(A) The fluorescence change of MCD15 due to the200 μM 4-cmc induced calcium release in different cell lines. (B) The fluorescence decrease of MCD15 due to the treatment of 15 μM CPA in the HEK 293 cells and the HEK 293 cells transiently transfected with CaR. N indicates the number of experiments.

The fluorescence of MCD1 between ionomycin and 10 mM calcium did not change significantly in Figure 3.25, although it shows good dynamic range *in vitro*. MCD15, with double mutations K198E and R220E on MCD1, showed the dynamic range of 1.10 C2C12 myoblasts. Although Mag-Fura-2 has the largest dynamic change over 0-10 mM Ca^{2+}, which is approximately 200%, the change induced by 4cmc still small (~3%) (not shown). The calcium concentration change is beyond the sensitive range of the sensor because the K_d of Mag-Fura-2 is approximately 50 μM, about 10-fold lower than MCD15. The fluorescence intensity change induced by CPA is comparable; probably due to the calcium change in the ER is in the similar sensitive range of those sensors. This result emphasizes the importance of the diversity of calcium binding affinities, which allows the calcium signal monitor in different compartments. In general, the dynamic range of ER-tagged MCD15 *in situ* was 30% of that of CatchER when ionomycin and 4-cmc were applied.

3.3.2 *Calibration*

Given that the protein folding can be different in the bacteria and the mammalian cells, protein expressed in the HEK 293 cells was used for the calcium titration to further verify the calcium binding. To exam the calcium binding affinity of MCD15 expressed in mammalian cells, non-tagged MCD15 was transfected and over-expressed in the cytoplasm in HEK 293 cells. RIPA buffer was used to lyse cells and the crude soluble protein including MCD15 was extracted by centrifugation. The buffer was changed to 10 mM Tris, pH 7.4 for the calcium titration. As shown in Figure 3.31, calcium addition induced immediate fluorescence emission increase and no photo-bleaching was observed during the whole experiment (~20 min). The kinetics of calcium binding was not able to be caught at the 1/sec data record rate. The average fluorescence intensity at each plateau was used to calculate the K_d. The calcium binding affinity of MCD15 expressed in HEK 293 cells was around 2 times lower than the protein purified from *E.coli*.. As the negative control, there is no calcium triggered fluorescence change found in the wild type mCherry (Figure 3.31B).

Considered the basal ER calcium concentration is cell-type dependent and the ER condition is difficult to be mimicked, the *in situ* calibration for MCD15 was conducted. Digitonin is used to specifically permeabilize the cytoplasma membrane, leaving the ER membrane intact to maintain MCD1x in the ER lumen. Ionomycin is used to reach the equilibrium of calcium concentration across membranes. Figure 3.32 shows the calibration curves in BHK, HeLa and C2C12 cells. The dissociation constant K_d was consistent, around 1.0 mM in these three cell lines. The lower apparent affinity obtained in ER lumen may be caused by its ion strength, the different diffusion rate due to the viscosity and competition with other calcium buffers like calsequestrin.

Although the dynamic range and binding affinity of the first generation of mCherry-based calcium binding proteins is not good enough for the physiological application, these pieces of the preliminary results give the strong support that the principle of this design strategy enables the quantitative detection.

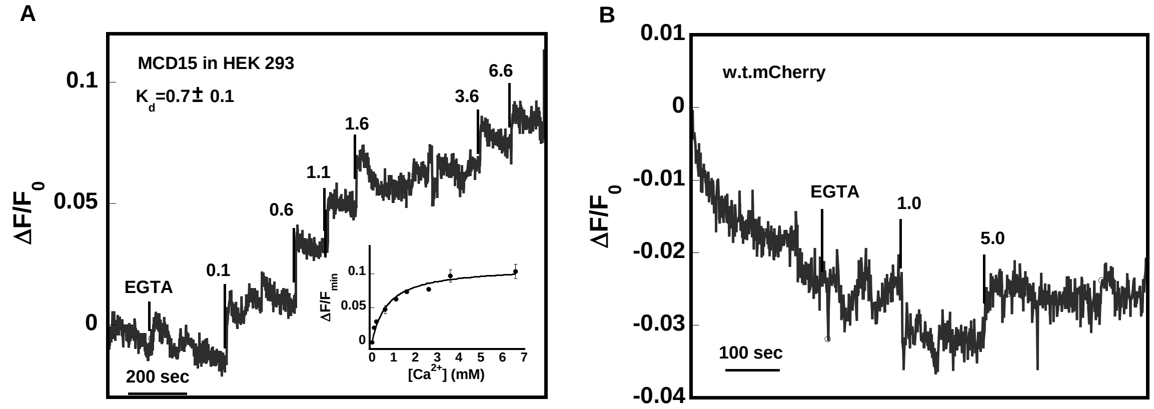

Figure 3.31. Calibration for MCD15 expressed in HEK 293 cells.
To mimic the cell imaging conducted by the microscope, the excitation wavelength was set as 550 nm. The data collection was paused when calcium was added in. MCD15 was extracted as the soluble protein after the cell lysis by RIPA solution and the total soluble protein was used in this calibration. (A) The representative time course of calcium titration to the MCD15. The inset shows the normalized fluorescence intensity increased as a function of [Ca^{2+}], which is averaged from two experiments. K_d was fit using equation 2.7, 0.7 ±0.1 mM. (B) The wild type mCherry was titrated by calcium in the same experimental condition.

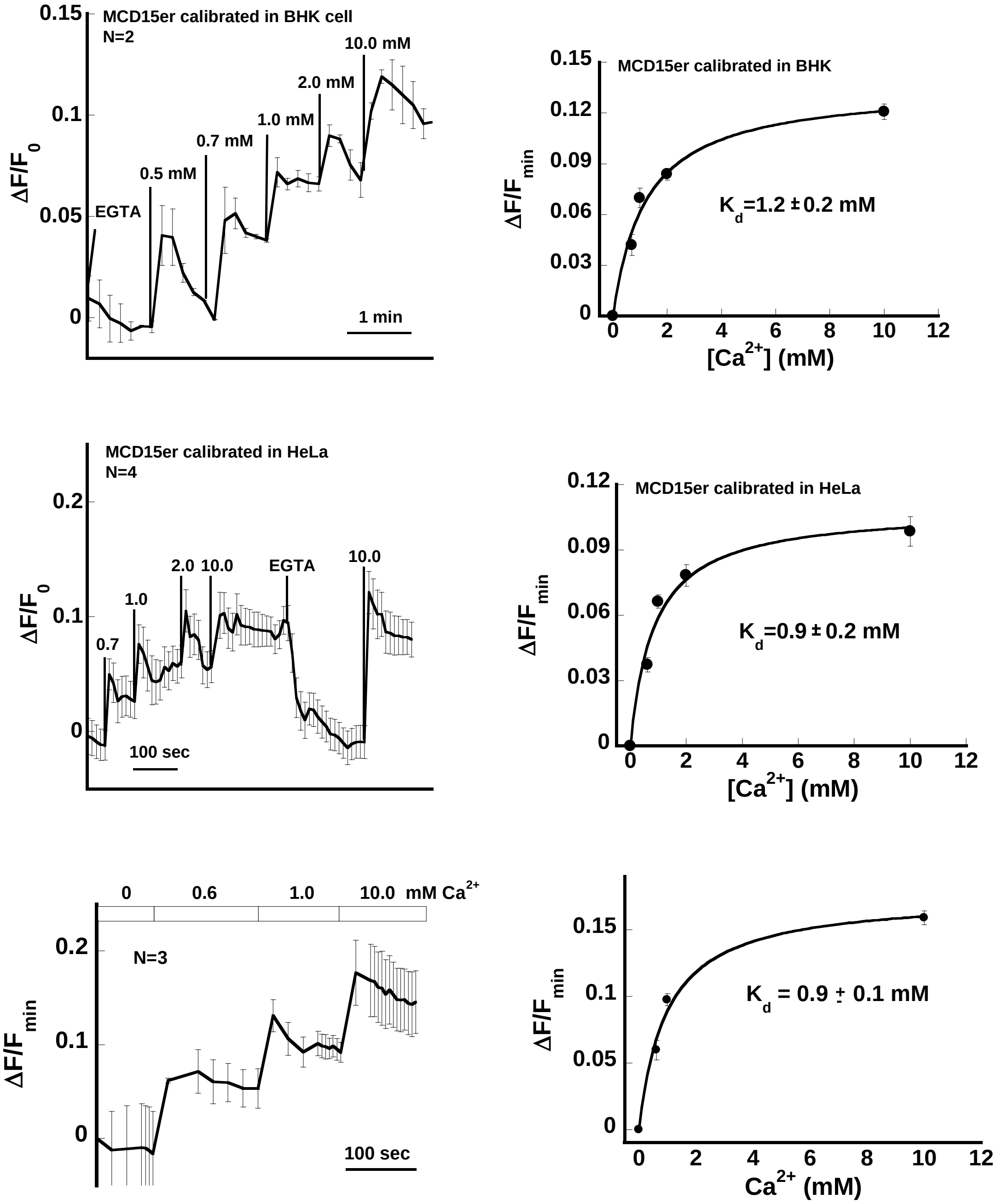

Figure 3.32. *In situ* calibration for MCD15er transfected in BHK, HeLa and C2C12 cells.
The average $\Delta F/F_{min}$ is calculated from N cells. The average value at each plateau was calculated for K_d fitting. The K_d was fit by Equation 2.7.

3.4 Discussion

3.4.1 *Design strategy of MCD1 (RapidER)*

MCD1 was designed based on several considerations including features of calcium binding geometry and charged residue preference obtained from statistical analysis of different classes of calcium binding proteins (66, 157, 158) and fast kinetics and calcium induced florescence change. We hypothesize that negatively charged ligand residues in a hemisphere coordination geometry with good solvent accessibility, electrostatic binding energy change, and the hydrogen bonding network of the chromophore are the key factors to control calcium binding affinity, kinetics, and calcium binding dependent change of optical properties. First, red florescent protein mCherry was chosen because of its noted photo-stability, fast chromophore maturation rate and low pK_a(109) that is important for reduce pH sensitivity when measuring calcium binding. Second, we used the “half shell” with reduced coordination number to create the calcium binding site on the surface of the beta barrel to allow easy entry and release without the spatial barrier from the calcium binding site. With the half shell calcium binding site composed primarily of Asp and Glu residues as the most predominant calcium binding ligands, the calcium binding affinity was expected to be lower than that of the classic EF-hand motifs. Differing from the classic calcium binding pocket that is consisted with 6-7 oxygen atoms, and forms a bipyrimidal shape with high calcium binding affinity and selectivity, it has less coordinator number and forms an open bowl-like geometry. Third, to couple calcium binding with optical property change without interfering with chromophore formation, we finally decided to mount the calcium binding site in pocket 1 according to located in the chromophore hydrogen-bonding network at the corresponding position in CatchER (Figure 3.1A and 3.32). Residue 145 is involved in flanking E144 and S146. The main chain oxygen of E144 forms a hydrogen bond with the chromophore tyrosyl through a bridging water molecule, and the side chain hydroxyl group of S146 has two conformers, serving as the hydrogen bond donor for the chromophore tyrosyl directly. Fourth, based on the kinetic study of the electrostatically driven interaction between protein and ligands (169-171), we further reason that mCherry with a larger negatively charged surface around the designed calcium binding site may exhibit a faster calcium association rate than CatchER. Compared to CatchER, the calculated electrostatic binding energy change of MCD1 was greater than that of CatchER (Table 3.5). The calculated negatively charged solvent accessible surface area (SASA) using PyMol in the designed calcium binding site was also larger in MCD1 than in CatchER.

Table 3.5 The electrostatic binding energy calculation

Proteins	$\Delta G_{elec\_binding}$ (kT)	Negatively charged SAA (Å^2)
MCD1	-73.03	655
CatchER	-59.48	589

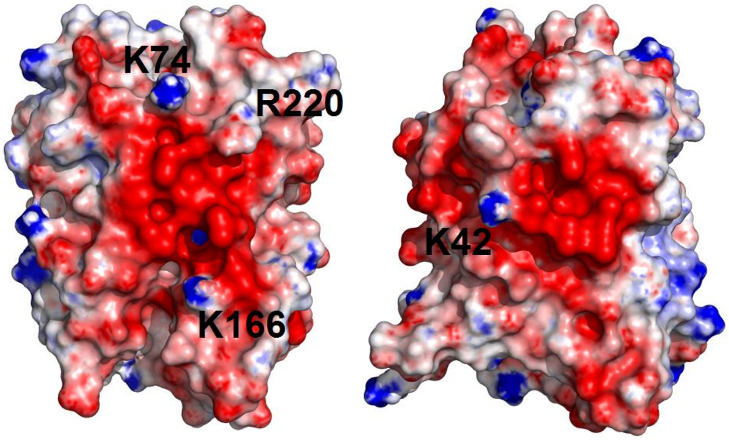

Figure 3.33. Comparison of the electrostatic surface between (left) MCD1 and (Right) CatchER.

3.4.2 *Key factors for binding affinity and kinetic properties*

Calcium binding accepts a flexible range of the coordination number ranging from 3-8. Because it is a soft metal, oxygen is preferred to be the coordinator. From the statistical analysis of the calcium binding sites in protein data bank, aspartic acid, glutamic acid, and water are the top three residues providing oxygen to bind calcium ion (157). The bipyrimidal shape formed by the oxygen atoms coordinating calcium is the classic one found in EF-hand motif. For the organic calcium chelators or dyes, EGTA and Fura-2 have four carboxylate groups, where the calcium is coordinated by 8 atoms including two nitrogen atoms. In either EF-hand motif or tetracarboxylate compounds, calcium is surrounded by oxygen/nitrogen atoms and there is also a steric barrier formed by the “arms” of the coordinators. Such steric hindrance may limit the calcium dissociation rate and contribute to the high affinity. Renner and the co-workers also reported that in the EF-hand loop the side chain length and acidity affected the Ca^{2+} dissociation rate due to the steric block and electrostatic barrier, respectively (172). The calcium binding geometry made of fewer coordinating ligands is observed in proteins shown in Figure 3.1 such as 1FZC and 1BJR. For the single calcium binding site in 1FZC, the number of oxygen ligand from the protein/water is 5/1, and 4/4 and 5/0 for two calcium binding sites in 1BJR. In both proteins, the ligands from protein moiety form a bowl-like geometry and the calcium ion is partially exposed to the solvent. For organic compounds, the calcium binding moiety was modified with less coordinators in order to increase the calcium dissociation rate such as Mag-Fura-2. In Mag-Fura-2, the calcium binding pocket contains three carboxylate groups with 3 formal charges, and there is a channel available for calcium to escape. Thus, the calcium binding affinity of Mag-Fura-2 and other tricarboxylate compounds is lower than those analogs with four carboxylate groups attributed by the higher calcium dissociation rate. There is another strategy to increase the k_{off} of calcium dyes, which is to add the electron attractive group like -NO_2 or -F in the 5 position of o-aminophenoxy ring. Such calcium dyes ended up with 5N or 5F in their name and have calcium binding affinity around 1-10 μM which is lower than the original tetracarboxylate calcium dyes but higher than those with tricarboxylate. The calcium binding association rate of these calcium dyes is in the magnitude of 10^8 $M^{-1}s^{-1}$. Therefore, the variance in K_d mainly results from the dissociation rate k_{off} as shown in Table 1.1. Clearly, the coordination number and the number of formal charge have a stronger effect on both k_{off} and K_d by determining the geometry and steric hindrance.

The calcium binding features of protein-based calcium indicators are mainly determined by the calcium binding moiety (calmodulin or troponin C) involved. The calcium binding affinity of both CaM and TnC is around 10^{-6}-10^{-7} M. The stoichiometry for both calmodulin and troponin C is 1:4, two calcium ions in each terminal domain. The calcium binding follows a cooperative manner in each domain, which may contribute to the slow calcium dissociation rate around 0.2-20 s^{-1}. In addition, the two domains are relatively independent, resulting in the biphasic calcium binding curve observed in Cameleon (38).

Efforts have been taken to reduce the Kd of these GECIs. In Cameleon 3, the mutation E104Q locating in the third EF-hand motif in CaM domain eliminated the high calcium binding component of the CaM C-domain and the K_d value is 4.4 μM. For Cameleon 4, the mutation E31Q located in the first EF-hand motif further decreases the binding affinity in CaM N-domain but does not significantly affect the high affinity C-domain. The resulting K_d of Cameleon 4 is 83 nM and 700 μM with a Hill coefficient 1.5 and 0.87 respectively (54). Palmer and co-workers switched the charged residue in the interface between M13 and CaM which decreased the apparent K_d (0.8 and 60 μM) and increased the k_{off} (256 s^{-1}) although the original purpose was to eliminate the perturbation of the normal calcium signaling by interaction with their intrinsic target proteins (38). A similar situation was observed in the recent version 6 of GCaMP, which was generated by altering the interface between M13 and CaM as well as the one between CaM and cpEGFP. GCaMP6f exhibited faster calcium response to action potentials in neuronal activity than other GCaMPs (91). This evidence shows that the apparent K_d of the calcium indicators involving CaM and M13 peptide is not only determined by the calcium binding motifs but also the linker and domain interface.

In a different scenario of TnC involved GECIs, TnC also has two terminal domains like CaM and N-terminal domain binds Ca^{2+} with lower affinity than C-domain, which is a regulatory site. The TnC molecule undergoes structural rearrangement after Ca^{2+} binding (173). TN-XL with faster kinetics than TN-L15 was created by switching the residue N and D at position 109, 111, 145 and 147 at the third and forth EF-hand motifs in C-terminal domain of TnC, where the calcium binding affinity was lowered (K_d=2.2 μM, Hill coefficient 1.7) and magnesium interference was abolished (174). The resulting off rate of TN-XL measured by stopped-flow spectrometer was around 5 s^{-1}, which was approximately 5-fold greater than TN-L15 and TN-XXL.

The cooperative binding, the slow dissociation kinetics and the high calcium binding affinity were signatures for native Ca^{2+} binding protein involved GECIs. In addition, the K_d was not controlled by the Ca^{2+} binding alone due to the multiple steps required for fluorescence signal change. Therefore, it is difficult to tune the binding affinity and kinetics as well as avoid cooperativity in the same construct by rational design. In contrast, CatchER was successful in fast kinetics, low calcium binding affinity and 1:1 stoichiometry by avoiding the native calcium binding moiety. In such a simplified calcium indicator as CatchER, the calcium sensing relies on the local dynamics in the calcium binding site. As a starting point, the simple calcium binding site in

CatchER was modified to increase the kinetics further by reducing the positively charged residues around the binding site.

Compared with CatchER, RapidER had a higher calcium binding affinity as well as faster kinetics, which is in agreement with the calculation of the electrostatic binding energy change and the negatively charged solvent accessible surface area. The faster calcium dissociation rates found in both CatchER and RapidER than in the EF-hand motif sensors is attributed to the geometry of the designed half-shell calcium binding site, where there is little steric barrier for calcium release. A similar comparison was also observed in tetracarboxylate and tricarboxylate calcium dyes fura-2 and mag-fura-2. As we discussed above, the electrostatic attractive functional group such as NO_2 and halide was added in the compound to reduce binding affinity and increase k_{off} without changing the coordination number and geometry. But it cannot be applied in proteins because the conjugated system was not able to form throughout the side chains. However, there were three positively charged residues K74, K166 and R220 around the calcium binding site in MCD1 compared to CatchER where there was only one K42 nearby (Figure 3.31). The edge of the enlarged negative circle may also be neutralized by these positive residues and thus increase the dissociation rate. The evidence for the role of the positive residues around the binding site can be found in the crystal structure of Ca^{2+}-CatchER, where there were two populations of calcium ion positions observed and both of them are coordinated by E147 but away from E223 and E225 which were close to K42. We hypothesized that the positively charged residues around the calcium binding site attracted electron density to reduce the electrostatic barrier.

3.4.3 *Positions of calcium binding sites*

RFP has a larger conjugated system than that in GFP, which was extended to the backbone of F65 before the cyclized tri-peptide (175, 176). The GFP was modified with several mutations to improve the oligomer character, brightness, photostability and maturation time (177). Like GFP, the chromophore environment of RFP plays important roles in maintaining the fluorescence. The side chain orientation of the neighboring residues in the β sheets is usually opposite. Those projecting to the interior of the β-can form hydrophobic or electrostatic interactions to participate in or protect the chromophore environment, while the others facing the solvent assist to keep the protein from aggregation or degradation. The residues with side chains in the interior of the protein have more direct contact with the chromophore so as to affect the optical property directly. For example, mutation of the E215 in mCherry resulted in the blue shift of the spectrum, where the original E215 was protonated and formed a hydrogen bond between the protonated carboxyl group and the imidazolinone ring nitrogen (159, 178). mBanana has the mutation I197E based on mTangerine, which may contribute to the increase of pKa from 5.7 to 6.7 due to the redistribution of the chromophore electron density (110). However, calcium binding in the surface of the β-barrel mainly involves the side chains protruding outside. In order to change the spectral properties by calcium binding, the calcium coordinators need to influence those residues in the chromophore environment.

As shown in Figure 3.1, in the chromophore of mCherry, the chromophore phenol hydroxyl group was close to the opening of the β-barrel, where a loop region is located. The corresponding location in GFP served as a tunnel to allow proton migration during excited state proton transfer. This phenolate oxygen formed the H-bonds to the side chain of S146 (both states), to the main chain of E144 through a bridging water molecule (wat1), and to the side chain of Q163. As mentioned above, E215 in mCherry was proposed to be protonated to form H-bond with the imidazolinone nitrogen. The position of this residue was relatively rigid because a network was observed among the chromophore, E215, Q42, S69 and a water molecule (wat4 in

Figure 3.1). Both main chains and side chains of these three residues together with the chromophore had contact with each other, leading to a tight association. H-bonds were found from the side chains of R95 and Q64 to the imidazolinone oxygen. Since the peptide bond connecting F64 and the chromophore was part of the conjugated system in mCherry, the main chain oxygen in F64 was also under consideration, which formed H-bonds with the side chain Q109 and S111 via water molecules.

We selected three potential calcium binding sites to affect the phenol group. RapidER in pocket 1 was one of them, including the mutation A145E in between E144 and S146. The pocket 2 included E144 and the pocket 3 had the mutation E164 adjacent to Q163. Both pocket 1 and 2 had mutations R216E next to E215. Pocket 4 was located near R95 and Q109, including mutations K92E and T108E. The results suggested that only the variants in pocket 1 and 2 showed the calcium dependent fluorescence change. The equilibrium-dialysis assay confirmed that mcP6 (K92E/E94/T108E/D110), belonging to the pocket 6 variants, also bind calcium with the comparable binding affinity as ones in pocket 1 and 2. The lifetime of Tb^{3+}-MCD1 FRET verified the calcium went to the expected position in MCD1. Calcium binding increase the lifetime of MCD1 and thus the quantum yield was enhanced. Therefore, the phenol hydroxyl group was more sensitive than others to the change of the electrostatic environment. It is the hot spot that has the major potential to affect the optical property.

The calcium dependent fluorescence change was decreased when it was expressed in the mammalian cells. Further modification was done to increase the dynamic range. For MCD15 (RapidER'), the mutation R220E on MCD1 outside the designed calcium binding pocket made the calcium induced fluorescence change detectable in si*tu*, without altering the *in vitro* optical and biophysical properties. However, the dynamic range of MCD15 (10%) is lower than other low-affinity calcium sensors (~30%). The limitation is possible to be overcome by either further suppressing the quantum yield of the calcium-free form or enhancing the brightness of the calcium-loaded form. It would be promising to have such a red fluorescent protein with the property of calcium triggered-fluorescence enhancement.

3.5 Summary and conclusions

This chapter introduces the strategy for designing a calcium binding site in the red fluorescent protein. To make the calcium binding affinity lower than that of those classic EF-hand motif involved binding proteins, the half shell is applied to the surface of β-barrel in mCherry. Several positions were selected to locate calcium binding sites. Only two in proximate to the chromophore tyrosine phenol (Pocket 1 and 2) showed the calcium dependent fluorescence change, although the variants in Pocket 3 4 and 5 can bind calcium based on the equilibrium-dialysis assay. The fluorescence change induced by Ca^{2+} binding in MCD2x is too small to be applied to detect $[Ca^{2+}]$ change. The insertion in Pocket 6 and all mutation in cp-mKate, as well as MCD14Y, MCD14YS and MCP4, are too harsh to reserve the protein folding, leading to loss of fluorescence. Further mutation based on MCD15 was carried out to improve the dynamic range *in situ*, but not substantial enhancement was obtained unfortunately.

In this chapter, MCD1 (RapidER), MCD14 and MCD15 (RapidER') were analyzed in detail to illustrate the biophysical property, the binding affinity and potential application *in situ*. This class of calcium binding proteins is featured with the calcium binding affinity of sub-millimoalr range, the pH independent calcium induced fluorescence change in physiological range, Ca^{2+} preference over the other common metals *in vivo* and the fast calcium association/dissociation rates close to diffusion limit. The calcium binding was further confirmed by using Tb^{3+} as a probe and NMR, which also suggested the local conformational change upon metal binding. The distance between the metal and the chromophore was determined by Tb^{3+} lifetime change in the Tb^{3+}-CRO FRET pair and the result was consistent with the measured distance in the modeled MCD1 structure and the crystal structure of the analog Ca^{2+}-CatchER. The ER-targeted MCD1xs were successfully expressed in HEK 293, BHK, HeLa and C2C12 cells at 37 º. The fine reticular network was observed indicating the correct the ER localization. The calcium sensing capability was evaluated by applying calcium ionophore ionomycin, RyR activators 4-cmc and caffeine, IP_3R activator histamine and SERCA pump inhibitor CPA. The expected fluorescence decrease was observed in all cell lines, suggesting the designed calcium binding proteins can be used as a probe to detect calcium change in the ER.

Even MCD15 has the largest fluorescence dynamic range compared to other designed proteins, the measurable fluorescence change is not as large as the GFP-based Ca^{2+} sensor CatchER. The underlying mechanism of calcium induced fluorescence change in CatchER may provide us the information to improve its dynamic range, which will be discussed in the Chapter 4 and 5.

4 THE DYNAMIC AND STRUCTURAL ANALYSIS OF THE GREEN FLUORESCENT CALCIUM INDICATOR CATCHER

4.1 Introduction

Green fluorescence protein (GFP) is a β-barrel protein consisted of 11 β strands and a helix passing through the interior of the can-like architecture. In the middle of the helix, there are three amino acids Ser, Tyr and Gly, undergoing an auto-catalytic cyclization to form the chromophore. The chromophore is a conjugated system with two aromatic rings, the tyrosine phenol ring (R) and the imidazolinone ring (R'), connected by the (R)C-C=C(R') bond. The tyrosine phenol hydroxyl may be deprotonated to from the chromophore anion, leading to the absorption at around 488 nm, while the absorption band was around 395 nm in the neutral form (179). It has been found that the absorption spectrum of the chromophore analogue hydroxy-benzylidene-imidazolidinone (HBDI) in the solution was generally blue-shifted (180), and the free rotation of the bridge of the two aromatic moieties in the excited state causes the lack of fluorescence (181). The native protein matrix is responsible for the fluorescence of GFP.

Thanks to the development of the crystallography, NMR spectroscopy, time-resolved fluorescence spectroscopy, ultrafast Raman spectroscopy, and other high-end techniques, the underlying mechanism of the interaction of protein and chromophore has been investigated for years. It is known that both the steric and electrostatic effects contribute to the bright fluorescence. The compact packing of the native protein restricts the photo-isomerization of the chromophore in the excited state. The presence of the intrinsic proton wire enables the excited proton transfer (ESPT), leading to the emission of the anionic chromophore at 510 nm. Mutagenesis was applied to analyze the key residues contributing to the proton transfer pathway and the conjugated system. By mutating the residue S65T, the chromophore anion is predominated and the proton wire was rearranged for the new chromophore environment. There were many evidences for such an adaptive protein matrix.

The re-routing proton wire has been found in the mutant S205A and S205V where the proton transfer pathway had T203 instead of S205 involved (182, 183), in the mutant T203I where the absorption originated from the anionic form was suppressed while in the mutant E222G where the anionic form was predominant (184). The color may be changed due to the alternation of the π electron density. The most important exploration was the yellow fluorescent protein (YFP) with T203Y providing the Y203-chromophore π-π stacking to increase the electron density. Many examples of the photo-switchable and photo-activated GFP derivatives can be found like the mutant E222Q (185) and T203H (186). Taken the advantages of those studies, the GFP variants were widely used in the fluorescence imaging and the development of biosensors. The spectral property varies in the circular permutated GFP/EGFP with different new terminus (187, 188). GCaMP is the cpEGFP 149-144 fused with M13 peptide and calmodulin (CaM) (189). The calcium binding to CaM triggered conformational change of CaM, which in turn formed the complex with M13 peptide and induced the global conformational change in which the change of cpEGFP moiety led to the increase of the fluorescence.

CatchER is the calcium sensor based on EGFP, which was designed to be targeted to the high calcium environment like the intracellular calcium store endoplasmic reticulum (ER) (66, 190). To create the calcium binding site on the β-barrel of the EGFP, five residues were replaced by the negatively charged aspartic acid or glutamic acid without changing the β stranded structure. The calcium binding site, including Glu147, Asp202, Glu204, Glu223 and Glu225, located in proximity to the chromophore hydroxyl group. There were two absorption peaks of CatchER in the neutral pH, 398 nm and 488 nm. Unlike EGFP, the protonated chromophore was dominated. The calcium binding resulted in the decrease of the 398 nm peak but increase of the 488 nm peak. In the absence of calcium, the fluorescence brightness was around 30% of EGFP. When calcium ion bound to the protein, there was about 50% enhancement of fluorescence observed.

The mechanism of calcium binding induced fluorescence enhancement was studied by crystallography, steady and dynamic fluorescence spectroscopy. The hypothesis was that calcium binding altered the local dynamic property of the calcium binding site by neutralizing the negative potential, which in turn changes electrostatic interaction in the chromophore environment, resulting in the fluorescence increase. The crystal structures of calcium free, calcium bound and gadolinium bound CatchER were solved. Different conformation of Thr203 and Glu222 was observed from wild type EGFP. Calcium binding to CatchER may lead to the rotation of the side chain of Glu222, which was considered to be responsible for the change of the optical properties. The dynamic fluorescence was investigated by the lifetime measurement, which providing evidence showing that the calcium binding inhibited the geminate quenching during the proton transfer and increased the lifetime of ESPT, which was consistent with our hypothesis. The crystal structure showed the double conformer of Glu222 in Ca^{2+}-CatchER but only one conformation without calcium, and raised the possibility that one conformer of Glu222 was deprotonated to maintain the neutral form and the other one was protonated so as to increase the portion of the anionic chromophore. However, it was not sufficient to explain how the calcium binding changed the electrostatic interaction around the chromophore. In this chapter, we reported that the calcium binding to CatchER lead to less fluctuation of the designed binding coordinators by NMR dynamic study and molecular dynamic simulation. The MD simulation further showed that the proton wires were altered in the presence of calcium ion.

4.2 Results and discussion

4.2.1 *Paramagnetic relaxation enhancement for probing the calcium binding site in CatchER*

The gadolinium ion is a paramagnetic ion and was used for the line broadening effect for recognizing the metal binding center of CatchER. A series of ratio of Gd^{3+}: CatchER was screened using Varian 600 MHz NMR spectrometer. To avoid the precipitation caused by Gd^{3+}, the buffer maintaining a lower pH was applied. The pH effect can be seen in Chapter 5 Figure 4.1. The assignment for the cross peaks in pH 6.5 buffer was traced and done (Figure 4.1). The titration of Gd^{3+} followed the ratio of $[Gd^{3+}]$:[CatchER] as 0:1, 0.1:1, 0.2:1, 0.5:1 and 1:1. Figure 4.2 shows the spectra overlay of Gd^{3+}-free and 1:1 equivalent CatchER. Figure 4.3 shows the HSQC spectra of CatchER without and with Gd^{3+} at 0.5 and 1 equivalent concentration as our protein. Since there is no pseudo-chemical shift change occurred by gadolinium, the disappeared cross peaks were resulted from the broadened line due to the R2 relaxation enhancement.

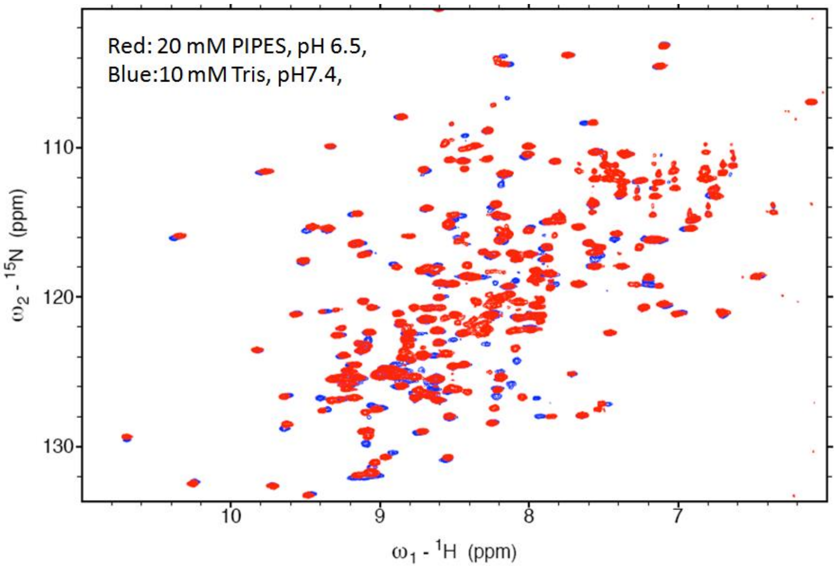

Figure 4.1. The ^1H-^{15}N HSQC spectra overlay of CatchER in different buffer solutions. (Red) 20 mM Pipes, pH 6.5, 10 mM KCl, 20% D_2O; (Blue) 10 mM Tris, pH 7.4, 10 mM KCl, 10% D_2O. The experiment was carried out at 37°C.

The intensity of all peaks decreased in a certain level by adding 0.5 equivalent amount of Gd^{3+}, about 30%, due to the dilution effect and some other systematic effects. There are 138 residues assigned in the metal-free CatchER ^{15}N-^{1}H HSQC spectrum, of which 77 residues were not influenced by the line broadening effect of Gd^{3+}. In the spectrum of CatchER with 0.5 equivalents Gd^{3+} (Figure 4.3 middle), several residues including Thr9, Glu90, Asp102, Phe130, Glu132, Tyr143, Phe165, Asp190, Asn198 and Gly228 showed the decreased height by more than 55%, while overall decrease was approximately 30%. However, the neighboring residues did not show decreased intensity. Here, two phenylalanines have the side chains protruding inwards. Thus, all residues have oxygen atoms exposed to the solvent and can interact with the positively charged Gd^{3+} ions but not specifically. In the spectrum of Gd^{3+} and CatchER at 1:1 equivalence (Figure 4.2 and 4.3 right panel), 109 peaks disappeared, in which among the 62 un-assigned peaks in the metal-free CatchER spectrum 48 of them were disappeared.

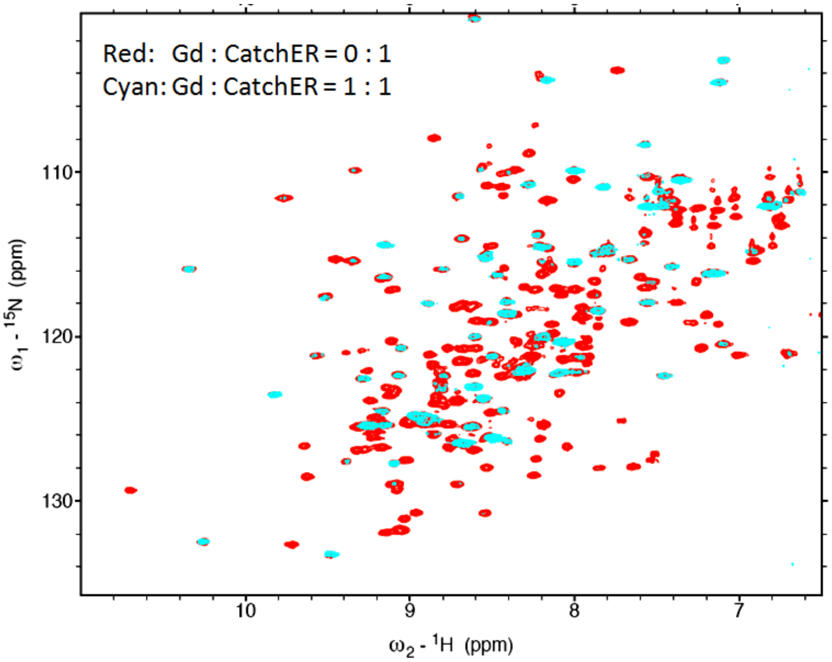

Figure 4.2. The ^{1}H-^{15}N HSQC spectra overlay of CatchER with (Cyan) and without (Red) Gd^{3+}. The final Gd^{3+} concentration was 200 μM, the same as [CatchER] in 20 mM Pipes, pH 6.5, 10 mM KCl, 20% D_2O. The experiment was carried out at 37°C.

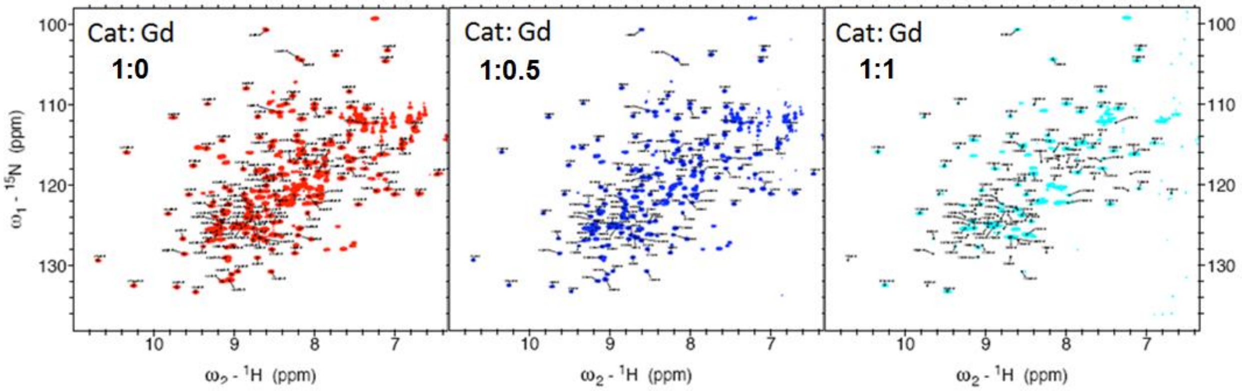

Figure 4.3. The ^{15}N-^{1}H HSQC spectra of Gd^{3+} titration to CatchER.
The ratio of metal to protein 0:1 (red), 0.5:1 (blue) and 1:1 (cyan). The ornaments indicate the assignment for cross peaks. Cat is short for CatchER. The experiment was carried out at 37°C and the protein was prepared in 20 mM Pipes, pH 6.5, 10 mM KCl, 20% D_2O.

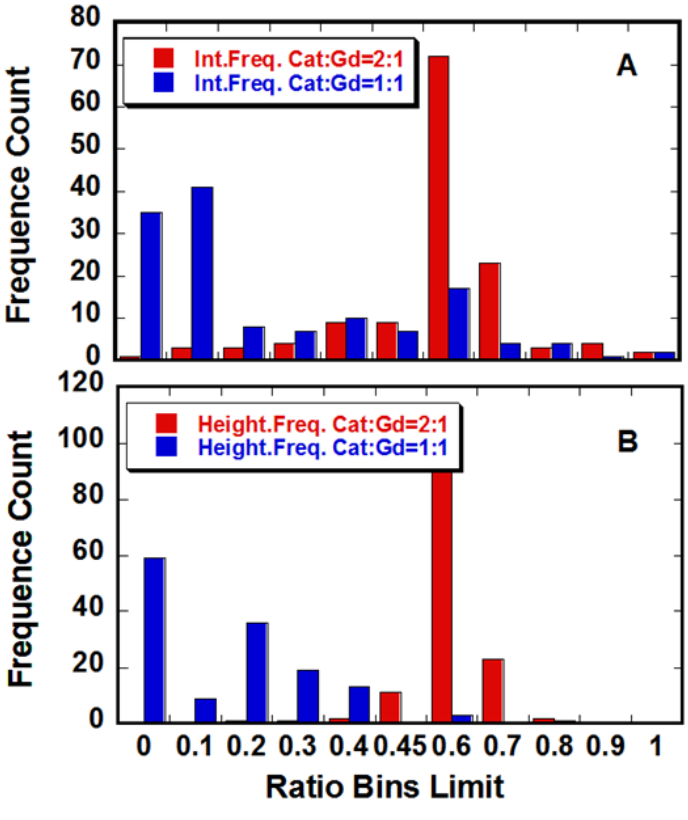

Figure 4.4. The histograms of the chemical shift change in Gd^{3+} titration.
The decreased intensity and disappeared peaks due to the broadening effect is presented by the frequency count as a function of the peak volume (A) and height (B) ratio of the Gd^{3+}-CatchER to the metal-free sample. Cat is short for CatchER.

The histogram of peaks with decreased intensity was obtained by the signal ratio (height or intensity) of the one with Gd^{3+} to the original CatchER without Gd^{3+}, where the ratio=0 indicated the disappeared peak and raito=1 indicated the unaffected peak. Using either the height or the volume to calculate the ratio, the statistical trend is similar (Figure 4.4). The first column in both volume and height ratio histograms suggests the population of the disappeared residues. Figure 4.5 depicts the distribution of residues of assigned, unassigned, and disappeared in the presence of the different amount of Gd^{3+} by colors.

As shown in Figure 4.5, the green residues were assigned, taking up to 60% of the surface of CatchER crystal structure. This area was in the opposite side of the designed calcium binding side (left in Figure 4.5A). Unfortunately, most residues in our designed calcium binding pocket were not able to be assigned, leaving this area in white color (right in Figure 4.5A). However, in the presence of 1 equivalent Gd^{3+} ions, the red color circles around the calcium binding pocket, which dominates the disappeared peaks, providing the boundary of the calcium binding area. In addition, Table 4.1 shows that 77% un-assigned peaks were gone in the presence of 1 equivalent Gd^{3+}. The pieces of information can not indicate which residues, but implies abundant un-assigned residues in the calcium binding area disappeared.

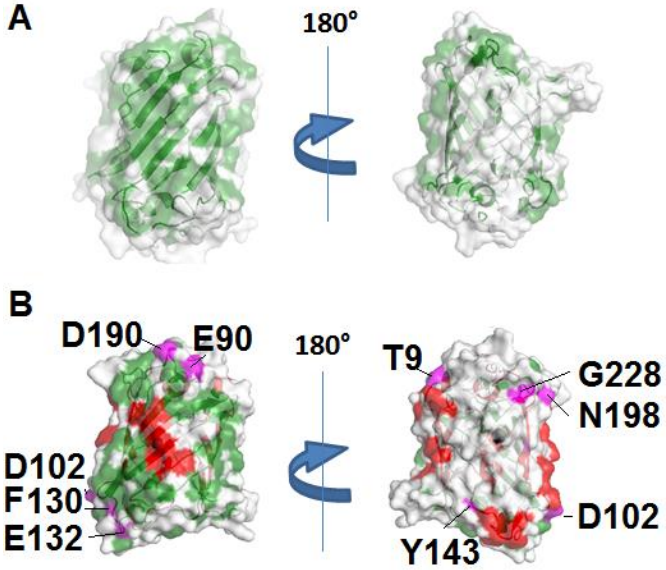

Figure 4.5. Mapping residues affected by Gd^{3+} PRE in the calcium loaded CatchER crystal structure. (A) Gd^{3+}:CatchER=0:1; (B) Gd^{3+}:CatchER=1:1. The region colored by white (un-assigned residues), green (assigned residues), red (disappeared peaks in CatchER HSQC spectrum with 1 equivalent Gd^{3+}), and magenta (disappeared peaks in CatchER HSQC spectrum with 0.5 equivalents Gd^{3+}) which are also labeled except Phe165 because its side chain faces to the interior of the barrel. The grey dot in B is calcium ion.

Table 4.1 The statistics of the cross peaks during the Gd^{3+} titration to CatchER.

[CatchER]:[Gd^{3+}]	Number of the assigned peaks		Number of the un-assigned peaks	
	Remained	Disappeared	Remained	Disappeared
1:0	138	NA	62	NA
1:1	77	61	14	48

In conclusion, the gadolinium titration resulted in the line broadening in CatchER HSQC spectra. In the CatchER spectrum with 1 equivalent Gd^{3+} ions, 44% assigned and 77% un-assigned residues were disappeared due to relaxation enhancement. Based on the disappeared circle around the calcium binding side and the distribution of un-assigned residues, the calcium binding pocket is the major area affected by the addition of Gd^{3+}. The result supports the crystal structure of holo-CatchER and also indicates a non-specific binding site (Asp19, Glu95, Glu124) with local high negative potential (Figure 4.5B colored in red).

4.2.2 *The dynamics analysis of CatchER*

CatchER was uniformly labeled by growing E. coli in the SF9 minimum medium supplemented with $^{15}NH_4Cl$. The protein was purified by Ni chelation column and prepared in 10 mM Tris, 10 mM KCl, pH 7.4, 10% D_2O and 1 mM NaN_3. All NMR data were collected in VARIAN 600 MHz at GSU facility at 37°C. Three serials of spectra were obtained separately. Each serial was recorded using the same gain and number of scans. For calcium loaded form, 10 R1 experiments with various relaxation delays were used: 0, 0.01, 0.06, 0.13, 0.23, 0.34, 0.48, 0.74, 1.0, 1.5, and eight relaxation delays were performed for R2 experiments: 0.01, 0.03, 0.05, 0.07, 0.09, 0.11, 0.13, 0.15. For NOE experiments, the proton recovery period d1 was set to 4.0 s.

The molecule tumbling ranged in pico-sec to nano-sec motion can be studied by collecting T1, T2 relaxation and intensity ratio of steady-state NOE. From R1, R2 and NOE, the dynamic parameters like J(0), $J(\omega_N)$, $J(0.87\omega_H)$, R2/R1, the order parameter S^2, correlation time τ_c and exchange rate R_{ex} can be obtained by reduced spectral density function mapping. The greater internal motion can be reflected by decrease of J(0) and $J(\omega_N)$ and increase of $J(0.87\omega_H)$. The chemical exchange is reflected by significantly increased J(0). R2/R1 decreases in residues where if there is the conformation change occurs. S^2 is the square of the generalized order parameter characterizing the amplitude of the internal motion, which can be used to justify the degree of the internal motion, ranged in 0-1. If $S^2=1$, it will stay in the same orientation at any time, meaning that this residue is completely rigid. The correlation time is the measure of how fast a molecule tumbling in the liquid, or the rate of molecule motion, which is different from the isotropic rotational correlation time τ_m. The exchange rate R_{ex} is a function of exchange rates, populations and chemical shifts of different conformations.

For either apo or holo CatchER, the R2/R1 is basically uniformly distributed as shown in Figure 4.6 within an acceptable error range (±2), indicating no specific conformational or solvent exchange occurring. The overall correlation time τ_m was estimated from the average R2/R1 (11.3 and 11.4 ns) was consistent with the optimized one by ModelFree program, 10.30±0.02 and 10.37±0.03 ns for apo and holo CatchER, respectively.

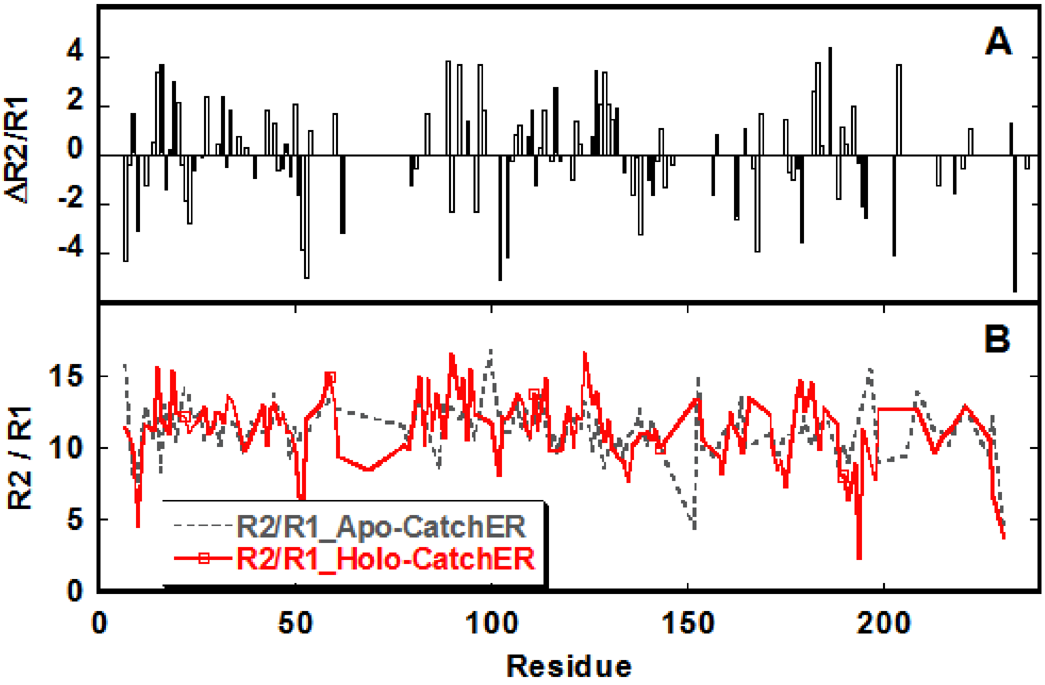

Figure 4.6. Comparison of the ratio R2/R1 of apo and holo CatchER.
(A) the difference between holo and apo CatchER. Residues with only R1 or R2 available were excluded.
(B) the absolute value of both apo and holo CatchER.

Figure 4.7 shows the comparison of the ratio $NOE_{on}/_{off}$ between apo and holo CatchER. The overall NOE ratio in apo form was smaller than the holo CatchER, suggesting calcium binding restrains the backbone flexibility and makes it more constricted, although the difference is not significant. In both apo and holo forms, it exhibits the flexibility in the stretch of 60-70 including the chromophore, and the terminus. There is exception including the regions 30-32 (SGE) and 42-45 (LTLK), and residues E95, A110, L125, L141, H181, which are less rigid in the presence of calcium.

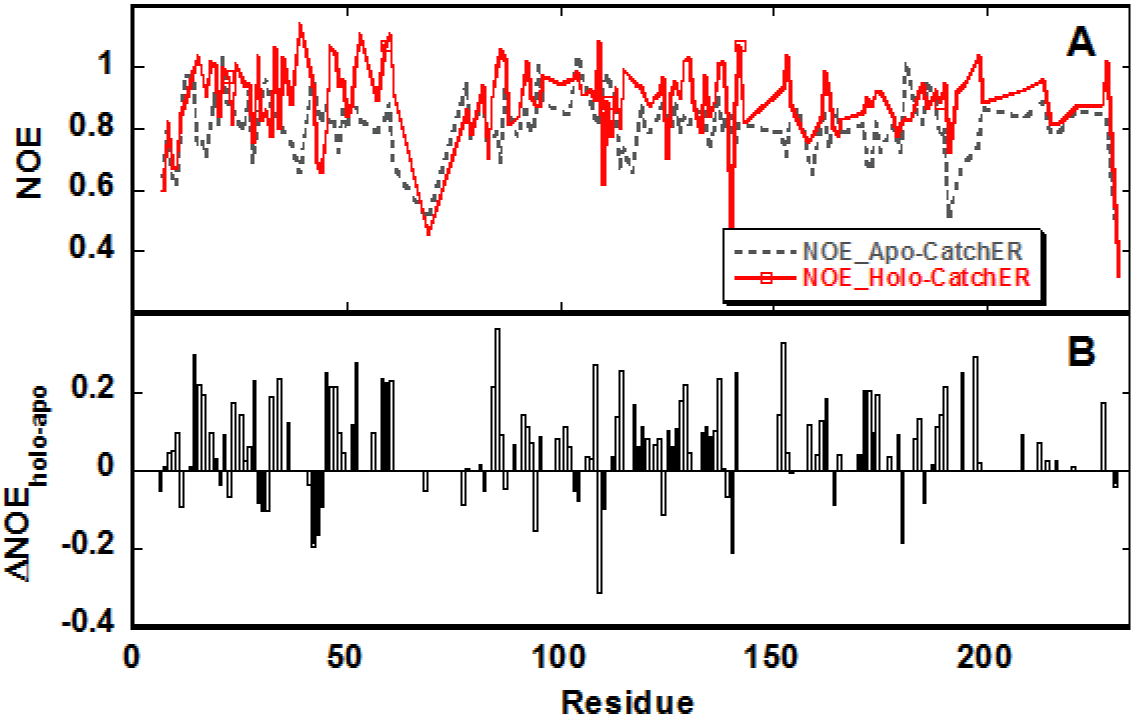

Figure 4.7. Comparison of the ratio NOE_{on}/NOE_{off} of apo and holo CatchER.
(A) the difference between holo and apo CatchER, (B) the absolute value of both apo and holo CatchER,

The order parameter S^2 reflecting the degree of internal motion, was fit by Modelfree using experimental R1, R2 and NOE and the crystal structures as templates. Residues resulting in big errors in fitting were excluded in the final model. The ranges of S^2 for apo and holo forms are 0.809-0.994 and 0.701-0.994, respectively. As shown in Figure 4.8, the overall S^2 value of holo CatchER is higher than the apo form, indicating that calcium binding makes the protein more rigid. In the pair comparison, substantial differences in the order parameter are observed in residue V12 (0.256), C48 (0.142), K126 (0.264) and A154 (0.170).

Since the amount of residues (39) remained in the final comparison is only 17% of the total residues (232), and 28% of the assigned residues (138), it is better to look at stretches or regions with a continuous trend instead of individual residues. Thus, the regions 82-88 (α-helix, DFFKSAM), and 190-196 (loop, DGPVLLP) are constrained by calcium binding, while regions 33-40 (loop, GEGDATYG) appears more dynamic.

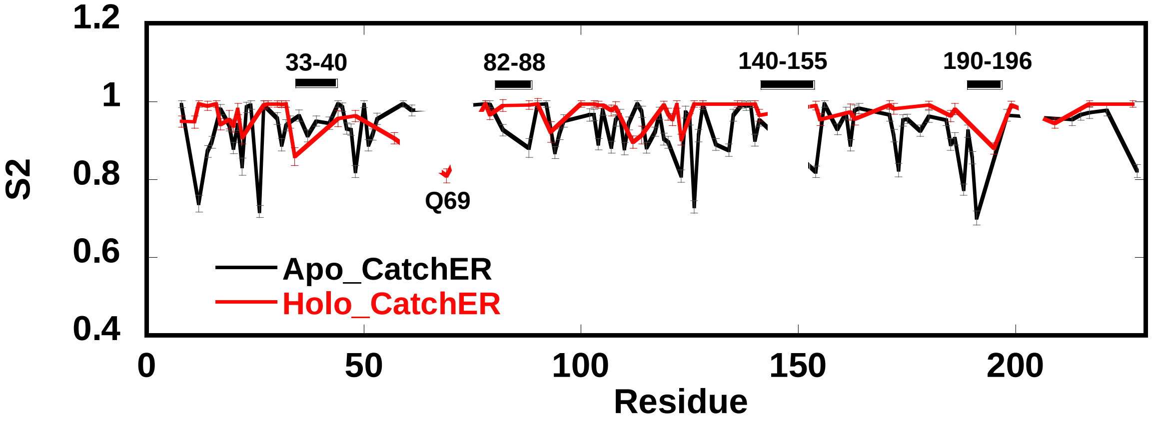

Figure 4.8. Comparison of the simulated S2 value calculated by Modelfree 4.0 of holo (red, solid) and apo (black, dash) CatchER.

Unfortunately, the designed calcium binding coordinating ligand residue Glu147 locating in the stretch 140-155 (β-strand, KLEYNYNEHNVYITAD) and the other four calcium coordinators (Asp202, Glu204, Glu223, Glu225) at the β sheets 201-206 and 221-226 are not able to be concluded here due to the big error during the fitting and simulation. However, the NOE difference between holo and apo forms is positive in the long segment of 200-228, implying the calcium binding freezes the designed coordinators to some extent.

The residue Q69 is the residue has two states and undergoes the change chemical exchange upon calcium binding according to Shen Tang's calcium titration: the slow exchange in the calcium loaded form while the fast exchange in the calcium free form. However, the NOE data did not show significant difference between the apo and holo CatchER, both of which suggest a flexible Gln69. The H-bond network around the chromophore involved in Gln69 is shown in Figure 4.9, where this residue interacts indirectly with the chromophore through water molecules through the H-bond network, Ser72, Gln94 and Glu222. There are proton wires existing in the interior of CatchER, formed by chromophore phenolic hydroxyl group, Ser205, E222, Ser72, Gln69, Asp82 and Glu5. Only Gln69 and Asp82 were assigned in the spectra, and Asp82 locates far away from the chromophore. Therefore, Q69 becomes the most representative one to indicate the dynamics of the chromophore environment.

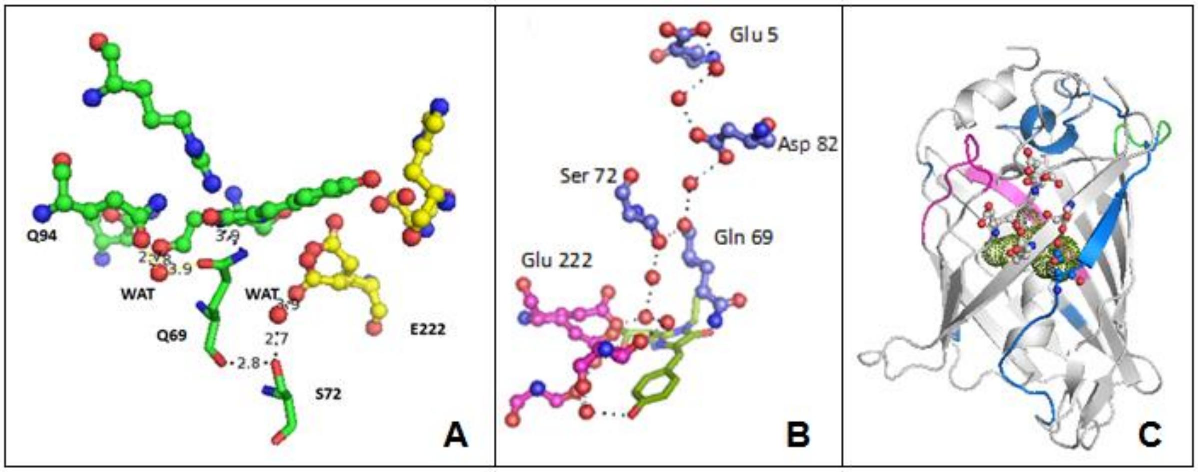

Figure 4.9. The flexible and rigid regions in the crystal structure of Ca^{2+}-CatchER.
(A) The Q69 H-bond network around the chromophore. Q69 indirectly contacts with E222 and Q94, both of which are key residues involved in the chromophore H-bond network. (B) The proton wires of the chromophore. (C) The summarized dynamics of CatchER: regions more rigid after calcium binding (blue), regions more flexible after calcium binding (magenta), alternative conformations in X-ray structure (green). The calcium coordinators are shown in stick-and-ball format.

Glu222 is the key residue involved in the proton wire of the chromophore and it has two conformations in both apo and holo CatchER. Basically, its side chain swings over 9.4° and 11.4° along the bond C-CA, in apo and holo forms, respectively. The larger degree in swinging in the Ca^{2+}-CatchER shortens the distance for the H-bonds between water molecules and Ser72 and Gln69, so that those residues are tied up more closely. In the calcium titration experiment observed by NMR, Gln69 showed the slow chemical exchanged in the presence of 6 mM calcium, which may be the result that Q69 is governed by the motion of Glu222. The X-ray structure reflects the average position of thousands of structure. Therefore, the dynamics of Q69, with the correlation time around 10^{-10}-10^{-9} s, is not necessary to be observed in the X-ray structure.

In the crystal structure of apo, Ca^{2+} and Gd^{3+} forms, residues showing two alternative conformations of side chains, include Leu15, Leu18, Ser30, Arg73, Gln80, Lys131, Glu132, Arg168, Glu172 and Thr186 and Glu225. The side chains of those residues protrude towards solvent and appear flexible. For the loop 155-159, two conformations are observed in 50% population each in the apo and metal binding CatchER. In NMR dynamic studies, this region also shows decreased steady-state NOEs in both apo and holo forms when compared with the neighboring residues, suggesting a flexible backbone, in agreement with the crystal structure. The NOEs of Leu15 and Glu172 in apo but not holo CatchER are smaller than the adjacent residues and lower than the average 0.790. For the other residues with alternative conformation, Leu18 was not assigned in apo CatchER; the NOEs for Ser30, Lys131 and Thr186 in both forms are greater than the average level, the resonances for Arg73, Gln80, Glu132, Arg168 and Glu225 were not assigned. The terminus and the other residues, for example, Gln69, are obviously more flexible in solution than in crystal.

4.2.3 *Line-shape fitting for on and off rate of calcium-CatchER complex*

The chemical exchange caused by interaction between the ligand and the protein results in the change of line shape due to the change of T2 relaxation. It is called fast exchanged if the exchange rate is far greater than δ_A-δ_B. Line broadening effect could be observed when the chemical exchange rate changes from the fast to the intermediate one because the T2 relaxation is affected. As a result, the line width change during the intermediate and fast exchange has a relationship with the exchange rate as Equation 4.1, which was rearranged to Equation 4.2 (191). The Lorentzian line shape was used for peak integration and line width determination. The scientific computing package NumPy was used for k_{off} fitting with the Levenberg-Marquardt algorithm. Equation 4.2 and 4.3 was referenced to NMR of Macromolecules A Practical Approach (Gordon C. K. Roberts, IRL Press 1993, ISBN 0-19-963224-3).

$$\Delta\nu_{1/2,ex} = \frac{4\pi\nu_0{}^2(\Delta\delta)^2 p_f p_b}{k_{on}[Ca^{2+}] + k_{off}}$$

$$p_f = \frac{[P]}{[P_t]} = \frac{K_d}{[Ca^{2+}] + K_d} \qquad \text{Equation 4.1}$$

$$p_b = \frac{[P \cdot Ca^{2+}]}{[P_t]} = 1 - p_f = \frac{[Ca^{2+}]}{[Ca^{2+}] + K_d}$$

$$\Delta\nu_{1/2,ex} = \frac{4\pi\nu_0{}^2(\Delta\delta)^2}{k_{off}} \times \frac{(K_d)^2[Ca^{2+}]}{(K_d + [Ca^{2+}])^3} = \frac{4\pi\nu_0{}^2(\Delta\delta)^2 p_f{}^2 p_b}{k_{off}} \qquad \text{Equation 4.2}$$

$$\Delta\nu_{1/2,ex} = \nu_{1/2,obs} - p_f\nu_{1/2,f} - p_b\nu_{1/2,b} \qquad \text{Equation 4.3}$$

$$\delta_{obs} - \delta_P = (\delta_{PL} - \delta_P) \times \frac{(K_d + [P_t] + [Ca^{2+}{}_t]) - \sqrt{(K_d + [P_t] + [Ca^{2+}{}_t])^2 + 4[P_t][Ca^{2+}{}_t]}}{2[P_t]} \qquad \text{Equation 4.4}$$

where p_f and p_b are the relative population of free protein and the calcium bound protein; K_d is the dissociation constant; k_{on} and k_{off} are the on and off rate of calcium binding, respectively; ν_0 is the spectrometer frequency of the observed nucleus in MHz; $\Delta\delta$ (ppm) is the chemical shift change between the calcium free and bound states at the concentration of $[Ca^{2+}]$; $\nu_{1/2}$ is the line width at half-height.

The fluorescence increase of CatchER is calcium dependent. The chemical shift change was also observed in some resonances by adding calcium, which underwent the intermediate to fast chemical exchange process. Residues Leu42, Thr43, Leu44, Phe46, Gln69 and Thr153 showed the significant resonance change, among which the line width change was observed in Leu42, Leu44 and Thr153. Figure 4.10C shows the selected peaks and the peak volume and line width was integrated and measured by Gaussian fit using NMRpipe. The chemical shift change and line width exchange was plotted in Figure 4.10 A and B and the fitting result was shown in Table 4.2. The dissociation constant of Leu42 and Leu44 was consistent with each other, but almost double as K_d of Thr153 and triple as Tyr143. The dissociation constant fitted using the fluorescence titration data was in agreement with Try143, 0.3 mM, which is the residue closest to the designed binding coordinator Glu147. It was assumed that the fluorescence enhancement by calcium binding was due to the local conformational change and the hydrogen bonding network alternation. The non-consistency of K_d calculated from different resonances indicated the sensitivity of residues to the calcium binding, which may reflect their correlation with the designed binding site. There was a hydrogen bond pair from the backbone of Leu42 and Glu222 observed in the crystal structure. Glu222 has been known as a key player in the chromophore hydrogen bond network and involved in the ESPT process. The chemical shift perturbation of Leu42 indirectly confirmed the calcium binding change affected hydrogen bonding in the chromophore environment.

The off rate fitted using the current data resulted in the big fitting error due to the lack of enough titration points. The averaged off rate was around 100 s^{-1}, which was only 1/7 as the one estimated from the stopped-flow experiment monitored by fluorescence signal. Because those residues were not directly involved in calcium binding, it can not rule out that the higher off rate may be observed in the calcium binding coordinators.

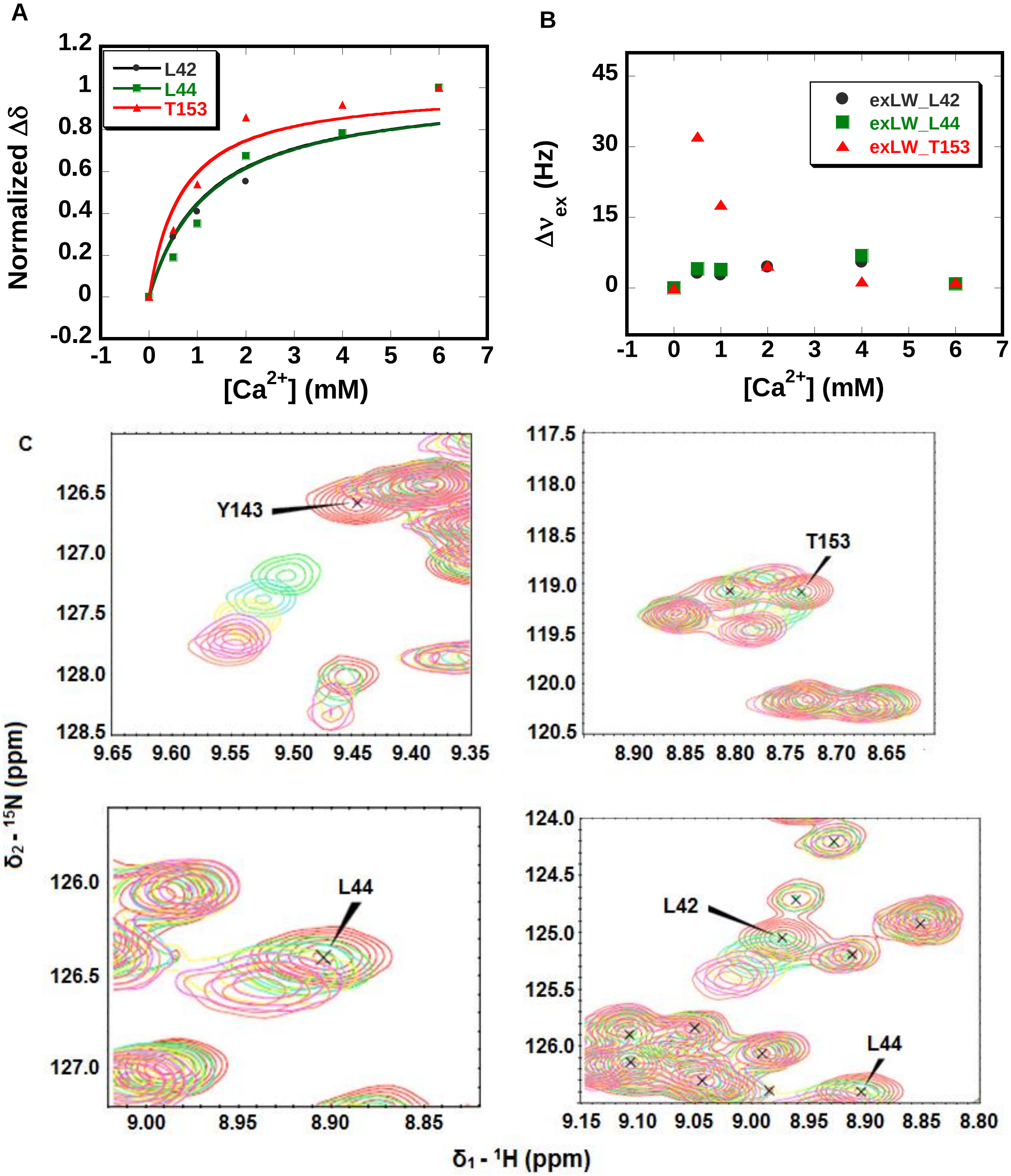

Figure 4.10. Titration of calcium for CatchER monitored by ^{1}H-^{15}N HSQC.
(A) The chemical shift change of Leu42, Leu44 and Thr153 resonance was fitted to obtain K_d using Equation 4.4. (B) The exchange line width at different calcium concentration, calculated using Equation 4.3.(C) The selected resonance at overlaid ^{1}H-^{15}N HSQC spectra of calcium titrated CatchER at 40 °using 600 MHz VARIAN NMR spectrometer.

Table 4.2 Summary of off rate and binding constants of resonance L42, L44 and T153.

Resonance	**k_{off} (s^{-1})**	**K_d (mM)**
L42	123 ±23	1.23
L44	55 ±20	1.24
T153	73 ±41	0.67

4.2.4 *Molecular dynamic simulation of calcium-free and loaded CatchER*

CatchER is the fluorescence protein EGFP based calcium sensor. The stoichiometry of calcium binding is 1:1, verified by Job's plot. The protein is consisted with 11 β strands and the chromophore was buried inside connecting two short α helices. The chromophore, p-hydroxybenzylidene-imidazolinone, is formed by automatic self-catalytic cyclization of three amino acids Thr, Tyr and Gly. It has been found that the fluorescence of CatchER is dependent on the calcium concentration. CatchER was derived from EGFP, with five site-mutagenesis residues in the β barrel in proximity to chromophore. The NMR spectra of calcium titration to ^{15}N labeled CatchER showed the chemical shift change of the residue Tyr143 which was close to one of the designed calcium binding site Glu147, and the chemical exchange from fast to intermediate of the residue Gln69, which is in the hydrogen bonding network of the chromophore. However, there was no significant difference observed in the crystal structure of calcium-free and loaded forms of CatchER with resolution of 1.66 and 1.10 Å, respectively. The X-ray crystal structure is the average one from thousands and even more individual structures, not reflecting the dynamic feature. Identical conformation of Gln69 and Tyr143 in the crystal structures of apo and holo CatchER can not rule out the possibility that the calcium binding site as well as chromophore has different dynamic feature in solution in the two states.

NMR is able to monitor the internal motion including molecular tumbling (ps) and peptide plane motion (ns), and the secondary structure and larger domain motion in μs to ms time scale, by different programs. The internal motion was illustrated by T1, T2 relaxation and NOE.

As discussed in **4.2.1**, the calcium binding to CatchER reduced the backbone internal motion as the order parameter S^2 was generally greater in the holo form. However, under the experimental condition, not all cross peaks were assigned, leaving gaps of 49-76, 142-152, 187-216, and 218-231, as shown in Figure 4.1-4.3. Unfortunately, the key residues the hydrogen bonding network of the chromophore falls in these regions including Gln69, Ser72, Thr203, Ser205 and Glu222, as well as the designed calcium binding site. In addition, the lack of information of the side chain in the NMR makes the major gap to understand the interaction between protein matrix and the chromophore. The molecular dynamics (MD) simulation is a complementary tool to the conventional experiments to find out the dynamic information of the microscopic interaction in a desired time scale up to microsecond. To investigate the effect of calcium binding on the dynamics of those residues, we used MD simulation to reveal the global conformational dynamics, backbone fluctuation, hydrogen bonding network and the torsion of the chromophore plane.

The GFP chromophore was extracted from crystal structure of CatchER. Gaussian 03 was used to optimize the geometry and calculate the electrostatic potential at the hf/6-31G* level for AMBER ff99SB force field. The complete structures of apo and holo forms were built by tLEAP module. The 10 Å water box was applied and the structures were minimized in an implicit generalized Born solvation model. The structures were heated to 300 K and relaxed for 50 ps. The simulation was carried out with ff99SB parameter set. SHAKE algorithm was used to restrain hydrogen vibration following a 2 fs timestep for equilibrium of 20 ns long at 300 K. Temperature was regulated by Langevin thermostat method. Trajectories were analyzed by PTRAJ module and VMD program.

4.2.4.1 Root mean square deviation (RMSD) and fluctuation (RMSF)

The global RMSD was calculated to find out the conformational change during the period of equilibrium. The global conformational change can be observed by backbone Cα, N and H using the first structure as reference. The fluctuation of RMSD during the simulation time suggests the conformation dynamics change. As shown in Figure 4.11A and C, both apo and holo forms of CatchER deviated 1.2 Å from the initial structure within first 3 ns. After that, the structures maintained in a steady state over 10 ns. A rise of RMSD value to 1.5 Å at approximately the 15th ns occurred in both structure although a delay of about 1 ns was observed in the holo form. In conclusion, in 20-ns simulation, there was no large conformational change (Cα RMSD > 2Å (192)) occurring in either apo or holo CatchER.

The Cα RMSF was calculated to find out the residues and areas with high fluctuation during the simulation time. In the original structure of EGFP, the electrostatic balance is one of the determinants to maintain the β barrel architecture. By introduction of the calcium binding site with the high negative potential, the local electrostatic repulsion force formed between the side chains of the mutated residues, which competed with the attraction force of the hydrogen bonds between the backbones of the neighboring β sheets. The fluctuation would occur due to the competition of the electrostatic force from the main chain and side chain, which may be diminished when calcium binds to neutralize the local negative potential. Figure 4.11B and D showed that RMSF from the apo, holo and the difference between them. The observation of Cα RMSF was consistent with the hypothesis that the fluctuation of fragments 143-150 and 198-209 decreased in the calcium-bound CatchER, where the designed calcium binding sites Glu147, Asp202 and Glu204 were included. It was not surprising that the fluctuation of 210- 230 backbone between apo and holo forms did not differ because the designed calcium coordinators Glu223 and Glu225 contributed less than the other 3 residues for calcium binding according to the crystal structure of the holo CatchER. Other than the β sheets directly involved in calcium binding, the fragment 163-181, which was in neighbor with β sheet 143-150, was also affected by the mutation indirectly.

In contrast, the RMSF for the whole residue in holo-CatchER was generally larger than the apo form. The fragments stabilized by calcium binding were indicated in Figure 4.11B, which were in agreement with the S2 calculation in Section 4.2.2. The effect of calcium binding on the whole residue also suggested that calcium binding reduced the fluctuation of the coordinator 147 and the neighboring β strand 168-177, as well as mainly increased the other regions. The Cα RMSF of Gln69 Cα in apo or holo form were 0.44 and 0.48, which was in the basal level. The simulation data suggested this residue did not fluctuate in 20 ns simulation at 300 K. However, the RMSF for the whole residue in apo and holo CatchER was 0.74 and 2.83, indicating that the calcium binding enhanced the fluctuation of the side chain.

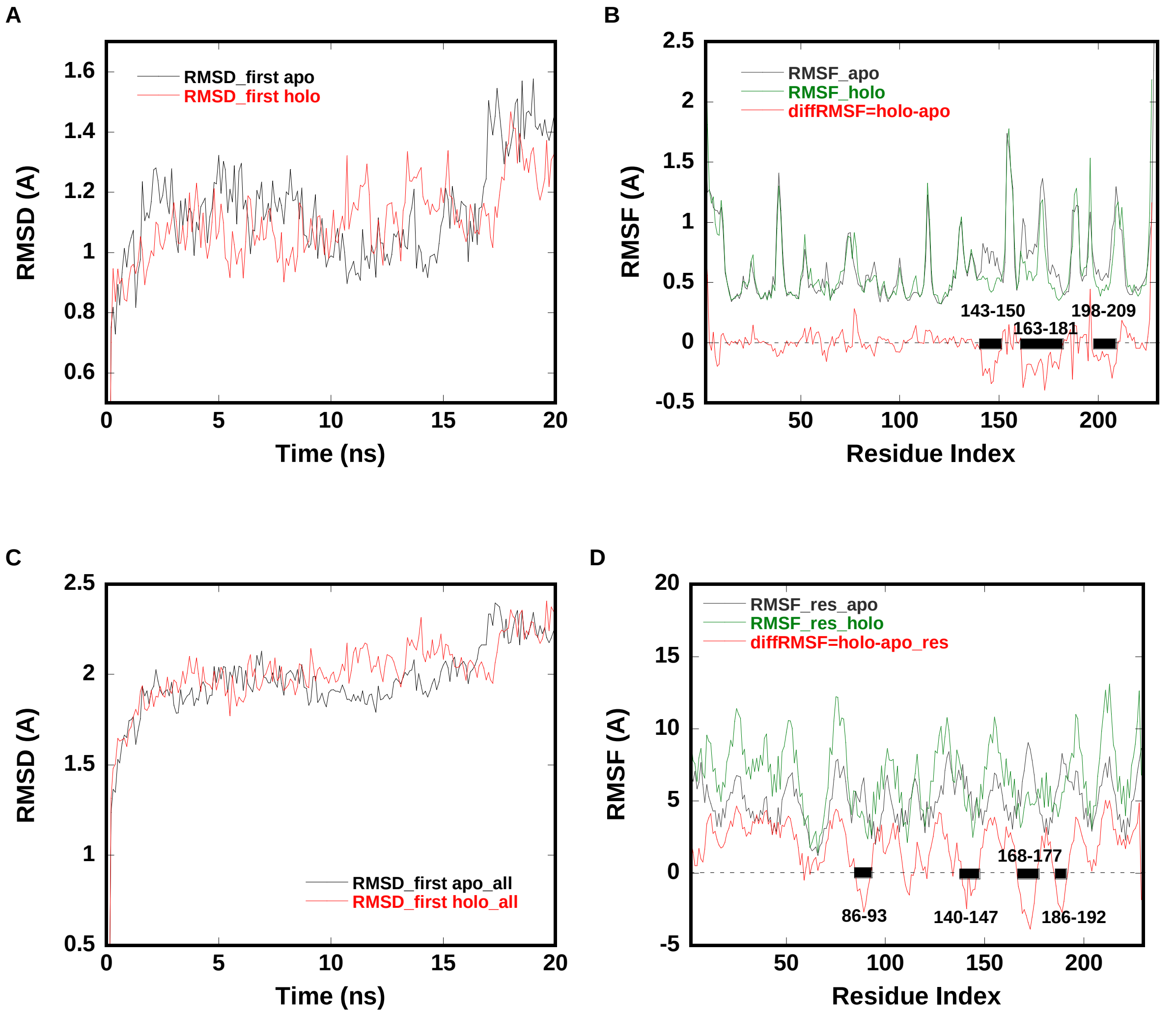

Figure 4.11. The RMDS and RMSF of 20-ns MD simulation.
(A) Backbone [Cα, N, H]-RMSD and (B) Cα RMSF differences for calcium-free and bound CatchER during 20-ns MD simulations. (C) All atom RMSD and (D) RMSF for each residue for calcium-free and bound CatchER during 20-ns MD simulations.

4.2.4.2 Hydrogen bonds in the chromophore environment

Hydrogen bonds of the trajectory were checked by PTRAJ module for the residues involved in the chromophore environment. The hydrogen bonds with occupancy greater than 5% was taken into account and will be discussed in the following paragraphs. Figure 4.12A shows the residues directly hydrogen bonding to the chromophore. The occupancy of the H-bond between the water molecule (WAT1) and chromophore tyrosine hydroxyl in Ca^{2+}-CatchER was as 600% as the apo form. In addition, the chromophore tyrosyl served as the hydrogen bond donor in the presence of calcium ion, while it was the acceptor without calcium. The pair of His148-ND1 and CRO-OH was found in the apo form, which was common in the GFP and EGFP, but not seen in the holo CatchER. The opposite way was observed for the residue Gln94 side chain and the CRO-O3, which was only present in the holo form. The tyrosyl group of Tyr92 and Tyr145 serves as the hydrogen bond donor, providing hydrogen to the chromophore O3 and OH, respectively. These two hydrogen bonds were not found in the crystal structure since the distance was beyond the H-bond cut-off. In the Ca^{2+}-CatchER, Gln94 and Tyr92 appeared to form H-bonds with either CRO-O3 or Gln69-OE1 dynamically, as shown in Figure 4.12B. In the apo-CatchER, the hydrogen bonds involving Gln69 were in a steady state with Ser72, a water molecule and Gln183 through the whole 20 ns long simulation, while in the presence of calcium Gln183 was substituted by Tyr92 and Gln 94 in the second 10 ns (See Appendix C).

Appendix C summarized the hydrogen bonds formed among the residues in the chromophore hydrogen bonding network, not directly with the chromophore. H-bonds involving Ser205 and Glu222 were similar between the apo and holo forms of CatchER, although the occupancy of H-bond pair Glu222-OE2 and Ser205-OG was 15.9% more in the presence of calcium. In both apo and holo forms, the backbone of Thr203 and His148 formed hydrogen bonds. In addition, the side chain of Thr203 served as H-bond donor to Leu201, which also accepted a hydrogen from a water molecule. In the calcium bound form, another water molecule can also share the electro-density with the backbone of Thr203 like His148. The hydrogen bond pair of His148-NE2 and Arg168-O was found in CatchER with and without calcium, and the side chain guanidine group of the latter one can also hydrogen bond to Glu147 main chain oxygen and side chain hydroxyl group in the apo form. Instead of association with the chromophore tyrosyl in the calcium free form, in the presence of calcium His148 and Asn146 formed the H-bond with the occupancy of 48%. The guanidine group of Arg73 can form hydrogen bonds with the side chain of the calcium coordinators Glu223 and Glu225 in both apo and holo forms, but the occupancy was higher in the apo form.

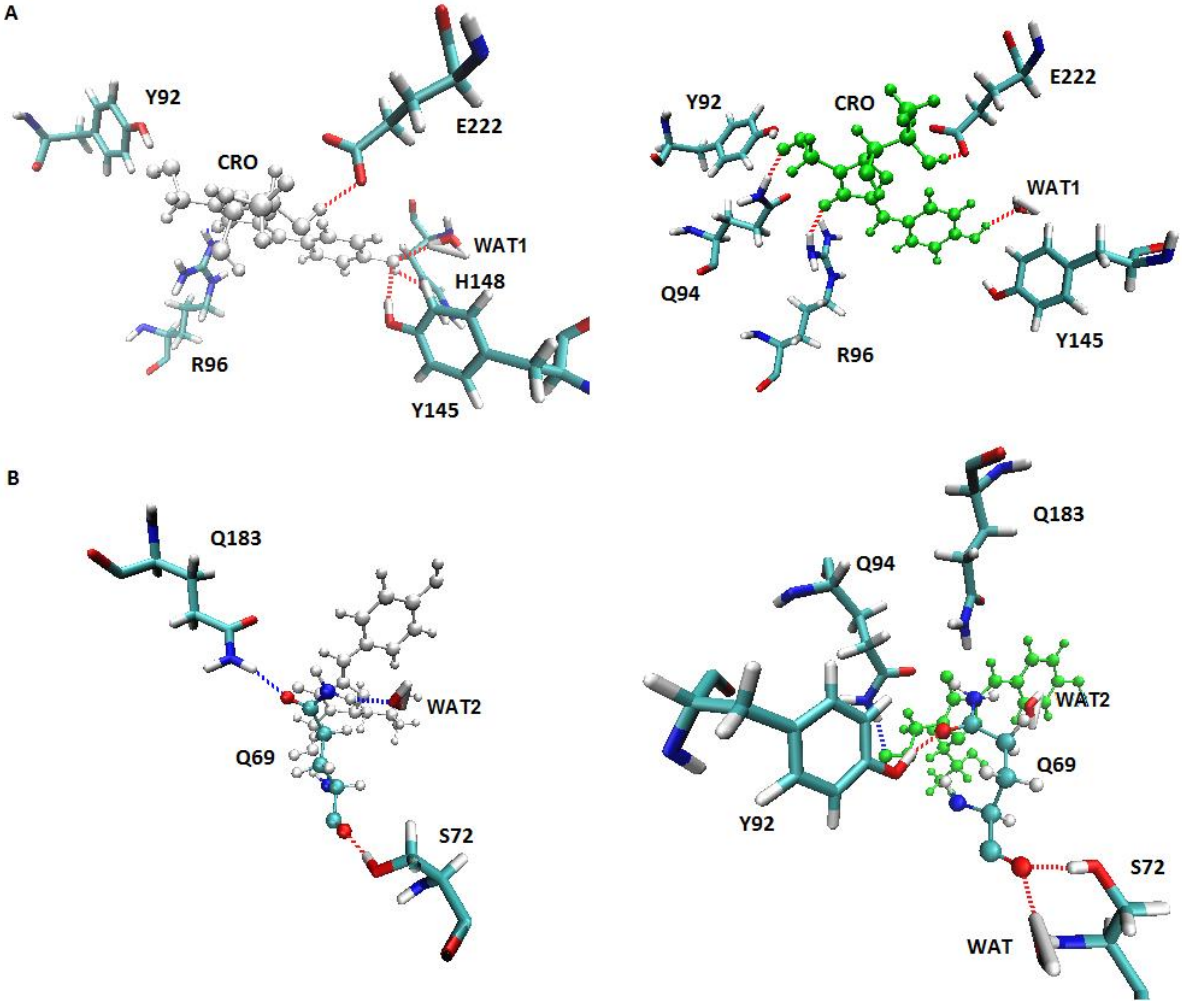

Figure 4.12. The snapshots of CatchER during 20-ns MD simulation.
The hydrogen bonds in the chromophore environment of calcium free (left) and calcium bound (right) CatchER. The hydrogen bond cut off was set as <3.0 angstroms, >120 degree, and >10% occupancy.

4.2.4.3 Torsion of chromophore planarity

The dihedral angle between the chromophore imidazolinone ring and tyrosine phenol ring reflected the torsion of the chromophore. The chromophore is a conjugated system, and the free energy is less if it is more planar. However, the protein matrix restricts the geometry of chromophore by both the electrostatic and hydrophobic interaction. Figure 4.13 showed the dihedral angle distribution along the time course. The two aromatic planes fluctuated within the angle of 13 º. In the presence of calcium the imidazolinone ring and the phenol ring were evenly distributed in both folded (positive) and extended (negative) modes, while the extended mode dominated in the apo form. The histogram of the ratio of counts of the extended and folded mode was shown in Figure 4.12B. The extended mode was favored in the apo-CatchER in the 10th-18th ns.

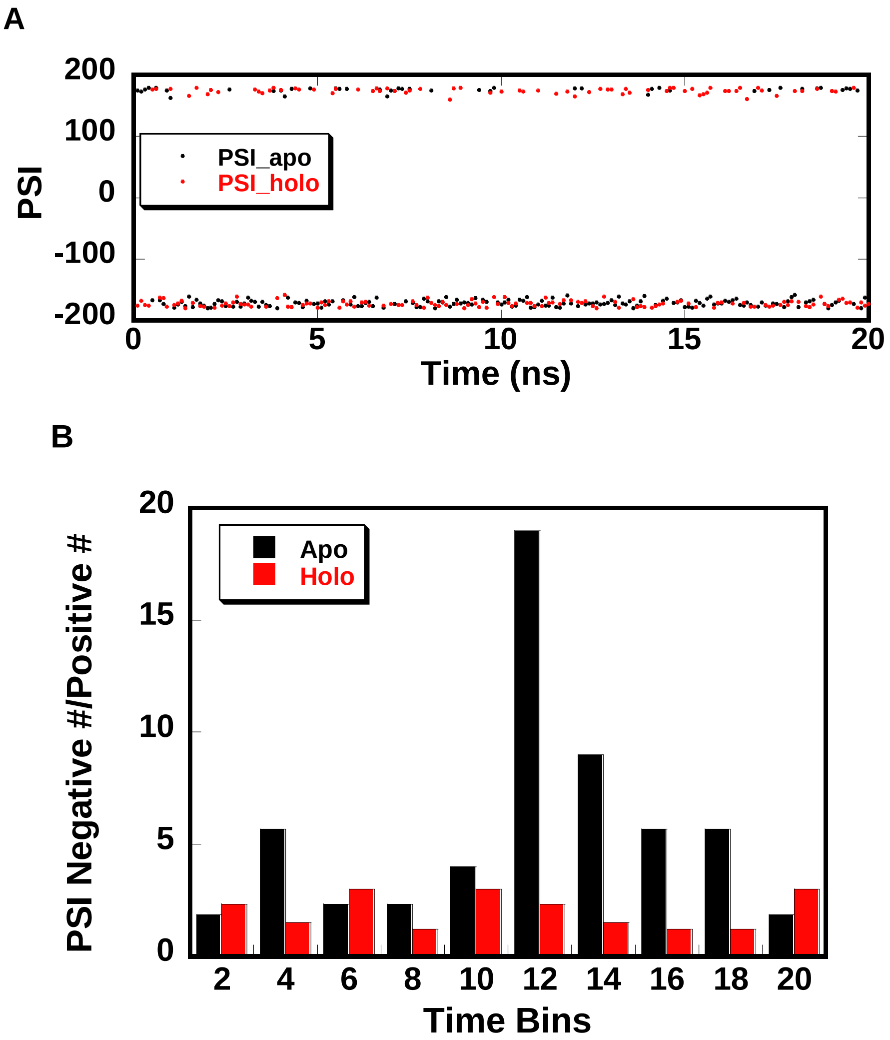

Figure 4.13. The dihedral angle between the chromophore imidazolinone and tyrosine phenol. (A) The dihedral angle defined by four atoms, CA2, CB2, CG2 and CD2, which was processed by PTRAJ module. (B) The ratio of the counts of negative to positive PSI angle in every 2 ns.

4.2.4.4 Conclusion

In the presence of calcium ion, the probability of hydrogen bonding was 98% between Ser205 to Glu222, 15% higher than that in the apo-CatchER. In the Ca^{2+}-CatchER, the water molecule close to the chromophore hydroxyl and Ser205 served as the H-bond acceptor with the occupancy of 92% to the chromophore hydroxyl. It was the bridging molecule to connect the chromophore, Ser205 side chain (6.5% occupancy) and Thr203 main chain (43% occupancy).

However, it was the hydrogen bond donor for the chromophore hydroxyl with the occurrence of 15.5%, for the main chain of Thr203 (5%) and for the His148-ND1 (8.5%) in the apo form. The proton wire consisted of the chromophore tyrosine hydroxyl, the bridging water, Ser205, Glu222 and the chromophore threonine hydroxyl, was disrupted by the introduction of the calcium binding site, which was known to be pivotal for the ESPT. Calcium binding rescued this proton transfer pathway.

There was a possible extended proton transfer pathway consisted of the side chain of Glu222, one or two water molecules and the hydroxyl of Thr203. The probability of this pathway was estimated to be 4.2% and 1.6% in the Ca^{2+}-bound and apo CatchER, respectively. It was likely that this extended proton wire reduced the electrostatic repulsion between the deprotonated Glu222 and the anionic chromophore, and affect the excited state proton transfer. The consequence was the increase of the anionic form in the optical spectrum and the longer fluorescence lifetime in the presence of calcium.

Regarding the calcium binding coordinators, Glu147, Asp202 and Glu204 contributed to the calcium binding. The association between side chains of Glu147 and Arg168 was diminished when calcium was bound. Glu223 and Glu225 in the calcium binding site were not actually involved in the calcium binding. Instead, the salt bridges formed between the side chains of Glu223, Glu225 and Arg73.

4.3 Summary and conclusions

In this chapter, I used NMR and MD simulation, as well as comparison of crystal structures to illustrate the Ca^{2+} binding effect on the structure and dynamics of CatchER. PRE experiment using Gd^{3+} as a probe was applied and successfully confirm the Ca^{2+} binding site. Later on, the crystal structures of both apo and holo-CatchER was obtained and showed the calcium ion present in the holo-CatchER, but there is no substantial structural difference observed between them.

NMR is the first choice to study the protein dynamics when the molecular size is less than 30 kDa. The T1, T2 and NOE data of CatchER was collected in the absence and presence of Ca^{2+} using VARIAN 600 MHz NMR spectrometer. There is no conformational or solvent exchange upon Ca^{2+} binding based on R2/R1 values. Heteronuclear NOE data suggests the overall structure is more rigid when calcium binds, which is consistent with the order parameter S2. The analysis of line width change upon Ca^{2+} titration provided the information of dissociation rate in the range of 100 s^{-1} according to L42, L44 and T153.

Due to lack of the complete peak assignment and missing information of the designed calcium binding site, molecular dynamic simulation was carried out to look into the effect of Ca^{2+} binding on the dynamics of CatchER. It was found that Ca^{2+} binding reduced the fluctuation of the designed calcium binding site and the hydrogen bonding network was altered. Particularly, the introduction of five negatively charged residues breaks the proton migration path and it is recovered by Ca^{2+} binding. It also provides evidence to support the findings in the Ca^{2+} effect on the fluorescence lifetime, which will be discussed in Chapter 5.

5 THE FLUORESCENCE LIFETIME OF THE GREEN FLUORESCENT CALCIUM INDICATOR CATCHER

5.1 Introduction

5.1.1 *Fluorescence lifetime of green fluorescent proteins*

The lifetime of fluorophore refers to the time between the photon absorption and emission. Basically, it is the average time of the fluorophore stays in its excited state. The lifetime is an important property of an individual fluorophore because it is directly determined by the decay rate constant k_r which determines the quantum yield. The relation of the lifetime, the decay rate constant and the quantum yield can be revealed by the following equations (Eq. 6.1-Eq.6.2).

$$\Phi = \frac{k_f}{\sum k} \qquad \text{Equation 5.1}$$

$$\tau = \frac{1}{\sum k} = \frac{1}{k_f + k_{ESPT} + k_{nr}} \qquad \text{Equation 5.2}$$

$$\Phi = \tau \times k_f \qquad \text{Equation 5.3}$$

The fluorescence emission is a kind of radiation emission, which is in first-order reaction kinetics. The photon number at the excited state at any time t is N(t), and at the t=0 is N(0). So there is $N(t)=N(0)*e^{(-kt)}$. The fluorescence decay follows the single or multi-exponential function, including the spontaneous radiation emission and non-radiative decay. Non-radiative decay includes quenching by dynamic collision, dipole-dipole energy transfer (chromophore cis-trans isomerization), internal conversion, excited state proton transfer, etc. The observed decay curve is the accumulated effect of spontaneous radiative and non-radiative decays.

GFP has attracted research interest for decades and is still shining (193). In 1996, Chattoraj and co-workers first proposed there were different forms (the protonated neutral chromophore as A form, an intermediate I form and the deprotonated anionic chromophore as B form) in GFP, which can convert to each other by proton migration (194). In the same year, the crystal structures of wild type GFP and its S65T mutant which was known as enhanced green fluorescent protein (EGFP) (195, 196). In 1997 and 2000, Palm and Remington reported the crystal structures of several mutants and summarized the spectral relevance to the three forms, and also described the residues that affected the proton transfer and further altered the spectra, respectively (197, 198).

Many pieces of evidence showed that the protein matrix maintains the bright fluorescence of GFP by providing the chromophore restrictions through hydrogen bonding network and steric hindrance. Usman and co-worker provided evidence to show that the synthesized GFP chromophore HBDI undergoes twisting of phenolate and imidazolidinone moieties upon excitation (S0-S1 transition) by detecting vibration of HBDI C=O stretching (181). Maddalo and co-workers also illustrated that the planarity of the chromophore is not energetically favored in the excited state (199). Fang and co-workers use the femtosencond Raman Spectroscopy to discussed the correlation between the native vibration of the chromophore triggered by photoexcitation and the protein transfer and suggested that a concerted chromophore motion in the time scale of 280 fs initiated ESPT (200).

The photodynamics of GFP was studied closely with the chromophore structure and conformation. The ultra-fast excited state dynamics was mapped out using the transient infrared spectroscopy (TIR) and Raman spectroscopy, suggesting the ESPT pathways and the conformational change of the chromophore. Using Raman spectroscopy and TIR, Bell, He, and Shellenberg and co-workers assigned the vibration modes and the bond stretching and formed a basis for the later study by those techniques (201-203). Stone-Ma and co-workers found out that the Glu222 was the final proton acceptor in ESPT (204). Armon and Leiderman and co-workers extended the view of the proton conduction in the protein matrix along proton wires and described the proton pathways including the proton exiting the beta-barrel by rotation of Thr203 and the slow re-entry (μs) from the other side of GFP (205, 206). Agmon later on provided the evidence by kinetics study to conclude the proton escape via Thr203 rotation was irreversible and changes the decay behavior from $t^{-1/2}$ to $t^{-3/2}$ (207). Residues involved in the classic ESPT pathway, including the chromophore phenolic hydroxyl group, Ser205, a water molecule and Glu222, are not necessary for GFP fluorescence. The S205A and S205V mutants adopted an alternative proton wire substituting Ser205 with Thr203 and enabled the proton transfer (182, 183).

Calcium transients are essential for intracellular calcium dependent biological processes(4). The amplitude, the duration and the kinetics of calcium concentration change, composite the code to regulate the downstream signaling. Such calcium signals are determined by the calcium gradients, the native calcium binding proteins and the calcium channels as well as pumps. Calcium indicators with a wide range of calcium binding affinities are needed to probe the spatial-temporal calcium dynamics in different sub-cellular compartments. The quantitative measurement is critical to understand [Ca^{2+}] change and the resting calcium level in intracellular calcium stores and subcellular compartments.

For imaging calcium changes in biological systems, much effort has been taken to develop the fluorescent calcium biosensor toolkit (54, 59, 91, 96, 208, 209). There are a broad range of choices for organic calcium dyes, including the ratiometric indicators like Fura and Indo series and the single wavelength indicators BAPTA, Fluo and Rhod series (210). These organic dyes have dissociation constant K_d ranged from 0.2-20 μM and are widely applied to monitor the intracellular calcium transients. However, some major challenges for quantitative monitoring calcium cellular responses using the static fluorescence microscopy remain, including uneven dye loading, leakage and photobleaching. The fluorescence lifetime imaging (FLIM) overcomes these limitations with its advantage of being independent of the concentration of fluorophore as well as the excitation light intensity and better quantitative(211, 212). In FLIM, lifetime measurement takes place at each pixel, revealing the spatial distribution of the fluorescent molecules and thus allowing a simultaneous recording of multiple fluorescent labels with reliable discrimination (213). In addition, it is sensitive to the change of the microenvironment such as pH, the ion strength, hydrophobocity, oxygen concentration and interaction with other macromolecules, and protein-protein/protein-ligand interactions *in situ*(214-217). Thus, it provides insights into the local environment of the fluorophore. The *in vivo* lifetime imaging utility is being developed for living small animals to monitor the treatment of diseases especially cancers(212, 218-220). The lifetime imaging of calcium indicators, Quin-2, Calcium Green 1 and Oregon Green BAPTA (OGBs) have been used to monitor intracellular calcium transients(221-223).

Genetically encoded calcium indicators (GECIs) based on fluorescent proteins benefit the calcium concentration detection in specific cellular compartments. The chimera proteins consist of calcium binding domains and fluorescent moieties, including GCaMP, Cameleon, Prericam and troponin C (TN) series, taking advantage of the intrinsic calcium binding properties of calmodulin or troponin C to induce the fluorescence intensity change upon calcium binding(54, 56, 60, 74, 95, 189). These calcium indicators with the K_d in the magnitude of 10^{-7} - 10^{-6} M and slow calcium dissociation rates are suitable to detect a calcium rise in cytosolic space but not for the calcium concentration change in the internal calcium stores such as the endoplasmic/sarcoplasmic reticulum (ER/SR).

To address the pressing need to detect the calcium concentration in a high-calcium environment such as the ER/SR, we have designed CatchER (Calcium sensor for detecting high concentration in the ER) as a sensitive fluorescence calcium probe(66). CatchER is created by the addition of a calcium binding site formed by five calcium ligand residues (residues 147, 202, 204, 223, and 225) in the beta-barrel in proximity of the phenol group of the chromophore from the single enhanced green fluorescent protein (EGFP) carrying the deprotonated chromophore (CRO) with resolution 1.20 (Figure 5.1). The excitation of both the neutral and anionic chromophore leads to the dominating anion emission at 510 nm, indicating the occurrence of the excited state proton transfer (ESPT). The fluorescence increase accompanied by the increasing calcium concentration, follows a 1:1 binding curve. The absorbance spectra showed that the population of the neutral form (ROH) decreased while the anionic form (RO^-) increased when calcium concentration increased. The fluorescence studies showed that the fluorescence intensity of the Ca^{2+}-bound CatchER increased when CatchER was excited at both neutral (λ_{abs} 395 nm) and anionic (λ_{abs} 488 nm) forms. CatchER exhibits unprecedented Ca^{2+} release kinetics with an off-rate estimated around 700 s^{-1} and appropriate Ca^{2+} binding affinity for detecting high concentration in the ER. We have shown that CatchER is able to measure the calcium concentration change in various cell types and monitor SR luminal Ca^{2+} in flexor digitorum brevis muscle fibers to determine the mechanism of diminished SR Ca^{2+} release in aging mice using the intensity-based fluorescence imaging(106).

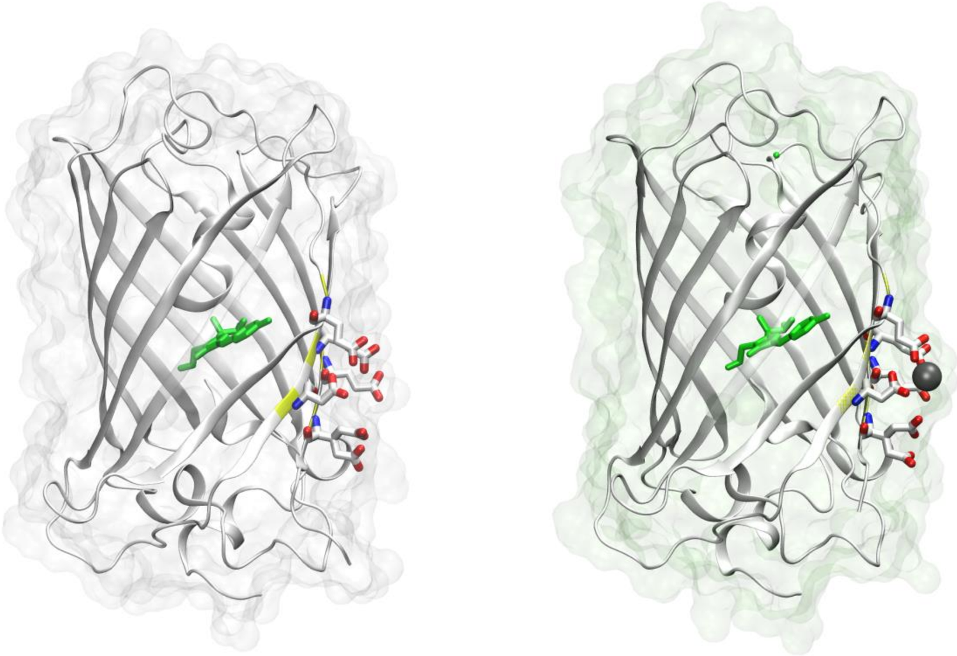

Figure 5.1. The crystal structure of apo (PDB ID: 4L1I)) and holo CatchER (PDB ID: 4L12). The residues shown in stick are the designed calcium binding site (147, 202, 204, 223, 225). Residues 164-168 were shown with 50% transparency. The residue shown in green is the chromophore. The atom shown in grey is the calcium atom. The oxygen atoms and nitrogen atoms are indicated in red and blue, respectively.

The dynamic properties of the excited CatchER, including its photophysical and photochemical properties, are still unknown. Indeed, the resulting apparent fluorescence lifetimes of both excited ROH (R*OH) and RO^- (R^*O^-) are in direct connection with the steady-state fluorescence measurements commonly used in molecular biology. In this chapter, we conducted the time-resolved fluorescence measurement to understand the fluorescence dynamic property change of CatchER induced by calcium. The goal of this study is to reveal the effect of Ca^{2+} on the ground state and the ESPT of CatchER. Our result shows that calcium binding alters the ionization state of CatchER chromophore and reduces the non-adiabatic proton geminate recombination (quenching) in the excited state to increase the apparent lifetime of indirectly excited anionic chromophore. It is the first protein based calcium indicator with the single fluorescent moiety to show the direct correlation between the lifetime and calcium binding. Our finding provides important insights into the strategy for designing calcium sensors and calcium-induced optical property changes.

5.1.2 *Lifetime imaging*

Since the fluorescence lifetime imaging (FLIM) was developed by Lakowicz in 1992, this technique has been widely used to image biological systems in complimentary with the static fluorescence microscopy (212). Fluorescence lifetime imaging takes advantage of being independent of the concentration of fluorophore and the excitation light intensity (211). In FLIM, lifetime measurement takes places at each pixel, revealing the spatial distribution of the fluorescent molecules and thus allowing simultaneous recording of multiple fluorescent labels with reliable discrimination (213). In addition, it is sensitive to the change of the microenvironment such as pH, the ion strength, hydrophobocity, oxygen concentration and interaction with other macromolecules (214). Thus, it provides our insights into the local environment of the fluorophore. The *in vivo* lifetime imaging utility is being developed for living small animals to monitor the treatment of diseases especially cancers (212, 218-220).

For imaging calcium change in the biological systems, much effort has been taken to develop the fluorescent calcium biosensor toolkit. The photostability and the calibration for each specimen make the major challenges for quantitative calcium imaging using the frequency-domain approach. The FLIM technology enables the more straightforward quantitative imaging to study the protein-protein interaction *in situ* by virtue of the fact that the lifetime measurement avoids the influence of fluorophore concentration. Calcium indicators, Quin-2, Calcium Green 1 and Oregon Green Bapta (OGBs), were applied to study the calcium transients using the lifetime imaging (221-223). The calcium binding induced the conformational change and the resulted donor lifetime decrease was observed in the FRET pair based calcium indicator TN-XXL, which was promising to be applied in FLIM (224). We conducted the lifetime measurement to understand the dynamic fluorescence property change of CatchER induced by calcium. The lifetime of excited state proton transfer was increased upon calcium binding. It is the first protein based calcium indicator with the single fluorescent moiety to show the correlation between the lifetime and calcium binding.

5.2 Results

5.2.1 *pH effect on the ground and excited-state prototropic behavior of CatchER*

The pH titration for the apo-CatchER monitored by absorption spectroscopy is shown in Figure 5.2. At pH 5.0, a single peak with the maximum at 395 nm was observed demonstrating the presence of only neutral Cro at these conditions. As the pH increased, the anionic chromophore peak at 488 nm rose at the expense of the neutral form. At neutral pH, CatchER showed the presence of both the neutral and anionic forms of chromophore (Cro) in the ground (detected by absorption spectroscopy) and in the excited (detected by emission spectroscopy) states. At pH 9.3, the neutral to anionic peak ratio was 0.74. At a pH higher than 9.3, the peak of the anionic form began to decrease and a shoulder around 465 nm was observed (not shown). At the same time, the peak maximum of the neutral chromophore was red-shifted and a shoulder was observed around 425 nm, indicating the degradation of protein at pH > 9.3. The pKa of CatchER chromophore of 7.6 was determined using the equation (1). Thus the anionic form of the chromophore was expected to be predominant at pH 10. However, the intensity of the neutral peak absorption was 60% of that at pH 5.0, implying that the portion of neutral chromophore was solvent-inaccessible. Similar behavior is known for the fluorescence of wild-type GFP (wt-GFP) that shows very weak pH dependence from 6-10 (225, 226). Alternatively, we propose that neutral Cro exists in two environments differing in the arrangement of the proton network around them. One such population can be easily titrated (we name it Cro1), while the other (Cro2) protects the Cro from the pH changes in the outside medium. From known extinction coefficients of the ROH and RO- in the GFP-type proteins and their synthetic chromophores(180) we estimate the relative populations of Cro1 and Cro2 as very close. Such splitting of the ROH population for the number of GFP variants has been already reported (227, 228).

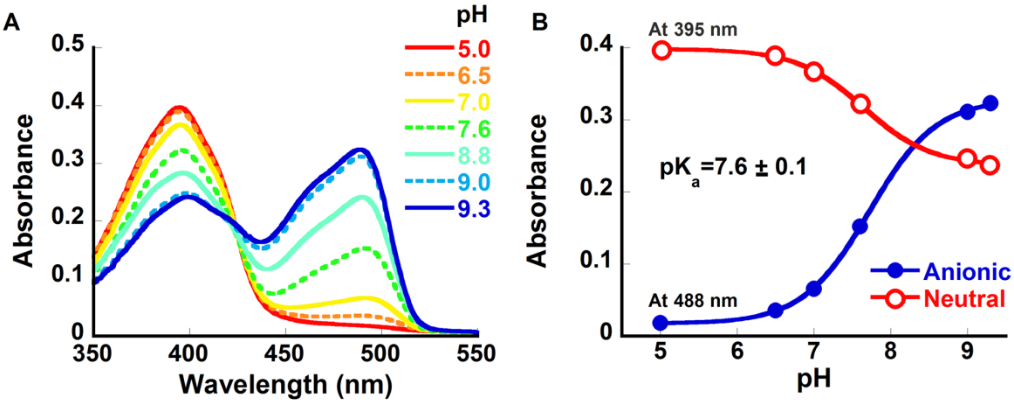

Figure 5.2. The pH profile of the absorbance of CatchER.
(A) the pH titration from 5-9.3; (B) the pK_a fitting by equation 2.10. The pH titration was carried out using 5 M KOH in a buffer cocktail consisted of 10 mM MES, 10 mM MOPS and 10 mM CAPS, pH 5.0.
(C) The fluorescence spectra of CatchER in H_2O at different pH from 5-9.3.

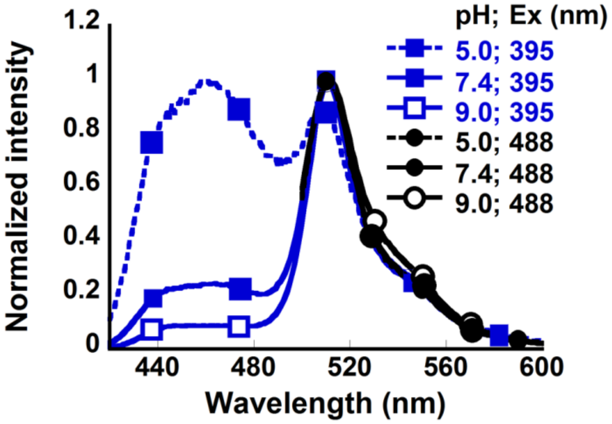

Figure 5.3. The emission spectra of CatchER in the pH cocktail buffer at different pH.
The excitation wavelength was 395 nm (blue) and 488 nm (black), and the emission spectra were collected in the range of 420-600 nm and 500-600 nm, respectively. Ex is short for excitation.

Figure 5.3 shows the emission spectra of CatchER at various pH levels. At pH 5.0 the excitation of CatchER led to a two-peak emission spectrum, the high energy band at 465 nm belonging to the neutral Cro (R*OH), while the band at 510 nm, due to the anionic Cro (R*O$^-$), formed via ESPT. With pH increase, the relative contribution of the 465 nm emission band decreased together with the relative population of the neutral Cro in the ground state (Figure 5.2). The emission maxima of the directly and indirectly excited anions (excited at 488 nm and 395 nm, respectively) are the same within the experimental error.

Fluorescence decay curves of R*OH at various pH are presented at Figure 5.4. The decay of R*OH at pH 5.0 belongs only to Cro2 which still exists in the neutral form at pH 9.6 (Figure 5.2). The non-exponential decay could be caused by the ESPT geminate recombination and non-homogenous distribution of Cro conformers in the protein(229).

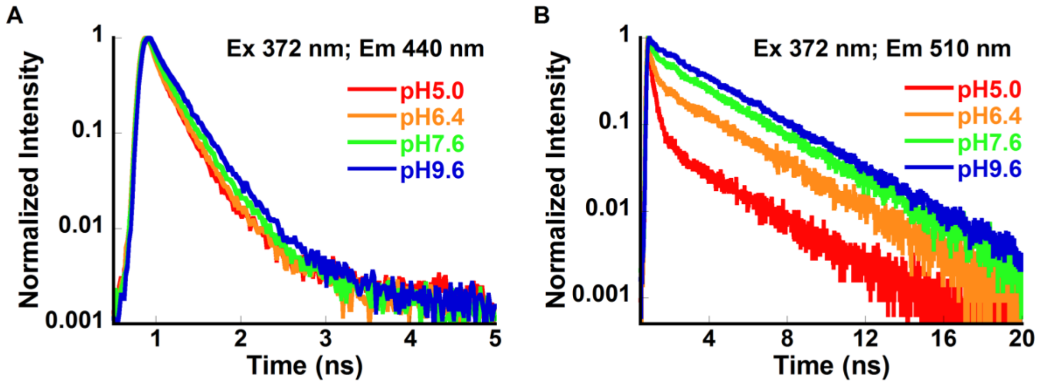

Figure 5.4. CatchER fluorescence decay at pH 5.0, 7.6 and 9.6.
The excitation wavelength was 372 nm and the emission wavelengths were 440 nm (A) and 510 nm (B).

5.2.2 *The ground and excited-state prototropic behavior of CatchER*

Fluorescence decay curves of R*OH and R*O- at pH 7.4 are shown in Figure 5.5. The decay of R*OH and the directly excited R*O$^-$ form followed the double or triple-exponential curve with the average lifetime of 0.19 ns and 2.61 ns, respectively. For the indirectly excited R*O$^-$ form, there was a fast quenching component detected within the first 2 ns, followed by the long time asymptotic decay closely approaching the lifetime of the directly excited R*O$^-$ (Table 5.1). To make sure that our observation is not an artifact caused by the experimental/instrument, we have measured the fluorescence kinetics of several GFP variants (wt-GFP, wt-GFP/S72V) and reproduced the published data. None of the known GFP variants exhibit such fluorescence kinetic behavior of the indirectly excited R*O$^-$.

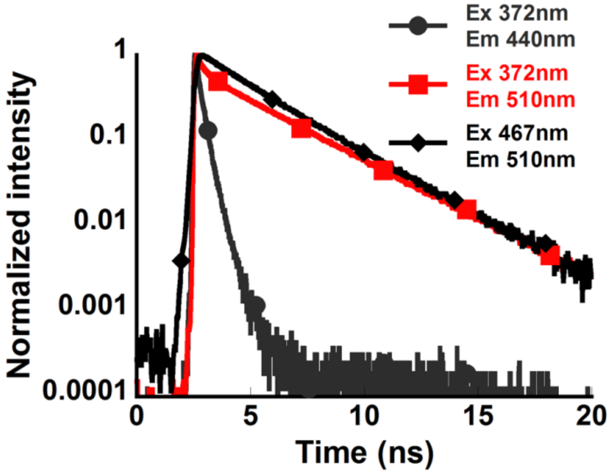

Figure 5.5. The decay of CatchER at pH 7.4.
The three forms are shown including R*OH (excited at 372 nm and emission at 440 nm), the directly R*O- (excited at 467 nm and emission at 510 nm) and indirectly excited R*O- (excited at 372 nm and emission at 510 nm, colored in red) at pH 7.4. Ex and Em are short for excitation and emission, respectively.

Upon calcium addition, the fluorescence decay of the directly excited R*OH and R*O- did not differ significantly. These results are in agreement with the previous observation that the quantum yield of CatchER was not affected by calcium when excited at 488 nm(66).

Meanwhile, the amplitude of the initial fast decay component observed in the indirectly excited R*O- was dramatically reduced and the lifetime for the long-time asymptotic decay increased in the presence of calcium (Figure 5.6). The average lifetime of the indirect excitation of anionic form was increased by 44% from 1.51 ns to 2.18 ns when calcium bound to CatchER.

Table 5.1 Values of the time constants (τ_i) and normalized (to 1) pre-exponential factors (A_i) of the multi-exponential function fitting the ps-emission transients of CatchER in various solvents.

In H_2O		τ_1 (ns)	A_1	τ_2 (ns)	A_2	τ_3 (ns)	A_3	τ_{ave} (ns)
Ex372;Em440	Apo	0.15±0.01	0.81±0.01	0.37±0.01	0.19±0.01	NA		0.19±0.01
	Holo	0.17±0.01	0.81±0.01	0.41±0.01	0.19±0.01			0.22±0.01
Ex372;Em510	Apo	0.16±0.03	0.47±0.03	0.73±0.24	0.09±0.04	3.14±0.03	0.44±0.02	1.51±0.10
	Holo	0.21±0.01	0.37±0.02	3.34±0.03	0.63±0.02	NA		2.18±0.06
Ex467;Em510	Apo	2.01±0.14	0.75±0.11	4.47±0.87	0.25±0.11	NA		2.61±0.06
	Holo	2.09±0.03	0.77±0.01	4.73±0.10	0.23±0.01			2.54±0.19
In D_2O		τ_1 (ns)	A_1	τ_2 (ns)	A_2	τ_3 (ns)	A_3	τ_{ave} (ns)
Ex372;Em440	Apo	0.12±0.01	0.79±0.08	0.31±0.06	0.21±0.06	NA		0.16±0.01
	Holo	0.14±0.01	0.87±0.01	0.40±0.01	0.13±0.01			0.17±0.01
Ex372;Em510	Apo	0.10±0.02	0.67±0.07	0.39±0.10	0.17±0.07	3.06±0.04	0.15±0.01	0.61±0.03
	Holo	0.13±0.01	0.60±0.04	0.41±0.10	0.15±0.05	3.42±0.01	0.25±0.01	0.99±0.05
Ex467;Em510	Apo	2.18±0.24	0.81±0.01	5.24±0.10	0.19±0.02	NA		2.55±0.16
	Holo	1.81±0.03	0.56±0.16	3.62±0.46	0.44±0.16			2.60±0.07

[a]The amplitude-weighted average lifetimes of τ_{ave} were calculated as ($\tau_{ave} = \sum_{i=1}^{n} \frac{A_i \tau_i}{\sum_{i=1}^{n} A_i}$).

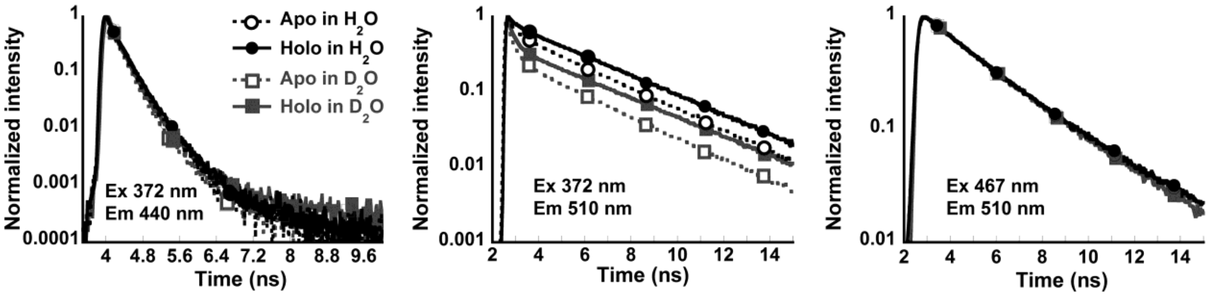

Figure 5.6. Fluorescence decay traces of apo-CatchER (dash line) and CatchER supplemented with 10 mM Ca^{2+} (Holo, solid line) in H_2O (black) and D_2O (grey).
(Left) CatchER was excited at 372 nm and emitted at 440 nm in the time range of 10 ns; (Middle) CatchER was excited at 372 nm and emitted at 510 nm in the time range of 15 ns; (Right) CatchER was excited at 467 nm and emitted at 510 nm in the time range of 15 ns. Ex and Em are short for excitation and emission, respectively.

At pH 7.4, both the neutral and anionic chromophores are present in the absorption spectra, with the peak height ratio A_{RO-}/A_{ROH} of 0.43, as shown in Figure 5.7. The emission maxima was observed at 510 nm when excited at either 395 nm or 488 nm, where the intensity of the indirectly excited R^*O^- was 45% of the directly excited species. With the addition of calcium, the population of the neutral and the anionic chromophore was changed, where the absorbance at 488 nm increased and the peak at 395 nm decreased, leading to the ratio A_{RO-}/A_{ROH} increase to

0.58. The static fluorescence spectra showed that the R*O$^-$ intensity was increased by 50% and 30% upon calcium binding when excited at 395 nm and 488 nm, respectively

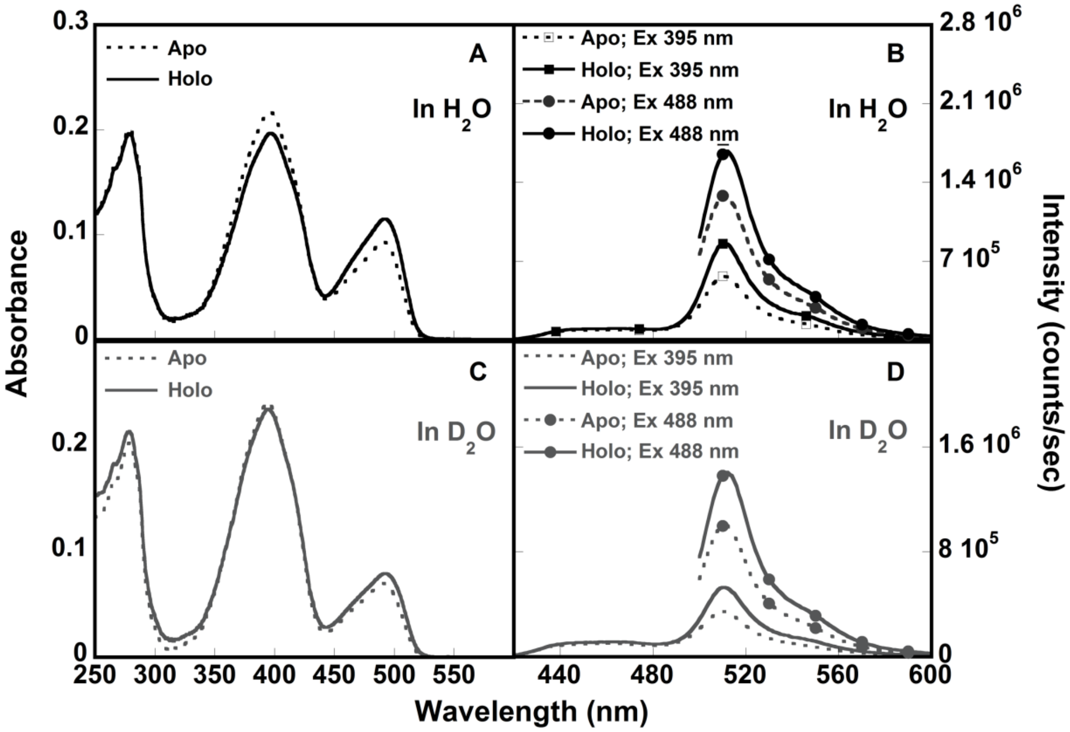

Figure 5.7. The UV/optical and fluorescence spectra of CatchER in H_2O (black) and D_2O (grey), in the absence (dash line) and presence of Ca^{2+} (solid line).
Protein samples were prepared in 10 mM Tris, pH 7.4. For fluorescence spectra, two sets of excitation/emission were applied: (1) excited at 395 nm and emission ranged from 420-600 nm, and (2) excited at 488 nm and emission ranged from 500-600 nm. Ex is short for excitation.

At the same time, in the emission spectra where the fluorescence intensity at 510 nm was normalized to unity (Figure 5.8), it was observed that the peak height ratio I_{R*OH}/I_{R*O-} ~ $1/(k_d\ \tau')$, where k_d is the proton dissociation rate during ESPT and τ' is average lifetime of the indirectly excited R*O$^-$ (230), was higher in the absence of calcium than that supplemented with calcium. The broad shoulder around 465 nm was originated from the emission of the neutral chromophore

R*OH. The emission at 510 nm was resulted from the indirectly excited R^*O^- of CatchER formed via ESPT. The higher ratio I_{R^*OH}/I_{R^*O-} in apo-CatchER than holo-CatchER indicated the larger population of R^*O^- remained in the excited state in addition to the calcium. Therefore, the calcium binding affects the acid-base equilibrium of the CatchER Cro in the ground state, causing increase of the anionic chromophore. On the other hand, the calcium binding reduces the proton geminate recombination therefore inhibiting the deactivation of the R^*O^-.

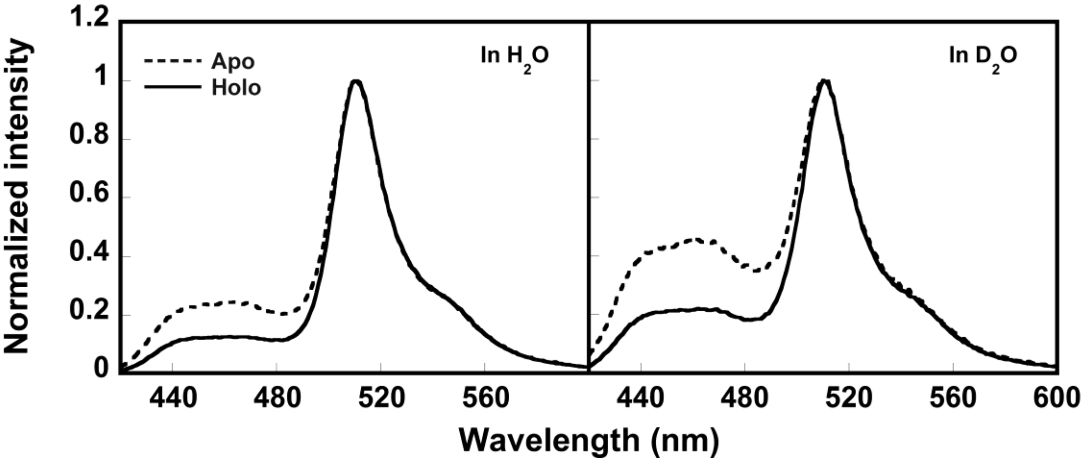

Figure 5.8. The normalized fluorescence emission spectra of apo (dash line) and holo CatchER (solid line) in H_2O (left) and D_2O (right).
CatchER was excited at 395 nm and emission spectra were collected from 420-600 nm. All spectra were normalized to the emission maxima at 510 nm.

5.2.3 *H/D kinetic isotope effect*

The fluorescence lifetime of CatchER with and without calcium was measured in D2O to obtain the H/D kinetic isotopic effect (KIE), in order to gain information about the ESPT-related rate-limiting steps in the photo-induced proton transfer cascade. No kinetic H/D isotopic effect was found in the fluorescence decay of the directly excited neutral and anionic forms at room temperature meaning that rates of proton dissociation as well as the decay of the R*OH and R*O- are non-sensitive to H/D exchange. However, the substantial H/D isotopic effect was observed for the indirectly excited R*O- (Figure 6), for which the average lifetime was 1.5 ns in H_2O and 610 ps in D2O. Interestingly, the amplitude of the quenching component was larger in D_2O than in H_2O (Table 5.1). It is known that the diffusion constant of the deuterium ion is 1.4-fold lower than the proton (231, 232). As a result, the deuteron could be restricted in the Cro environment, facilitating the reprotonation of the latter. We hypothesize that while in H_2O, the proton is prone to escaping from the Cro vicinity, causing less geminate recombination. Therefore, in the static fluorescence spectra the higher ratio IR*OH/IR*O- of CatchER in D2O (Figure 8) does not mean slower proton dissociation, which leads to H/D KIE about 5 in wt-GFP for the lifetime of the indirectly excited R^*O^- (194). On the contrary, larger geminate proton quenching of R^*O^- was observed in D_2O which resulted in the decreased average fluorescent lifetime. Altogether, the H/D KIE and the Ca^{2+} effects on the non-adiabatic geminate recombination were similar.

5.2.4 *Analysis of hydrogen bond by molecular dynamics simulation*

To provide the structural basis for our observed optical and prototropic behavior of CatchER, we have performed the MD simulation in the static state using our recent determined X-ray structures of calcium free (PDB ID: 4L1I) and calcium loaded (PDB ID: 4L12) CatchER (190). Table 5.2 shows the probability of hydrogen bonds (H-bonds) formed in the chromophore environment including Cro, H148, T203, S205 and E222 and bridging water molecules labeled as in Figure 5.9. In Ca2+-CatchER, the hydrogen-bond network can be found from the Cro tyrosyl (Cro-OH), WAT1, S205-OG and finally to E222-OE2. The Cro tyrosyl served as a H-bond donor to the bridging water molecule WAT1 connecting S205 with an occupancy of 92%. The probability to form the H-bond between S205 side chain (S205-OG) and WAT1 is 6.5%, and 98.5% for the H-bond between S205 and E222. In contrast, WAT1 was the H-bond donor for the Cro tyrosyl with the occurrence of 15.5% in apo-CatchER, and the H-bond between the S205 hydroxyl and the bridging water (WAT1) was missing. Instead, the Cro tyrosyl served as the H-bond donor for the H148-ND1 with the occupancy of 41.5%.

Table 5.2 Hydrogen bond analysis in the chromophore environment by MD simulation

Donor[a]	Acceptor[a]	Occupancy	
		Apo	Holo
CRO-OG1	E222-OE2	88.5	91.5
WAT1	CRO-OH	15.5	N/A
CRO-OH	WAT1	N/A	92.0
CRO-OH	H148-ND1	41.5	N/A
WAT1	S205-OG	N/A	6.5
S205-OG	E222-OE2	85	98.5
H148-N	T203-O	44.5	54.5
WAT2	E222-OE1	16.5	NA
WAT2	T203-OG1	10.5	31
WAT3	E222-OE1	43	40
WAT2	WAT3	24.5	35.5
Q69-NE2	WAT2	40.5	68.5

[a] The residue and atoms names of H-bond donors and acceptors were given based on the pdb files.

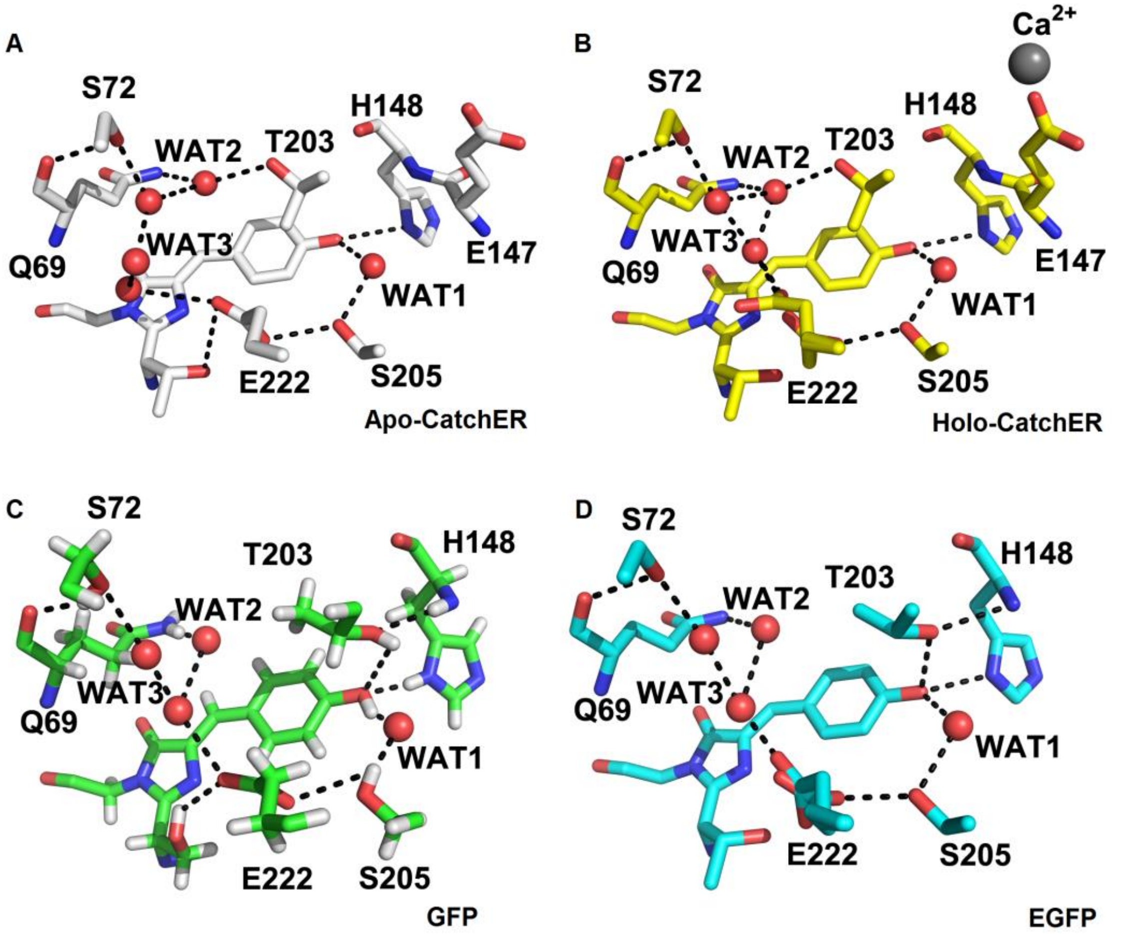

Figure 5.9**.** The comparison of crystal structures of (A) apo-CatchER (PDB ID: 4L1I), (B) Ca^{2+}-CatchER (PDB ID: 4L12), (C) GFP (PDB ID: 2WUR) and (D) EGFP (PDB ID: 4EUL).
The H-bonds are shown in the black dash line with the cut off of 3.5 . Only side chains were shown in S72, T203, S205 and E222.

In the other side from the side chain of Q69, proton can migrate to E222. Here, water molecules including WAT2 and WAT3 connected side chains of E222, Q69 and T203. In both apo and Ca^{2+} loaded CatchER, the water molecule WAT2 served as the proton donor for both T203 side chain and WAT3. Although the probability of WAT2-WAT3-E222 was higher in Ca^{2+}-CatchER, it was found that WAT2 can directly form the H-bond to the E222 side chain with the occupancy of 16.5%, resulting in the comparable possibility of proton migrating to the E222 side chain with and without Ca^{2+}.

5.3 Discussion

5.3.1 *Calcium effect on CatchER fluorescence lifetimes*

Previously, we discovered that optical properties CatchER resemble those of several GFP mutants. Excitation of both the neutral and excited forms resulted in a single wavelength of maximum emission at different pH as shown in Figure 5.3. Therefore, in contrast to the wt-GFP, there is no need to introduce intermediate anionic states(194), and the simplest kinetic scheme describing the prototropic behavior of CatchER could be depicted as shown in Scheme 5.1.

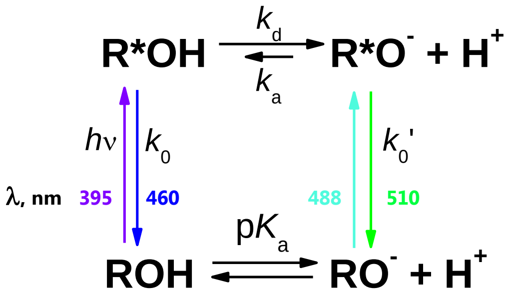

Scheme 5.1. Simple two-level ESPT kinetic scheme.

Here $1/k_0 = \tau_0$ and $1/k_0’=\tau_0’$ are the fluorescence lifetimes of the excited protonated (R*OH) and deprotonated (R*O$^-$) Cro, k_d and k_a are the apparent rate constants of the excited-state dissociation and reprotonation. The ground state population of CatchER is represented by Cro1 and Cro2, differing in their pH-susceptibility, and not existing in the dynamic equilibrium (otherwise both population would be deprotonated at pH 9.3). These chromophores are spectrally indistinguishable in both absorption and emission spectra, therefore the observed ROH, RO$^-$, R*OH and R*O$_-$ spectral bands are the superposition of Cro1 and Cro2 spectra. The excited-state R*OH decay lifetimes of pure Cro2 at pH 9.6 and 1/1 Cro1-Cro2 mixture at pH 5.0 (Figure 5.4) do not differ by more than a factor of two, demonstrating similar ESPT dissociation reactivity for both forms. Although the Cro1 and Cro2 cannot be differentiated in the apo-CatchER crystal structure(190), Ca^{2+}-CatchER, and the side chain of E222 in Ca^{2+}-CatchER shows double conformer in a 1:1 occupancy, probably responsible for Cro1 and Cro2 populations.

The non-exponential fluorescence of the indirectly excited R^*O^- found in CatchER shown in Figure 5.4B has also been observed in a number of “super” photoacids (233, 234). The fast quenching component was interpreted as the non-adiabatic proton geminate quenching. This mechanism proposed by Agmon and co-workers(235-238) expands the Scheme 5.1 into two reaction steps. The photo induced protolytic dissociation of R*OH, with an intrinsic rate constant k_d, leads to formation of the contact ion pair (CIP) R*O-…H^+, whereas adiabatic recombination with rate constant k_τ may re-form the excited acid. Additionally, back protonation may proceed also by a non-adiabatic pathway, involving proton quenching with a rate constant k_q. Separation of a CIP from the contact radius to infinity is described by the transient numerical solution of the Debye-Smoluchowski equation (DSE). As in Scheme 5.1, all excited species decay to the ground state, but the decay rate k_0” for the CIP is usually much slower than all chemical and diffusion processes and can be ignored. Therefore, our work is the first observation of the fluorescent protein with non-adiabatic proton geminate recombination.

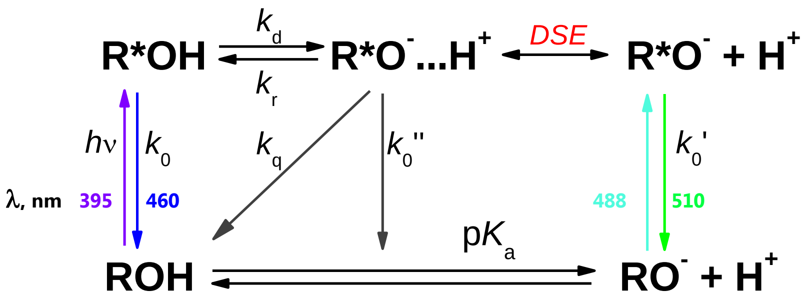

Scheme 5.2. Two-step diffusion-influenced ESPT kinetic scheme.

The ESPT dissociation rate k_d as well as both k_0 and k_0’ were calcium-independent. The average fluorescence lifetime of directly excited anionic chromophore was consistent with the reported lifetime of EGFP (2.54 ns)(239) in an acceptable error range. However, the non-adiabatic geminate recombination rate k_q was inhibited by Ca^{2+}. As a result, a larger population of R^*O^- remained in the excited state, resulting in a higher ratio I_{R^*O-} /I_{R^*OH}, which was in agreement with the observation shown in Figure 5.8. Calcium binding also leads to the increase of the long-time asymptotic decay τ_0' when the anionic form R^*O^- was indirectly excited.

5.3.2 *Structural effect in CatchER on the ground state spectra*

The unique optical properties of GFP has attracted extensive research interest for decades (193). In 1996, Chattoraj and co-workers first proposed there were different forms (the protonated neutral chromophore as A form, an intermediate I form and the deprotonated anionic chromophore as B form) in GFP, which can convert to each other by proton migration(194). The ESPT occurs in the wt-GFP, allowing it to emit as an anionic form when the neutral chromophore is excited. In the same year, the crystal structures of wt-GFP and its S65T mutant, known as enhanced green fluorescent protein (EGFP), were published (195, 196). The spectral property has been altered due to the mutation S65T in EGFP, where the anionic chromophore with the absorption maximum wavelength at 395 nm dominates, while wt-GFP has a larger population of neutral chromophore at pH 7.0.

It was proposed that E222 in EGFP was protonated to avoid the electrostatic clash with the anionic chromophore because the hydroxyl group of chromophore T65 side chain formed the H-bond with the main chain O of V61 as mentioned by Ormö(196). In addition, the pK_a of the acidic amino acids buried inside the protein was found to be larger than those in solution(205). Therefore the carboxyl group of E222 is protonated to serve as the H-bond donor to the T65 side chain. On the other hand, the phenolate moiety of the of the EGFP Cro is deprotonated, forming three H-bonds with T203 side chain hydroxyl, H148 ND1 and a water molecular, three of which function as the H-bond donors. In wt-GFP, the neutral chromophore tyrosyl forms three H-bonds, with T203, H148 and a water molecular as well. However, the chromophore tyrosyl serves as the H-bond donor to the water molecular here, shown in the crystal structure with the atomic resolution of 0.9 Å (PDB ID: 2WUR) (Figure 9)(240).

With five mutations on the β-barrel surface of EGFP, the spectral property of CatchER is closer to wt-GFP than EGFP, where the protonated neutral chromophore is dominated at pH 7.0. As shown in Figure 5.9, the crystal structure of CatchER recently determined by us(190) demonstrates that the side chain of T203 projects the opposite direction of the chromophore tyrosyl. Therefore, the H-bond between T203 and chromophore existing in both wt-GFP and EGFP is no longer in CatchER. In addition, the H-bond network with the cut-off of 3.5 Å was found in the E222 side chain carboxyl, Q69 side chain amide, T203 side chain hydroxyl and water molecules (WAT2, WAT3) as shown in Figure 5.9. The less H-bond donors around the chromophore of CatchER lead to the tyrosyl group being prone to be protonated, which is also observed in cpEGFP 149-144 (189, 241).

The pH profile of apo and holo-CatchER suggested the pKa of holo-CatchER was a little lower than the apo form, implying the chromophore is more deprotonated upon calcium binding(66). This is in agreement with the optical spectra of CatchER in the absence and presence of calcium, showing the shift of the acid-base equilibrium. Since calcium binding does not alter the conformation of T203, perhaps such acid-base equilibrium shift originated from other residues in the chromophore H-bond network. It is observed that the distance between H148-ND1 and the tyrosyl of chromophore is 3.3 and 3.2 Å, a reasonable range for a H-bond formation in both apo and holo forms of CatchER, respectively. Upon calcium binding, the electrostatic neutralization of one ligand E147 resulted in the redistribution of electron density through bonds by inductive effect, which in turn may increase the pK_a of the H148 side chain. Thus, the protonated side chain of H148 can help to stabilize the deprotonated Cro tyrosyl. This assumption was in agreement with the MD simulation results that the deprotonated H148-ND1 was the H-bond acceptor in the pair (Cro-tyrosyl)-(H148-ND1) in apo-CatchER, but not in the holo form.

5.3.3 *Effect of calcium binding site and calcium binding on excited state proton transfer in CatchER*

The photodynamics of GFP was studied closely with the chromophore structure and conformation. In 1997 and 2000, Palm and Remington reported the crystal structures of several mutants and summarized the spectral relevance to the three forms, and also described the residues that affected the proton transfer and further altered the spectra including Y66, H148, T203, S205 and E222(197, 198). The ultra-fast excited state dynamics was mapped out using the transient infrared spectroscopy (TIR) and Raman spectroscopy. By these techniques, the vibration modes and the bond stretching were assigned, which formed a basis for the later study by those techniques(201-204). The S205A and S205V mutants adopted an alternative proton wire substituting S205 with T203 and enabled the proton transfer(182, 183, 242), suggesting that the chromophore can be adaptive to the new environment.

The ESPT pathway was revealed as the tyrosyl of the chromophore, the bridging water molecule, S205 and E222, where E222 was the final proton acceptor in ESPT(204). The excitation at neutral Cro leads to the protolytic photo-dissociation which releases a proton. The proton randomly migrates through the GFP proton wires to either escape to the protein or recombine with the chromophore. In the wt-GFP the proton can exit the protein from the small hole near the

Y66 phenol hydroxyl group by the rotation of T203, where the proton diffuses to the solvent (206). Agmon and co-workers extended the view of the proton conduction in the protein matrix along 1D proton wires and described the proton pathways including the proton exiting the beta-barrel by rotation of T203 and the slow re-entry (µs) from the other side of GFP(205, 206). They later concluded that the 1D proton diffusion accompanied by the escape via T203 rotation was irreversible and changes the long-time asymptotic behavior of R*OH fluorescence from t-1/2 to t-3/2 (207). In their proposed proton transport pathway(205), T203 was switchable and enabled the proton to exit the protein matrix instead of protonation of E222. In this theory, T203 hydroxyl in the anionic B-state of GFP accepts the proton of Cro-OH and donates the H-bond to the main chain of H148, so called the "out state" of T203. The "out state" was observed in the Ca2+-GCaMP2 (PDB ID: 3EVR) and EGFP (PDB ID: 4EUL)(241, 243), as well as in the wt-GFP crystal structure of higher resolution (PDB ID: 2WUR) where there was only one conformer of T203 observed. In the acid A-state of GFP, T203 adopts the "in" conformer, in which the side chain of T203 rotates 120° from the "out" state and T203-OH is not able to form the H-bond to Cro-OH. The wt-GFP (PDB ID: 1GFL) and circular permutated EGFP (PDB ID: 3EVP) show the conformation of T203 as the "in" state.

As mentioned in section 5.3.1, only "in" state of T203 side chain was observed in both apo and Ca^{2+}-CatchER crystal structures. Based on the MD simulation, the water molecule WAT2 served as the H-bond donor for both T203 hydroxyl and indirectly for E222 via the other water molecules. The H-bond between Q69-WAT2-T203 can stabilize the side chain position and make the rotation less possible. Such the absence of the "threonine switch" proposed by Agmon (205) would prevent the proton from escaping the beta-barrel, and increase its probability to recombine with the parent R^*O^-.

The longer average lifetime of indirectly excited anionic chromophore (caused by retarded proton geminate recombination) measured in the presence of calcium versus the apo-CatchER is proposed to arise from the different arrangement of the proton wire with and without calcium binding. In the 20 ns MD simulation, it was observed that the proton wire consisting of the chromophore tyrosyl, the bridging water (WAT1), S205 and E222, was disrupted by the introduction of the negatively charged Ca^{2+} binding site, which was known to be pivotal for ESPT. Ca^{2+} binding rescued this proton transfer pathway. Such a disturbed proton wire (Cro-WAT1-S205-E222) in apo-CatchER can explain the larger population of the geminate recombination phenomenon due to the lack of an efficient proton migration path.

The broken proton migration pathway also explains the inverse H/D kinetic isotope effect. As mentioned earlier, the H/D KIE is probably not related to the inhibition of k_d like in the wt-GFP where the ESPT was five times slower in D_2O (194). Instead, the slow diffusion of deuterium makes it easier to reprotonate the protonated chromophore (both adiabatically and non-adiabatically), especially in the situation where the deuterium has little chance to travel to the H-bond acceptor, leading to the shorter average lifetime of indirectly excited R^*O^-.

5.3.4 *Calcium effect on proton-entry in CatchER*

Ca^{2+}-CatchER and Gd^{3+}-CatchER provide the view to understand the structure relevance. E222 is the key residue involved in the proton wires of the chromophore described by Agmon and Leiderman. In CatchER’s crystal structure, it has two conformations in all apo, calcium and gadolinium bound CatchER. The crystal structure only reflects the average static status, suggesting the occupancies by E222 are possible. The angle between the two possible locations of the side chain of E222 is 9.4 °and 11.4 °(CB-CA, in apo and Ca^{2+} forms, respectively. The larger degree in swinging in the Ca^{2+}-CatchER shortens the distance for the H-bonds between water molecules and S72, so that those residues are tied up more closely. In the calcium titration experiment observed by NMR, Q69 showed the slow chemical exchange in the presence of 6 mM calcium, while the intermediate chemical exchange without calcium. Q69 is bonded to E222 through S72 and two water molecules only when the side chain of E222 is in the proximate position. As calcium bound, the length of the proton wire through E222 to E5 was shortened and the force was strengthened, facilitating the proton re-entry.

5.4 Summary and conclusions

In summary, binding of Ca^{2+} to CatchER results in the increase of the dominating green emission from this protein. Such fluorescence increase is caused by the combination of thermodynamic (change of the ground-state acid-base equilibrium) and the kinetic factors. The latter is mostly based on the unusual dependence of the non-adiabatic proton geminate recombination on Ca^{2+} binding and H/D isotope exchange. Our results demonstrate that CatchER is the first example of proton geminate recombination in fluorescent proteins. Such unusual utilization of this photoinduced process in metalloproteomics opens new horizons in this rapidly expanding area. Our finding here opens new strategy to tune the fluorescence properties of the metalloproteins by metal binding that alters the intraprotein photo-induced proton transfer. CatchER is also the first GECI of the single wavelength calcium detection that has the feature of calcium dependent lifetime change. For the FRET pair based calcium indicator TN-XXL, the donor lifetime decrease was observed upon calcium binding. However, the small dynamic range of the donor lifetime change (10-20%) and the complexity of the multiexponential decay were not optimal for the FLIM (97, 224). Harvey and the co-workers showed that the lifetime decrease from 3.1 to 2.2 ns (by 30%) was able to be detected by FLIM (215). Hence, such an increase (>40%) of the average lifetime (caused by the change of the amplitude ratio for two decaying components) of indirectly excitation of R^*O^- enables CatchER to quantitatively monitor calcium dynamics by lifetime imaging in the future.

6 THE SPECIFIC TARGETING CATCHER TO THE CYTOSOLIC SIDE OF ENDOPLASMIC RETICULUM MEMBRANE

6.1 Introduction

The calcium homeostasis is required for the normal calcium signaling and maintained by calcium pumps, buffers and channels in sub-cellular compartments. For the electrically excitable cells, Ca^{2+} induced calcium release (CICR) from the SR/ER is closely related to the action potential in skeletal and cardiac myocytes, as well as neural cells. Many diseases have been found to be related with mutants of ryanodine receptor and SERCA which can cause the abnormal ER/SR calcium content, calcium leaking, or altered channel kinetics. The excitation contraction coupling in skeletal muscles relies on the coupling of activation of ryanodine receptor 1 (RyR1) and the dihydropyridine receptor (DHPR), leading to CICR from the SR. There are evidence showing that mutants of SR calcium transport ATPase (SERCA) and RyR account for the Malignant Hyperthermia (MH) and the Central Core Disease (CDD) (244-246). The activation of cardiac myocytes requires the addition of ~100 μM Ca^{2+} in cytosol, from the calcium source SR(23). The cardiac ryanodine receptor (RyR2), IP_3R and SERCA2a are three pivotal channels for the Ca^{2+} mobilization from SR to cytosol during this agonist-induced process. Dysfunction of these proteins has been proved to be the leading cause of heart failure with increasing evidence collected both from animals and humans (24, 25). The prolonged increase of the cytosolic Ca^{2+} level in cardiac myocytes will result in down regulation of Ca^{2+} signaling proteins in cardiac hypertrophy, leading to defects of muscle contraction and relaxation and ultimately heart failure(26). Alzheimer's disease (AD) is the worldwide aged disease that is characterized as extensive synaptic and neuronal loss. Although the cause of AD still remains unclear, abnormal expression level of calcium signaling proteins has been found from animal models and postmortem brain samples.

The increased Ca^{2+} level in neuron cells due to the extensive release of calcium ion from ER triggers a series of signaling process and affect the synaptic stability and neuronal health (27).

To understand the calcium signaling, calcium indicators have been widely used. The tool kit of organic calcium dyes almost covers the requirement for the calcium binding affinity from hundreds of nano-molar to sub-millimolar and the color palette has extended to the spectrum from blue to far-red. One feature limiting the application of calcium dyes is the lack of specific targeting. The genetically encoded calcium indicators (GECIs) were developed to fulfill the gap. Even though, most of them are still expressed without the targeting sequence and located in the cytoplasm, where the calcium transient is the overall outcome of both inward and outward flux. It is an important step forward to illustrate the calcium signal required for the downstream process. However, it will be powerful if one can deconvolute the total calcium change, because the upstream calcium pumps and channels are the determinants. Targeting the probe is not only to a sub-cellular domain like ER/SR and mitochondria, but also the membrane in proximity to calcium channels.

On one hand, the heterogeneity of calcium channel distribution on SR membrane was found in skeletal muscle by Ma and Blatter and co-workers in 1995 and 1996 (247, 248). The uneven structural distribution causes functional heterogeneity as well. Thus, it is more elaborated to investigate the spatio-temporal calcium release through RyR channels to illustrate the calcium signaling and kinetics. On the other hand, the kinetics of calcium release is mainly governed by the activation of RyR. It is believed that the kinetics of CICR is related to the coupling of DHPR and RYR1 for the skeletal muscle and the resulted EC coupling rate is affected, which was observed in the slow-twitch and fast-twitch muscle (155). The calcium has both activation and inactivation effect on RyR. The calcium dependent channel activity exhibits a bell shape as function of calcium concentration. In the low calcium concentration around 10-100 nM, RyR1 is activated but closed when its concentration reached 100 μM (155). The calcium stimulation speed and the resting calcium level would affect the CICR rate due to the competition between the activation and inactivation sites. The altered CICR rate will in turn affect the downstream actions.

The DHPR and RyR1 coupling is a key factor for the EC coupling. The cleft between the T-tubule and SR membrane is narrow and the fast calcium accumulation during CICR in a short time around milli-second results in a locally high calcium concentration, which is considered to account for the following activation of troponin and RyR1 deactivation. The calcium concentration change in such space attracts interest. Here we explored the targeting sequence from the segments of the transmembrane domains of RyR1, and used FKBP12-CatchER chimera protein to anchor CatchER to the ER membrane and allow CatchER to face cytoplasm, in order to investigate the amplitude and kinetics of calcium release from the SR during CICR.

6.2 Results

6.2.1 *Molecular cloning*

To obtain the clone of CatchER-FKBP fusion protein, the FKBP12 was fused to the C-terminal of CatchER without any targeting sequence in pcDNA3.1(+). A linker of Gly-Gly-Ser-Gly-Gly, along with the restriction enzyme *ClaI* site was inserted between CatchER and FKBP12. The rabbit ryanodine receptor 1 (GenBank: X15209) transmembrane domain M5 and M10, based on Zorato's RyR1 topology model (249), were applied as the ER membrane anchoring sequence. Taylor and co-workers reported that the extended Z5 (4551-4597) only can anchor GFP to the ER membrane (250). Z10 (4907-4943) is composed of 37 amino acids, which is the last transmembrane (TM) domain in Taylor’s models and also covers the last TM domain in Zorato’s model.

The extended Z5 and Z10 was fused to the C terminal, or N terminal of CatchER with neither calreticulin targeting sequence nor ER retention sequence (Lys-Asp-Glu-Leu), to allow the protein to face to the cytosol, respectively. The consensus translation initiation Kozak sequence (gccaccATGG) was placed between the Z10 sequence followed by a proline and CatchER. A linker composed of four amino acids Ser-Leu-Pro-Ala was inserted between CatchER and extended Z5 (eZ5, equivalent to TMD1 in Taylor's model) to separate the transmembrane region from the calcium sensor. The hot start KOD DNA polymerase kit was used for the PCR reaction. The ligation was carried out using T4 DNA ligase (New England Biolabs) at 4 ℃ for 48 h.

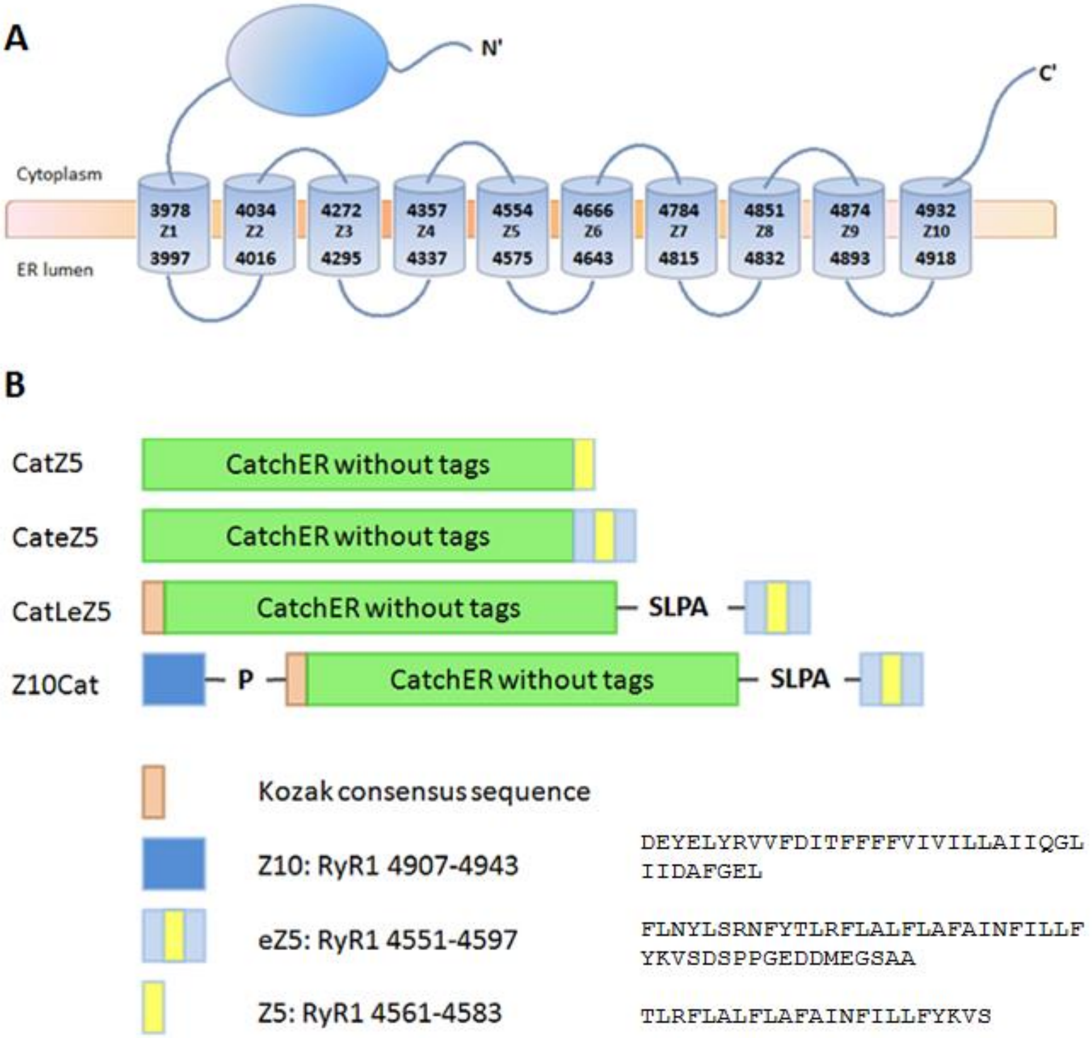

Figure 6.1. Construct of ER-anchoring CatchER.
(A) The Zozrato's RyR1 topology model. The M5 and M10 are the selected anchoring sequences. (B) The chimera of Z10-CatchER-Z5.

6.2.2 *Differentiation of C2C12 myoblast*

C2C12 myoblasts were induced to differentiate by changing 2% FBS DMEM. Cells were observed under ZEISS microscopy and the pictures were shown in Figure 6.2. In 24 h after changing medium, the tubule-like cells were observed and most of them aligned in some order. In 48 h, many cells were merged and the multiple nucleuses can be seen in one cell. In 96 h, the myotubules were observed. In 144 h, the myotubules were self-arranged in parallel. The differentiated C2C12 myotubules will be used in the future study for specific targeting CatchER to the ER/SR membrane.

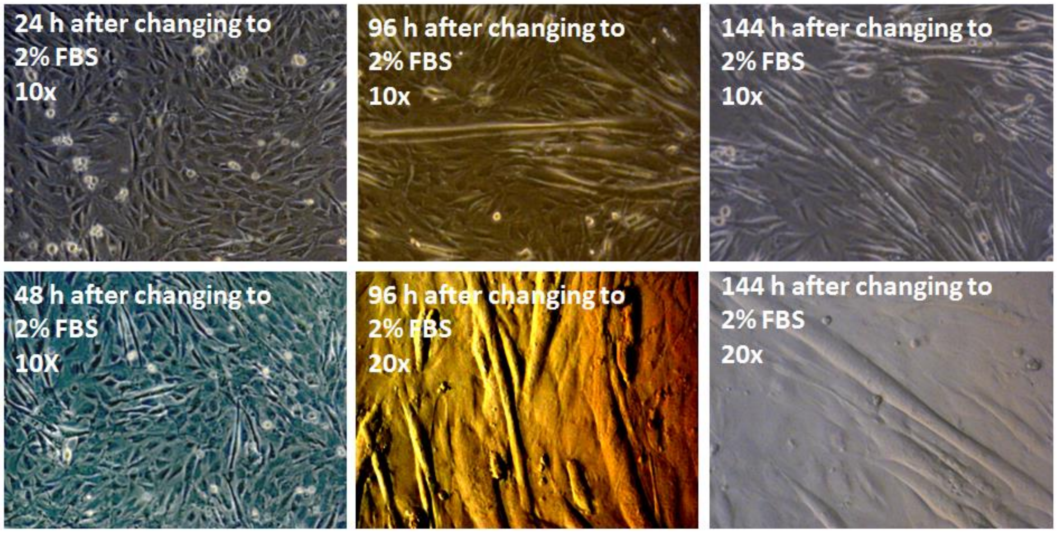

Figure 6.2. Induced differentiation of C2C12 myoblasts.
The differentiation medium was applied when the cell confluency was around 70%, and fresh medium was applied every other day. The images were taken by ZEISS microscope.

6.2.3 *The fluorescent immunostaining*

All ER membrane targeted constructs, including CatZ5, CateZ5, CatLeZ5, and Z10Cat were tested by fluorescence immunostaining for the cellular distribution C2C12 myoblasts. The confluency of C2C12 cells were maintained at approximately 30-40% to avoid the differentiation. The 0.5 mm thick cover slip was used for seeding cells and 1.5 μg plasmid DNA were transfected and cells were cultured at 30 ℃ for 48 h before imaging. Cells were fixed to the cover slip with 3.7% formaldehyde. Triton X-100 and digitonin were used for permeablizing membranes for different purposes. Digitonin is able to form complex with sterol like cholesterol which is one component of the cell membrane, but not in the ER membrane, and thus disrupt the packing of the lipid bi-layer. Triton X-100 is a kind of detergent which can solubilize all membrane. The cover slip was blocked by PBS containing 5% BSA and the primary antibody (anti-GFP or anti-Calnexin) was added. The secondary antibody conjugated with Alexa Fluor dyes were applied for imaging using the confocal microscopy ZEISS LSM 700. To note, the resolution of confocal imaging is around 50-100 nm, not able to distinguish whether the protein is anchored in the ER membrane or free in the ER lumen.

CatchER with calreticulin targeting sequence and the ER retention signal peptide KDEL was expressed in the ER with a fine reticular network distribution and co-localized with calnexin as shown in Figure 6.3A. Particularly, CatchER was located in the ER lumen because the anti-GFP antibody can only reach the cytosol protein with only digitonin treatment. In compared to CatchER, anti-Calnexin antibody reacted with calnexin when only cell membrane was permeabilized. It is in agreement with the expectation because the epitope of the anti-Calnexin antibody recognizes the C-terminal of calnexin, which is in the cytosolic side of the ER membrane. With treatment of digitonin without pre-fixation, the self-fluorescence of Z10Cat expressed C2C12 myoblasts showed the reticular architecture (Figure 6.3B), which was colocalized with calnexin as well, indicating CatchER was associated with the ER membrane and CatchER was located in the cytosol. The fluorescence of CatZ5, CateZ5 and CatLeZ5 was not as bright as CatchER (Table 6.1). Therefore, anti-GFP antibody was applied for visualizing the distribution of targeted CatchER. Similarly with Z10Cat, the ER reticular network was observed for these three targeted sequences (Figure 6.4), suggesting the membrane association and the location in the cytosolic side. However, the result of confocal imaging can not rule out the possibility that there is Z10Cat remaining in the ER lumen.

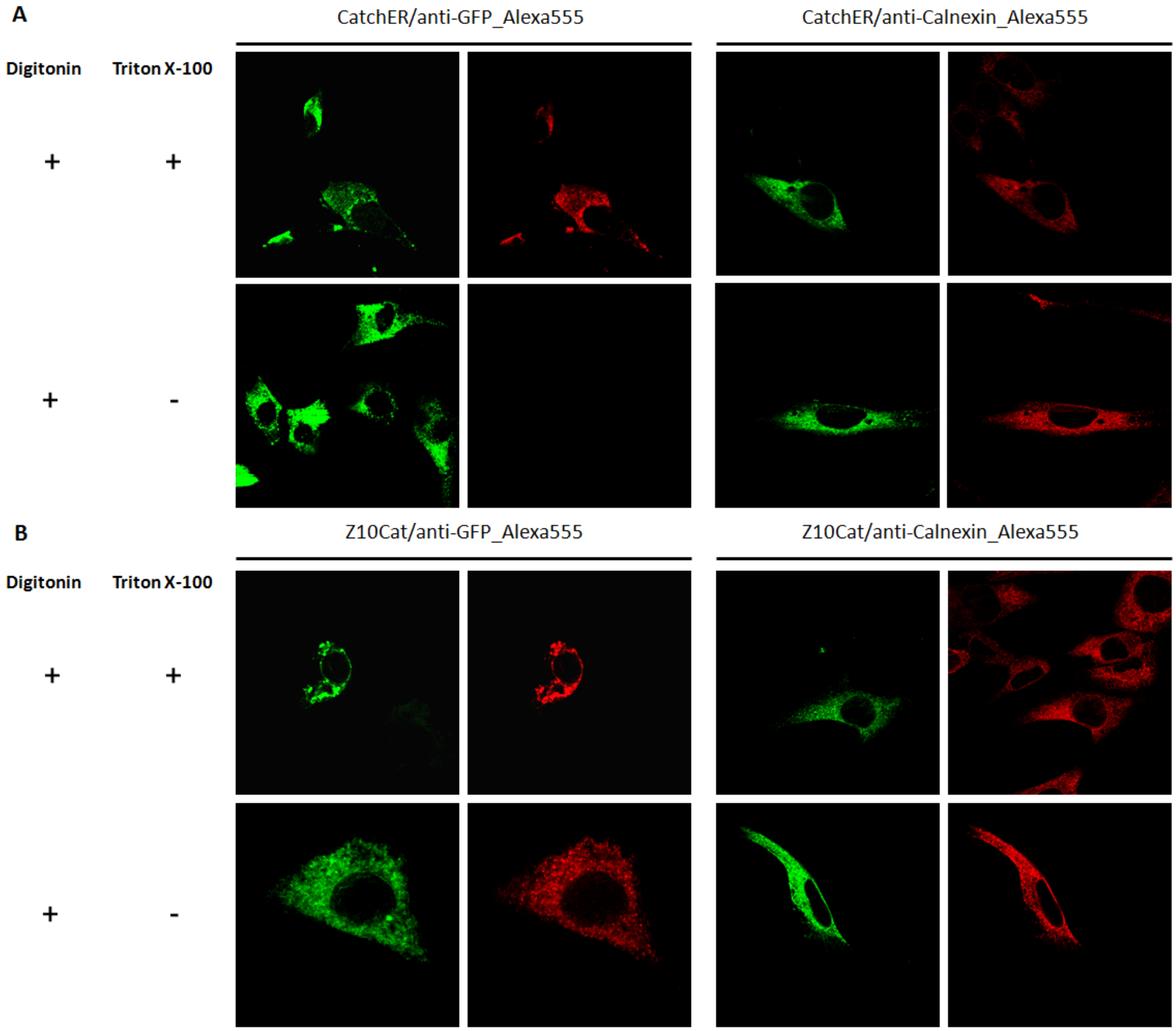

Figure 6.3. The confocal images of targeted CatchER in non-differentiated C2C12 myoblasts. (A) ER-lumen targeting with calreticulin targeting sequence and ER retention peptide, (B) Z10Cat. (Left) Green: fluorescence from CatchER self-fluorescence; Red: Alexa Fluor 555 anti-GFP antibody; (Right) Green: fluorescence from CatchER self-fluorescence; Red: Alexa Fluor 555 anti-calnexin antibody. Before fixed with formaldehyde, digitonin at the final concentration of 25 μM was added to PBS and incubation for 3 min to permeabilize plasma membrane. After fixing, incubation with 0.2% Triton X-100 in for 5 min PBS was carried out to disrupt all cell membranes.

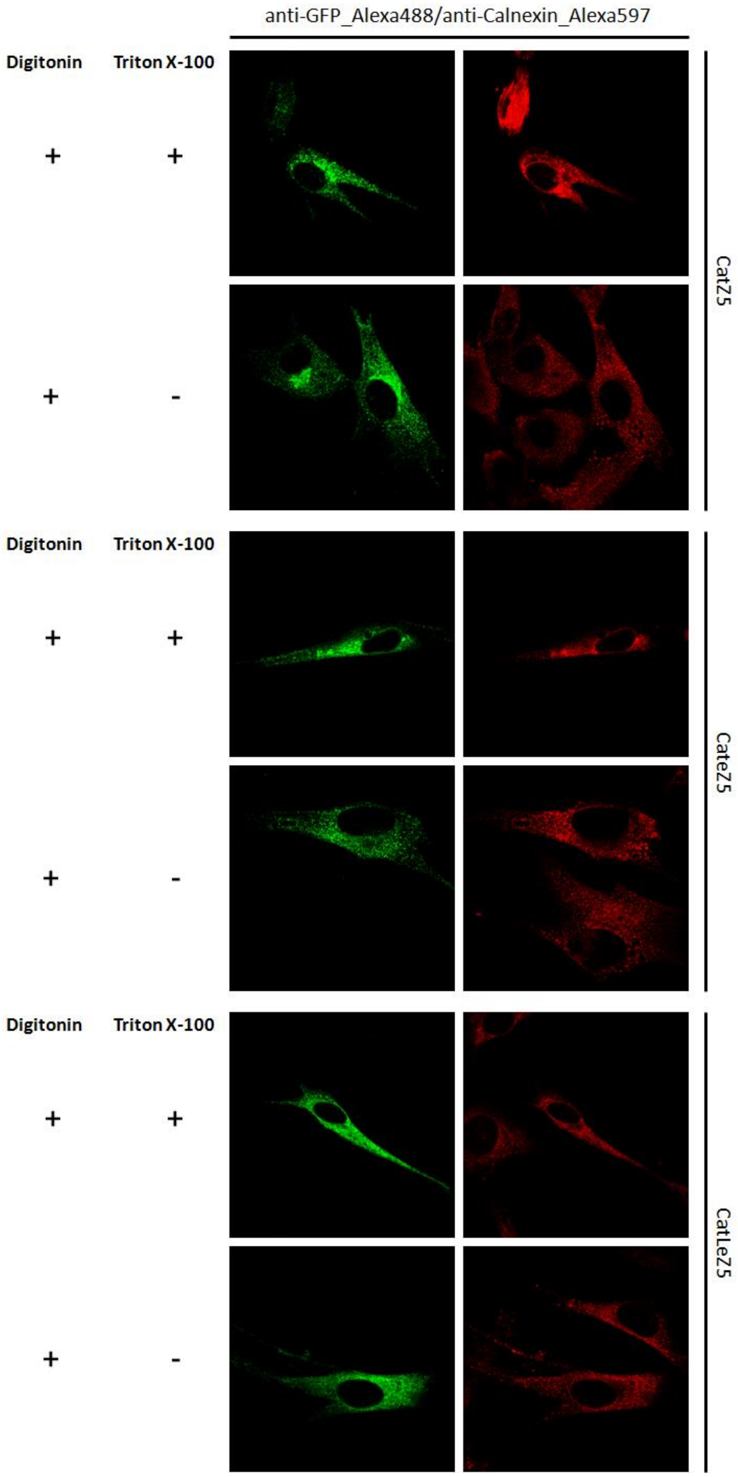

Figure 6.4. The confocal images of targeted CatchER in non-differentiated C2C12 myoblasts.
Both anti-GFP and anti-Calnexin antibodies were used together. The secondary antibody conjugated with Alexa Fluor488 was used for GFP and Alexa Fluor597 for calnexin. Before fixed with formaldehyde, digitonin at the final concentration of 25 μM was added to PBS and incubation for 3 min to permeabilize plasma membrane. After fixing, incubation with 0.2% Triton X-100 in for 5 min PBS was carried out to disrupt all cell membranes.

6.2.4 *Cell imaging*

Cell imaging studies were carried out to evaluate the CatchER fused with FKBP and the ER anchoring sequences. The 1.5-2.0 μg plasmid DNA encoding the targeted CatchER was transfected to non-differentiated C2C12 myoblasts at the confluency around 30% and cells were cultured at 30 ℃ for 36-48 h. To express CatchER in the induced differentiated C2C12 cells, DMEM was substituted with the differentiation medium containing 2% FBS when the cell confluency reached 70%. The 2 μg plasmid DNA was transfected in 72 h after changing medium. Cells were cultured at 30 ℃ for 1 week before imaging.

Figure 6.5A illustrates the calcium concentration change induced by RyR1 agonist 4-cmc (100 μM), ATP (100 μM), SERCA pump inhibitor thapsigargin (1 μM), ionomycin (10 μM) and digitonin (25 μg/ml), which was monitored by CatFKBP in C2C12 myoblasts. In the myoblasts, by applying 4-cmc, it took around 75 sec to reach the maximum decrease of 25% of the initial fluorescence intensity. It was followed by the full recovery for approximately 2 min. Similar result can be observed in caffeine addition. Ionomycin caused the fluorescence decrease by 20%, although thapsigargin triggered fluorescence change was negligible. Digitonin permebilized cell membrane and fluorescence immediately dropped by around 90%. Before any drug treatment, the fluorescence was observed for the whole cell, indicating the distribution of CatFKBP was mainly in cytosol. Overexpression of CatFKBP may result in the excess FKBP domain in the cytoplasma, so that the typical reticular network was not observed. After permeabilized by digitonin, only 10% fluorescence remained while the cells were still observed in the bright field image, suggesting the fluorescent CatchER leaked out of cells. Therefore, the possibility opens that the endogeneous FKBP dominantly occupied the RyR1 FKBP binding site and CatFKBP was in free form in cytosol. Thus, the fluorescence decreased triggered by 4-cmc and ionomycin was caused by the CatFKBP remaining in ER lumen.

After differentiation began, the distribution of C2C12 cells in the petri dish was rearranged and cells grew in parallel generally and the cells appeared long and thin (Figure 6.5B). In addition, the DNA transfection efficiency in the differentiated C2C12 cells was low. As a result, only a single cell in the observation field was record. The fluorescence intensity was not as bright as CatchER expressed in C2C12 myoblasts. Two regions of interest (ROIs) were selected from the same cell. The whole cell was bright and there was not reticular-like pattern observed. However, the color contrast formed between the nucleus and cell plasma can be distinguished, and the nucleus region looked darker. After digitonin permeabilization, the fluorescence maintained in the perinuclear region, while only auto-fluorescence was seen in other regions, implying that the majority of CatFKBP was free in cytosol and a portion was able to bind RyR1. Applying caffeine caused fluorescence intensity drop by around 7%. Without extracellular calcium, it did not recover after 4-cmc triggered fluorescence decrease. After being permeabilized, intensity decreased slightly by adding 4-cmc. All the drug treatment indicated there was CatchER expressed in ER lumen.

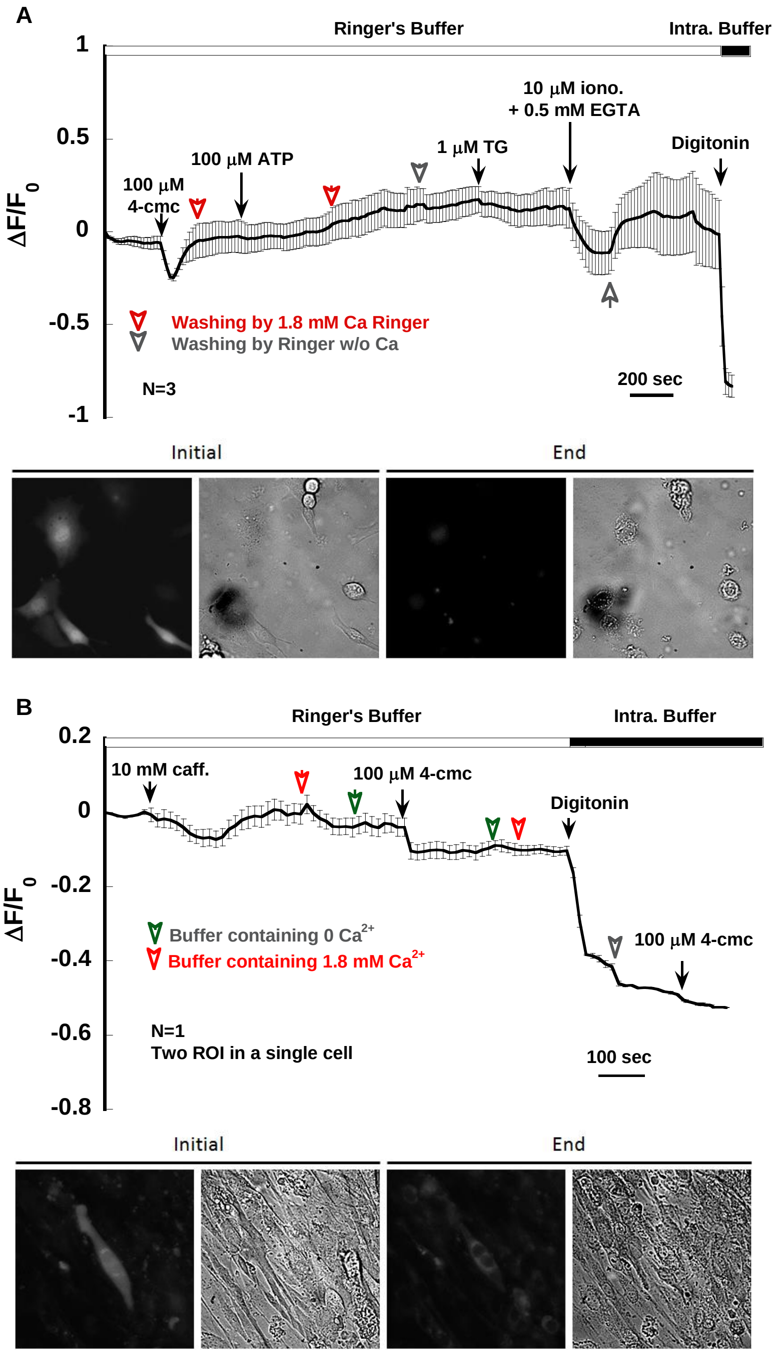

Figure 6.5. CatFKBP responding to drugs in (A) non-differentiated and (B) induced differentiated C2C12 cells.

The $\Delta F/F_0$ time course was averaged from N cells/ROIs, and the experimental event markers were labeled. The fluorescence and bright filed images at the beginning and the end of the time course were shown in the bottom panel.

Figure 6.6A shows the time course of fluorescence of CatZ5 in response to different reagents including 4-cmc, caffeine, ionomycin, ATP and digitonin. By applying 100 μM 4-cmc, fluorescence intensity decrease by 20% and the time to peak was 90 sec. In the presence of 1.8 mM extracellular Ca^{2+}, CatZ5 intensity recovered to the beginning level in around 2 min after it reached the minimum value. Without the extracellular calcium, the fluorescence also can recover back to the initial state (data not shown). Regarding the response of ATP treatment, some cells appeared more sensitive than the other and there was a slight increase observed in the average fluorescence, but the change was not significant. These phenomenon indicate that the response of CatZ5 was the same as CatchER, implying the location of CatZ5 was in ER lumen. However, the evidence was also observed that there was a portion of CatZ5 located in cytosol. First, the thapsigargin caused the fluorescence increase by 5%; second, the fluorescence increased by 7% and 10% when ionomycin was perfused in the presence of 0 and 5 mM Ca^{2+}, respectively. CatZ5 intensity remained 60% as its initial level after cells were permeabilized by digitonin. Applying intracellular calibration solution containing 10 mM Ca^{2+} triggered the fluorescence increase by 20%. The fluorescence images showed the cell was bright other than the nucleus region before any treatment applied to cells, but there was not typical reticular network observed. At the end of the data collection, fluorescence was dimmer than that of the initial but the pattern did not change.

For differentiated C2C12 cells, several nucleus can be found in the long tubule-like cell (Figure 6.6B). The basal fluorescence intensity was very low. A perinuclear pattern of fluorescence was observed. Three ROIs were selected in the single cell for the calcium imaging. Both caffeine and 4-cmc caused intensity drop a bit, around 3% and 5% respectively, in the absence of extracellular calcium, and then recovered back. The time-to-peak for the 4-cmc induced fluorescence decrease was 110 sec, longer than that in non-differentiated C2C12 myoblast. After permeabilized, intensity dropped by around 40%, indicating approximately half of CatZ5 was either free in cytosol or not anchored to the membrane. The remaining CatZ5 responded to the switch of low and high calcium solution.

There was not enough evidence showing the Z5 could anchor CatchER to ER membrane. The RyR1 activator induced CatZ5 response indicated the CatZ5 was in ER lumen, while the phenomenon that the intensity increased after adding ionomycin and thapsigargin suggested CatZ5 was in cytosol side. The amplitude of fluorescence increase induced by thapsigargin and ionomycin was small because cytosolic Ca^{2+} concentration is much smaller than CatchER's K_d, and the luminal sensor would cancel out the increase outside ER. The free cytosolic CatZ5 contributed to the fluorescence increase triggered by ionomycin and thapsigargin, but it can not rule out the possibility that there was CatchER anchored in the ER membrane. Thus, the data implied three possibilities of CatZ5 location in C2C12 myoblast, ER lumen, ER membrane and free in cytosol. In the differentiated cells, the amplitude of fluorescence decrease was much less (20% and 5%) when adding RyR1 activator, and the cell membrane permeabilization caused fluorescence loss was similar as non-differentiated C2C12 cells, implying that there was less CatZ5 in ER lumen, because more signal from the cytosolic side can contribute to cancel out the fluorescence decrease of luminal CatZ5.

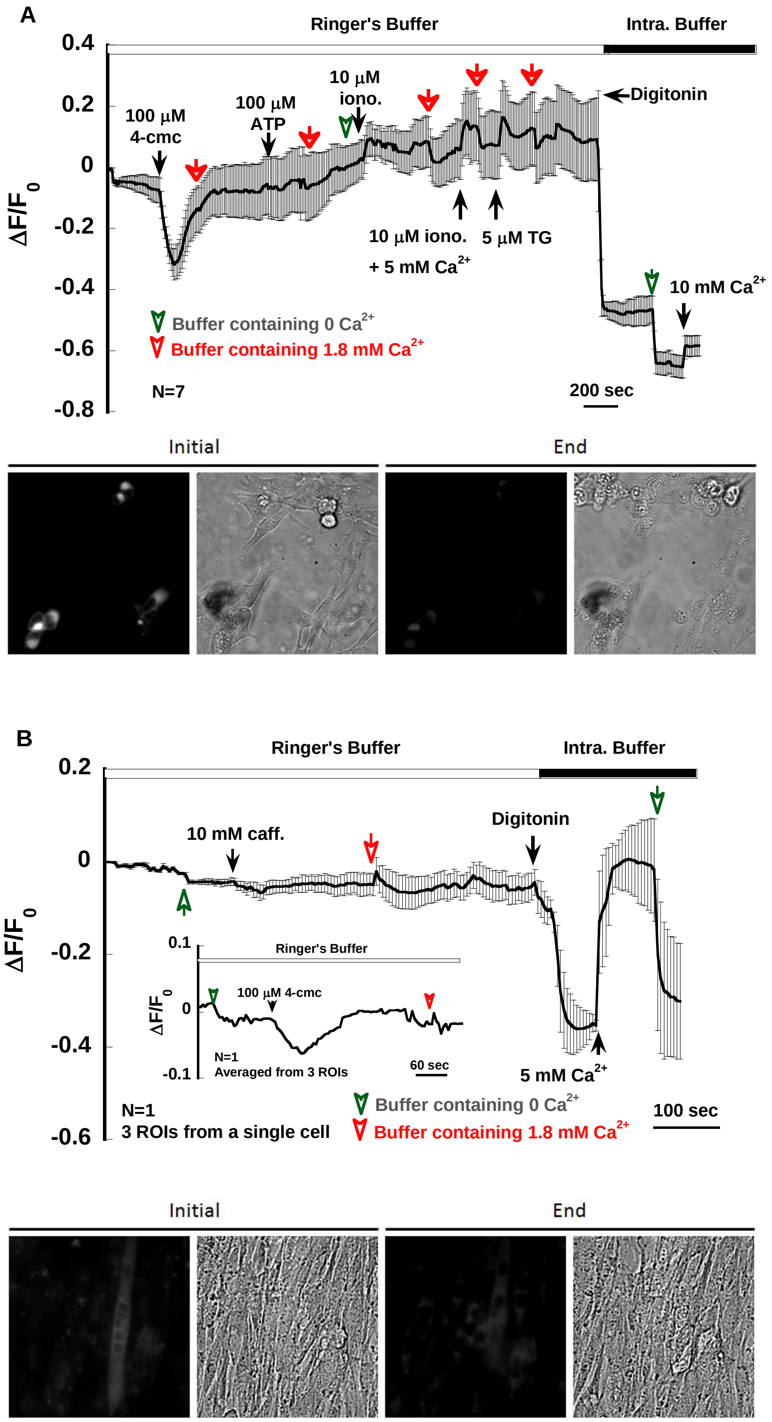

Figure 6.6. The calcium imaging of CatZ5 transfected to (A) C2C12 myoblasts and (B) differentiated C2C12 cells.

Caffeine, 4-cmc and digitonine were applied and the time points of reagents addition were labeled. The inset of panel B shows the 4-cmc induced fluorescence change in another cell other than the one treated with caffeine. The fluorescence and bright field images were taken in the beginning and the end of the imaging record.

To enhance membrane anchoring, the extended Z5 (eZ5) was fused to C-terminal of CatchER. Figure 6.7A illustrates the fluorescence change induced by 4-cmc, caffeine, digitonin and solution with high calcium. Similarly with CatZ5, the perinuclear pattern of fluorescence was observed (Figure 6.7A, initial fluorescence snapshot), although the basal fluorescence was dim and the photo-bleaching can not be ignored. The treatment with 4-cmc and caffeine induced fluorescence change was negligible, indicating there was less CatchER domain inside the ER lumen than CatZ5 transfected C2C12 myoblast. After being permeabilized with digitonin, the fluorescence intensity did not change significantly, suggesting no free CateZ5 existing in cytosol. Applying high calcium can triggered increase of fluorescence by approximately 10%, which was reversible if the solution was replaced with the one containing no calcium.

Figure 6.7B shows the fluorescence time course of the differentiated C2C12 cells treated with 4-cmc, caffeine and digitonin. The fluorescence intensity decreased by 5% was induced by 10 mM caffeine, which was not recovered after caffeine was washed away with Ringer's buffer. No fluorescence change was observed by adding 4-cmc. After permeabilization, the fluorescence intensity dropped by 60%. Perfusing intracellular solution containing 10 mM Ca^{2+} triggered the slight increase of fluorescence. The images taken before and after the experiment showed the ER-like pattern. The image collected right after applying digitonin showed a similar pattern but the intensity was dimmer than the initial one. Although the autofluorescence can be seen due to the long exposure time (0.2 sec), the fluorescence from GFP domain was still can be distinguished.

Before differentiation, eZ5 fragment can target CatchER to intracellular membranes, because the green fluorescence showed a perinuclear pattern, and the fluorescence intensity did not change by digitonin addition. There was not luminal CatchER because the fluorescence intensity was not changed by 4-cmc and caffeine. After differentiation began, CateZ5 leaked out of the cells when cell membrane was leaky, suggesting the membrane anchoring was not tight.

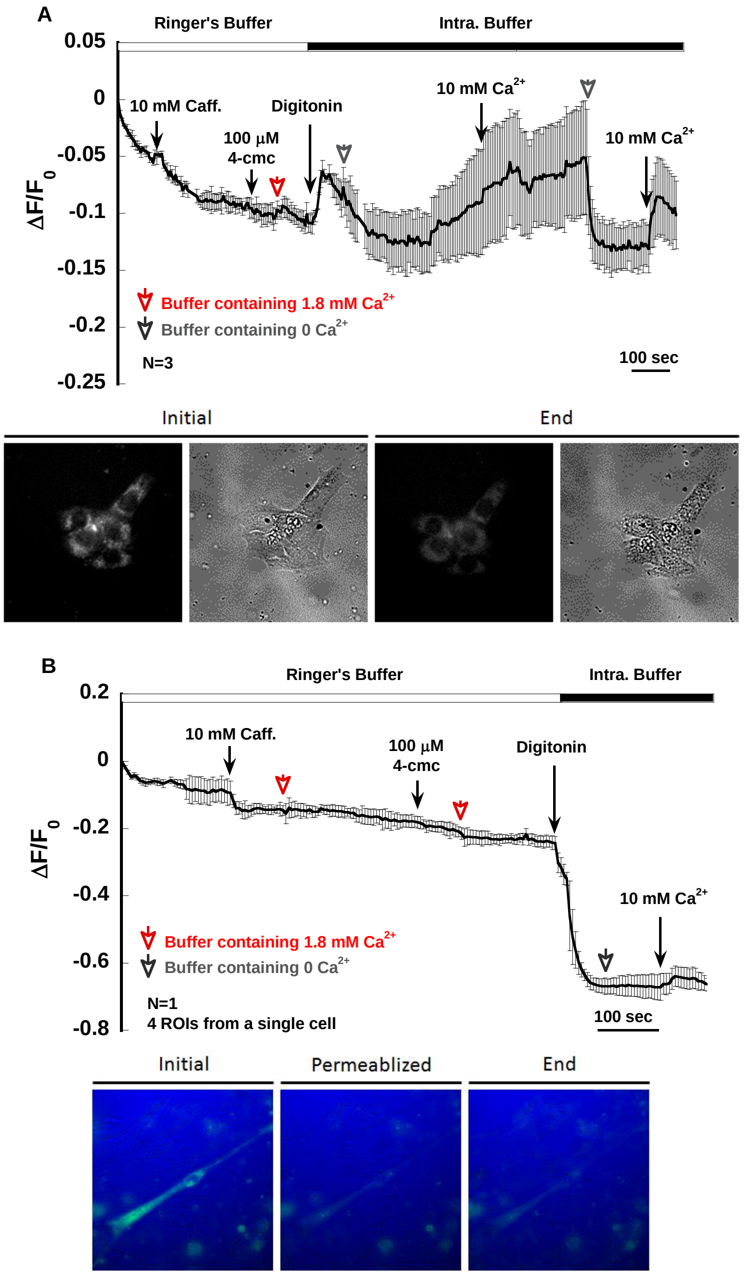

Figure 6.7. The calcium imaging of CateZ5 transfected (A) C2C12 myoblasts and (B) differentiated C2C12 cells.

The confluence was around 30% when imaging. Caffeine, 4-cmc and digitonin were applied and the time points were labeled. The fluorescence and bright field images were taken in the beginning, when just permeabilized by digitonin and the end of the experiment.

Due to the limitation of the brightness of CateZ5, it is complicated to subtract the photo-bleaching and autofluorescence from the total observed fluorescence. To enhance fluorescence, a linker composed of four amino acids Ser-Leu-Pro-Ala was inserted between CatchER and the eZ5 fragment (251). Under the microscope, cells appeared brighter than CateZ5, the one without the linker, and the fluorescence pattern was similar with CatchER, CatZ5 and CateZ5. As shown in Figure 6.8A, treatment of 50 μM 4-cmc had no effect on the fluorescence, while the higher dose of 100 μM made the intensity decreased by 7%, with the time-to-peak of 70 sec. The fluorescence recovered to the resting level by itself. Applying caffeine caused the decrease of fluorescence as well and the amplitude of decrease was 5%. Both RyR1 activators induced CatLeZ5 response suggested the prescience of the luminal CatchER domain. After permeablized, fluorescence remained around 50% as its initial level, indicating the approximately half of CatLeZ5 was free in cytosol and washed away. Adding 4-cmc induced a slight but not significant fluorescence increase, which was contributed by the cytosol-facing CatchER overcoming the opposite signal from ER lumen or background noise. When the CatchER faces cytosolic side, the average increase of calcium did not fall in the sensitive region of CatchER. As a result, the fluorescence change was small, which was consistent with our expectation. Applying 10 mM Ca^{2+} solution resulted in the increase of intensity by 10%. After differentiation began, the fluorescence pattern was not changed (Figure 6.8B). Similarly with the non-differentiated cells, 4-cmc caused the decrease of fluorescence by 10%. The time-to-peak was 40 sec. The loss of fluorescence induced by digitonin was around 10%, less than that in non-differentiated cells. The fluorescence was increased in response to high calcium solution with an amplitude of 20%.

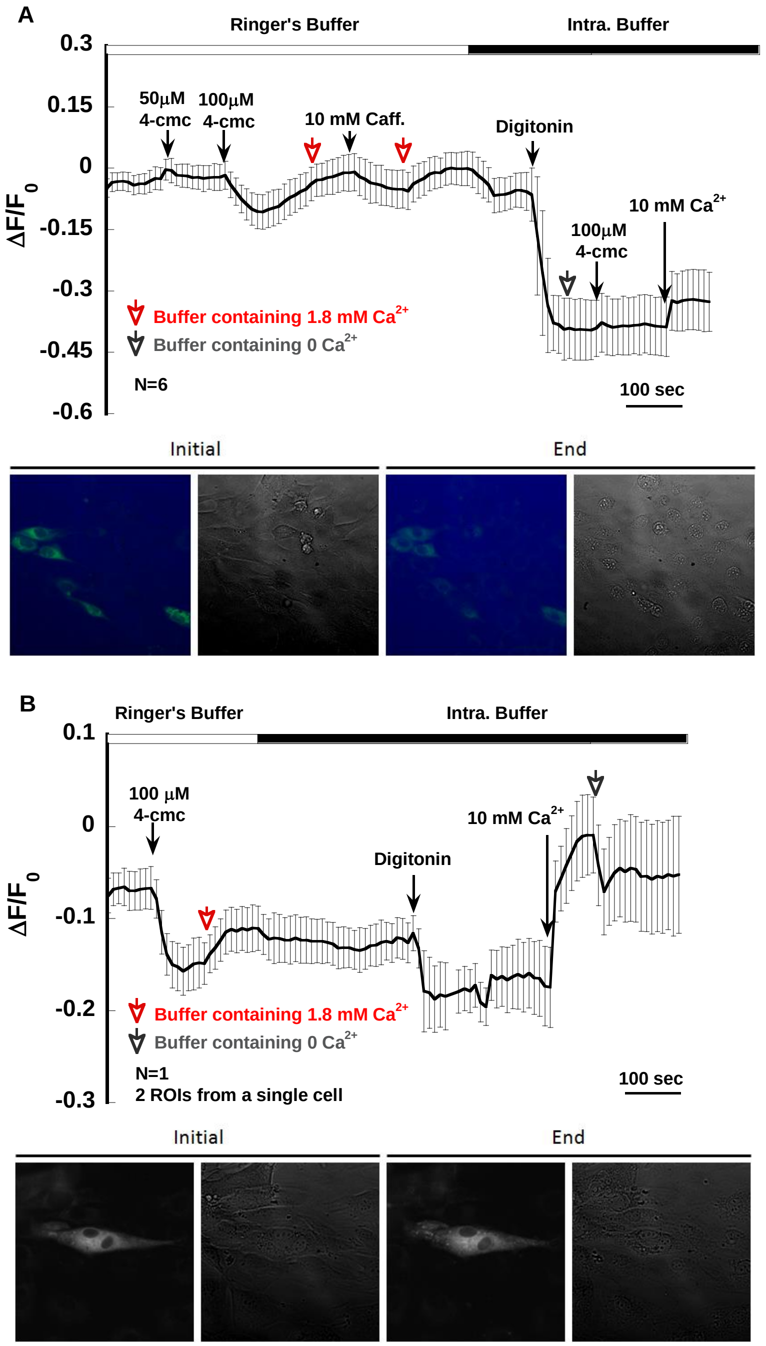

Figure 6.8. The calcium imaging of CatLeZ5 transfected non-differentiated C2C12 myotubules. The confluence was around 30% when imaging. Caffeine and digitonine were applied and depicted. The fluorescence and bright field images were taken in the beginning and the end of the experiment.

Although the brightness was enhanced by inserting the linker, the presence of free cytosolic and the luminal CatLeZ5 still remained problems. Another transmembrane domain of RyR1

Z10, the last one in Zorato’s model was fused to N-terminal of CatchER as described in ***6.2.1***. The resulting construct Z10Cat was brighter than CatLeZ5, and the brightness under microscope was comparable with CatchER. The perinuclear ER-like pattern was observed. From the calcium imaging, as shown in Figure 6.9, CatchER domain in ER lumen responded to caffeine and 4-cmc induced calcium release. Fluorescence decreased by adding ionomycin as well. The decrease of fluorescence was 5% for caffeine, and 10% and 4% for 200 and 100 μM 4-cmc respectively. After permeabilized by digitonin, the fluorescence decreased by approximately 10%, indicating the loss of Z10Cat. Perfusion with solution with 10 mM Ca^{2+} resulted in the fluorescence increase by 10%.

Surprisingly, after permeabilized by digitonin, the fluorescence was sensitive to the switch of Ringer's buffer and the intracellular solution. The amplitude of fluorescence increase in the presence in high Na^+ Ringer's buffer was 40-50%. The major difference between the two solutions is the Na^+/K^+ ratio. The pH difference between them was 0.2, following Hofer’s protocol, which can cause 5-10% fluorescence intensity difference for purified CatchER. However, in physiological condition, it is less possible to involve so much sodium in cytosol, so this effect may not be concerned in the following discussion.

For differentiated C2C12 cells, as shown in Figure 6.8B, Z10Ca responded like ER luminal CatchER, where 4-cmc and caffeine induced fluorescence decrease by 6% (2 min), and 10% (40 mM) and 4% (10 mM). There was around 30% fluorescence decrease after digitonin treatment, more than that observed in non-differentiated C2C12 cells. The dynamic range of 10% was seen in response to 10 mM Ca^{2+}.

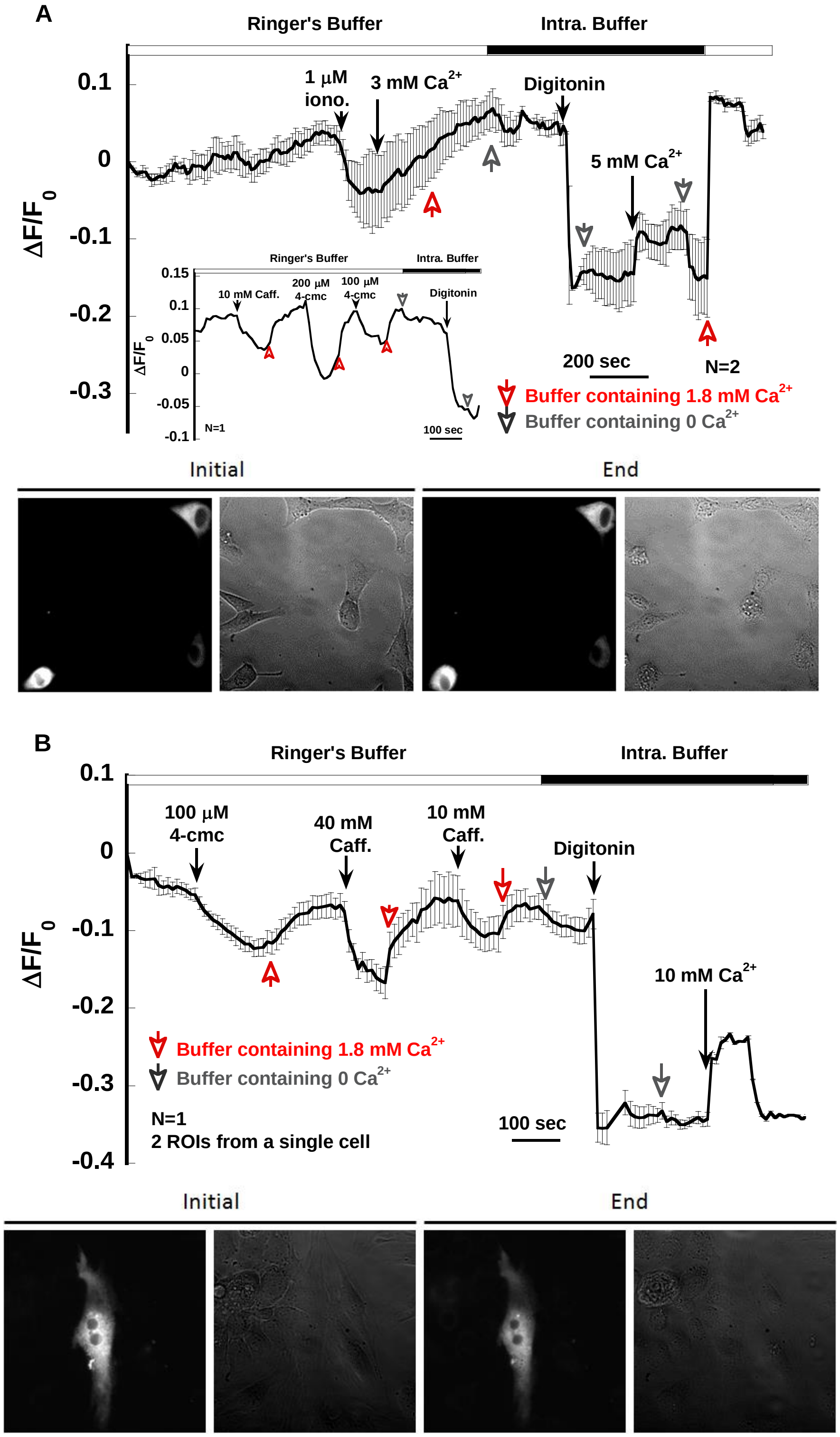

Figure 6.9. The calcium imaging of Z10Cat transfected to (A) C2C12 myoblasts and (B) differentiated C2C12 cells.

Caffeine, 4-cmc, ionomycin and digitonin were applied and the time points were labeled. The fluorescence and bright field images were taken in the beginning and the end of the experiment. The inset shows the time course of fluorescence in panel A was data collected from the other cell.

6.3 Discussion

During the differentiation, multiple nucleus are present in a single cell, ER develops to be SR, the SR/plasma membrane junction forms, the expression level of RyR1 and SERCA increased dramatically while IP_3R expression was declined (252), RyR1 re-localizes and accumulates at the terminal cisternae, and the expression of Orai1 also emerges (253). Almost all tagged CatchER behaved differently in non-differentiated and differentiated C2C12 cells, suggesting both the calcium signaling and the structural arrangement of organelles vary during muscle development. The challenge of ER/SR targeting comes out that it is complicated to find a targeting sequence which is able to fix the calcium probe to ER membrane through the differentiation process.

Table 6.1 lists the amplitude and the time-to-peak of 4-cmc induced calcium release detected by CatchER with different targeting fragments in C2C12 myoblast and differentiated cells, as well as the loss of CatchER fluorescence after digitonin permeabilization. The performance of the same protein in different states during differentiation of C2C12 varies, which can not be predicted currently. The main goal of this study is to select the sequence allowing to target CatchER to SR membrane to investigate the calcium dynamics in the plasma/SR membrane junction. As a result, evaluation of the performance in the differentiated cells would be more meaningful in this case. It is notable that using the current microscope setting is not able to capture such fast calcium transients happening in the cisternae cleft. It was not expected to see the fluorescence increase by activating RyR1 with a frame rate of 1 shot/15 sec. The parameters evaluated in the present experimental conditions are the brightness and the capability of ER/SR membrane anchoring.

Binding FKBP to RyR1 (254) is the pre requisite for CatFKBP targeting to the ER. Thus, it was not surprised that CatFKBP was fail to form a reticular network in C2C12 myoblasts lacking the RyR1 expression and it could form the prinuclear pattern after permeabilization of plasma membrane in differentiated myotubule (Figure 6.5B). The calcium imaging for CatFKBP demonstrated that this construct could be used in differentiated C2C12 cells after the plasma membrane was permeabilized. However, the endogenous FKBP occupies the RyR1 so that the binding of CatFKBP decreases. As a result, the cell line stably expressing CatFKBP and with knocked down FKBP would be favored in the future study. From the case of CatFKBP, it is notable that overexpression of any endogenous protein would cause interference of normal signaling pathways.

To avoid that, only transmembrane domains with no channel activity were considered in this study. To minimize the interaction between CatchER and the targeting domain, the peptide length was limited as short as possible. Hence, a single transmembrane domain was first taken into account. The 23 amino acid-long Z5 failed to target the fusion protein to the membrane in either C2C12 myoblasts or the differentiated C2C12 cells. Compared to Z5, the longer sequence eZ5 appeared a much better ER targeting in the C2C12 myoblast. The result is in agreement with the previous report indicating the eZ5 sequence alone is sufficient for ER targeting of RyR1 in COS cells (250). However, the eZ5 of 47 amino acids was not successful in the differentiated one either. Besides that, the fusion with the transmembrane domains also traded in the brightness. Among the current four RyR1 transmembrane fragment fused CatchER, CatLeZ5 was more promising because it takes the advantage of good targeting in the differentiated C2C12 cells and relatively good brightness.

The comparison of all constructs with CatchER was shown in Table 6.1. The brightness was normalized to Z10Cat (100%). At the same experimental condition, the intensity of CatchER was out of the detection range and appeared saturated so the quantitative comparison between ER membrane tagged-CatchER with ER-lumen tagged CatchER was not available.

Table 6.1 Data summary of CatchER with different tags in calcium imaging

Tagged CatchER	C2C12 myoblast					Differentiated C2C12 cells				
	4-cmc %	Time-to peak(sec)	k_{off} (s^{-1})	Digitonin %	Brightness %	4-cmc %	Time-to-peak (sec)	k_{off} (s^{-1})	Digitonin %	Brightness %
CatchER	30	60	0.022	10	Saturated[a]	NA	NA	NA	NA	NA
Cat-cyt	10	60	0.034	100	Saturated[a]	NA	NA	NA	NA	NA
Cat-FKBP	25	75	0.050	90	>150 [b]	8	15	0.024	50	40
CatZ5	20	90	0.034	40	39	5	110	0.014	40	44
CateZ5	0	0	NA	0	20	0	0	NA	60	53
Cat-LeZ5	7	70	0.024	50	55	10	40	0.032	10	95
Z10Cat	4	80	0.035	10	100	6	120	0.044	30	112

[a] The intensity reached the maximum of the detection range at the same setting as the tagged CatchER.

[b] The exposure time for CatFKBP was shorter than the other tagged CatchER, 0.13 sec and 0.20 sec, respectively.

The plasma membrane of cells used for immunostaining was permeablized before fixation with formaldehyde. The free tagged CatchER was washed away and only the ER membrane targeted CatchER or luminal CatchER will be detected. The fine reticular network was observed for all RyR1 fragments fused CatchER by the confocal microscope. Figure 6.2 showed the comparison of CatchER with and without triton X-100 treatment, suggesting that the antibody was not able to access the ER with digitonin only. It showed conclusively that fusion with the single or combination of RyR1 transmembrane domains can maintain proteins in the ER membrane and localize them in the cytosolic side. However, the colocalization analysis for the calnexin and CatchER with and without these targeting sequences showed no difference, with a Person's coefficient around 0.8, indicating that confocal imaging is not able to distinguish whether the protein is in the lumen or in the other side. In order to do so, the Western-blot could be applied to the trypsin digested extracted ER fraction according to the protocol established by MacLennan's group (255).

The presence of luminal CatchER was confirmed by the calcium imaging experiments, based on the fact that the RyR1 activators (4-cmc and caffeine) that induced calcium release from ER resulted in the fluorescence decrease (Table 6.1). In the Cat-cyt transfected C2C12 cells, the CatchER without any tag, there was also a 10% fluorescence decrease caused by 4-cmc addition, implying that the incompletely matured protein in the ER may sense the calcium concentration change there. Therefore, we propose that detection of the calcium release from ER/SR was attributed to the luminal CatchER that not been transported to the final location as the most likely explanation. Utilization of the stable cell line may solve the problem.

The brightness was sacrificed when any sequence was fused. CatZ5 and CateZ5 suffer the problem of low basal intensity, which was estimated only 10% of CatchER. With a low starting intensity, the It is promising to use the linker to improve the brightness. Compared with CateZ10 and Z10Cat, the Kozak consensus sequence did help for expression and it will be added to other constructs.

6.4 Summary and conclusions

To measure the spatial-temporal calcium change in the cleft between the SR cisternae and transverse tubule in the skeletal muscle, a series of targeting sequences was designed to anchor the calcium indicator to SR membrane. To avoid the interference of over-expressed intrinsic SR membrane proteins, fragments of RyR1 membrane domains were selected to be candidates. In this chapter, four RyR1 transmembrane fragments plus FKBP were fused to CatchER. The cellular protein localization was observed by immuno-fluorescence staining and the result showed

CatchER was successfully anchored in the ER membrane in C2C12 cells. The performance of calcium sensing evaluated by calcium imaging suggested CatchER was present in both ER lumen and cytosol. This work will be continued by screening more ER transmembrane domains as well as the fragments of DHPR which locates in the plasma membrane of skeletal muscle and physically couples RyR1.

7 THE DYNAMIC STUDY OF THE COMPLEX OF CALMODULIN AND PEPTIDES

7.1 Introduction

Calmodulin (CaM) is a ubiquitous calcium binding protein that serves as a signal transducer to regulate a variety of intracellular calcium-dependent signaling. Calcium binding induced large global change of CaM enables it to bind a diversity of target proteins such as kinase and ion channels for the downstream activities (256). The activation of those target proteins by CaM binding is determined by the mode of CaM-target interaction, which is also affected by the calcium concentration change in cytoplasm (257). CaM has four calcium binding EF-hand motifs, two in each terminal lobe. The calcium binding affinity is not equivalent for the four binding sites (258, 259). In addition, association with the target peptide could change the calcium binding affinity (260).

CaM adopts different conformations to interact with its target proteins of which the interface usually forms a helical structure. The hydrophobic interaction is the major driving force for association between CaM and the peptide. According to the arrangement of two lobes of CaM, the CaM conformation was classified as collapsed, full extended, and dimerized, although it was reported some peptide binding only half of CaM (PDB ID: 1CFF) (261). Based on the positions of the hydrophobic residues in the peptide, the CaM binding mode was simply classified as 1-10, 1-14, 1-16 and IQ-motif by Yap (123) (Figure 7.1). The CaM binding mode forms the structural basis for the functional regulation and helps to understand the unknown CaM regulation mechanism.

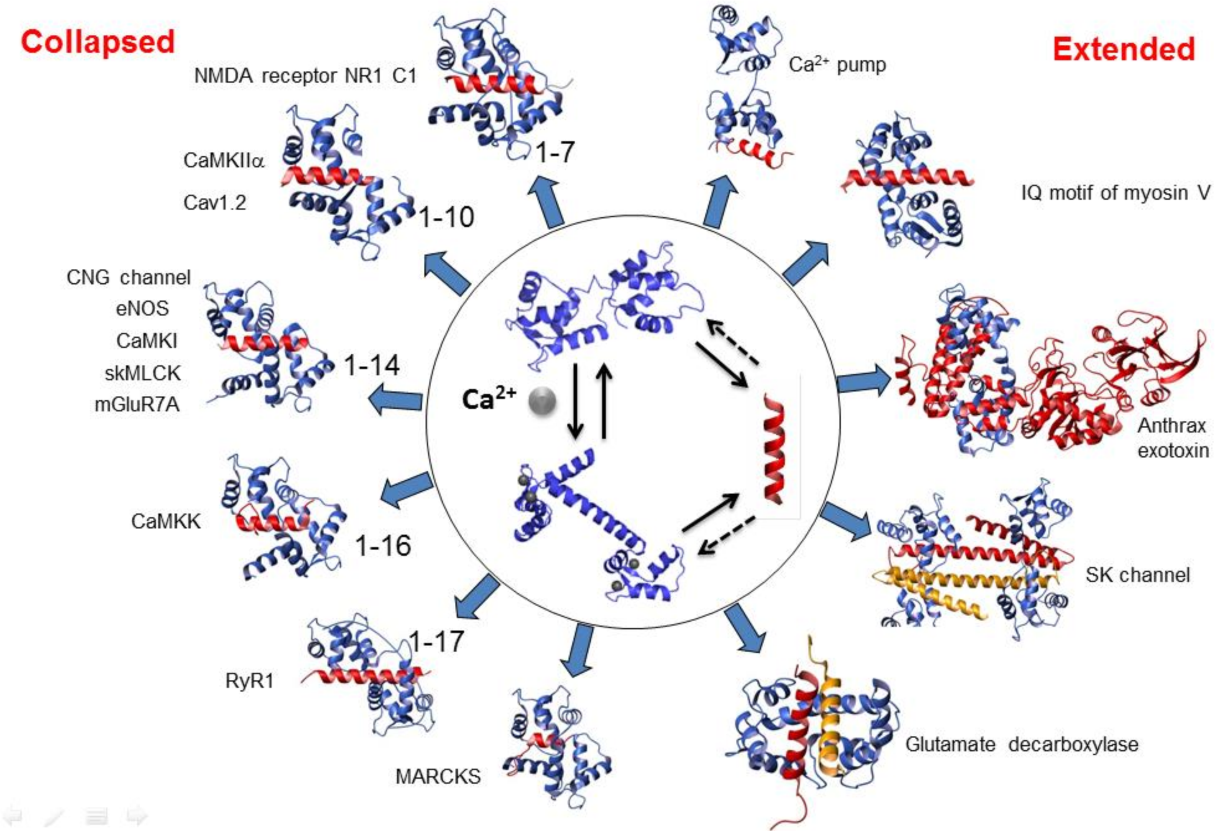

Figure 7.1. The binding modes of CaM and peptide complex.
The red color indicates the peptide. The figure was provided by Dr. Hing Wong.

The classic 1-10 and 1-14 modes is featured as the antiparallel orientation of CaM and the peptide, where the N terminal of CaM associates with the 10th or 14th residue of the peptide and the CaM C-terminal is in contact with the first one of the peptide by the hydrophobic interaction. The antiparallel contact was determined by the electrostatic interaction because the C-terminal of CaM was more acidic than N-terminal (262). For example, the Ca^{2+}/Calmodulin dependent kinase I (CaMKI) and CaM follows the 1-14 binding mode in which the basic N-terminal of CaMKI is associated with the acidic C-terminal of CaM.

The IQ motif has the pattern (FILV)Qxxx(RK)Gxxx(RK)xx(FILVWY), forming α helix (123), which can form complex with either apo or holo CaM. The conerved glutamine associates with CaM with hydrogen bond and the hydrophobic residues in the N and C terminal of IQ motif contact with both N and C terminus of CaM in either parallel or antiparallel orientation, respectively. The conserved basic residues electrostatically interact with the acidic residues of CaM. The conformation of CaM was usually extended when it binds the IQ motif; however, the conformational change of the IQ motif could occur after CaM is occupied by calcium ions (263).

The different orientations of the terminal lobes of CaM and the relative angle enables the NMR residual dipolar coupling (RDC) a good approach to understand how CaM accommodates the target peptide since RDC data provides the long-range structural constrains which makes the calculation and refinement of structure convenient based on the model structure.

7.2 Results and discussion

7.2.1 *The binding mode of CaM and N-terminal intracellular loop of connexin 43*

Gap junction plays role in cell communication, and is important for cell growth, differentiation and development (264). The function of gap junction is regulated by pH, membrane voltage and Ca^{2+}/CaM. Gap junction is composed with 12 closely packed unit called connexin. Each connexin has four transmembrane domains. Six connexin units form a connexon and two connexons in two adjacent cells dock together, forming a gap junction channel. Connexin 43 (Cx43) is a gap junction protein, belonging to the alpha family, mainly expressing in heart and fetal cochlea (265). Lurtz and co-workers reported that CaM and Ca^{2+} regulated the gap junction channel (266). However, there is no structural evidence showing the interaction between CaM and Cx43. By using the calmodulin target database (http://calcium.uhnres.utoronto.ca/ctdb/ctdb/) (IFVSVPTLLYLAHVFYVMRKEEKLN), four predicted CaM binding sites were obtain (Figure 7.2), where there are two in both N and C-terminal loop and the other two are in the intracellular loop.

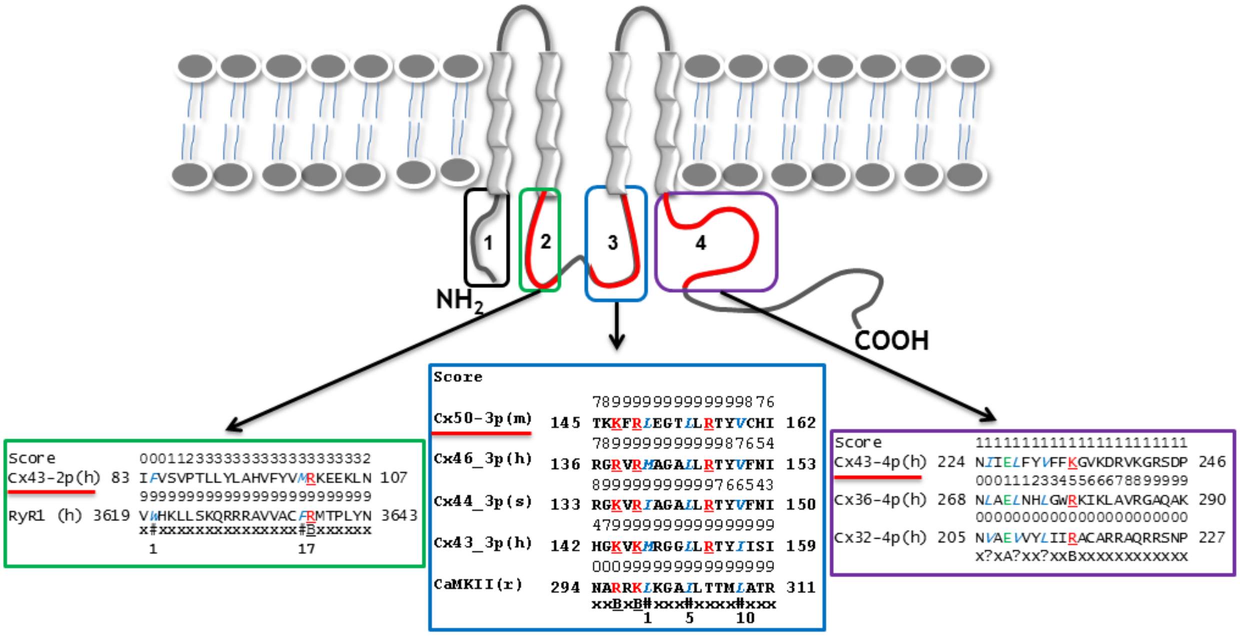

Figure 7.2. The cartoon of connexin 43 topology and predicted CaM binding sites.
The four CaM binding sties are indicated with rectangular frames. The sequences of sites 2-4 were shown and compared with other CaM targets. The figure was provided by Dr. Yanyi Chen.

To understand the binding mode of the complex between CaM and the N-terminal intra-cellular loop of connexin 43 (Cx43np), the NMR residual dipolar coupling (RDC) approach was applied. The assignment of the CaM-Cx43np complex was achieved by monitoring the change in chemical shift during Cx43np peptide titration (Figure 7.3). The anisotropic component was obtained by adding the phage and no change in the NMR spectra were observed. The assignment was done for 90/148 residues. The RDC fitting was carried out for 12 structures of CaM-peptide complex and Ca^{2+}-CaM, as well as the half CaM of each complex, by the software REDCAT developed by Dr. James Prestegard (267). The results are shown in Table 7.1. The good fitting was indicated by the small value of the Q factor. The CaM-Cx43np complex showed the best fit for the complex of CaM and the gating domain of the calcium activated potassium channel (SK) 413-489 (1G4Y). The N (1-65) and C (93-148) terminal domains fitted best with CaM-chicken smooth muscle myosin light chain kinase (1CDL) and CaM-RyR1-3614-3643 (2BCX), respectively. Since the RDCs of the two domains of CaM in the CaM-Cx43np complex cannot be fit simultaneously to the same crystal structure, the Cx43np accommodated in CaM in a way different from any kind of existing binding mode.

The binding mode of CaM-SKp413-489 (1G4Y) was extended, and the complex was formed by 2 CaM and 2 peptides in the crystal structure, where calcium only occupied N-domain of CaM. There was a helix-turn-helix motif in the N-terminal of the peptide, which was in contact with C-domain of CaM, while the C-terminal of the peptide inserted in the holo-N-domain and the bent central helix of the other CaM (268).

The crystal structure of CaM-smMLCK (1CDL) demonstrated that the peptide spacing was in the classic 1-14 binding mode (269). The peptide Trp5 interacted with the C domain of CaM (Leu105, Met124, Glu127, Ala128 and Met144), and Leu18 were in contact with the N domain of CaM (Leu32, Met51, Val55 and Met 71). CaM binds the peptide Ryanodine receptor 1 3614-3643 in a flexible 1-17 binding mode (270). It was reported that in 1-17 peptide spacing pattern the two domains of CaM were more flexible and the domain motion was more independent compared to 1-10 and 1-14 peptide anchoring mode. The hydrophobic residue Trp3620 in the N-terminal of the peptide was in contact with the hydrophobic cavity which was formed by Phe92, Leu105, Met124, Met 144 and Met145 in the C-domain of CaM. Similar to the interaction between C-terminal of peptide and N-CaM in 1-14 binding mode, the C-terminal Phe3636 was inserted into the hydrophobic pocket formed by Leu32, Met51, Val55, Ile63 and Met71 of CaM.

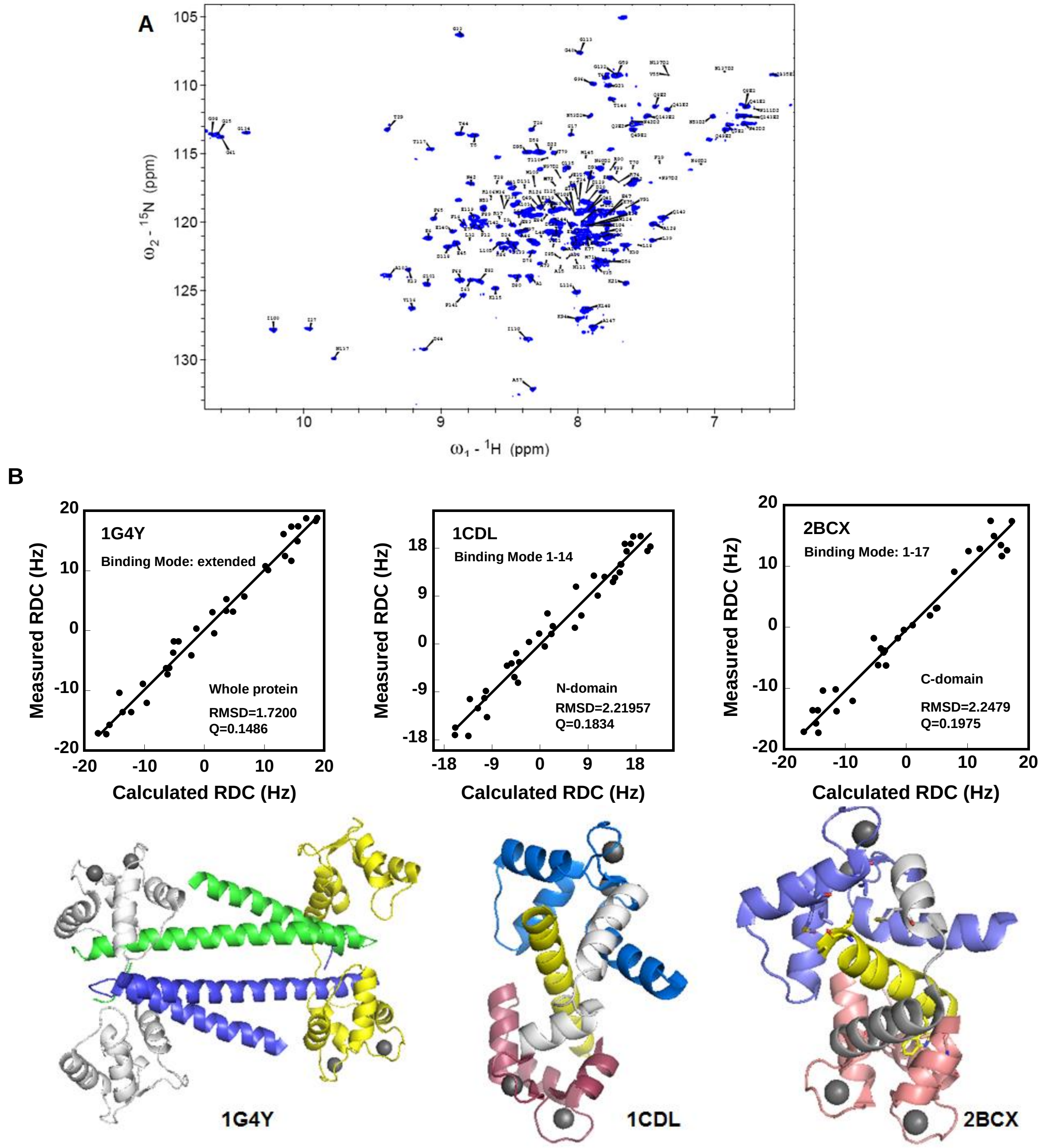

Figure 7.3. The ^{15}N-HSQC of holo-CaM interacted with the peptide Cx43np.

The peptide was commercially synthesized. The final concentrations for CaM and the peptide were 0.8 mM and 1.6 mM, respectively. Samples were prepared in Bis-tris, pH 6.5, 100 mM KCl, 10% D_2O. At this ratio, CaM was not saturated by the peptide since minor peaks were observed in the spectra. The experiment was run using Varian 800 MHz NMR spectrometer at 37 ℃. (A) The spectrum assignment of the isotropic and anisotropic complex of CaM-Cx43np. (B) RDC fitting revealed the good fit of CaM-Cx43np complex, N and C domains to 1G4Y, 1CDL and 2BCX, and the number of residues in fitting were 33, 38 and 31 over 90 assigned residues, respectively. (C) The crystal structures of 1G4Y, 1CDL and 2BCX. Yellow color in 1CDL and 2BCX indicates the peptide; pink color indicates the C-domain and blue color indicates the N-domain.

Table 7.1 The RDC fitting of CaM-Cx43np to different CaM-peptide complex

PDB ID	Target protein	Binding Mode	N-domain		C-domain		Whole complex	
			Q	RMSD	Q	RMSD	Q	RMSD
1CDM	peptide calmodulin-dependent protein kinase ii	1-10	0.18	2.28	0.15	1.69	0.18	2.11
1CDL	peptide calmodulin-dependent protein kinase ii alpha chain	1-14	0.12	1.55	0.25	2.25	0.18	2.22
1CFF	Ca^{2+} pump	C-CaM	0.16	1.73	0.24	2.10	0.26	2.55
1G4Y	Gating domain of K^+ channel	Extended	0.15	1.85	0.18	1.79	0.15	1.72
1IQ5	Ca^{2+}/calmodulin dependent kinase kinase	1-16	0.15	1.87	0.18	2.04	0.18	2.04
1K93	Adenylate cyclase domain of anthrax edema factor	Extended	0.18	2.08	0.17	2.06	0.21	1.81
1NIW	Endothelial nitric-oxide synthase	1-14	0.17	2.16	0.20	2.12	0.17	2.07
1NWD	Plant glutamate decarboxylase	Collapsed	0.12	1.51	0.32	2.22	0.24	2.64
1SY9	Cyclic-nucleotide-gated olfactory channel	1-14	0.18	2.29	0.22	2.25	0.17	2.03
2BCX	Ryanodine receptor I	1-17	0.15	1.89	0.13	1.50	0.20	2.25
2HQW	Glutamate NMDA receptor subunit zeta 1	1-7	0.15	1.84	0.20	1.91	0.18	2.08
2IX7	Myosin 5A	Extended	0.22	2.46	0.26	2.02	0.24	2.24
3CLN	Calcium-bound CaM	Ca^{2+}-CaM	0.13	1.59	0.15	1.70	0.25	2.05

The common feature of 1CDL and 2BCX is that in both complexes CaM adapts a collapsed conformation, where the α-helical central linker between the N and C domains is partially bent which enables the two domains to wrap the targeted peptide. In contrast, the conformation of CaM in 1G4Y was extended and dimerized, where the central helix was flexible and the N domain was occupied by calcium leaving the apo C domain alone. Indeed, the 1-17 binding mode was similar to 1-14 spacing pattern and the bending angle of the linker is the only difference. The Q factors of RDC fitting for the full length of 1CDL, 2BCX and 1G4Y were 0.18, 0.20 and 0.15, respectively. The number of residues in the final RDC fitting with 1G4Y was only 33, and the similar amount of residues was used in fitting for the half domains. Considering the residue number for fitting and the overall Q factor, it was assumed that both N and C domain of CaM are interacting with the Cx43np peptide via van der Waals force and CaM prefers a more extended conformation than the classic collapsed ones (1-10, 1-14, 1-16 and 1-17).

7.2.2 *The dynamics study by T1, T2 and NOE for the complex of CaM-Cx43np*

Molecule dynamic study for peptide bound holo-CaM was carried out using Varian 600 MHz spectrometer. T1, T2, NOE and Tau-C data were collected for further analysis. The assignment was done for 76/148 residues by monitoring the cross peaks during peptide titration (Figure 7.1). The relaxation delay time for 10 experiments was set as 0, 0.01, 0.06, 0.13, 0.23, 0.34, 0.48, 0.74, 1.0 and 1.5 s for the T1 relaxation, and T2 was determined by performing seven experiments with the delays as 0.01, 0.03, 0.05, 0.07, 0.11, 0.13 and 0.15 s. For NOE experiment, the proton recovery period before data acquisition was 4.0 s. The relaxation R1 and R2 were obtained by monoexponential fitting, and the NOE was calculated by the intensity ratio with and without the saturation of proton magnetization.

The global rotational correlation time was 6.2 ns, calculated using the average R2/R1 ratio, and they were 6.0 and 5.9 ns for the N and C domains of CaM, respectively. The domain motion at both terminals was consistent. The greater R2/R1 value for residues D80 and S81 than the average value indicated that this region underwent the conformational exchange, which was in the middle of the central linker. The relatively smaller NOE ratio of D80 also suggested it was flexible, in good agreement with the R2/R1. Figure 7.4 only shows the S2 which had the good fit to the template, demonstrating the flexible regions at the C domain of CaM, consistent with the

NOE data. The same region was found to be flexible as well in the complex 2BCX but no conformational exchange expected by R2/R1.

The C-domain K115 and L116 were relatively flexible than neighboring residues as shown in the heteronuclear NOE. This flexible region lied in the loop connecting the EF-hand III and EF-hand IV. The same flexible loop was observed in the C-domain of the complex 2BCX, where the adjacent residue E114 caused the electrostatic interaction with K3626 of the RyR1 peptide.

Taken the dynamic and RDC data into consideration, it was concluded that both N and C domains of CaM associated together to bind the peptide Cx43np. The contact between the peptide and the two domains was similar as 1-14 binding mode. The central linker around D80 was flexible and the conformational exchange was expected. Such conformational exchange might unwind the central helix and induce the bending, which in turn could affect the interaction between the peptide and CaM.

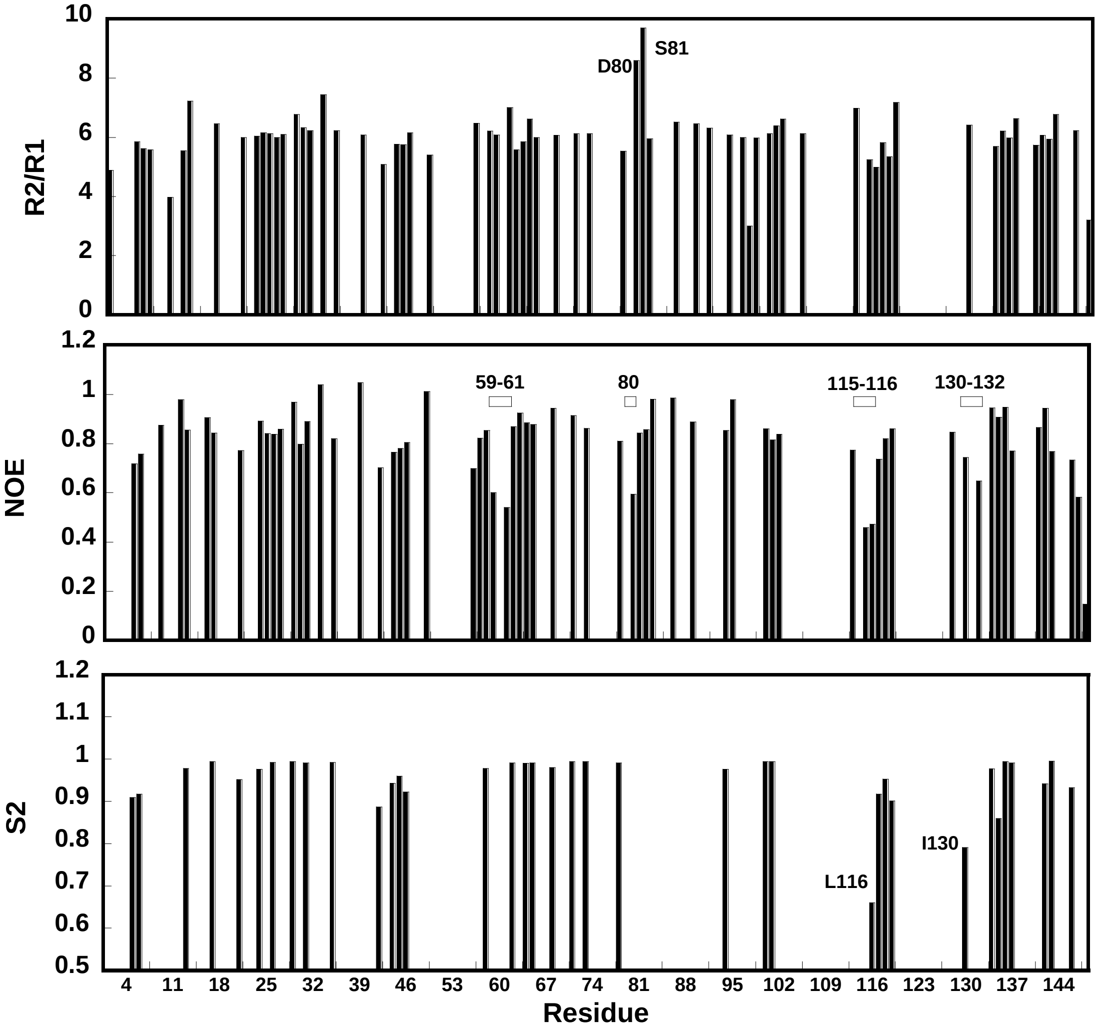

Figure 7.4. The dynamics analysis of CaM-Cx43np complex by T1, T2 and NOE.

7.2.3 *Calmodulin interacting with ryanodine receptor fragment 1977-1998*

Ryanodine receptor (RyR) is the ER membrane protein regulating the Ca^{2+} release from the ER. Low intracellular Ca^{2+} activates the RyR while high concentration inhibits its function. The bell-shape like channel activation by intracellular Ca^{2+} can be altered by CaM. Previously, Dr. Jie Jiang in Yang's group showed that the RyR channel opening was modulated by calmodulin and Ca^{2+} (271). Studies of the interaction between CaM and RyR have been taken for decades

(272-275). However, the size of RyR (565 kDa for a monomer) makes the big challenge for the structural analysis.

In this chapter, the RDC experiment will be applied to investigate the binding mode of apo-CaM-RyR1p1975-1999. Before conducting the experiment, a few HSQC spectra were collected to exam the quality of the sample. Figure 7.5 showed the ^{1}H-^{15}N HSQC spectra of the complex of CaM-RyRp1977-1998. Compared to the apo-CaM spectrum in blue, the one in the presence of RyR1p1975-1998 in red showed the substantial chemical shift perturbation (Figure 7.5A). It was clear that the sample of this batch contained some contamination in that the spectrum of apo-CaM in the presence of RyR1p1975-1999 colored in green did not overlap with this collected one (Figure 7.5B). Calcium was the first potential substance to contaminate the sample since CaM has very high the calcium binding affinity. Thus, the holo-CaM ^{1}H-^{15}N HSQC spectra was used as reference. Figure 7.5C shows the spectrum overlapping with that of the holo-CaM.

There were four residues in the downfield of f2 (^{1}H), G25, G61, G98 and G134, far apart from others, which avoided the problem of peak overlapping. In the apo-CaM, only the glycine residues in the N domain G25 and G61 showed up, while four of them could be detected in the holo-CaM. The absence of the two glycines in the C-domain without calcium rise from the flexible and less ordered structure of apo-C-CaM. When N-domain was bound by calcium, the chemical shift change occurred in G25 and G61. In the spectrum of this specific sample, four glycines can be detected and the chemical shift of glycines in the N-domain was consistent with those in the apo-CaM. The comparison of four signature cross peaks of glycines implied that C-domain of CaM was occupied by the trace amount of calcium. Considered the commercial peptide may contain a certain amount of calcium, 5 mM EGTA may not be sufficient to maintain a near-to-zero calcium environment. More EGTA will be added to remove the free calcium.

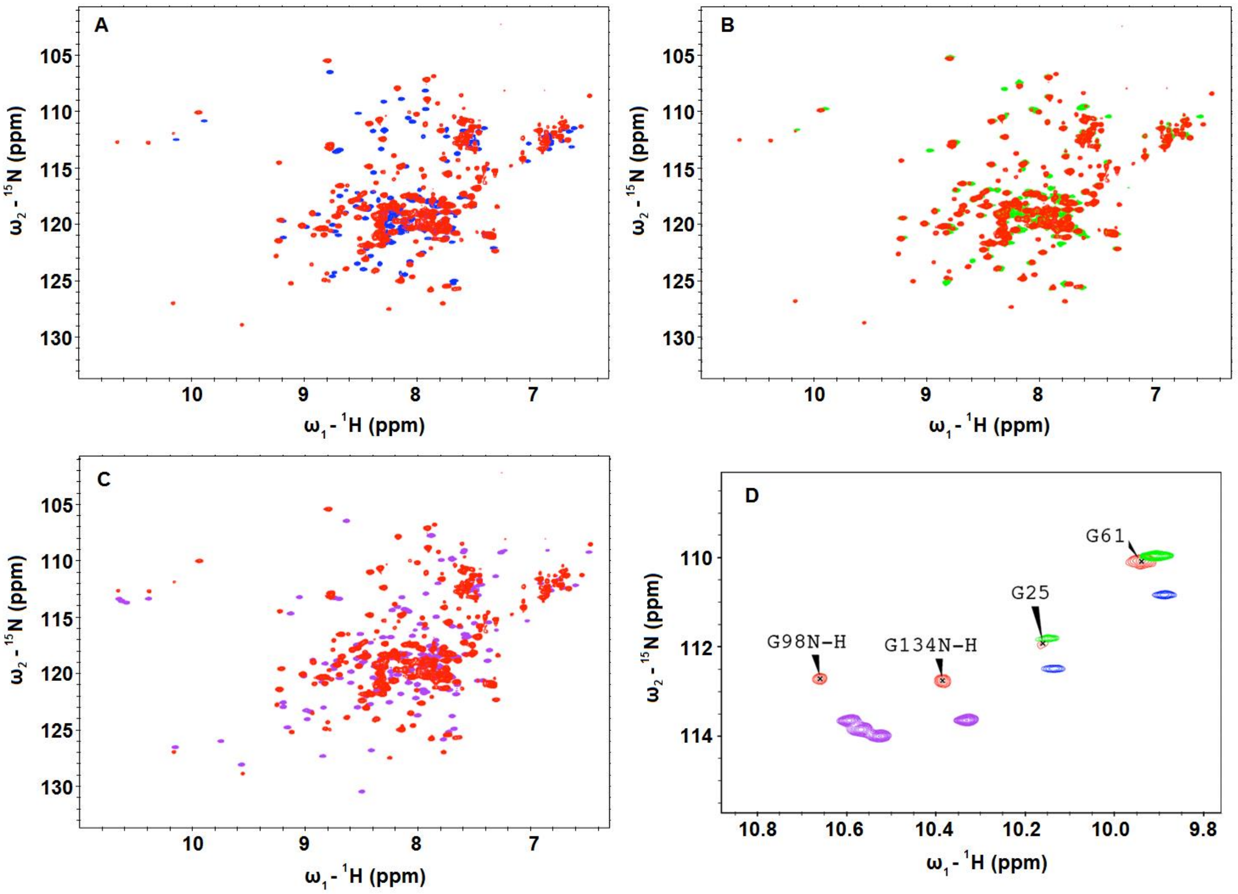

Figure 7.5. The ^{1}H-^{15}N HSQC spectra comparison of apo-CaM (Blue), holo-CaM (purple), apoCaM-pRYR1975-1999 (green) and the tested CaM-pRYR1975-1999 (Red).
Samples were prepared in 10 mM Bis-tris, pH 6.5, 100 mM KCl, 10% D$_2$O. All spectra were collected using 600 MHz Varian at 25°C. (A) The superimposed spectra of the apo-CaM and the tested sample. (B) The superimposed spectra of the previous apo-CaM-pRyR1975-1999 complex and the tested sample. (C) The superimposed spectra of holo-CaM and the tested sample. (D)The zoom-in spectra were manually shifted in D to conveniently observe the difference.

7.3 Summary and conclusions

The interaction between calmodulin (CaM) and its target peptides (1) the N-terminal intracellular loop of connexin 43 (Cx43np) and (2) the peptide 1977-1998 of RyR1 was studied by NMR. The residual dipolar coupling and dynamics analysis illustrated that both terminal domains of CaM wrapped around Cx43np simultaneously, along with bending and unwinding the central helix. The anchoring pattern is close to 1-14 and 1-17 mode but the central helix is more extended.

The analysis of the complex CaM-RyR1977-1998 provided a good example that using the signature Glycine residues (G25, G61, G98 and G134) to judge the Ca^{2+} occupancy in N and C terminus. In the presence of the trace amount of Ca^{2+}, the C-domain of CaM in the complex is first loaded with Ca^{2+}. This work will be continued to find out the binding mode of apo-CaM with the peptide RyR1977-1998.

8 NMR OF DIMETHYLATED LYSINE IN CALMODULIN AND CALCSIUM-SENSING RECEPTOR (CASR)

8.1 Conformational change of calcium sensing receptor extracellular domain (CaSR-ECD) induced by calcium and ligand binding

8.1.1 *Using methyl group as a probe to study the ligand-protein interaction*

The challenge to study the structure and conformation of macromolecules, especially the membrane protein, rises from the molecular size and the solubility. Application of NMR for the large molecules was limited by its size due to the broadened line width caused by the short T2 relaxation time and slow tumbling rate. Thanks to the selective labeling approach, the high-molecular-weight protein can successfully be investigated by NMR. The isotropic hetero-labeling method is particular useful for obtaining structural information about large membrane proteins by NMR since it can simplify the spectrum. In addition, the methyl group can be used as a probe to investigate the protein dynamics and interactions with ligands. The resonance of methyl groups is intense due to the attached three protons and the fast tumbling rate makes the peak narrow. The HMQC experiments can be conducted to obtain the high resolution and sensitivity spectra because the magnetization transfer pathway of the methyl group and the macromolecules can be isolated due to their different relaxation rates (276-278).

The Lys side chain can be methylated by formaldehyde and the methyl signal is easily detected by using ^{1}H-^{13}C HMQC. This methodology was pre-tested using CaM as a model (Appendix D) since CaM has 8 Lys residues and the assignment was done by Zhang and co-workers (279). The selectively labeling of the methyl group was also applied to the hydrophobic residues including isoleucine, leucine, valine, alanine and methionine (280, 281). Those residues are usually buried in the interior of the hydrophobic core of proteins.

Calcium sensing receptor (CaSR) belongs to the family C G-protein coupled receptor (GPCR). It mainly expresses in the parathyroid gland, regulating the secretion of parathyroid hormone (PTH) (282). PTH is essential to maintain the calcium homeostasis in human body. Extracellular calcium concentration change can through CaSR induce intracellular calcium oscillation which encodes the signaling for the downstream cellular events (283). The L-amino acids have been reported to enhance the EC_{50} of extracellular Ca^{2+} (284). However, no direct evidence shows the Ca^{2+} or the L-amino acids bind CaSR extracellular domain (CaSR-ECD). In this chapter, the structural analysis for the interaction between CaSR and Ca^{2+} as well as L-Phe and glutathione (GSH) was carried out. There are 41 Leu, 30 Phe, 4 Met and 25 Lys distributed in CaSR-ECD. In this dissertation, ^{15}N Phe-labeled expressed mammalian CaSR-ECD was first expressed and the [^{13}C-dimethylated-Lys]-CaSR-ECD was also used to determine the calcium and amino acids induced conformational change.

The calcium-sensing receptor ECD with His-tag was expressed by HEK cells in Dr. Kelley Mormene’s lab in UGA (285-289). To further overcome the inhomogeneous glycan in wild type CaSR-ECD, Dr. Moremen uses his developed novel Lec1 mutant HEK 293 cell line to express CaSR-ECD with only mannose on the protein surface instead of the native complex glycan. The experimental condition and parameters were optimized to obtain the desired yield.

The dimethylation of lysine was done by reacting with formaldehyde under the reduced condition at 4 ℃ for 16 h. The reaction condition was optimized to allow the complete dimethylation. The formaldehyde was added twice together with Dimethylaminoborane (DMAB, purchased from Sigma-Aldrich) for reductive methylation. For each time, the mole ratio of formaldehyde and lys was 3:1 and the ratio of DMAB to formaldehyde was 3:1. The time interval of two additions was 3 hours. The mono-methylated peak can be easily differentiated because the chemical shift is in the range of 30-35 ppm while the dimethylated lysine has peaks in the range of 42-48 ppm. ^{1}H-^{13}C HMQC was applied in 600, 800 and 900 MHz VARIAN NMR spectrometers. The spectral width of C13 channel is 3000 Hz, 16 scans were applied and 64 for each scan increment. The decoupling power for C13 was 38 and the acquisition time was 0.2 sec. The water signal was suppressed by PRESAT pulse sequence provided by VNMRJ.

These expressed proteins were shown to be native as judged by their conformations and functional ligand binding. The mammalian expressed ECD forms a dimer with a molecular weight of 200 kDa in the non-reducing SDS-PAGE gel and determined by PFG-NMR (290, 291). Glutathione is the analog of Phe to bind CaSR-ECD and the binding affinity is stronger than Phe so that GSH is added to CaSR to study the ligand induced additional conformational change in the presence of calcium. Conformational changes can be monitored by 2D NMR using the ^{15}N- or ^{13}C-labeled ECD domain (292). Figure 8.1 shows the HSQC spectrum of the selectively labeled ^{15}N-Phe in CaSR-ECD. The chemical shift change of these labeled Phe residues upon addition of calcium was observed, although the 30 Phe peaks are not dispersed as expected. Four regions were cut for detailed analysis as indicated in Figure 8.1 A, and the chemical shift change as well as the peak line width difference was dramatic as shown in Figure 8.1 B. In the region 1, increased calcium concentration brought the two peaks closer and closer, which moved apart from each other upon the final added GSH. To avoid the interference from the complicated glycosylation, Lec 1 HEK cell mutant was applied for expression of CaSR-ECD with the mannose-type N-linked oligosaccharides. Figure 8.1C shows the better peak dispersion of the ^{15}N-Phe CaSR expressed in Lec1 mutant in ^{1}H-^{15}N HSQC spectrum.

Further information has been obtained by specifically labeling of the side chain of lysine with ^{13}C by reductive methylation (293), since the methyl group is excellent for probing the change of Lys structure and dynamics of large proteins with high sensitivity because of its high mobility and three protons, where seven out of 25 Lys residues are near the predicted Ca^{2+}-/ligand-binding site in ECD. Unfortunately, this approach was less successful in the case of CaSR-ECD. As shown in Figure 8.2, all Lys dimethyl groups merged to form one big peak, which was also observed in another [^{13}C-dimethylated Lys]-G protein-coupled receptor rhodopsin (294). The peak (^1H: 2.4 ppm, ^{13}C: 44 ppm) of N-terminal dimethylated amino group moved upon calcium titration while the big peak stayed no changed. However, the addition of glutathione clearly induced conformational change in that there were two more peaks were detected (Figure 8.2 Ba) and the chemical shift change of the existing peaks was observed as well. The similar calcium induced conformational change can be observed by performing ^1H-^{15}N HSQC to the uniformly labeled, deuterated ^{15}N, ^{13}C-CaSR-ECD (Figure 8.3), where the peaks are well dispersed although the peak amount is much less as expected.

In conclusion, calcium induced conformational change of CaSR-ECD can be confirmed by NMR using the selectively isotropic labeled protein. The additional conformation change upon the glutathione was also observed in the presence of calcium. Additional labeling will be performed for other isotopes such as I, M, L and V in collaboration with Moremen’s group as reported(281, 295, 296). The large movements in loop and hinge regions of proteins will be studied using paramagnetic probes, such as lanthanide ions or nitroxide spin-labels. This method is particularly suitable and will allow us to obtain long-distance constraints (between 20 to 35 Å) of the ECD of the CaSR (297) by paramagnetic relaxation enhancement (PRE) as reported (298).

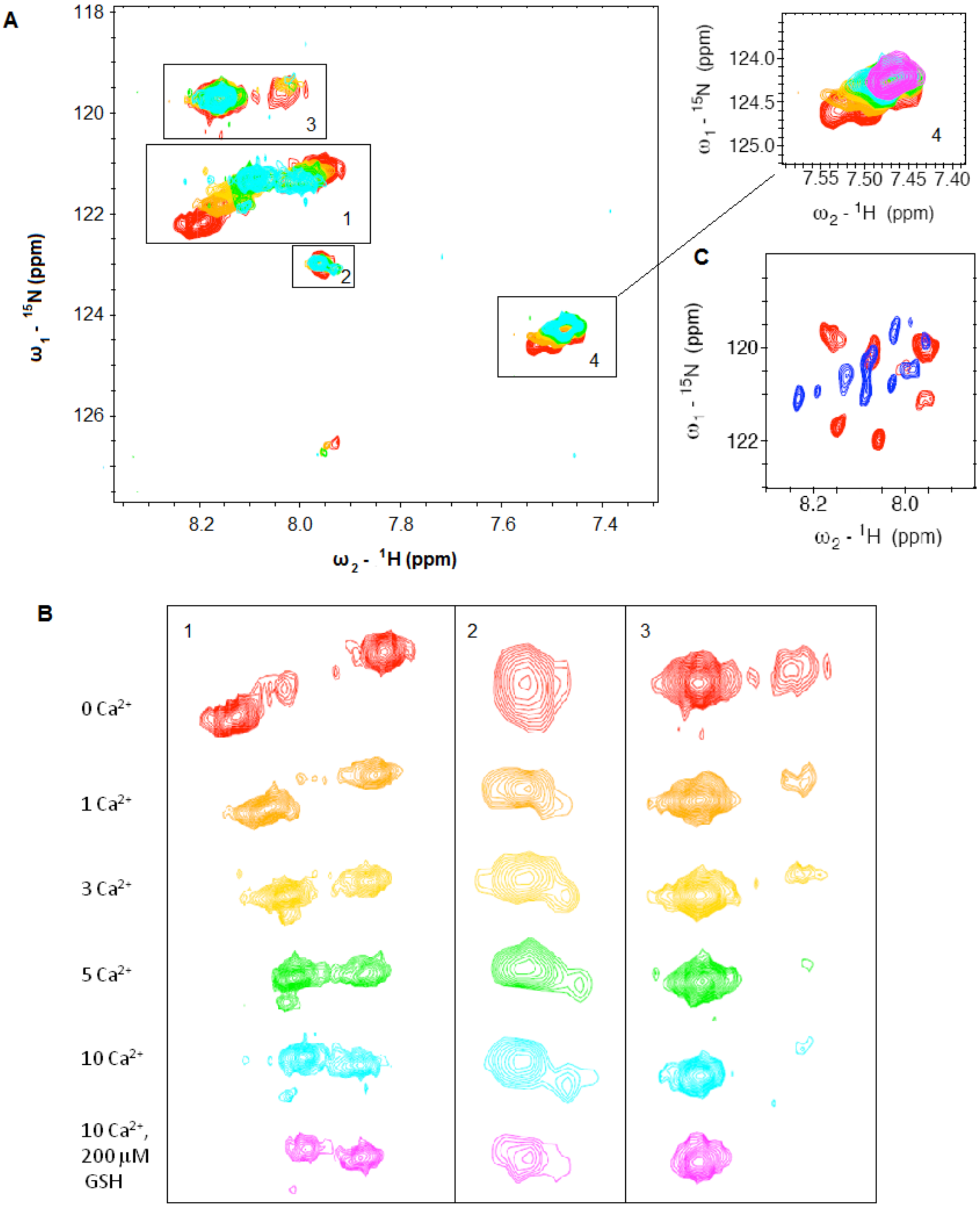

Figure 8.1. ^{1}H-^{15}N HSQC spectra of calcium titration of ^{15}N-Phe selectively labeled CaSR-ECD. The protein was expressed from HEK 293 cells and concentrated to be 150 µM in 10 mM Tris, pH 7.4, 20% D_2O. The water gate was applied in ^{1}H-^{15}N HSQC. (A) The overlaid HSQC spectra of ^{15}N-Phe labeled CaSR-ECD in different calcium concentration. calcium titration was conducted from 0 to 10 mM, and 200 µM glutathione was supplemented in the end to mimic the amino acid binding. (B) The chemical shift change upon calcium titration in different regions indicated in the panel A. (C) HSQC spectra of ^{15}N-Phe labeled by HER293 mutant Lec1 expression with chemical shift changes upon addition of Ca^{2+}. Lec1 ex-

pression without complex glycosylation sharpens resonance. The region is the area corresponding to the zone 1, 2 and 3 in the panel A.

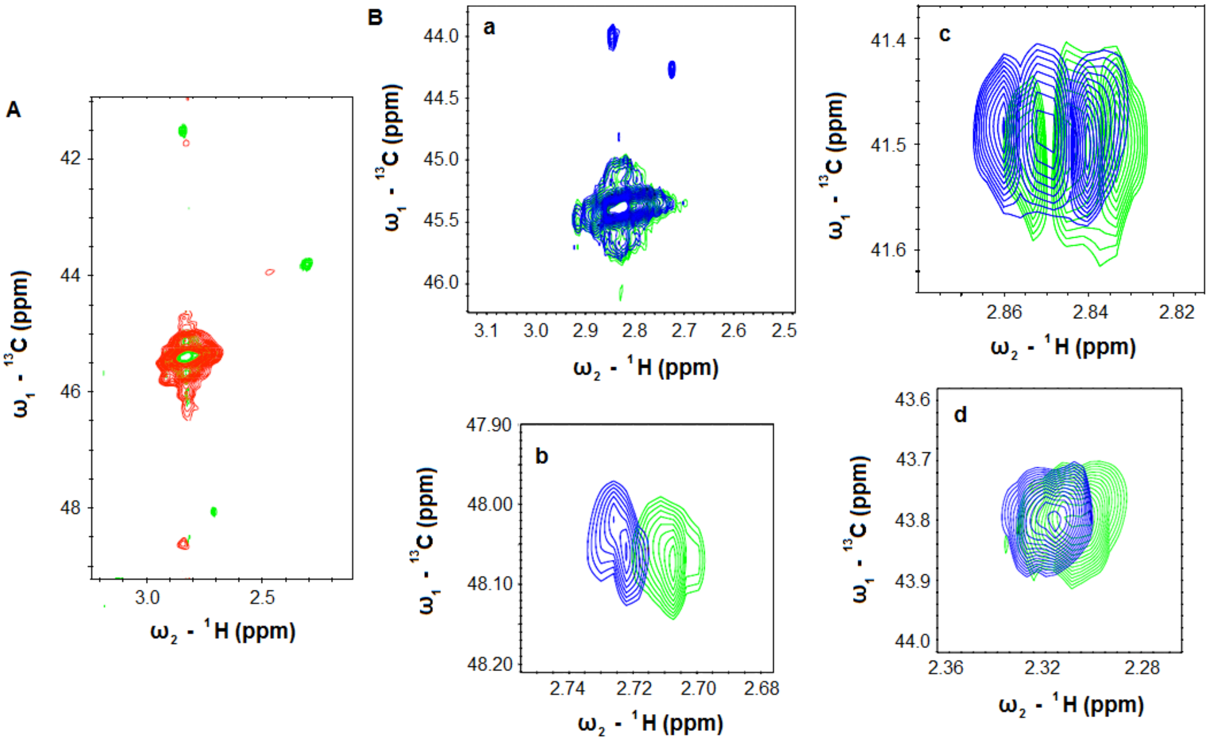

Figure 8.2. The^{1}H-^{13}C HMQC spectra of [^{13}C-dimethylated-Lys]-CaSR-ECD expressed in HEK293 cells. (A) The overlaid HMQC spectra of 50 μM protein in 10 mM Tris, pH 8.5, 20% D_2O (Red) and the one supplemented with 5 mM Ca^{2+} (Green). (B) a-d: The different regions of the overlaid HMQC spectra of CaSR-ECD in presence of 5 mM Ca^{2+} (Green) and the one supplemented with 50 μM Glutathione (Blue). Additional glutathione induced chemical shift change and two new peaks in the panel B(a).

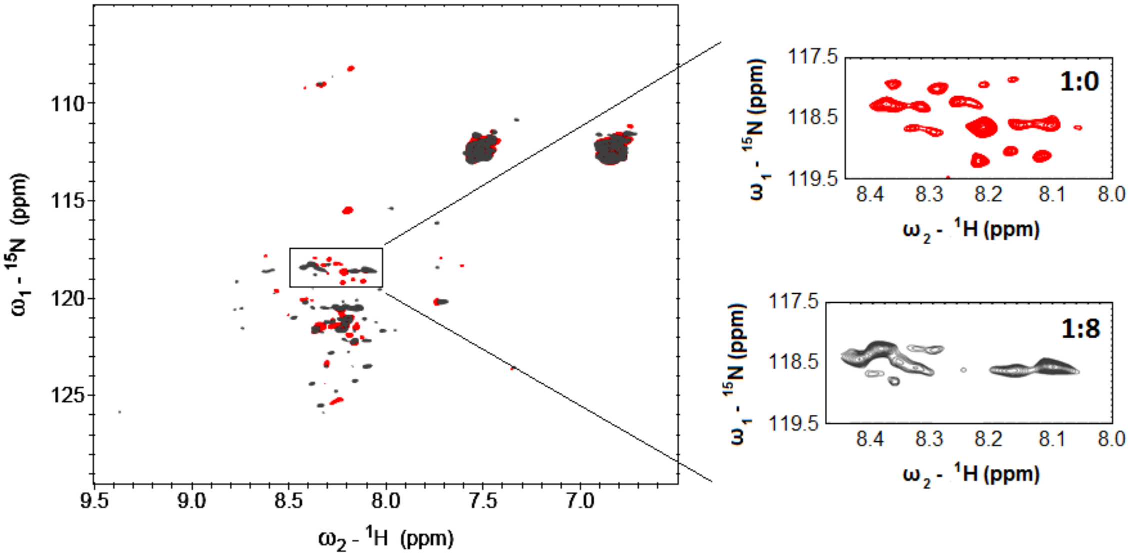

Figure 8.3. The ^{1}H-^{15}N HSQC spectrum of the bacterial expressed CaSR-ECD.
The sample was grown in D_2O and uniformly ^{15}N, ^{13}C labeled. The red spectrum is the sample of 200 µM protein in 10 mM Tris, pH 7.4, 30% D_2O. The grey spectrum is the one titrated with 1.6 mM Ca^{2+}. The dispersion of peaks were obtained and the calcium induced chemical shift change can be observed.

8.1.2 *Using STD-NMR to study the ligand binding to CaSR-ECD*

Because of the big size of dimerized CaSR-ECD, it was difficult to obtain the high-quality NMR spectra of sparse labeled protein. Alternatively, saturation transfer difference NMR (STD-NMR) could be used to verify the interaction between the ligand and protein by monitoring the signal from the ligand (L-Phe). In STD-NMR, the magnetization is transferred from the protein to the ligand, where the bound ligand is also saturated and shows the decreased intensity. The effective saturation transfer is determined by the k_{off} and the T1 relaxation rate of the protein (299). It is advantageous to identify the low affinity binding with K_d in the mM range (300). In this chapter, the 1D proton STD-NMR was conducted to demonstrate the L-Phe binding to CaSR-ECD.

The HEK 293 mutant Lec1 expressed CaSR-ECD was used in STD-NMR. The protein with the final concentration of 10 or 20 µM was prepared in 10 mM Tris, pH 7.4 in >95% D_2O.

L-Phe prepared in the same buffer solution was titrated and the spectra were collected using Varian 800 MHz NMR spectrometer at 25°C. To avoid saturation at L-Phe, the irradiation frequency was set at -1 ppm. The reference frequency was at 30 ppm. The saturation duration was 3.0 sec.

Figure 8.4 A and C showed the 1D spectra comparison between CaSR-ECD and those supplemented with ligands. The peaks arising from the ligand were identified. For Phe, there were three peaks at 7.15, 7.20 and 7.25 ppm and GSH showed peaks at 2.00, 2.35, 2.75 ppm. As shown in Figure 8.4B, the intensity difference was observed when 0.5 mM Phe was added and it was increased as adding Phe, demonstrating Phe bound to CaSR-ECD. In contrast, the intensity difference was not obvious until 2 mM GSH was added, which may be explain by the non-effective saturation transfer because of the high-affinity GSH binding (EC_{50}=2 μM). Although the increase [GSH] also led to the increased STD signal, it can not rule out the possibility of the non-specific sticking to the protein.

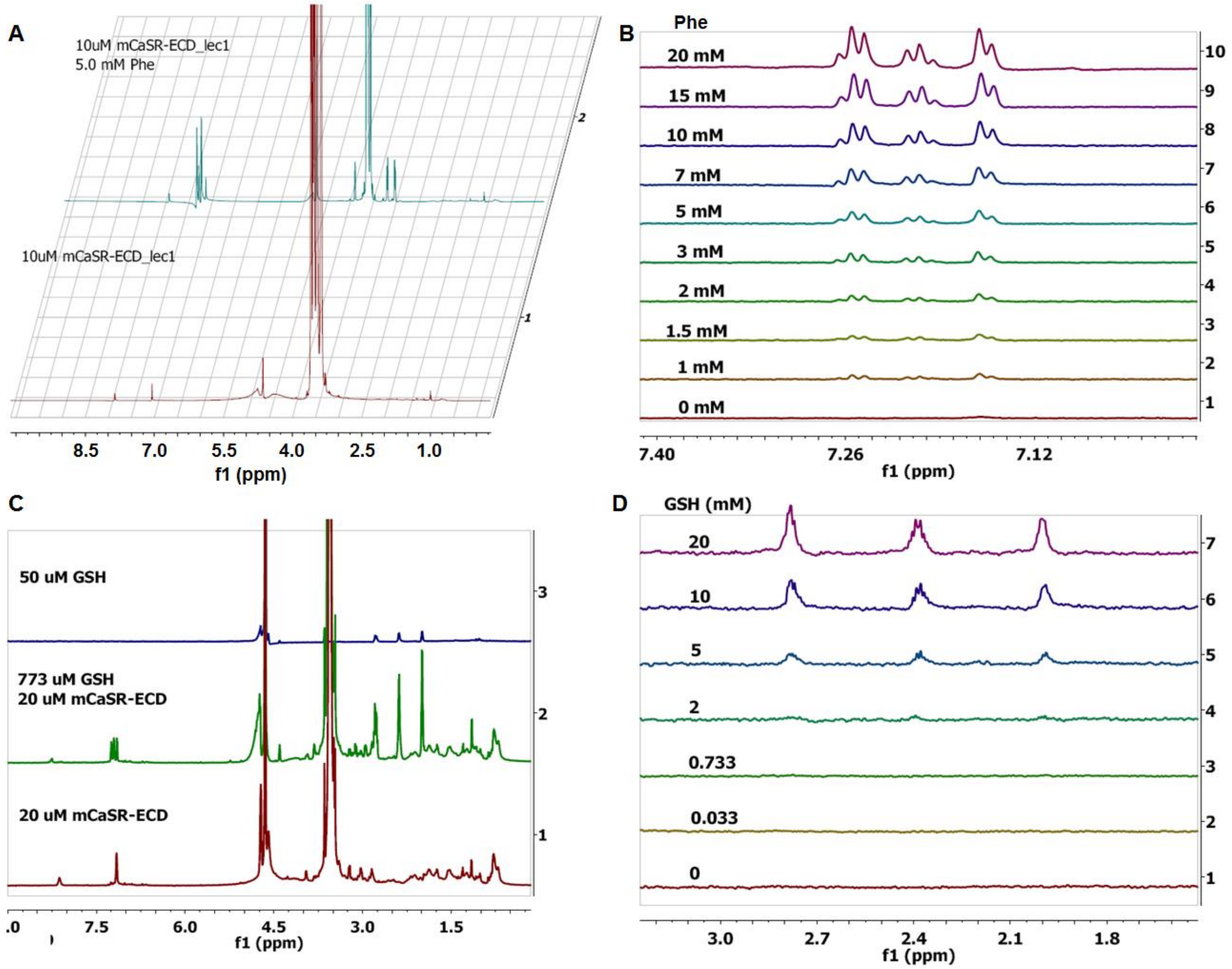

Figure 8.4. The 1D proton and STD spectra of CaSR-ECD titration with L-Phe and GSH.
The protein with the final concentration of 10 μM was prepared in 10 mM Tris, pH 7.4 in >95% D_2O. L-Phe and GSH prepared in the same buffer solution was titrated and the spectra were collected using Varian 800 MHz NMR spectrometer at 25°C. (A) The 1D spectral comparison between 10 μM CaSR-ECD and the one supplemented with 5 mM Phe. (B) The STD spectra of Phe titration to 20 μM CaSR-ECD. (C) The 1D spectral comparison among 50 μM GSH, 20 μM CaSR-ECD and 20 μM CaSR-ECD supplemented with 773 μM GSH. (D) The STD spectra of GSH titration to 20 μM CaSR-ECD.

In the presence of Ca^{2+}, the STD spectra were also observed in Phe titration and the enhancement of the intensity difference was similar as the set without Ca^{2+}. The calcium effect was shown in Figure 8.5A. For the intensity difference was reduced upon Ca^{2+} addition to Phe-CaSR-ECD complex, while it increased in GSH-CaSR-ECD. However, the direct observation of the spectra difference was not accurate because the sample was diluted by adding Ca^{2+} and it was probably somewhat lost during the titration. Thus, the calculated STD amplification factor was used to quantify the difference, which was given by Equation 8.1. The dissociation constant Kd can be obtained by plotting STD-AF versus the ligand concentration (Euqation 8.2).

$$STD-AF=\frac{I_{ref}-I_{sat}}{I_{ref}}\times\frac{[L]_T}{[P]} \qquad \text{Equation 8.1}$$

$$STD-AF=\frac{\alpha_{std}[L]}{K_D+[L]} \qquad \text{Equation 8.2}$$

The I_{ref} and I_{sat} were the ligand peak when irradiating protein at 30 ppm and -1 ppm, respectively. $[L]_T$ was the total ligand concentration and [P] was the protein concentration. The a_{sat} indicated the STD-AF when the protein was saturated by the ligand.

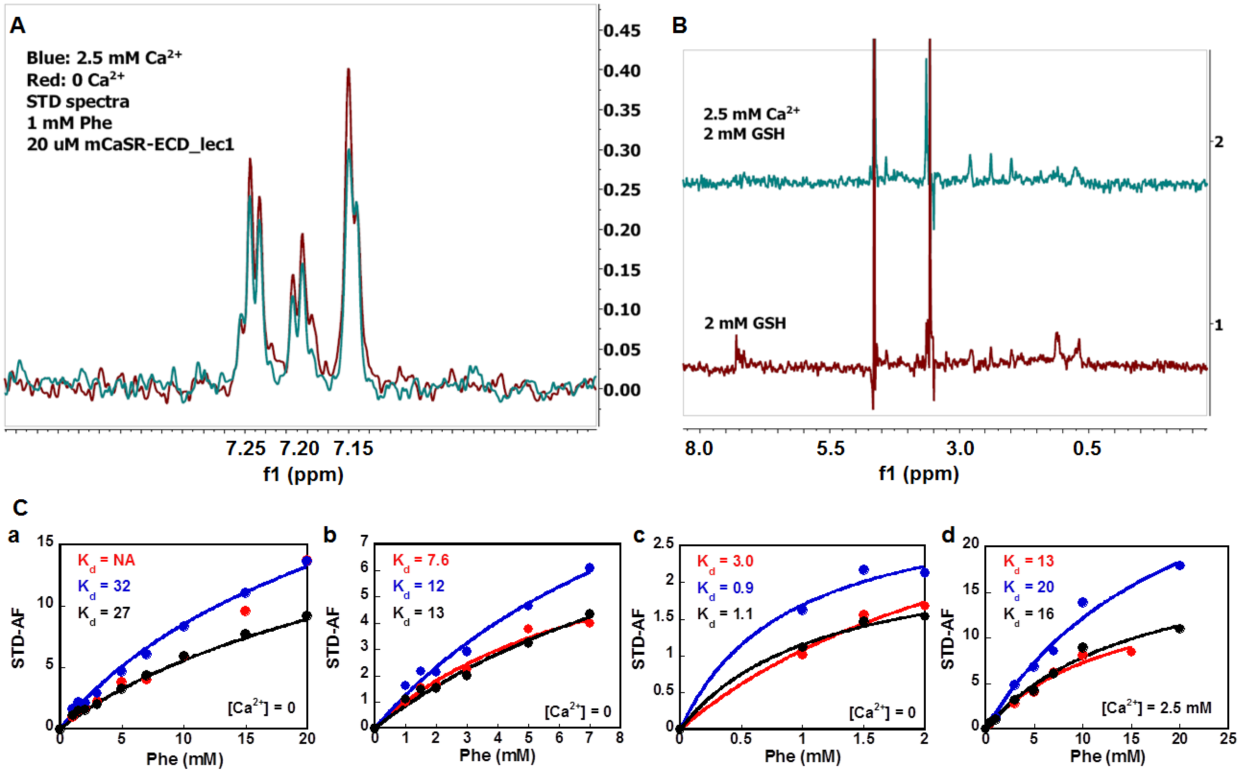

Figure 8.5. The STD spectra comparison between Ca2+ free and loaded CaSR-ECD.
(A) The STD spectra of20 μM CaSR-ECD with 1mM Phe in the absence (Red) and presence (blue) of 2.5 mM Ca^{2+}. (B) The STD spectra of20 μM CaSR-ECD with 2mM GSH in the absence (Red) and presence

(blue) of 2.5 mM Ca^{2+}. (C) The relationship between STD-AF and L-Phe concentration. The titration range of Phe was 0-20 mM. In the full range (a), 0-7 mM (b) and 0-2 mM (c), different K_d values were obtained by using Equation 8.2. (d) The K_d fitting for the full range 0-20 mM Phe in the presence of 2.5 mM Ca^{2+}.The red, blue and black color indicated the peak at 7.25, 7.20 and 7.15 ppm.

The Phe binding to CaSR-ECD appeared to have multiple phases (Figure 8.5Ca). Using the initial 0-2 mM Phe for K_d fitting obtained the highest binding affinity and was lower than the EC_{50} (5 mM). By fitting from 0-7 mM Phe, the calculated K_d was comparable to EC_{50}. When the Phe concentration was more than 10 mM, the STD-AF kept increasing and seemed no saturation, which might be due to the non-specific binding. In the presence of Ca^{2+}, only one binding process was observed. Compared Figure 8.5Ca and 8.5Cd, the peak 2 and 3 (7.20 and 7.15 ppm) in the presence of 2.5 mM Ca^{2+} showed a greater STD-AF and the K_d was smaller, suggesting Ca^{2+} binding enhance the Phe binding.

8.2 Lipid interaction induced conformational change of SecA fragments

SecA is an essential ATPase for protein secretion in bacteria. SecA is soluble and possesses low levels of intrinsic ATPase activity in solutions free of phospholipids, and transforms to be an integral membrane protein when interacting with lipids to function as a protein-conducting channel in a complex form with SecYEG (301-303). It have been found by Dr. Phang-Cheng Tai's group that SecA, without interacting with SecYEG, forms pore ring-structure with a pore-size of 2-3 nm in the anionic lipids as observed by TEM and AFM (304-307). Such a unique feature attracts interests to explore the underlying mechanism.

Soluble SecA has two separable domain fragments: an N-terminal 68 kDa (N68: 1-609) domain which possesses high ATPase activity that is down-regulated by the 34-kDa C-terminal domain (C34) (308-311), and shows high-affinity binding to SecYEG in the membranes (312).

C34 has also been shown to be involved in SecA dimerization (312, 313), and in SecB/lipid binding (314). The N-domain containing the long helical SD domain (1-668) can form the pore structure in lipids and but show no channel activity. However, these two SecA domains can associate together to function the same as the integral SecA (315). Binding to signal peptides and to lipids causes significant conformational changes of SecA (316-320).

Various X-ray structures of soluble bacterial SecA fragments have been obtained but all of them lack the un-structured C-terminal tail (304, 321-326) (Figure 8.6). By using solution NMR as a complementary tool, several SecA domains structures in solution have been resolved including the last 22 amino acids in the C terminal, and an inter-conversion between open and closed conformation around PBD domain (327-332). Here, we want to use differential isotope labeling, site-directed mutagenesis and high resolution NMR to systematically define the conformational changes in a helical scaffold domain and two interacting hydrophobic helices that interact with lipids and are critical for the formation of pore structures to function as protein-conducting channel activity for ion-current and protein translocation.

The sub-domain NMR structures of soluble C34 (610-901) have been analyzed (327, 328). The soluble C34 can also bind to lipids (312). This domain was reconstituted with lipids to determine whether it induced any changes by NMR. The lipid induced conformational change can be visualized by examining residues that have changes either in chemical shifts or line width by selectively labeled the domains, e.g. $^{13}CH_3$-Met and $^{13}CH_3$-Lys, to avoid the peak overlapping issue due to the large molecule size (283, 329, 333). There are 20 Lys spread at different locations of SecA C34 and most of them are exposed to solvent. It is found that the SD domain is essential for the pore formation and two helices after the SD domain are involved in store the channel activity. The hydrophobic interaction inside C34 is shown in Figure 8.6C, where the electrostatic interaction between K750 and V829, K764 and L667, V669, is observed (Figure 8.6B).

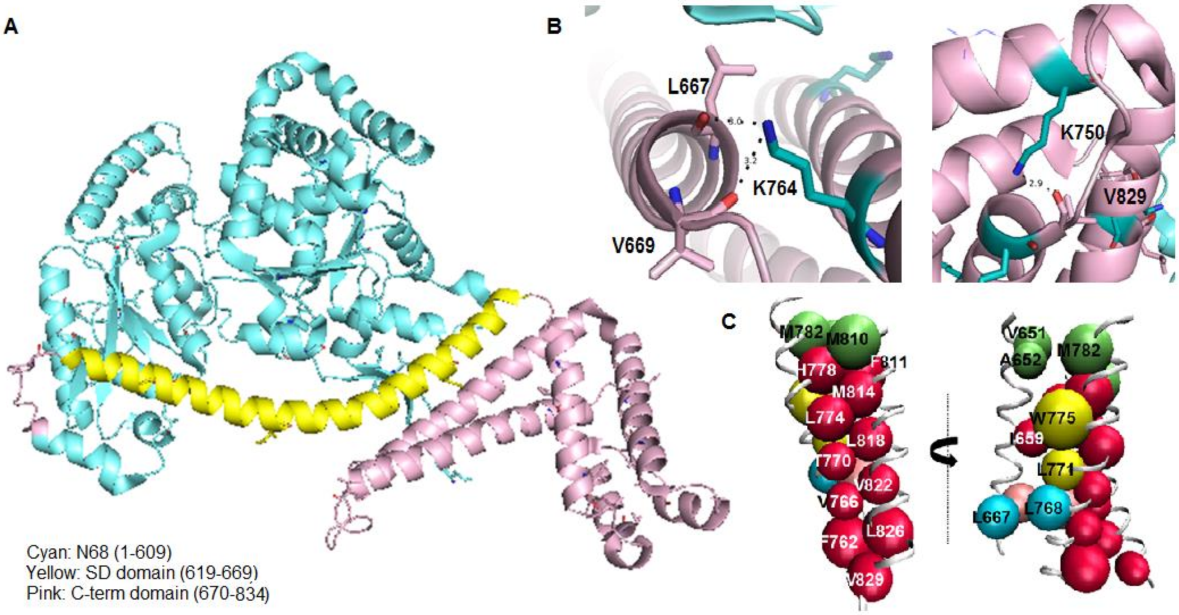

Figure 8.6. The structure analysis of SecA.
(A) The crystal structure of SecA (PDB ID: 2FSF). The N68 fragment is colored by cyan. The C34 fragment includes the yellow and pink regions plus the unstructured C-terminal tail (67 aa) of which the X-ray structure has not been solved. (B) The lysine involved electrostatic interaction in the C34 fragment. The side chain amino groups of K764 and K750 form the hydrogen bond with the main chain oxygen of L667, V669 and V829. (C) The beads mode of the hydrophobic interactions between helices 650-670, 760-785 and 808-830.

There are relatively few lysine residues that may be labeled by reductive methylation in the lipid environment. The presence of lipids indeed induces conformational changes of C34, resulting in different Lys residues for di-methylation as shown in Figure 8.7A. The acquired ^{1}H-C^{13} HSQC spectrum of specifically labeled ^{13}CH$_3$-Met N68 showed the similar peak position as reported data (Figure 8.7B) (329). With ^{13}C-Met labeling for N609 and N619, the M612 can be assigned. The lipid-induced change can be determined by the chemical shift change. For the uniformly labeled ^{15}N-C34, ^{1}H-^{15}N HSQC spectra appeared similar as the reported data, in which most of peaks are not able to be seen due to the rigid structure and only a few residues in the flexible tail (around 70 aa) is NMR detectable (Figure 8.7C). The assignment was borrowed from the published spectrum by Gelis (329). The chemical shift perturbation upon reconstitution to lipids confirmed the interaction between C-tail of SecA and lipids.

The selective labeling simplified the NMR spectrum. By this method, we can achieve the residue assignment fast. It is confirmed that the C-tail of SecA can interact with lipids. N68 fragment may also associates with lipids but not as significantly as C34. To further pin down the key determinants for such interaction using C34 and N68 by the high resolution NMR, we can (1) use the PRE with NO labeling of Cys residues can be applied (334); (2) measure the transverse relaxation of both apo- and ligand-loaded forms to explore the dynamics of SecA and its fragments.

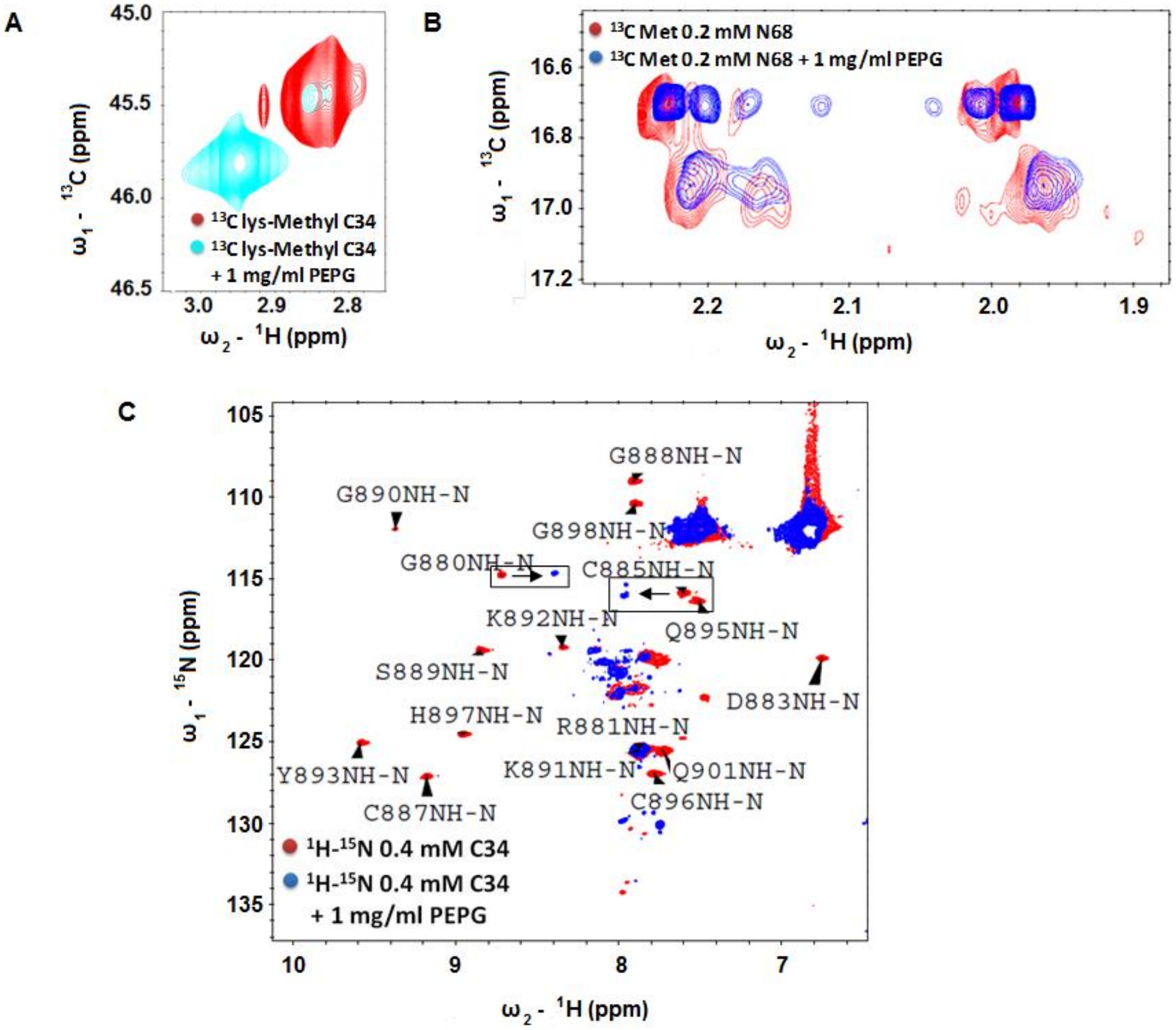

Figure 8.7**.** NMR study of selectively labeled SecA fragment N68 and C34.
(A) ^{1}H-^{13}C HMQC spectrum of ^{13}C-lysine-methylation of C34 without (red) and with (cyan) lipids. (B)The color indicates the pair-wise hydrophobic interaction. **C**, ^{13}C-Met HMQC spectrum of N609 before (red) and after (blue) adding PEPG lipids. (C) ^{1}H-^{15}H HSQC NMR spectrum of C34 before (red) and after (blue) adding PEPG lipids. The black box indicates the chemical shift of residues caused by lipids binding.

8.3 Summary and conclusions

This chapter described the methodology of studying ligand interactions with large proteins by NMR. The NMR signal of methyl group instead of the whole molecule was detected to avoid the short T2 of the large molecule. By reductive methylation of lysine residues, (1) the conformational change of the extracellular domain of CaSR induced by Ca^{2+} and GSH binding, and (2) the conformational change of SecA-C34 induced by lipid-protein interaction, were successfully observed. The ^{15}N-Phe labeled CaSR-ECD expressed by mammalian cells and the deuterated uniformly ^{15}N labeled CaSR-ECD expressed by bacteria confirmed the calcium and amino acid analog binding induced conformational change. The STD-NMR results provided the evidence of the direct binding of Phe and CaSR-ECD, and Ca^{2+} binding enhanced the Phe binding. The signal of $^{13}CH_3$-Met in SecA-N68, and uniformly ^{15}N labeled SecA-C34 confirmed the conformational change upon lipid interaction as well.

9 MAJOR DISCOVERIES AND SIGNIFICANCE

The organic calcium dyes and the protein-based calcium probes have merged to reveal the relationship between the intracellular calcium dynamics and the calcium-dependent physiological phenomenon. However, the utilization of natural calcium binding protein such as calmodulin and troponin limits the application in the low calcium environment like cytoplasm due to the intrinsic high calcium binding affinity of calmodulin and troponin. To obtain a complete picture of calcium movements, it is necessary to have calcium probes that can sense calcium concentration change in calcium stores like the endoplasmic reticulum and mitochondria. The major challenges to design this kind of calcium probes are that (1) we have to start a new calcium binding coordination differing from the classic EF-hand motif; (2) the calcium binding needs to induce the appropriate conformational change which will not disturb the global folding but conduct the fluorescence intensity change.

Through year of efforts, we found our way to develop the calcium probes targeted to high calcium environment, the GFP based green fluorescent calcium indicator CatchER and mCherry based red fluorescent calcium indicator, MCD1 (RapidER). By statistically analyzing the calcium binding coordination, the half shell geometry with concentrated negative potential was utilized to attract calcium ion with lower binding affinity than the classic bipyramidal calcium pocket. To minimize the perturbation of the folding, the calcium binding site was designed in the single fluorescence protein by mutagenesis without domain insertion. We take the advantage of the electrostatic property to drive the local conformation and dynamic change, which causes the repulsion force in the calcium binding site without calcium ion and relaxation after calcium binding. The equilibrium-dialysis assay, NMR and fluorescence spectroscopy confirmed calcium binds to the designed proteins. The calcium concentration change reflected by the fluorescence was successfully observed and validated *in vitro* and *in situ*. The kinetic study demonstrated the faster calcium association and disassociation rate of CatchER and MCD1 than other protein based calcium sensors currently, which is an important step forward to allow detection of calcium dynamics in the electrical excitable cells. Compared to the green CatchER, MCD1 shows less pH-dependent fluorescence change in the physiological condition. In addition, the red shifted excitation wavelength enables a broader application for simultaneous recording using multiple sensors. This research expands the calcium indicator toolkit not only to detect a broader range of calcium concentration but also to a larger fluorescence spectrum window.

To achieve a better fluorescence dynamic range, the underlying mechanism of calcium induced fluorescence increase was investigated in this dissertation. Through the analysis of CatchER in the ground and excited state, we found that calcium binding shifted the CatchER chromophore acid-base equilibrium in the ground state to generate increase of proportion of the anionic form and retarded the geminate recombination to accumulate more anionic form via proton transfer in the excited state by exciting the neutral chromophore. Employing the calcium binding site disturbs the classic hydrogen bonding network existing in w.t.-EGFP chromophore, leading to the geminate recombination. It is the first time to observe the phenomenon of geminate recombination in the world of fluorescent proteins. Calcium binding rescues the proton migration pathway, reduces the geminate quenching and then increases the fluorescence lifetime of the indirectly excited anionic chromophore. The substantial Ca^{2+} binding induced lifetime increase (44%) enables the future application of CatchER in the lifetime imaging, which is more quantitative compared to the intensity-based imaging method.

The heterogeneous distribution of intracellular calcium is determined by the calcium movement and diffusion among organelles. The resulted spatial-temporal calcium dynamics is essential in signal transduction. The specific targeting especially to the space in proximity to calcium channels will enable the detection of the amount and the kinetics of calcium concentration change in the first place and later connection of the calcium ion migration chain. In this dissertation, we focused on the cleft between SR terminal cisternae and T-tubule, where calcium ions accumulate quickly once they release from SR upon coupling between DHPR and RyR1 due to an action potential. Instead of using an intact membrane protein to locate our calcium sensor CatchER, we selected the transmembrane fragments from RyR1 to avoid the over-expression of any intrinsic native protein. The confocal imaging result showed that the fusion of the selected fragments of RyR1 allowed to anchor CatchER in ER membrane, although the orientation was not completely the same. This work set the base for future screening of membrane anchoring sequences and will be continued.

Residual dipolar coupling (RDC) and protein dynamics study was carried out to understand the interaction between calmodulin and the connexin 43 N-terminal loop. The dynamic T1, T2, NOE, and S2 parameters suggested that both terminal domains move accordingly, the central linker around D80 is flexible and the conformational exchange is expected. Such conformational exchange might unwind the central helix and induce the bending, which in turn could affect the interaction between the peptide and CaM. The RDC fitting for the N and C domains of CaM suggested that N domain fits 1-14 mode as 1CDL and C domain fits 1-17 mode as 2BCX. In both binding mode, CaM adaptes the collapsed conformation to wrap around the peptide, and the central helix is bent and partial unwound. For the full length RDC fitting, the extended CaM in 1G4Y has the best fit, which is a dimer and the central linker was flexible. Since the interactions of both terminal domains with the peptide fails to fit in the same complex model, a binding mode other than any existing one may occur in CaM-Cx43np complex, in which both N and C domains contact with the target peptide but more extended than that in the classic collapsed conformation.

The large molecular size makes the study of the interaction between a ligand and a protein challenging especially when using NMR spectroscopy. It is common to observe overlapped peaks or spectra with a large amount of missing peaks due to the broad line width that caused by the slowing tumbling rate of macromolecules, even in the deuterated proteins. The methyl group, of which the faster tumbling rate superimposes that of the macromolecule and the bonded three protons, enables the resonance intense and narrow in a ^{1}H-^{13}C spectrum. In this dissertation, the calcium sensing receptor (CaSR) and bacterial membrane protein SecA were reductively methylated by H^{13}CHO and HMQC was applied to detect the interaction between proteins and ligands/lipids. Efforts were also taken to obtain the HSQC and HMQC spectra of [^{15}N-Phe]-CaSR-ECD and [^{13}C-Met]-SecA. Using those selectively labeled proteins, the calcium and glutathione induced conformational change in CaSR-ECD was observed, as well as the lipids interaction induced conformational change in SecA. The advantage of applying 1D proton STD-NMR to illustrate the low-affinity ligand-protein binding was shown in the study of Phe-CaSR interaction. Thus, the protocol of utilizing the selective labeling approach was built in our lab for other projects involving macromolecule-ligand interactions.

REFERENCES

1. Rizzuto R, Bernardi P, & Pozzan T (2000) Mitochondria as all-round players of the calcium game. *J Physiol* 529 Pt 1:37-47.
2. Haller T, Dietl P, Deetjen P, & Volkl H (1996) The lysosomal compartment as intracellular calcium store in MDCK cells: a possible involvement in InsP3-mediated Ca2+ release. *Cell Calcium* 19(2):157-165.
3. Brown EM, Pollak M, & Hebert SC (1995) Sensing of extracellular Ca2+ by parathyroid and kidney cells: cloning and characterization of an extracellular Ca(2+)-sensing receptor. *Am J Kidney Dis* 25(3):506-513.
4. Clapham DE (2007) Calcium signaling. *Cell* 131(6):1047-1058.
5. Berridge MJ, Bootman MD, & Lipp P (1998) Calcium--a life and death signal. *Nature* 395(6703):645-648.
6. Feske S (2007) Calcium signalling in lymphocyte activation and disease. *Nat Rev Immunol* 7(9):690-702.
7. Lewis RS (2001) Calcium signaling mechanisms in T lymphocytes. *Annual review of immunology* 19:497-521.
8. Corbett EF & Michalak M (2000) Calcium, a signaling molecule in the endoplasmic reticulum? *Trends Biochem Sci* 25(7):307-311.
9. Petersen OH, Tepikin A, & Park MK (2001) The endoplasmic reticulum: one continuous or several separate Ca(2+) stores? *Trends Neurosci* 24(5):271-276.
10. Verkhratsky A & Petersen OH (2002) The endoplasmic reticulum as an integrating signalling organelle: from neuronal signalling to neuronal death. *Eur J Pharmacol* 447(2-3):141-154.
11. Bers DM (2003) Dynamic imaging in living cells: windows into local signaling. *Sci STKE* 2003(177):PE13.
12. Galione A & Churchill GC (2002) Interactions between calcium release pathways: multiple messengers and multiple stores. *Cell Calcium* 32(5-6):343-354.
13. Giovannucci DR, *et al.* (2002) Cytosolic Ca(2+) and Ca(2+)-activated Cl(-) current dynamics: insights from two functionally distinct mouse exocrine cells. *J Physiol* 540(Pt 2):469-484.
14. Putney JW (2005) Capacitative calcium entry: sensing the calcium stores. *Journal of Cell Biology* 169(3):381-382.
15. Torres M, *et al.* (2010) Prion protein misfolding affects calcium homeostasis and sensitizes cells to endoplasmic reticulum stress. *PLoS One* 5(12):e15658.
16. Hajnoczky G, Csordas G, & Yi M (2002) Old players in a new role: mitochondria-associated membranes, VDAC, and ryanodine receptors as contributors to calcium signal propagation from endoplasmic reticulum to the mitochondria. *Cell Calcium* 32(5-6):363-377.
17. Hoppe UC (2010) Mitochondrial calcium channels. *FEBS Lett* 584(10):1975-1981.
18. Sztretye M, *et al.* (2011) Measurement of RyR permeability reveals a role of calsequestrin in termination of SR Ca2+ release in skeletal muscle. *J Gen Physiol* 138(2):231-247.
19. Sztretye M, *et al.* (2011) D4cpv-calsequestrin: a sensitive ratiometric biosensor accurately targeted to the calcium store of skeletal muscle. *J Gen Physiol* 138(2):211-229.
20. Csordas G, *et al.* (Imaging interorganelle contacts and local calcium dynamics at the ER-mitochondrial interface. *Mol Cell* 39(1):121-132.
21. Polakova E, Zahradnikova A, Jr., Pavelkova J, Zahradnik I, & Zahradnikova A (2008) Local calcium release activation by DHPR calcium channel openings in rat cardiac myocytes. *J Physiol* 586(16):3839-3854.
22. Shuai J, Pearson JE, Foskett JK, Mak DO, & Parker I (2007) A kinetic model of single and clustered IP3 receptors in the absence of Ca2+ feedback. *Biophys J* 93(4):1151-1162.

23. Dibb KM, Graham HK, Venetucci LA, Eisner DA, & Trafford AW (2007) Analysis of cellular calcium fluxes in cardiac muscle to understand calcium homeostasis in the heart. *Cell Calcium* 42(4-5):503-512.
24. Kawase Y & Hajjar RJ (2008) The cardiac sarcoplasmic/endoplasmic reticulum calcium ATPase: a potent target for cardiovascular diseases. *Nat Clin Pract Cardiovasc Med* 5(9):554-565.
25. Periasamy M & Kalyanasundaram A (2008) SERCA2a gene therapy for heart failure: ready for primetime? *Mol Ther* 16(6):1002-1004.
26. Prasad AM & Inesi G (2010) Downregulation of Ca2+ signalling proteins in cardiac hypertrophy. *Minerva Cardioangiol* 58(2):193-204.
27. Supnet C & Bezprozvanny I (2010) Neuronal Calcium Signaling, Mitochondrial Dysfunction, and Alzheimer's Disease. *J Alzheimers Dis*.
28. Andreyev A & Fiskum G (1999) Calcium induced release of mitochondrial cytochrome c by different mechanisms selective for brain versus liver. *Cell Death Differ* 6(9):825-832.
29. Harr MW & Distelhorst CW (2010) Apoptosis and autophagy: decoding calcium signals that mediate life or death. *Cold Spring Harb Perspect Biol* 2(10):a005579.
30. Deniaud A*, et al.* (2008) Endoplasmic reticulum stress induces calcium-dependent permeability transition, mitochondrial outer membrane permeabilization and apoptosis. *Oncogene* 27(3):285-299.
31. Heath-Engel HM, Chang NC, & Shore GC (2008) The endoplasmic reticulum in apoptosis and autophagy: role of the BCL-2 protein family. *Oncogene* 27(50):6419-6433.
32. Rong YP*, et al.* (2009) The BH4 domain of Bcl-2 inhibits ER calcium release and apoptosis by binding the regulatory and coupling domain of the IP3 receptor. *Proc Natl Acad Sci U S A* 106(34):14397-14402.
33. Distelhorst CW & Shore GC (2004) Bcl-2 and calcium: controversy beneath the surface. *Oncogene* 23(16):2875-2880.
34. Pinton P & Rizzuto R (2006) Bcl-2 and Ca2+ homeostasis in the endoplasmic reticulum. *Cell death and differentiation* 13(8):1409-1418.
35. Foyouzi-Youssefi R*, et al.* (2000) Bcl-2 decreases the free Ca2+ concentration within the endoplasmic reticulum. *Proc Natl Acad Sci U S A* 97(11):5723-5728.
36. Xu C, Xu W, Palmer AE, & Reed JC (2008) BI-1 regulates endoplasmic reticulum Ca2+ homeostasis downstream of Bcl-2 family proteins. *J Biol Chem* 283(17):11477-11484.
37. Sano R*, et al.* (2012) Endoplasmic reticulum protein BI-1 regulates Ca(2)(+)-mediated bioenergetics to promote autophagy. *Genes & development* 26(10):1041-1054.
38. Palmer AE, Jin C, Reed JC, & Tsien RY (2004) Bcl-2-mediated alterations in endoplasmic reticulum Ca2+ analyzed with an improved genetically encoded fluorescent sensor. *Proc Natl Acad Sci U S A* 101(50):17404-17409.
39. Giuffrida ML*, et al.* (2009) Beta-amyloid monomers are neuroprotective. *J Neurosci* 29(34):10582-10587.
40. Demuro A*, et al.* (2005) Calcium dysregulation and membrane disruption as a ubiquitous neurotoxic mechanism of soluble amyloid oligomers. *J Biol Chem* 280(17):17294-17300.
41. Lansbury PT, Jr. (1999) Evolution of amyloid: what normal protein folding may tell us about fibrillogenesis and disease. *Proc Natl Acad Sci U S A* 96(7):3342-3344.
42. Shankar GM*, et al.* (2008) Amyloid-beta protein dimers isolated directly from Alzheimer's brains impair synaptic plasticity and memory. *Nat Med* 14(8):837-842.
43. Kayed R*, et al.* (2003) Common structure of soluble amyloid oligomers implies common mechanism of pathogenesis. *Science* 300(5618):486-489.
44. Demuro A, Parker I, & Stutzmann GE (2010) Calcium signaling and amyloid toxicity in Alzheimer disease. *J Biol Chem* 285(17):12463-12468.
45. Berridge MJ (2010) Calcium hypothesis of Alzheimer's disease. *Pflug Arch Eur J Phy* 459(3):441-449.

46. Supnet C & Bezprozvanny I (2010) The dysregulation of intracellular calcium in Alzheimer disease. *Cell Calcium* 47(2):183-189.
47. Tsien RY (1980) New calcium indicators and buffers with high selectivity against magnesium and protons: design, synthesis, and properties of prototype structures. *Biochemistry* 19(11):2396-2404.
48. Tsien RY, Rink TJ, & Poenie M (1985) Measurement of cytosolic free Ca2+ in individual small cells using fluorescence microscopy with dual excitation wavelengths. *Cell Calcium* 6(1-2):145-157.
49. Minta A, Kao JP, & Tsien RY (1989) Fluorescent indicators for cytosolic calcium based on rhodamine and fluorescein chromophores. *J Biol Chem* 264(14):8171-8178.
50. McCombs JE & Palmer AE (2008) Measuring calcium dynamics in living cells with genetically encodable calcium indicators. *Methods* 46(3):152-159.
51. Kendall JM, Badminton MN, SalaNewby GB, Campbell AK, & Rembold CM (1996) Recombinant apoaequorin acting as a pseudo-luciferase reports micromolar changes in the endoplasmic reticulum free Ca2+ of intact cells. *Biochem J* 318:383-387.
52. Ohmiya Y & Hirano T (1996) Shining the light: The mechanism of the bioluminescence reaction of calcium-binding photoproteins. *Chem Biol* 3(5):337-347.
53. Persechini A, Lynch JA, & Romoser VA (1997) Novel fluorescent indicator proteins for monitoring free intracellular Ca2+. *Cell Calcium* 22(3):209-216.
54. Miyawaki A, *et al.* (1997) Fluorescent indicators for Ca2+ based on green fluorescent proteins and calmodulin. *Nature* 388(6645):882-887.
55. Palmer AE, *et al.* (2006) Ca2+ indicators based on computationally redesigned calmodulin-peptide pairs. *Chem Biol* 13(5):521-530.
56. Heim N & Griesbeck O (2004) Genetically encoded indicators of cellular calcium dynamics based on troponin C and green fluorescent protein. *Journal of Biological Chemistry* 279(14):14280-14286.
57. Miyawaki A, Griesbeck O, Heim R, & Tsien RY (1999) Dynamic and quantitative Ca2+ measurements using improved cameleons. *Proc Natl Acad Sci U S A* 96(5):2135-2140.
58. Akke M, Skelton NJ, Kordel J, Palmer AG, & Chazin WJ (1993) Effects of Ion-Binding on the Backbone Dynamics of Calbindin-D9k Determined by N-15 Nmr Relaxation. *Biochemistry* 32(37):9832-9844.
59. Griesbeck O, Baird GS, Campbell RE, Zacharias DA, & Tsien RY (2001) Reducing the environmental sensitivity of yellow fluorescent protein. Mechanism and applications. *J Biol Chem* 276(31):29188-29194.
60. Nagai T, Yamada S, Tominaga T, Ichikawa M, & Miyawaki A (2004) Expanded dynamic range of fluorescent indicators for Ca(2+) by circularly permuted yellow fluorescent proteins. *Proc Natl Acad Sci U S A* 101(29):10554-10559.
61. Miyawaki A, Nagai T, Shimozono S, Fukano T, & Mizuno H (2002) Circularly permuted green fluorescent proteins engineered to sense Ca2+ and their application to imaging of subcellular Ca2+ dynamics. *RIKEN Review* (49):5.
62. Reiff DF, *et al.* (2005) In vivo performance of genetically encoded indicators of neural activity in flies. *J Neurosci* 25(19):4766-4778.
63. Nagai T, *et al.* (2002) A variant of yellow fluorescent protein with fast and efficient maturation for cell-biological applications. *Nat Biotechnol* 20(1):87-90.
64. Nakai J, Ohkura M, & Imoto K (2001) A novel high signal-to-noise Ca2+ probe composed of a single green fluorescent protein. *Biophys J* 80(1):168a-168a.
65. Nakai J, Ohkura M, & Imoto K (2001) A high signal-to-noise Ca2+ probe composed of a single green fluorescent protein. *Nat Biotechnol* 19(2):137-141.
66. Tang S, *et al.* (2011) Design and application of a class of sensors to monitor Ca2+ dynamics in high Ca2+ concentration cellular compartments. *Proc Natl Acad Sci U S A* 108(39):16265-16270.

67. Hendel T, *et al.* (2008) Fluorescence changes of genetic calcium indicators and OGB-1 correlated with neural activity and calcium in vivo and in vitro. *J Neurosci* 28(29):7399-7411.
68. Tian L, Hires SA, & Looger LL (2012) Imaging neuronal activity with genetically encoded calcium indicators. *Cold Spring Harbor protocols* 2012(6):647-656.
69. Grienberger C & Konnerth A (2012) Imaging calcium in neurons. *Neuron* 73(5):862-885.
70. Yuste R, MacLean J, Vogelstein J, & Paninski L (2011) Imaging action potentials with calcium indicators. *Cold Spring Harbor protocols* 2011(8):985-989.
71. Baylor SM & Hollingworth S (2010) Calcium indicators and calcium signalling in skeletal muscle fibres during excitation-contraction coupling. *Prog Biophys Mol Biol*.
72. Hires SA, Tian L, & Looger LL (2008) Reporting neural activity with genetically encoded calcium indicators. *Brain cell biology* 36(1-4):69-86.
73. Smetters D, Majewska A, & Yuste R (1999) Detecting action potentials in neuronal populations with calcium imaging. *Methods-a Companion to Methods in Enzymology* 18(2):215-221.
74. Whitaker M (2010) Genetically Encoded Probes for Measurement of Intracellular Calcium. *Method Cell Biol* 99:153-182.
75. Ramdya P, Reiter B, & Engert F (2006) Reverse correlation of rapid calcium signals in the zebrafish optic tectum in vivo. *Journal of neuroscience methods* 157(2):230-237.
76. Kabbara AA & Allen DG (2001) The use of the indicator fluo-5N to measure sarcoplasmic reticulum calcium in single muscle fibres of the cane toad. *J Physiol-London* 534(1):87-97.
77. Zima AV, Picht E, Bers DM, & Blatter LA (2008) Termination of cardiac Ca2+ sparks role of intra-SR [Ca2+], release flux, and intra-SR Ca2+ diffusion. *Circulation Research* 103(8):E105-E115.
78. Picht E, DeSantiago J, Blatter LA, & Bers DM (2006) Cardiac alternans do not rely on diastolic sarcoplasmic reticulum calcium content fluctuations. *Circ Res* 99(7):740-748.
79. Choi YM, Kim SH, Chung S, Uhm DY, & Park MK (2006) Regional interaction of endoplasmic reticulum Ca2+ signals between soma and dendrites through rapid luminal Ca2+ diffusion. *Journal of Neuroscience* 26(47):12127-12136.
80. Sanchez G, Hidalgo C, & Donoso P (2003) Kinetic studies of calcium-induced calcium release in cardiac sarcoplasmic reticulum vesicles. *Biophys J* 84(4):2319-2330.
81. Escobar AL, Monck JR, Fernandez JM, & Vergara JL (1994) Localization of the site of Ca2+ release at the level of a single sarcomere in skeletal muscle fibres. *Nature* 367(6465):739-741.
82. Hofer AM & Machen TE (1993) Technique for Insitu Measurement of Calcium in Intracellular Inositol 1,4,5-Trisphosphate-Sensitive Stores Using the Fluorescent Indicator Mag-Fura-2. *P Natl Acad Sci USA* 90(7):2598-2602.
83. Hofer AM (2006) Measurement of free [Ca2+] changes in agonist-sensitive internal stores using compartmentalized fluorescent indicators. *Methods Mol Biol* 312:229-247.
84. Landolfi B, Curci S, Debellis L, Pozzan T, & Hofer AM (1998) Ca2+ homeostasis in the agonist-sensitive internal store: Functional interactions between mitochondria and the ER measured in situ in intact cells. *Journal of Cell Biology* 142(5):1235-1243.
85. Woods CE, Novo D, DiFranco M, & Vergara JL (2004) The action potential-evoked sarcoplasmic reticulum calcium release is impaired in mdx mouse muscle fibres. *J Physiol* 557(Pt 1):59-75.
86. Hollingworth S, Zhao MD, & Baylor SM (1996) The amplitude and time course of the myoplasmic free [Ca2+] transient in fast-twitch fibers of mouse muscle. *Journal of General Physiology* 108(5):455-469.
87. Liu YW, Kranias EG, & Schneider MF (1997) Regulation of Ca2+ handling by phosphorylation status in mouse fast-and slow-twitch skeletal muscle fibers. *Am J Physiol-Cell Ph* 273(6):C1915-C1924.
88. Hollingworth S, Zeiger U, & Baylor SM (2008) Comparison of the myoplasmic calcium transient elicited by an action potential in intact fibres of mdx and normal mice. *J Physiol-London* 586(21):5063-5075.

89. Zucker RS (1993) The Calcium-Concentration Clamp - Spikes and Reversible Pulses Using the Photolabile Chelator Dm-Nitrophen. *Cell Calcium* 14(2):87-100.

90. Marvin JS*, et al.* (2013) An optimized fluorescent probe for visualizing glutamate neurotransmission. *Nat Methods* 10(2):162-170.

91. Chen TW*, et al.* (2013) Ultrasensitive fluorescent proteins for imaging neuronal activity. *Nature* 499(7458):295-300.

92. Zhou XX, Chung HK, Lam AJ, & Lin MZ (2012) Optical control of protein activity by fluorescent protein domains. *Science* 338(6108):810-814.

93. Fosbrink M, Aye-Han NN, Cheong R, Levchenko A, & Zhang J (2010) Visualization of JNK activity dynamics with a genetically encoded fluorescent biosensor. *Proc Natl Acad Sci U S A* 107(12):5459-5464.

94. Miranda JG*, et al.* (2012) New alternately colored FRET sensors for simultaneous monitoring of Zn(2)(+) in multiple cellular locations. *PLoS One* 7(11):e49371.

95. Griesbeck O, Baird GS, Campbell RE, Zacharias DA, & Tsien RY (2001) Reducing the environmental sensitivity of yellow fluorescent protein - Mechanism and applications. *Journal of Biological Chemistry* 276(31):29188-29194.

96. Zhao Y*, et al.* (2011) An expanded palette of genetically encoded Ca(2) indicators. *Science* 333(6051):1888-1891.

97. Mank M*, et al.* (2008) A genetically encoded calcium indicator for chronic in vivo two-photon imaging. *Nat Methods* 5(9):805-811.

98. Teleman O, Drakenberg T, Forsen S, & Thulin E (1983) Calcium and cadmium binding to troponin C. Evidence for cooperativity. *Eur J Biochem* 134(3):453-457.

99. Iida S & Potter JD (1986) Calcium binding to calmodulin. Cooperativity of the calcium-binding sites. *J Biochem* 99(6):1765-1772.

100. Bayley P, Ahlstrom P, Martin SR, & Forsen S (1984) The Kinetics of Calcium-Binding to Calmodulin - Quin-2 and Ans Stopped-Flow Fluorescence Studies. *Biochem Bioph Res Co* 120(1):185-191.

101. Berlin JR & Konishi M (1993) Ca2+ transients in cardiac myocytes measured with high and low affinity Ca2+ indicators. *Biophys J* 65(4):1632-1647.

102. Falke JJ, Drake SK, Hazard AL, & Peersen OB (1994) Molecular Tuning of Ion-Binding to Calcium Signaling Proteins. *Q Rev Biophys* 27(3):219-290.

103. Yang JJ, Gawthrop A, & Ye YY (2003) Obtaining site-specific calcium-binding affinities of calmodulin. *Protein Peptide Lett* 10(4):331-345.

104. Pologruto TA, Yasuda R, & Svoboda K (2004) Monitoring neural activity and [Ca2+] with genetically encoded Ca2+ indicators. *J Neurosci* 24(43):9572-9579.

105. Jimenez-Moreno R, Wang ZM, Messi ML, & Delbono O (2010) Sarcoplasmic reticulum Ca2+ depletion in adult skeletal muscle fibres measured with the biosensor D1ER. *Pflug Arch Eur J Phy* 459(5):725-735.

106. Wang ZM, Tang S, Messi ML, Yang JJ, & Delbono O (2012) Residual sarcoplasmic reticulum Ca2+ concentration after Ca2+ release in skeletal myofibers from young adult and old mice. *Pflug Arch Eur J Phy* 463(4):615-624.

107. Wang ZM, Tang S, Messi ML, Yang JJ, & Delbono O (2012) Residual sarcoplasmic reticulum Ca2+ concentration after Ca2+ release in skeletal myofibers from young adult and old mice. *Pflugers Arch* 463(4):615-624.

108. Baird GS, Zacharias DA, & Tsien RY (2000) Biochemistry, mutagenesis, and oligomerization of DsRed, a red fluorescent protein from coral. *Proc Natl Acad Sci U S A* 97(22):11984-11989.

109. Shaner NC*, et al.* (2008) Improving the photostability of bright monomeric orange and red fluorescent proteins. *Nat Methods* 5(6):545-551.

110. Shaner NC*, et al.* (2004) Improved monomeric red, orange and yellow fluorescent proteins derived from Discosoma sp. red fluorescent protein. *Nature Biotechnology* 22(12):1567-1572.

111. Weissleder R (2001) A clearer vision for in vivo imaging. *Nat Biotechnol* 19(4):316-317.

112. Heim R, Cubitt AB, & Tsien RY (1995) Improved green fluorescence. *Nature* 373(6516):663-664.
113. Shcherbo D, *et al.* (2007) Bright far-red fluorescent protein for whole-body imaging. *Nat Methods* 4(9):741-746.
114. Pletnev S, *et al.* (2008) A crystallographic study of bright far-red fluorescent protein mKate reveals pH-induced cis-trans isomerization of the chromophore. *J Biol Chem* 283(43):28980-28987.
115. Shcherbo D, *et al.* (2009) Far-red fluorescent tags for protein imaging in living tissues. *Biochem J* 418(3):567-574.
116. Yang K (2001) Prokaryotic calmodulins: recent developments and evolutionary implications. *Journal of molecular microbiology and biotechnology* 3(3):457-459.
117. Wang CL (1985) A note on Ca2+ binding to calmodulin. *Biochem Biophys Res Commun* 130(1):426-430.
118. Linse S, Helmersson A, & Forsen S (1991) Calcium binding to calmodulin and its globular domains. *J Biol Chem* 266(13):8050-8054.
119. Forse ́n S, Vogel HJ, & Drakenberg T (1986) Biophysical studies of calmodulin, in Calcium and Cell Function. ed Cheung WY (Academic Press, New York.), pp 113-157.
120. Martin SR, Andersson Teleman A, Bayley PM, Drakenberg T, & Forsen S (1985) Kinetics of calcium dissociation from calmodulin and its tryptic fragments. A stopped-flow fluorescence study using Quin 2 reveals a two-domain structure. *Eur J Biochem* 151(3):543-550.
121. Black DJ, Selfridge JE, & Persechini A (2007) The kinetics of Ca(2+)-dependent switching in a calmodulin-IQ domain complex. *Biochemistry* 46(46):13415-13424.
122. Johnson JD, Snyder C, Walsh M, & Flynn M (1996) Effects of myosin light chain kinase and peptides on Ca2+ exchange with the N- and C-terminal Ca2+ binding sites of calmodulin. *J Biol Chem* 271(2):761-767.
123. Yap KL, *et al.* (2000) Calmodulin target database. *J Struct Funct Genomics* 1(1):8-14.
124. Zuhlke RD, Pitt GS, Deisseroth K, Tsien RW, & Reuter H (1999) Calmodulin supports both inactivation and facilitation of L-type calcium channels. *Nature* 399(6732):159-162.
125. Kuboniwa H, *et al.* (1995) Solution structure of calcium-free calmodulin. *Nat Struct Biol* 2(9):768-776.
126. Persechini A & Stemmer PM (2002) Calmodulin is a limiting factor in the cell. *Trends Cardiovas Med* 12(1):32-37.
127. Persechini A, Lynch JA, & Romoser VA (1997) Novel fluorescent indicator proteins for monitoring free intracellular Ca2+. *Cell Calcium* 22(3):209-216.
128. Porumb T, Yau P, Harvey TS, & Ikura M (1994) A calmodulin-target peptide hybrid molecule with unique calcium-binding properties. *Protein Eng* 7(1):109-115.
129. Blais J, Douki T, Vigny P, & Cadet J (1994) Fluorescence quantum yield determination of pyrimidine (6-4) pyrimidone photoadducts. *Photochem Photobiol* 59(4):402-404.
130. Grabolle M, *et al.* (2009) Determination of the Fluorescence Quantum Yield of Quantum Dots: Suitable Procedures and Achievable Uncertainties. *Anal Chem*.
131. Zou J, *et al.* (2007) Developing sensors for real-time measurement of high Ca2+ concentrations. *Biochemistry* 46(43):12275-12288.
132. Canada RG (1983) Terbium binding to neoplastic GH3 pituitary cells. *Biochem Biophys Res Commun* 111(1):135-142.
133. Honig B & Nicholls A (1995) Classical electrostatics in biology and chemistry. *Science* 268(5214):1144-1149.
134. Shen MY & Sali A (2006) Statistical potential for assessment and prediction of protein structures. *Protein Sci* 15(11):2507-2524.
135. Melo F & Sali A (2007) Fold assessment for comparative protein structure modeling. *Protein Sci* 16(11):2412-2426.

136. Patton C, Thompson S, & Epel D (2004) Some precautions in using chelators to buffer metals in biological solutions. *Cell Calcium* 35(5):427-431.
137. Patton C (Ca-EGTA Calculator v1.2 using constants from NIST database #46 v8.
138. Bers DM & Guo T (2005) Calcium signaling in cardiac ventricular myocytes. *Ann N Y Acad Sci* 1047:86-98.
139. Berridge MJ (1998) Neuronal calcium signaling. *Neuron* 21(1):13-26.
140. Hardingham GE, Arnold FJ, & Bading H (2001) Nuclear calcium signaling controls CREB-mediated gene expression triggered by synaptic activity. *Nat Neurosci* 4(3):261-267.
141. Spitzer NC (2008) Calcium: first messenger. *Nature Neuroscience* 11(3):243-244.
142. Riccardi D & Brown EM (2010) Physiology and pathophysiology of the calcium-sensing receptor in the kidney. *American journal of physiology. Renal physiology* 298(3):F485-499.
143. Smajilovic S & Tfelt-Hansen J (2007) Calcium acts as a first messenger through the calcium-sensing receptor in the cardiovascular system. *Cardiovascular Research* 75(3):457-467.
144. Canaff L, *et al.* (2001) Extracellular calcium-sensing receptor is expressed in rat hepatocytes. coupling to intracellular calcium mobilization and stimulation of bile flow. *J Biol Chem* 276(6):4070-4079.
145. Hardingham NR, *et al.* (2006) Extracellular calcium regulates postsynaptic efficacy through group 1 metabotropic glutamate receptors. *J Neurosci* 26(23):6337-6345.
146. Rios E & Pizarro G (1991) Voltage sensor of excitation-contraction coupling in skeletal muscle. *Physiol Rev* 71(3):849-908.
147. Schneider MF (1994) Control of calcium release in functioning skeletal muscle fibers. *Annual review of physiology* 56:463-484.
148. Baylor SM & Hollingworth S (2003) Sarcoplasmic reticulum calcium release compared in slow-twitch and fast-twitch fibres of mouse muscle. *J Physiol* 551(Pt 1):125-138.
149. Bean BP (2007) The action potential in mammalian central neurons. *Nature reviews. Neuroscience* 8(6):451-465.
150. Locknar SA, Barstow KL, Tompkins JD, Merriam LA, & Parsons RL (2004) Calcium-induced calcium release regulates action potential generation in guinea-pig sympathetic neurones. *J Physiol* 555(Pt 3):627-635.
151. Sandler VM & Barbara JG (1999) Calcium-induced calcium release contributes to action potential-evoked calcium transients in hippocampal CA1 pyramidal neurons. *J Neurosci* 19(11):4325-4336.
152. Borst JG & Sakmann B (1999) Effect of changes in action potential shape on calcium currents and transmitter release in a calyx-type synapse of the rat auditory brainstem. *Philosophical transactions of the Royal Society of London. Series B, Biological sciences* 354(1381):347-355.
153. Lopez-Lopez JR, Shacklock PS, Balke CW, & Wier WG (1995) Local calcium transients triggered by single L-type calcium channel currents in cardiac cells. *Science* 268(5213):1042-1045.
154. Cannell MB, Cheng H, & Lederer WJ (1995) The control of calcium release in heart muscle. *Science* 268(5213):1045-1049.
155. Fill M & Copello JA (2002) Ryanodine receptor calcium release channels. *Physiol Rev* 82(4):893-922.
156. Berridge MJ, Bootman MD, & Roderick HL (2003) Calcium signalling: dynamics, homeostasis and remodelling. *Nat Rev Mol Cell Biol* 4(7):517-529.
157. Kirberger M, *et al.* (2008) Statistical analysis of structural characteristics of protein Ca2+-binding sites. *J Biol Inorg Chem* 13(7):1169-1181.
158. Yang W, *et al.* (2003) Rational design of a calcium-binding protein. *Journal of the American Chemical Society* 125(20):6165-6171.
159. Shu X, Shaner NC, Yarbrough CA, Tsien RY, & Remington SJ (2006) Novel chromophores and buried charges control color in mFruits. *Biochemistry* 45(32):9639-9647.

160. Wang X, *et al.* (2010) Analysis and prediction of calcium-binding pockets from apo-protein structures exhibiting calcium-induced localized conformational changes. *Protein Sci* 19(6):1180-1190.
161. Shui B, *et al.* (2011) Circular permutation of red fluorescent proteins. *PLoS One* 6(5):e20505.
162. Seefeldt B, *et al.* (2008) Fluorescent proteins for single-molecule fluorescence applications. *J Biophotonics* 1(1):74-82.
163. Yang W, Wilkins AL, Li S, Ye Y, & Yang JJ (2005) The effects of Ca2+ binding on the dynamic properties of a designed Ca2+-binding protein. *Biochemistry* 44(23):8267-8273.
164. Linse S, *et al.* (1991) Electrostatic contributions to the binding of calcium in calbindin D9k. *Biochemistry* 30(1):154-162.
165. Brittain HG, Richardson FS, & Martin RB (1976) Terbium (III) emission as a probe of calcium(II) binding sites in proteins. *J Am Chem Soc* 98(25):8255-8260.
166. Hink MA, Visser NV, Borst JW, van Hoek A, & Visser AJWG (2003) Practical use of corrected fluorescence excitation and emission spectra of fluorescent proteins in Forster resonance energy transfer (FRET) studies. *J Fluoresc* 13(2):185-188.
167. Antonie J.W.G. Visser, Eugene S. Vysotski, & Lee J (2011) Critical Transfer Distance Determination Between FRET Pairs
168. Fu PKL & Turro C (1999) Energy transfer from nucleic acids to Tb(III): Selective emission enhancement by single DNA mismatches. *Journal of the American Chemical Society* 121(1):1-7.
169. Schreiber G & Fersht AR (1996) Rapid, electrostatically assisted association of proteins. *Nat Struct Biol* 3(5):427-431.
170. Radic Z, Kirchhoff PD, Quinn DM, McCammon JA, & Taylor P (1997) Electrostatic influence on the kinetics of ligand binding to acetylcholinesterase. Distinctions between active center ligands and fasciculin. *J Biol Chem* 272(37):23265-23277.
171. Scott AM, Antal CE, & Newton AC (2013) Electrostatic and hydrophobic interactions differentially tune membrane binding kinetics of the C2 domain of protein kinase Calpha. *J Biol Chem* 288(23):16905-16915.
172. Renner M, Danielson MA, & Falke JJ (1993) Kinetic control of Ca(II) signaling: tuning the ion dissociation rates of EF-hand Ca(II) binding sites. *Proc Natl Acad Sci U S A* 90(14):6493-6497.
173. Houdusse A, Love ML, Dominguez R, Grabarek Z, & Cohen C (1997) Structures of four Ca2+-bound troponin C at 2.0 A resolution: further insights into the Ca2+-switch in the calmodulin superfamily. *Structure* 5(12):1695-1711.
174. Mank M, *et al.* (2006) A FRET-based calcium biosensor with fast signal kinetics and high fluorescence change. *Biophys J* 90(5):1790-1796.
175. Wachter RM, Watkins JL, & Kim H (2010) Mechanistic diversity of red fluorescence acquisition by GFP-like proteins. *Biochemistry* 49(35):7417-7427.
176. Miyawaki A, Shcherbakova DM, & Verkhusha VV (2012) Red fluorescent proteins: chromophore formation and cellular applications. *Curr Opin Struct Biol* 22(5):679-688.
177. Rizzo MA, Davidson MW, & Piston DW (2009) Fluorescent protein tracking and detection: fluorescent protein structure and color variants. *Cold Spring Harbor protocols* 2009(12):pdb top63.
178. Piatkevich KD, *et al.* (2013) Extended Stokes shift in fluorescent proteins: chromophore-protein interactions in a near-infrared TagRFP675 variant. *Sci Rep* 3:1847.
179. Creemers TMH, Lock AJ, Subramaniam V, Jovin TM, & Volker S (1999) Three photoconvertible forms of green fluorescent protein identified by spectral hole-burning (vol 6, pg 557, 1999). *Nature Structural Biology* 6(7):706-706.
180. Dong J, Solntsev KM, & Tolbert LM (2006) Solvatochromism of the green fluorescence protein chromophore and its derivatives. *J Am Chem Soc* 128(37):12038-12039.
181. Usman A, *et al.* (2005) Excited-state structure determination of the green fluorescent protein chromophore. *J Am Chem Soc* 127(32):11214-11215.

182. Erez Y*, et al.* (2011) Structure and excited-state proton transfer in the GFP S205A mutant. *J Phys Chem B* 115(41):11776-11785.
183. Shu X*, et al.* (2007) An alternative excited-state proton transfer pathway in green fluorescent protein variant S205V. *Protein Sci* 16(12):2703-2710.
184. Ehrig T, O'Kane DJ, & Prendergast FG (1995) Green-fluorescent protein mutants with altered fluorescence excitation spectra. *FEBS Lett* 367(2):163-166.
185. Abbruzzetti S*, et al.* (2010) Photoswitching of E222Q GFP mutants: "concerted" mechanism of chromophore isomerization and protonation. *Photochem Photobiol Sci* 9(10):1307-1319.
186. Patterson GH & Lippincott-Schwartz J (2002) A photoactivatable GFP for selective photolabeling of proteins and cells. *Science* 297(5588):1873-1877.
187. Zapata-Hommer O & Griesbeck O (2003) Efficiently folding and circularly permuted variants of the Sapphire mutant of GFP. *BMC Biotechnol* 3:5.
188. Baird GS, Zacharias DA, & Tsien RY (1999) Circular permutation and receptor insertion within green fluorescent proteins. *P Natl Acad Sci USA* 96(20):11241-11246.
189. Nakai J, Ohkura M, & Imoto K (2001) A high signal-to-noise Ca(2+) probe composed of a single green fluorescent protein. *Nat Biotechnol* 19(2):137-141.
190. Zhang Y*, et al.* (2013) Structural basis for a hand-like site of the calcium sensor CatchER with fast kinetics. *Acta Crystallogr D Biol Crystallogr* 69.
191. Malmendal A*, et al.* (1998) When size is important. Accommodation of magnesium in a calcium binding regulatory domain. *J Biol Chem* 273(44):28994-29001.
192. Dobbins SE, Lesk VI, & Sternberg MJE (2008) Insights into protein flexibility: The relationship between normal modes and conformational change upon protein-protein docking. *P Natl Acad Sci USA* 105(30):10390-10395.
193. Dedecker P, De Schryver FC, & Hofkens J (2013) Fluorescent proteins: shine on, you crazy diamond. *J Am Chem Soc* 135(7):2387-2402.
194. Chattoraj M, King BA, Bublitz GU, & Boxer SG (1996) Ultra-fast excited state dynamics in green fluorescent protein: Multiple states and proton transfer. *P Natl Acad Sci USA* 93(16):8362-8367.
195. Yang F, Moss LG, & Phillips GN, Jr. (1996) The molecular structure of green fluorescent protein. *Nat Biotechnol* 14(10):1246-1251.
196. Ormo M*, et al.* (1996) Crystal structure of the Aequorea victoria green fluorescent protein. *Science* 273(5280):1392-1395.
197. Palm GJ*, et al.* (1997) The structural basis for spectral variations in green fluorescent protein. *Nat Struct Biol* 4(5):361-365.
198. Remington SJ (2000) Structural basis for understanding spectral variations in green fluorescent protein. *Methods Enzymol* 305:196-211.
199. Maddalo SL & Zimmer M (2006) The role of the protein matrix in green fluorescent protein fluorescence. *Photochem Photobiol* 82(2):367-372.
200. Fang C, Frontiera RR, Tran R, & Mathies RA (2009) Mapping GFP structure evolution during proton transfer with femtosecond Raman spectroscopy. *Nature* 462(7270):200-204.
201. Bell AF, He X, Wachter RM, & Tonge PJ (2000) Probing the ground state structure of the green fluorescent protein chromophore using Raman spectroscopy. *Biochemistry* 39(15):4423-4431.
202. Schellenberg P, Johnson E, Esposito AP, Reid PJ, & Parson WW (2001) Resonance Raman scattering by the green fluorescent protein and an analogue of its chromophore. *Journal of Physical Chemistry B* 105(22):5316-5322.
203. X H, Bell AF, & Tonge PJ (2002) Isotopic labeling and normal-mode analysis of a model green fluorescent protein chromophore. *Journal of Physical Chemistry B* 106(23):6056-6066.
204. Stoner-Ma D*, et al.* (2005) Observation of excited-state proton transfer in green fluorescent protein using ultrafast vibrational spectroscopy. *J Am Chem Soc* 127(9):2864-2865.
205. Agmon N (2005) Proton pathways in green fluorescence protein. *Biophysical Journal* 88(4):2452-2461.

206. Leiderman P, Huppert D, & Agmon N (2006) Transition in the temperature-dependence of GFP fluorescence: from proton wires to proton exit. *Biophys J* 90(3):1009-1018.

207. Agmon N (2007) Kinetics of switchable proton escape from a proton-wire within green fluorescence protein. *J Phys Chem B* 111(27):7870-7878.

208. Rizzuto R, Simpson AW, Brini M, & Pozzan T (1992) Rapid changes of mitochondrial Ca2+ revealed by specifically targeted recombinant aequorin. *Nature* 358(6384):325-327.

209. Grynkiewicz G, Poenie M, & Tsien RY (1985) A new generation of Ca2+ indicators with greatly improved fluorescence properties. *J Biol Chem* 260(6):3440-3450.

210. Paredes RM, Etzler JC, Watts LT, Zheng W, & Lechleiter JD (2008) Chemical calcium indicators. *Methods* 46(3):143-151.

211. Lakowicz JR & Geddes CD (1991) *Topics in fluorescence spectroscopy: Lifetime-based Sensing* (Plenum Press, New York) pp v. <1-10>.

212. Lakowicz JR, Szmacinski H, Nowaczyk K, Berndt KW, & Johnson M (1992) Fluorescence lifetime imaging. *Anal Biochem* 202(2):316-330.

213. Kumar ATN, Raymond SB, Bacskai BJ, & Boas DA (2008) Comparison of frequency-domain and time-domain fluorescence lifetime tomography. *Opt Lett* 33(5):470-472.

214. Gannot I, Ron I, Hekmat F, Chernomordik V, & Gandjbakhche A (2004) Functional optical detection based on pH dependent fluorescence lifetime. *Laser Surg Med* 35(5):342-348.

215. Harvey CD, Yasuda R, Zhong H, & Svoboda K (2008) The spread of Ras activity triggered by activation of a single dendritic spine. *Science* 321(5885):136-140.

216. Yasuda R, *et al.* (2006) Supersensitive Ras activation in dendrites and spines revealed by two-photon fluorescence lifetime imaging. *Nat Neurosci* 9(2):283-291.

217. Huang PC, *et al.* (2010) Visualization of the Orai1 homodimer and the functional coupling of Orai1-STIM1 by live-cell fluorescence lifetime imaging. *Microsc Microanal* 16(3):313-326.

218. Bloch S, *et al.* (2005) Whole-body fluorescence lifetime imaging of a tumor-targeted near-infrared molecular probe in mice. *J Biomed Opt* 10(5):054003.

219. Godavarty A, Sevick-Muraca EM, & Eppstein MJ (2005) Three-dimensional fluorescence lifetime tomography. *Medical physics* 32(4):992-1000.

220. Ardeshirpour Y, *et al.* (2012) In Vivo Fluorescence Lifetime Imaging Monitors Binding of Specific Probes to Cancer Biomarkers. *Plos One* 7(2).

221. Lakowicz JR, Szmacinski H, Nowaczyk K, & Johnson ML (1992) Fluorescence lifetime imaging of calcium using Quin-2. *Cell Calcium* 13(3):131-147.

222. Lakowicz JR, *et al.* (1994) Fluorescence lifetime imaging of intracellular calcium in COS cells using Quin-2. *Cell Calcium* 15(1):7-27.

223. Agronskaia AV, Tertoolen L, & Gerritsen HC (2004) Fast fluorescence lifetime imaging of calcium in living cells. *J Biomed Opt* 9(6):1230-1237.

224. Geiger A, *et al.* (2012) Correlating calcium binding, Forster resonance energy transfer, and conformational change in the biosensor TN-XXL. *Biophys J* 102(10):2401-2410.

225. Ward WW (1981) Properties of the coelenterate green fluorescent proteins. *Bioluminescence and Chemiluminescence: Basic Chemistry and Analytical Applications*, eds DeLuca MA & McElroy WD (Academic Press, New York), pp 225-234.

226. Campbell TN & Choy FYM (2001) The Effect of pH on Green Fluorescent Protein: a Brief Review. *Molecular Biology Today* 2(1):1-4.

227. Leiderman P, *et al.* (2007) Ultrafast excited-state dynamics in the green fluorescent protein variant S65T/H148D. 3. Short- and long-time dynamics of the excited-state proton transfer. *Biochemistry* 46(43):12026-12036.

228. Fron E, *et al.* (2013) Revealing the excited-state dynamics of the fluorescent protein Dendra2. *J Phys Chem B* 117(8):2300-2313.

229. Gepshtein R, Leiderman P, & Huppert D (2008) Origin of the nonexponential dynamics of excited-state proton transfer in wt-green fluorescent protein. *Journal of Physical Chemistry B* 112(24):7203-7210.

230. Solntsev KM, Al-Ainain SA, Il’ichev YV, & Kuzmin MG (2005) Effects of long-chain alkyl substituents on the protolytic reactions of naphthols. *Journal of Photochemistry and Photobiology A: Chemistry* 175(2–3):178-191.
231. Roberts NK & Northey HL (1974) Proton and Deuteron Mobility in Normal and Heavy-Water Solutions of Electrolytes. *J Chem Soc Farad T 1* 70(2):253-262.
232. Lewis GN & Doody TC (1933) The mobility of ions in (HHO)-H-2-O-2. *Journal of the American Chemical Society* 55:3504-3506.
233. Solntsev KM & Agmon N (2000) Dual asymptotic behavior in geminate diffusion-influenced reaction. *Chemical Physics Letters* 320(3–4):262-268.
234. Solntsev KM, *et al.* (2004) Excited-state proton transfer reactions of 10-hydroxycamptothecin. *J Am Chem Soc* 126(39):12701-12708.
235. Pines E, Huppert D, & Agmon N (1988) Geminate recombination in excited-state proton-transfer reactions: Numerical solution of the Debye--Smoluchowski equation with backreaction and comparison with experimental results. *The Journal of chemical physics* 88(9):5620-5630.
236. Agmon N, Pines E, & Huppert D (1988) Geminate recombination in proton-transfer reactions. II. Comparison of diffusional and kinetic schemes. *The Journal of chemical physics* 88(9):5631-5638.
237. Gopich IV, Solntsev KM, & Agmon N (1999) Excited-state reversible geminate reaction. I. Two different lifetimes. *The Journal of chemical physics* 110(4):2164-2174.
238. Agmon N (1999) Excited-state reversible geminate reaction. II. Contact geminate quenching. *The Journal of chemical physics* 110(4):2175-2180.
239. van Thor JJ (2009) Photoreactions and dynamics of the green fluorescent protein. *Chem Soc Rev* 38(10):2935-2950.
240. Shinobu A, Palm GJ, Schierbeek AJ, & Agmon N (2010) Visualizing proton antenna in a high-resolution green fluorescent protein structure. *J Am Chem Soc* 132(32):11093-11102.
241. Wang Q, Shui B, Kotlikoff MI, & Sondermann H (2008) Structural basis for calcium sensing by GCaMP2. *Structure* 16(12):1817-1827.
242. Simkovitch R, Huppert A, Huppert D, Remington SJ, & Miller Y (2013) Proton Transfer in Wild-Type GFP and S205V Mutant Is Reduced by Conformational Changes of Residues in the Proton Wire. *J Phys Chem B* 117(40):11921-11931.
243. Arpino JA, Rizkallah PJ, & Jones DD (2012) Crystal structure of enhanced green fluorescent protein to 1.35 A resolution reveals alternative conformations for Glu222. *PLoS One* 7(10):e47132.
244. Ducreux S, *et al.* (2004) Effect of ryanodine receptor mutations on interleukin-6 release and intracellular calcium homeostasis in human myotubes from malignant hyperthermia-susceptible individuals and patients affected by central core disease. *J Biol Chem* 279(42):43838-43846.
245. McCarthy TV, Quane KA, & Lynch PJ (2000) Ryanodine receptor mutations in malignant hyperthermia and central core disease. *Human mutation* 15(5):410-417.
246. Mekahli D, Bultynck G, Parys JB, De Smedt H, & Missiaen L (2011) Endoplasmic-reticulum calcium depletion and disease. *Cold Spring Harb Perspect Biol* 3(6).
247. Ma JJ (1995) Desensitization of the Skeletal-Muscle Ryanodine Receptor - Evidence for Heterogeneity of Calcium-Release Channels. *Biophysical Journal* 68(3):893-899.
248. Blatter LA, Tsugorka A, Shirokova N, & Rios E (1996) Eager triads in skeletal muscle: Heterogeneous distribution of voltage-elicited Ca2+ release revealed by confocal microscopy. *Biophysical Journal* 70(2):Tuam5-Tuam5.
249. Ma J, Hayek SM, & Bhat MB (2004) Membrane topology and membrane retention of the ryanodine receptor calcium release channel. *Cell Biochem Biophys* 40(2):207-224.
250. Meur G, Parker AK, Gergely FV, & Taylor CW (2007) Targeting and retention of type 1 ryanodine receptors to the endoplasmic reticulum. *J Biol Chem* 282(32):23096-23103.
251. George RA & Heringa J (2002) An analysis of protein domain linkers: their classification and role in protein folding. *Protein Eng* 15(11):871-879.

252. Arai M, Otsu K, MacLennan DH, & Periasamy M (1992) Regulation of sarcoplasmic reticulum gene expression during cardiac and skeletal muscle development. *Am J Physiol* 262(3 Pt 1):C614-620.
253. Kiviluoto S, *et al.* (2011) STIM1 as a key regulator for Ca2+ homeostasis in skeletal-muscle development and function. *Skeletal muscle* 1(1):16.
254. Jayaraman T, *et al.* (1992) FK506 binding protein associated with the calcium release channel (ryanodine receptor). *J Biol Chem* 267(14):9474-9477.
255. Du GG, Sandhu B, Khanna VK, Guo XH, & MacLennan DH (2002) Topology of the Ca2+ release channel of skeletal muscle sarcoplasmic reticulum (RyR1). *Proc Natl Acad Sci U S A* 99(26):16725-16730.
256. Carafoli E & Klee CB (1999) *Calcium as a cellular regulator* (Oxford University Press, New York) pp xiii, 642 p.
257. Crivici A & Ikura M (1995) Molecular and structural basis of target recognition by calmodulin. *Annu Rev Biophys Biomol Struct* 24:85-116.
258. Yang JJ, Gawthrop A, & Ye Y (2003) Obtaining site-specific calcium-binding affinities of calmodulin. *Protein Pept Lett* 10(4):331-345.
259. VanScyoc WS, *et al.* (2002) Calcium binding to calmodulin mutants monitored by domain-specific intrinsic phenylalanine and tyrosine fluorescence. *Biophysical Journal* 83(5):2767-2780.
260. Crouch TH & Klee CB (1980) Positive cooperative binding of calcium to bovine brain calmodulin. *Biochemistry* 19(16):3692-3698.
261. Elshorst B, *et al.* (1999) NMR solution structure of a complex of calmodulin with a binding peptide of the Ca2+ pump. *Biochemistry* 38(38):12320-12332.
262. Vetter SW & Leclerc E (2003) Novel aspects of calmodulin target recognition and activation. *Eur J Biochem* 270(3):404-414.
263. Schumacher MA, Crum M, & Miller MC (2004) Crystal structures of apocalmodulin and an apocalmodulin/SK potassium channel gating domain complex. *Structure* 12(5):849-860.
264. Saez JC, Berthoud VM, Branes MC, Martinez AD, & Beyer EC (2003) Plasma membrane channels formed by connexins: their regulation and functions. *Physiol Rev* 83(4):1359-1400.
265. Liu XZ, *et al.* (2001) Mutations in GJA1 (connexin 43) are associated with non-syndromic autosomal recessive deafness. *Hum Mol Genet* 10(25):2945-2951.
266. Lurtz MM & Louis CF (2003) Calmodulin and protein kinase C regulate gap junctional coupling in lens epithelial cells. *Am J Physiol Cell Physiol* 285(6):C1475-1482.
267. Valafar H & Prestegard JH (2004) REDCAT: a residual dipolar coupling analysis tool. *J Magn Reson* 167(2):228-241.
268. Schumacher MA, Rivard AF, Bachinger HP, & Adelman JP (2001) Structure of the gating domain of a Ca2+-activated K+ channel complexed with Ca2+/calmodulin. *Nature* 410(6832):1120-1124.
269. Meador WE, Means AR, & Quiocho FA (1992) Target enzyme recognition by calmodulin: 2.4 A structure of a calmodulin-peptide complex. *Science* 257(5074):1251-1255.
270. Maximciuc AA, Putkey JA, Shamoo Y, & Mackenzie KR (2006) Complex of calmodulin with a ryanodine receptor target reveals a novel, flexible binding mode. *Structure* 14(10):1547-1556.
271. Jiang J, *et al.* (2010) Site-specific modification of calmodulin Ca(2)(+) affinity tunes the skeletal muscle ryanodine receptor activation profile. *Biochem J* 432(1):89-99.
272. Rodney GG, Wilson GM, & Schneider MF (2005) A calmodulin binding domain of RyR increases activation of spontaneous Ca2+ sparks in frog skeletal muscle. *J Biol Chem* 280(12):11713-11722.
273. Menegazzi P, *et al.* (1994) Identification and characterization of three calmodulin binding sites of the skeletal muscle ryanodine receptor. *Biochemistry* 33(31):9078-9084.
274. Gangopadhyay JP & Ikemoto N (2011) Aberrant interaction of calmodulin with the ryanodine receptor develops hypertrophy in the neonatal cardiomyocyte. *Biochem J* 438(2):379-387.

275. Xiong LW, *et al.* (2002) Lobe-dependent regulation of ryanodine receptor type 1 by calmodulin. *J Biol Chem* 277(43):40862-40870.
276. Tugarinov V & Kay LE (2003) Ile, Leu, and Val methyl assignments of the 723-residue malate synthase G using a new labeling strategy and novel NMR methods. *J Am Chem Soc* 125(45):13868-13878.
277. Tugarinov V, Hwang PM, Ollerenshaw JE, & Kay LE (2003) Cross-correlated relaxation enhanced 1H[bond]13C NMR spectroscopy of methyl groups in very high molecular weight proteins and protein complexes. *J Am Chem Soc* 125(34):10420-10428.
278. Tugarinov V & Kay LE (2003) Side chain assignments of Ile delta 1 methyl groups in high molecular weight proteins: an application to a 46 ns tumbling molecule. *J Am Chem Soc* 125(19):5701-5706.
279. Zhang M & Vogel HJ (1993) Determination of the side chain pKa values of the lysine residues in calmodulin. *J Biol Chem* 268(30):22420-22428.
280. Takeuchi K, Ng E, Malia TJ, & Wagner G (2007) 1-13C amino acid selective labeling in a 2H15N background for NMR studies of large proteins. *J Biomol NMR* 38(1):89-98.
281. Ruschak AM & Kay LE (2010) Methyl groups as probes of supra-molecular structure, dynamics and function. *J Biomol NMR* 46(1):75-87.
282. Kos CH, *et al.* (2003) The calcium-sensing receptor is required for normal calcium homeostasis independent of parathyroid hormone. *J Clin Invest* 111(7):1021-1028.
283. Huang Y, *et al.* (2010) Calmodulin regulates Ca2+-sensing receptor-mediated Ca2+ signaling and its cell surface expression. *J Biol Chem* 285(46):35919-35931.
284. Conigrave AD, Mun HC, & Lok HC (2007) Aromatic L-amino acids activate the calcium-sensing receptor. *J Nutr* 137(6 Suppl 1):1524S-1527S; discussion 1548S.
285. Zhao P, *et al.* (2012) Proteomic identification of glycosylphosphatidylinositol anchor-dependent membrane proteins elevated in breast carcinoma. *J Biol Chem* 287(30):25230-25240.
286. Abbott KL, *et al.* (2008) Focused glycomic analysis of the N-linked glycan biosynthetic pathway in ovarian cancer. *Proteomics* 8(16):3210-3220.
287. Gonzalez DS, Karaveg K, Vandersall-Nairn AS, Lal A, & Moremen KW (1999) Identification, expression, and characterization of a cDNA encoding human endoplasmic reticulum mannosidase I, the enzyme that catalyzes the first mannose trimming step in mammalian Asn-linked oligosaccharide biosynthesis. *J Biol Chem* 274(30):21375-21386.
288. Huang HH & Stanley P (2010) A testis-specific regulator of complex and hybrid N-glycan synthesis. *The Journal of cell biology* 190(5):893-910.
289. Liu S, *et al.* (2007) Spin-labeled analogs of CMP-NeuAc as NMR probes of the alpha-2,6-sialyltransferase ST6Gal I. *Chem Biol* 14(4):409-418.
290. Lee HW, *et al.* (2002) Isolated EF-loop III of calmodulin in a scaffold protein remains unpaired in solution using pulsed-field-gradient NMR spectroscopy. *Biochim Biophys Acta* 1598(1-2):80-87.
291. Huang Y, *et al.* (2009) A single EF-hand isolated from STIM1 forms dimer in the absence and presence of Ca2+. *FEBS J* 276(19):5589-5597.
292. Tugarinov V, Hwang PM, Ollerenshaw JE, & Kay LE (2003) Cross-correlated relaxation enhanced 1H[bond]13C NMR spectroscopy of methyl groups in very high molecular weight proteins and protein complexes. *Journal of the American Chemical Society* 125(34):10420-10428.
293. Bokoch MP, *et al.* (2010) Ligand-specific regulation of the extracellular surface of a G-protein-coupled receptor. *Nature* 463(7277):108-112.
294. Klein-Seetharaman J, *et al.* (2004) Differential dynamics in the G protein-coupled receptor rhodopsin revealed by solution NMR. *Proc Natl Acad Sci U S A* 101(10):3409-3413.
295. Tugarinov V, Kanelis V, & Kay LE (2006) Isotope labeling strategies for the study of high-molecular-weight proteins by solution NMR spectroscopy. *Nat Protoc* 1(2):749-754.

296. Tugarinov V & Kay LE (2005) Methyl groups as probes of structure and dynamics in NMR studies of high-molecular-weight proteins. *Chembiochem : a European journal of chemical biology* 6(9):1567-1577.
297. Liu Y, Kahn RA, & Prestegard JH (Dynamic structure of membrane-anchored Arf*GTP. *Nat Struct Mol Biol* 17(7):876-881.
298. Siriwardena AH, Tian F, Noble S, & Prestegard JH (2002) A straightforward NMR-spectroscopy-based method for rapid library screening. *Angewandte Chemie* 41(18):3454-3457.
299. Venkitakrishnan RR, Benard O, Max M, & Markley JL (2012) Use of NMR saturation transfer difference spectroscopy to study ligand binding to membrane proteins. *Methods Mol Biol* 914:47-63.
300. Meyer B & Peters T (2003) NMR spectroscopy techniques for screening and identifying ligand binding to protein receptors. *Angewandte Chemie* 42(8):864-890.
301. Hartl FU, Lecker S, Schiebel E, Hendrick JP, & Wickner W (1990) The binding cascade of SecB to SecA to SecY/E mediates preprotein targeting to the E. coli plasma membrane. *Cell* 63(2):269-279.
302. Lill R, Dowhan W, & Wickner W (1990) The ATPase activity of SecA is regulated by acidic phospholipids, SecY, and the leader and mature domains of precursor proteins. *Cell* 60(2):271-280.
303. van der Wolk JP, Boorsma A, Knoche M, Schafer HJ, & Driessen AJ (1997) The low-affinity ATP binding site of the *Escherichia coli* SecA dimer is localized at the subunit interface. *Biochemistry* 36(48):14924-14929.
304. Wang HW, *et al.* (2003) Ring-like pore structures of SecA: implication for bacterial protein-conducting channels. *Proc Natl Acad Sci U S A* 100(7):4221-4226.
305. Chen Y, Tai PC, & Sui SF (2007) The active ring-like structure of SecA revealed by electron crystallography: conformational change upon interaction with SecB. *J. Struct. Biology* 159(1):149-153.
306. Wang H, Na B, Yang H, & Tai PC (2008) Additional *in vitro* and *in vivo* evidence for SecA functioning as dimers in the membrane: dissociation into monomers is not essential for protein translocation in *Escherichia coli*. *J. Bacteriol.* 190(4):1413-1418.
307. Hamman BD, Chen JC, Johnson EE, & Johnson AE (1997) The aqueous pore through the translocon has a diameter of 40-60 A during cotranslational protein translocation at the ER membrane. *Cell* 89(4):535-544.
308. Karamanou S, *et al.* (1999) A molecular switch in SecA protein couples ATP hydrolysis to protein translocation. *Mol. Microbiol.* 34(5):1133-1145.
309. Mitchell C & Oliver D (1993) Two distinct ATP-binding domains are needed to promote protein export by Escherichia coli SecA ATPase. *Mol Microbiol* 10(3):483-497.
310. Nakatogawa H, Mori H, & Ito K (2000) Two independent mechanisms down-regulate the intrinsic SecA ATPase activity. *The Journal of biological chemistry* 275(43):33209-33212.
311. Price A, Economou A, Duong F, & Wickner W (1996) Separable ATPase and membrane insertion domains of the SecA subunit of preprotein translocase. *The Journal of biological chemistry* 271(49):31580-31584.
312. Dapic V & Oliver D (2000) Distinct membrane binding properties of N- and C-terminal domains of Escherichia coli SecA ATPase. *The Journal of biological chemistry* 275(32):25000-25007.
313. Hirano M, Matsuyama S, & Tokuda H (1996) The carboxyl-terminal region is essential for Sec-A dimerization. *Biochem Biophys Res Commun* 229(1):90-95.
314. Breukink E, *et al.* (1995) The C terminus of SecA is involved in both lipid binding and SecB binding. *The Journal of biological chemistry* 270(14):7902-7907.
315. Chen X, Brown T, & Tai PC (1998) Identification and characterization of protease-resistant SecA fragments: secA has two membrane-integral forms. *J Bacteriol* 180(3):527-537.
316. Ahn T & Kim H (1998) Effects of nonlamellar-prone lipids on the ATPase activity of SecA bound to model membranes. *J. Biol. Chem.* 273(34):21692-21698.

317. Breukink E, Demel RA, de Korte-Kool G, & de Kruijff B (1992) SecA insertion into phospholipids is stimulated by negatively charged lipids and inhibited by ATP: a monolayer study. *Biochemistry* 31(4):1119-1124.
318. Keller RC, *et al.* (1996) Mode of insertion of the signal sequence of a bacterial precursor protein into phospholipid bilayers as revealed by cysteine-based site-directed spectroscopy. *Biochemistry* 35(9):3063-3071.
319. Ulbrandt ND, London E, & Oliver DB (1992) Deep penetration of a portion of Escherichia coli SecA protein into model membranes is promoted by anionic phospholipids and by partial unfolding. *The Journal of biological chemistry* 267(21):15184-15192.
320. Zimmer J & Rapoport TA (2009) Conformational flexibility and peptide interaction of the translocation ATPase SecA. *J Mol Biol* 394(4):606-612.
321. Sharma V, *et al.* (2003) Crystal structure of Mycobacterium tuberculosis SecA, a preprotein translocating ATPase. *Proc Natl Acad Sci U S A* 100(5):2243-2248.
322. Papanikolau Y, *et al.* (2007) Structure of dimeric SecA, the *Escherichia coli* preprotein translocase motor. *J. Mol. Biol.* 366(5):1545-1557.
323. Osborne AR, Clemons WM, Jr., & Rapoport TA (2004) A large conformational change of the translocation ATPase SecA. *Proc. Natl. Acad. Sci. U S A* 101(30):10937-10942.
324. Hunt JF, *et al.* (2002) Nucleotide control of interdomain interactions in the conformational reaction cycle of SecA. *Science* 297(5589):2018-2026.
325. Sardis MF & Economou A (2010) SecA: a tale of two protomers. *Mol Microbiol* 76(5):1070-1081.
326. Vassylyev DG, *et al.* (2006) Crystal structure of the translocation ATPase SecA from Thermus thermophilus reveals a parallel, head-to-head dimer. *J. Mol. Biol.* 364(3):248-258.
327. Matousek WM & Alexandrescu AT (2004) NMR structure of the C-terminal domain of SecA in the free state. *Biochim Biophys Acta* 1702(2):163-171.
328. Dempsey BR, *et al.* (2004) Solution NMR structure and X-ray absorption analysis of the C-terminal zinc-binding domain of the SecA ATPase. *Biochemistry* 43(29):9361-9371.
329. Gelis I, *et al.* (2007) Structural basis for signal-sequence recognition by the translocase motor SecA as determined by NMR. *Cell* 131(4):756-769.
330. Chou YT, Swain JF, & Gierasch LM (2002) Functionally significant mobile regions of Escherichia coli SecA ATPase identified by NMR. *J Biol Chem* 277(52):50985-50990.
331. Keramisanou D, *et al.* (2006) Disorder-order folding transitions underlie catalysis in the helicase motor of SecA. *Nat Struct Mol Biol* 13(7):594-602.
332. Palladino P, *et al.* (2011) Structural determinants of protein translocation in bacteria: conformational flexibility of SecA IRA1 loop region. *J Pept Sci* 17(4):263-269.
333. Macnaughtan MA, Kane AM, & Prestegard JH (2005) Mass spectrometry assisted assignment of NMR resonances in reductively 13C-methylated proteins. *J Am Chem Soc* 127(50):17626-17627.
334. Loria JP, Rance M, & Palmer AGr (1999) A Relaxation-Compensated Carr−Purcell−Meiboom−Gill Sequence for Characterizing Chemical Exchange by NMR Spectroscopy. *Journal of the American Chemical Society* 121(10):2331-2332.

APPENDICES

Appendix A Scripts for NMR data processing

Resi_sorting-1.py

```
    import sys, string
    a=open('<filename>', "r")
    b=open('presort.txt', 'w')
    lines=a.readlines()
    for i in range(0, len(lines)):
        if i>=3:
b.write(lines[i])
a.close()
b.close()
```

Resi-sorting-2.py

```
    import sys, string, re
    a1=open('presort.txt', "r")
    new=open('sorted_aligned.txt', 'w')
    lines1=a1.readlines()
    splitter=re.compile(r'[\D]')
    t=[]
    resinum_list=[]
    resinum_sort=[]
    for i in range(0, len(lines1)):
        t.append(lines1[i].split())
    for j in range(0, len(lines1)):
```

```
    resinum_list.append(splitter.split(t[j][0]))
    resinum_sort.append(resinum_list[j][1])
    t[j][0]=t[j][0].replace(t[j][0],resinum_sort[j])
for n in range(len(t)):
    t[n][0]=int(float(t[n][0]))
t.sort()
for x in range(0,len(t)):
    t[x].insert(3,'\n')
t1=t
t2=[]
t2.append(t1[0])
for x in range(0, len(t1)-1):
    if t1[x+1][0]!=t1[x][0]+1:
        diff = t1[x+1][0] - t1[x][0]
        for index in range(1, diff+1):
            t2.append([t1[x][0]+index, '0', '999', '\n'])
    else:
        t2.append(t1[x+1])
for y in range(0,len(t2)):
   t2[y][0]=str(t2[y][0])
for z in range(0,len(t2)):
    t2[z]='\t'.join(t2[z])
t2=''.join(t2)
#print t2
new.write(t2)
new.close()
```

```
        a1.close()
```

To convert nmrpipe output to sparky readable file *.ucsf for TauC data processing (tosparky.com)

```
#!/bin/csh
pipe2ucsf test1.ft2 1.ucsf
pipe2ucsf test2.ft2 2.ucsf
pipe2ucsf test3.ft2 3.ucsf
pipe2ucsf test4.ft2 4.ucsf
pipe2ucsf test5.ft2 5.ucsf
pipe2ucsf test6.ft2 6.ucsf
pipe2ucsf test7.ft2 7.ucsf
pipe2ucsf test8.ft2 8.ucsf
```

To generate the Modelfree input mfdata (mfdata-gen.py)

```
import string
afile=open('input.txt','r')
mfdata=open('mfdata.txt','w')
lines=afile.readlines()
alist=[]
blist=[]
for i in range (1, len(lines)):
        alist.append(lines[i].split())
blist=alist
```

```
newlist=['spin\t','sample_','n','\n','R1\t','599.863\t','R1','\t','0.030\t','1\n','R2\t','599.863\t','R2','\t','0.300\t','1\n','NOE\t','599.863\t','NOE','\t','0.040\t','1\n','\n']
for n in range (0, len(alist)):
	pos1=newlist.index('spin\t')+2
	newlist.pop(pos1)   #remove the value at the given index
	newlist.insert(pos1,blist[n][0])
	pos2=newlist.index('R1\t')+2
	newlist.pop(pos2)
	newlist.insert(pos2,blist[n][1])
	pos3=newlist.index('R2\t')+2
	newlist.pop(pos3)
	newlist.insert(pos3,blist[n][2])
	pos4=newlist.index('NOE\t')+2
	newlist.pop(pos4)
	newlist.insert(pos4,blist[n][3])
	table=".join(newlist)
	print table
	mfdata.write(table)
afile.close()
mfdata.close()
```

To evaluate the accuracy of the output of Modelfree (sim_acc_val.py)

```
import string, math
afile=open('simu_acc.txt','r')
lines=afile.readlines()
```

```
alist=[]
a=[]
acc=[]
for n in range(0, len(lines)):
        alist.append(lines[n].split())
a=alist
extra=[]
for x in range(0,len(alist)):
        if len(alist[x])!=6:
                extra.append(alist[x])
for x in range(0,len(extra)):
        a.remove(extra[x])
a.remove(a[0])
for i in range(0, len(a)):
        for j in range(0,len(a[0])):
        a[i][j]=float(a[i][j])
for i in range(0,len(a)/3):
        Esum=((a[i][1]-a[i][4])/a[i][2])**2+((a[i+len(a)/3][1]-a[i+len(a)/3][4])/a[i+len(a)/3][2])**2+((a[i+len(a)/3*2][1]-a[i+len(a)/3*2][4])/a[i+len(a)/3*2][2])**2
        Csum=(0.1*a[i][4]/a[i][2])**2+(0.1*a[i+len(a)/3][4]/a[i+len(a)/3][2])**2+(0.1*a[i+len(a)/3*2][4]/a[i+len(a)/3*2][2])**2
        perc=Esum/Csum
        if perc>0.5:
                print a[i][0]
        acc.append(str(perc))
seq=[]
```

```
for i in range(0,len(a)/3):
        seq.append(str(a[i][0]))
out=open('sim-acc-out.txt','w')
for i in range (0, len(seq)):
        out.write(".join([seq[i],'\t',acc[i],'\n']))
afile.close()
out.close()
```

Appendix B Protocols for NMR data processing

NMR Diffusion Experiment and Data Processing Using 600 MHz Spectrometer Computer

Put sample in the Shigemi NMR tube. The material above and below protein sample should be the same to obtain good diffusion data.

Experiment set-up:

Type explib to find the experiment with pulse sequence “diffusion-led” (under Hing’s profile, it should be exp29)

Type jexp29 to go to the diffusion experiment and then type dg to show the parameters.

Adjust pw by typing pw=x.xx

Array gradient level by typing array

>Parameter: gzlvl1

>Steps: 40

>Initial value: 100

>Increment: 400 (the strongest gradient level will be 15700)

Check parameters and run by typing ga. (Usually nt=320; ss=32 in 600 MHz. This pulse sequence is not sensitive as 1D proton, so more scans are required than normal 1D.)

It is better to check whether the water signal is overflow by a test run (set, gzlvl1=15700, ss=4, nt=32, and run). The stronger the gradient level, the less intensity of protein peaks but higher water intensity will be generated. The gradient steps and level is dependent on the decay of the molecule. If it decays fast, both the gradient steps and max level can be reduced.

Processing:

Directly from the varian:

1. After diffusion experiment is complete, (exp29) type **wft (1)** to phase the data for the first spectrum.
2. Type **vs?** to find out what the scale is and set it higher.
3. Choose a peak in the spectrum that is not the solvent peak, and put the cursor on the peak and left click.
4. Type **nl**. Write down the peak height and frequency.
5. Type **wft (2)** and type nl again to write down peak height and frequency.
6. Repeat steps 4 and 5 for all 40 spectra for the same peak.

Using Mnova:

1. Copy the data directory (***.fid) to the local PC installed Mnova.
2. File-Open-Open Fid file under data directory.

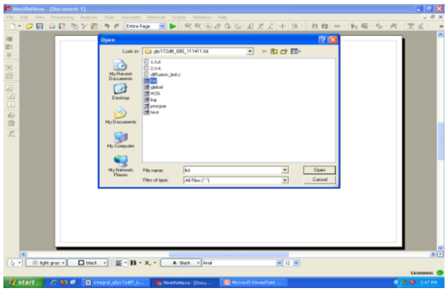

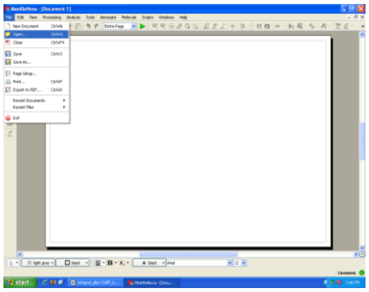

3. Hold shift key and arrow up/down key to select first spectrum, which is the active spectrum.

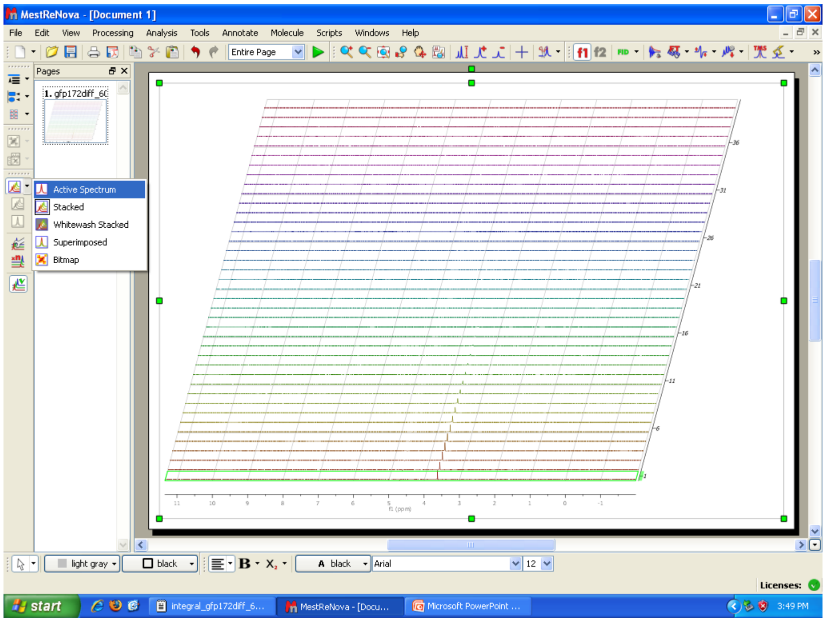

4. Use the mouse middle wheel to adjust the intensity.

5. Phase the first spectrum manually. Right click on the spectrum and select manual phase. Adjust phase by dragging mouse up or down while holding either right (PH1) or left (PH0) button of mouse in the light blue window. Hold Ctrl key for the fine tune. Adjust pivot point if you can not get right phase and adjust the phase again.

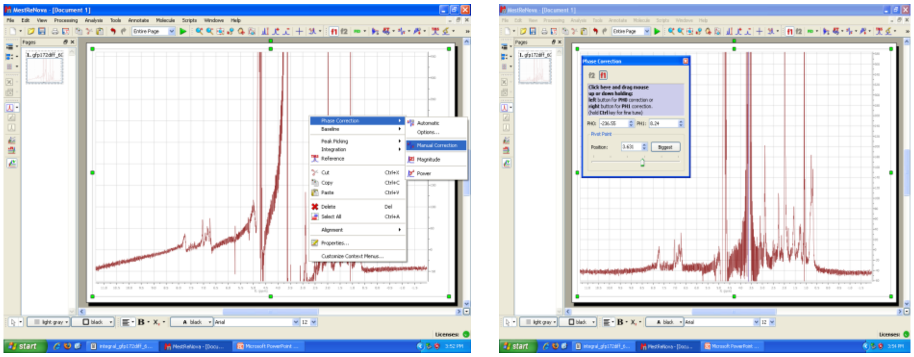

Click here and drag mouse up or down holding: left button for PH0 correction or right button for PH1 correction. (hold Ctrl key for fine tune)

PH0: -236.55 PH1: 0.24

6. Select stacked spectrum. Increase the peak intensity and look at the decay. Choose protein peaks which decays slower than the buffer peak. Expand the protein peak to be integrated by zooming in.

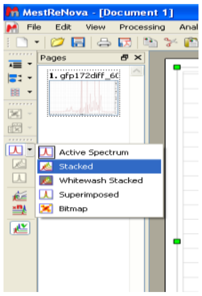

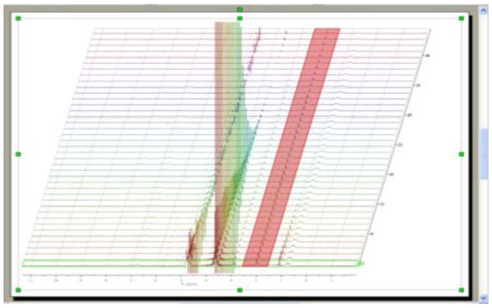

7. To integrate the selected region, go to Analysis – Integration – Manual. You may also go back to the active spectrum to see a single one instead of the stacked spetra, which is easier to select the region to be integrated. The baseline regions beside the peak are also needed to be integrated.

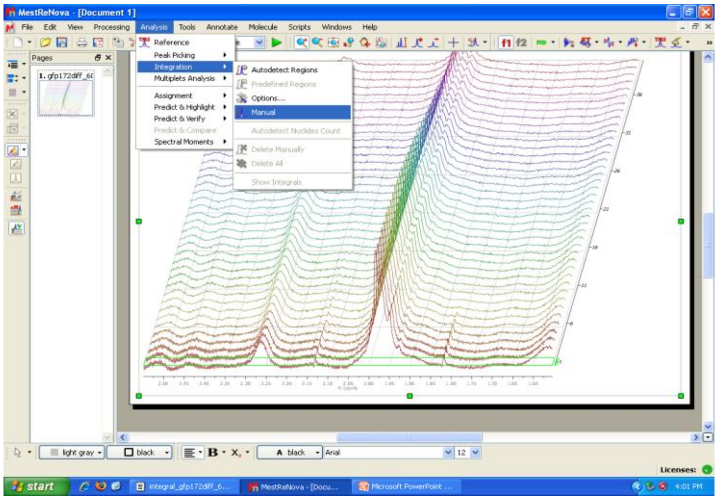

8. Save the integration. Go to File- Save as and choose MestReNova integrals (*.txt) from the Save as type. Put the file name and click Save.

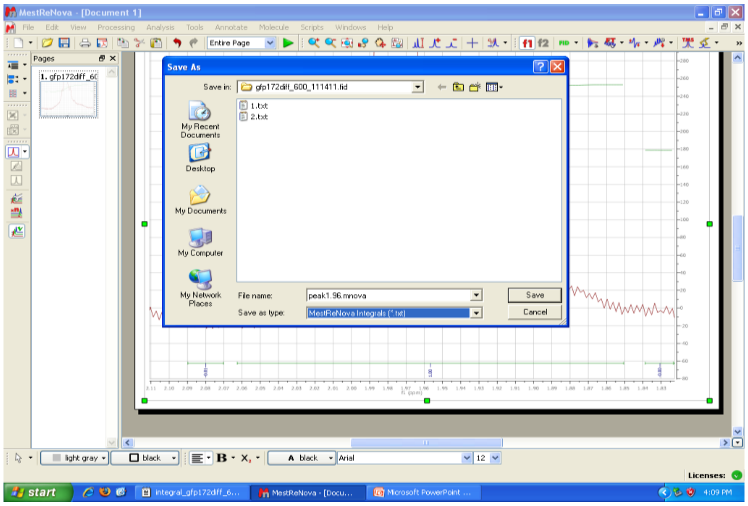

Save in: gfp172diff_600_111411.fid

File name: peak1.96.mnova

Save as type: MestReNova Integrals (*.txt)

9. Open data file from Excel:

A: Data sets number; B: Fid name; C and D: integrated peak region in ppm; E: Normalized peak; F: Integrated value for data fitting. The rest of columns are similar but for baseline area integration. Subtract baseline from integrated protein peak. Use KGraph to get diffusion constant.

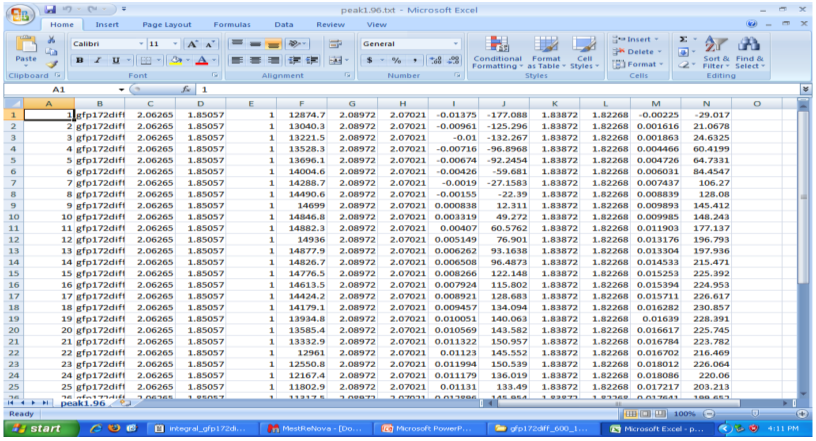

	A	B	C	D	E	F	G	H	I	J	K	L	M	N	O
1	1	gfp172diff	2.06265	1.85057	1	12874.7	2.08972	2.07021	-0.01375	-177.088	1.83872	1.82268	-0.00225	-29.017	
2	2	gfp172diff	2.06265	1.85057	1	13040.3	2.08972	2.07021	-0.00961	-125.296	1.83872	1.82268	0.001616	21.0678	
3	3	gfp172diff	2.06265	1.85057	1	13221.5	2.08972	2.07021	-0.01	-132.267	1.83872	1.82268	0.001863	24.6325	
4	4	gfp172diff	2.06265	1.85057	1	13528.3	2.08972	2.07021	-0.00716	-96.8968	1.83872	1.82268	0.004466	60.4199	
5	5	gfp172diff	2.06265	1.85057	1	13696.1	2.08972	2.07021	-0.00674	-92.2454	1.83872	1.82268	0.004726	64.7331	
6	6	gfp172diff	2.06265	1.85057	1	14004.6	2.08972	2.07021	-0.00426	-59.681	1.83872	1.82268	0.006031	84.4547	
7	7	gfp172diff	2.06265	1.85057	1	14288.7	2.08972	2.07021	-0.0019	-27.1583	1.83872	1.82268	0.007437	106.27	
8	8	gfp172diff	2.06265	1.85057	1	14490.6	2.08972	2.07021	-0.00155	-22.39	1.83872	1.82268	0.008839	128.08	
9	9	gfp172diff	2.06265	1.85057	1	14699	2.08972	2.07021	0.000838	12.311	1.83872	1.82268	0.009893	145.412	
10	10	gfp172diff	2.06265	1.85057	1	14846.8	2.08972	2.07021	0.003319	49.272	1.83872	1.82268	0.009985	148.243	
11	11	gfp172diff	2.06265	1.85057	1	14882.3	2.08972	2.07021	0.00407	60.5762	1.83872	1.82268	0.011903	177.137	
12	12	gfp172diff	2.06265	1.85057	1	14936	2.08972	2.07021	0.005149	76.901	1.83872	1.82268	0.013176	196.793	
13	13	gfp172diff	2.06265	1.85057	1	14877.9	2.08972	2.07021	0.006262	93.1638	1.83872	1.82268	0.013304	197.936	
14	14	gfp172diff	2.06265	1.85057	1	14826.7	2.08972	2.07021	0.006508	96.4873	1.83872	1.82268	0.014533	215.471	
15	15	gfp172diff	2.06265	1.85057	1	14776.5	2.08972	2.07021	0.008266	122.148	1.83872	1.82268	0.015253	225.392	
16	16	gfp172diff	2.06265	1.85057	1	14613.5	2.08972	2.07021	0.007924	115.802	1.83872	1.82268	0.015394	224.953	
17	17	gfp172diff	2.06265	1.85057	1	14424.2	2.08972	2.07021	0.008921	128.683	1.83872	1.82268	0.015711	226.617	
18	18	gfp172diff	2.06265	1.85057	1	14179.1	2.08972	2.07021	0.009457	134.094	1.83872	1.82268	0.016282	230.857	
19	19	gfp172diff	2.06265	1.85057	1	13934.8	2.08972	2.07021	0.010051	140.063	1.83872	1.82268	0.01639	228.391	
20	20	gfp172diff	2.06265	1.85057	1	13585.4	2.08972	2.07021	0.010569	143.582	1.83872	1.82268	0.016617	225.745	
21	21	gfp172diff	2.06265	1.85057	1	13332.9	2.08972	2.07021	0.011322	150.957	1.83872	1.82268	0.016784	223.782	
22	22	gfp172diff	2.06265	1.85057	1	12961	2.08972	2.07021	0.01123	145.552	1.83872	1.82268	0.016702	216.469	
23	23	gfp172diff	2.06265	1.85057	1	12550.8	2.08972	2.07021	0.011994	150.539	1.83872	1.82268	0.018012	226.064	
24	24	gfp172diff	2.06265	1.85057	1	12167.4	2.08972	2.07021	0.011179	136.019	1.83872	1.82268	0.018086	220.06	
25	25	gfp172diff	2.06265	1.85057	1	11802.9	2.08972	2.07021	0.01131	133.49	1.83872	1.82268	0.017217	203.213	

10. Fitting data by KGraph by exp(-m1*m0^2); m1=x.xxx (m0 is gradient strength)

$$Intensity = \exp[-(\gamma g \delta)^2 D(\Delta - \frac{\delta}{3})]$$

$$m1 = (\gamma \delta x / 32768)^2 D(\Delta - \frac{\delta}{3})$$

$$\frac{m1_{ref}}{D_{ref}} = \frac{m1}{D}$$

$$m0 = gzlvl1 = \frac{gradient\_strength \times 32768}{x}$$

γ is the gyromagnetic ratio $\gamma_{proton} = 2.675 \times 10^8$ rad s^{-1} T^{-1}

g is the gradient strength

Δ is the delay time between two pulses and δ is the delay time in gradient channel. Both are constant in the experiment.

D is the diffusion constant.

RDC J-modulation data processing protocol

1. Before starting, you need Linux system or Mac OS, perl, Sybyl, GNUplot.
2. In the fid directory, type **csh** to use C-shell.
3. Go to the data result directory xxx.fid
4. Create a new sub-directory by **mkdir Isotropic,** move all files to Isotropic.
5. Under the directory Isotropic, create a new sub-directory by mkdir Data.
6. Copy scripts NH-jmod4edit.pl to the result data directory xxx.fid; copy make_seperate2.pl and fitR_all.pl to the Data directory. So the directory tree will be:

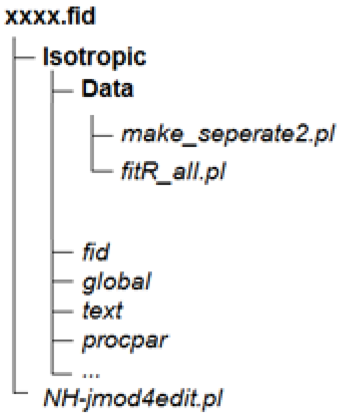

7. Then type **NH-jmod4edit.pl Isotropic Delta**. Isotropic is the name of the directory that contains all the fid files. This command will process the first fid. After this step, a file called test1.ft2 will be generated in the Isotropic directory.
8. Type **nmrDraw** to open the NMRDraw program.
9. Select the file test1.ft2 to open. Adjust the phase of the data. Only require to adjust the first one and then the other ones will be automatically phased in the same way as the first one.
10. Edit the ft2.com file to correct the phase. Under Linux: gedit ft2.com; Under Mac: xedit ft2.com
11. In the fid directory, type **NH-jmod4edit.pl Isotropic Delta spark**. This will process all the fid files and generate .ucsf files for each fid.
12. Open the Sparky program. Open the .ucsf files and assign the peaks. Open the HSQC which has been assigned. Check whether the RDC spectra are shifted compared to HSQC. If so, adjust them back according to HSQC spectrum by clicking st. Move mouse cursor to the HSQC and select all peaks by clicking pa, copy all assignment by clicking oc; move mouse cursor to one RDC spectrum and paste assignment by clicking op.
13. Repeat step 12 for all .ussf files.

14. Save the peak list with data height flag on. Open the peak list window by clicking lt. Click Option button and check “Data height”, “Assignment” and “Frequency (ppm)”. Click Save and save them as *.list under the Data directory.
15. Repeat 14 to save peak lists of all *.ucsf.
16. After saving all the peak lists for each fid, go to the Data directory and type **./make_seperate2.pl**, this will generate .dat files for each assigned peak.
17. Type **./fitR_all.pl**. This will generate a file called fit, in which you can find the coupling constants (J) for the assigned signals of the isotropic sample. The program gnuplot must be correctly installed first. To do this in Mac OS X 10.4:
18. Install Aquaterm 1.0.0.dmg, which is under ~/Joy/. This step is required by OS X10.4.
19. Install gnuplot-4.0.0.dmg. Or compile gnuplot-4.4.4. Both are under ~/Joy/. To compile gnuplot-4.4.4, unpack the tar file by `tar xpf gnuplot-4.4.4.tar`; go to the gnuplot-4.4.4 directory, and type `./configure`, many message about your system will show up; type `make check`, which will compile gnuplot and do the self-checking; type `sudo make install`, and type the password.
20. This program can only run under bash, not fully functions under c-shell. So don’t run fitR_all.pl under C-shell, even not working in the terminal which was changed to C-shell and then changed back to bash. Otherwise many errors will occur and no results come out.
21. You can use command `more fit` to see the fit file. It contains three columns, residue assignment, coupling constant and the error. Note that the column is not sorted as the residue number but the alphabetical order.
22. Repeat the above steps for the data collected with aligning medium and obtain the file fit containing J+D.

23. Calculate the RDC by subtracting the coupling constant of the isotropic sample from the aligned sample. RDC=(J+D)-J.

24. Save the RDC as a single column .txt file. For residues that their RDCs cannot be determined, give a value of 999 instead. So every residue must have a RDC value.

25. Open the REDCAT program by typing **REDCAT.tcl**.

File → **Prepare Input**.

Enter the name of your PDB file under **PDB Input file**.

The pdb file should contain H atom coordinates. This can be done by adding H in Sybyl. The pdb file should contain only ATOM ….

Enter a name for the output REDCAT file (for example: xxx.redcat).

Fill in other info:

Atom 1 = N

Atom 2 = H

Gap = 0

Max RDC =24350

Error = 10% of the range of RDC (for example, if RDCs are from -15 to 20, then range = 35, error = 35 × 10% = 3.5)

Click the **Run** button. After the .redcat file is prepared, click **OK**, and **Done**.

File → **Load**

Load the .redcat file, which is generated at step 21 and named at step 19.

File → **Import RDC Tool** → **Two Column ASCII**

Select the single column .txt file and open. NOTE: the first residue in rdc.txt should be the same as the pdb structure. e.g. the pdb starts from the resi#3, so the first two rdc values will be deleted.

Make sure that the residues with RDC values of 999 and missing coordinates are unselected.

Hit the **Run** button.

You will see a table showing each of the residues in either grey meaning not used, green meaning rdc accepted or red meaning rdc rejected.

Tools → **Error Analysis** → **Perform Error Analysis**

Unselect those residues with large error (remove residues step by step, from those with large error), clear the window and **Run** again. Repeat this until there is no red residue.

Tools → **Solution** → **Get Solutions**

If there is no solution, continue unselecting residues with high error until there is solution.

If there is solution, get the best solution.

Tools → **Solution** → **Get Best Solution**. **The values of Sxx, Syy, Szz and Euler angles will be given in the best solution.**

Tools → **Calculations** → **Calculate** → **Substitute RDC**

Enter the Sxx, Syy, Szz, and the Euler angles to calculate. Select error: constant value = 0.

Click '**Calculate RDC**'. A file called "plotcorr.dat" will be generated, which contains two columns, the first one is calculated RDC and the second one is measured RDC. Plot them in KGraph and fit the data using Y=X equation. Y=Calculated RDC and X=Measured RDC.

Processing and analyzing dynamic data and preparation for Modelfree.

1. Processing T1, T2, and NOE data the same way as regular HSQC data.
2. Assigned the peaks.
3. Integrate peak volume by clicking it.
4. Selected all peaks (pa) and type it. Unselect the first one “allow … motion”
5. Integrated the selected peaks (pi), this may take a while.
6. Open the peak list (lt), in the option, select volume, then update, then save the list using filename starting with the T1 or T2 (s), for example, 0.01lista.filename.list.
7. Repeat the above steps for all spectra.
8. Run make_separateT.pl to generate the volume vs time table for each residue.dat.
9. Run fitall_T1(T2).pl to fit the decay of the peak volume using the equation y = m1*exp(-M0/m2). M0 = relaxT, m1 is the initial volume at relaxT = 0, m2 is T1 or T2. For CD2, T1 ~700 ms, T2 ~100 ms.
10. Copy the T1 (s), T2 (s) and both NOE on and off to Excel and calculate the R1, R2 and NOE ratio of on over off
11. Make a table with four columns: Residue, R1, R2 and NOE ratio. Copy the table to the notepad and save it as txt format. The filename should be input.txt.
12. Run mfdata-gen.py to generate the mfdata file.

Protocol of TauC data processing

1. Prepare scripts: separate_2d.c, cut.sh, fid_8.com, ft2.com, ft2_8.com, tosparky.com, getcro.pl, calcTauC.pl; and save them under the fid data directory (xxx.fid).
2. To split the fid from one to 8 fids
    a. Compile the script separate_2d.c (on the unix prompt type: gcc separate_2d.c)
    b. Once you have compiled it correctly, you will see a file generated, called a.out.
    c. Edit cut.sh. If there is n values in the Delta array, you can find fid1 - fidn ni np. You will just execute the script cut.sh (on the unix prompt type: cut.sh). If the script works correctly, you will see 8 additional fids
3. Check fid_8.com. There are 8 convertions included. Type ./fid.com to convert the fid from Varian to NMRpipe format. Files named test1.fid, test2.fid….test8.fid will be generated.
4. Type ./ft2.com to generate test1.ft2. Then use ft2.com to process the data. Open NMRDraw to correct the phase. Then correct the phase by editing the ft2_8.com file, and type ./ft2_8.com.
5. Convert the files into Sparky format by typing csh tosparky.com. It will generate .ucsf files.
6. Assign the spectra and calculate TauC.
    a. Open all the spectra in Sparky, as well as a spectrum already assigned. Don’t adjust the peak position because the peak will move from TROSY position to the normal decouple position in the 8 spectra increment. Assign the peaks. (You can overlay the 1.ucsf and the assigned spectrum by (ol). Try to shift 1.ucsf and overlay peaks with assigned one by (st) first. Then copy the ornaments to 1.ucsf. Using center peak (pc) to move ornament to the center of the peaks. Then shift the spectrum back. The corre-

sponding ornaments will shift along with the peaks. Copy the ornament of n.ucsf to n+1.ucsf.

b. Once you have assigned, type pa to select all of the peaks. Type rh to open the relaxation peak fitting window. Click the ‘set up’ button to open another window, select the spectra and assign the time (time (ms) = 1000 × Delta, the unit of Delta is sec). Click close once done. Then type rh again in any of the spectrum, it will calculate the decay time. Save this as raw-data.list.

c. You will use the "getcro.pl" script to convert the data to frequency, (in unix prompt type: ./getcro.pl raw-data.list > data.cc). The second column in data.cc will be η. Check data.cc, and delete the rows with either zero or negative values.

d. Now to calculated the TauC, use the "calcTauC.pl", (in the unix prompt type: ./calcTauC.pl data.cc > data.TauC) this will give you the TauC. The first column should be residue number, the second column should be TauC, and the third column is error.

Appendix C Analysis of hydrogen bonds of MD simulation for CatchER

Binding site: 222 224 201 203 146 (all minus 1 from the original)

hbond net work around cro: 66 202 204 221, water 230-236, 81 71 68 6 147

Data was saved to series hbt,

data was sorted, intra-residue interactions are NOT included,

Distance cutoff is 3.00 angstroms, angle cutoff is 120.00 degrees

Hydrogen bond information dumped for occupancies > 0.1

Dumping schematic of time series after each h-bond key follows:

```
|        .        -         o         x         *         @        |
 0-5%    5-20%    20-40%    40-60%    60-80%    80-95%    95-100%  occupancy

DONOR             ACCEPTORH          ACCEPTOR

atom#:res@atom            atom#:    res@atom           atom#:res@atom  %occc     distance          angle
         lifetime         max       occ
```

Apo

```
| 3500:221@OE2|  996       :66@HG1                  995:66@OG1 |     88.5      2.752     (0.12)    13.76(-7.54)
         8.9(-7.8) 33      |**@*@x@@**x*x*****@|
| 1013:66@O2  |  1488      :95@HH12        1486:95@NH1 |    69.5      2.804     (0.09)    34.36(-11.41)       7.3(-7.9)
         32      |-@@**x**x@**x*@.   |
| 1013:66@O2  |  1491      :95@HH22        1489:95@NH2 |    41        2.825     (0.1)     44.84(-10.36)       1.6(-1.5)
         10      |xxoxxoo-o.----...-@|
| 1016:66@O3  |  1415      :91@HH 1414     :91@OH  |          55.5      2.826     (0.1)     30.4(-12.66)        2.8(-2.4)
         11      |x  o--oxo*xxoxx*x*@|
| 1006:66@OH  |  2289      :144@HH                  2288:144@OH |    31.5      2.878     (0.09)    18.64(-10.15)
         1.8(-1)           4         | o--ox-- --....-.* |
| 1006:66@OH  |  3641      :235@H1 3640    :235@O  |          15.5      2.839     (0.09)    25.75(-12.01)       1.2(-0.4)
         2       |..... ...--.-. .o. |
| 2333:147@ND1|  1007      :66@HH 1006     :66@OH  |          41.5      2.806     (0.11)    40.69(-13.11)       2.4(-2.3)
         10      |xx..--oxooxxxx.-   |
```

Holo

```
| 3500:221@OE2 | 996       :66@HG1                  995:66@OG1 |     91.5      2.725 ( 0.12)       14.54(7.20)
         11.4(7.9) 32      |@x@**@**@**x*@@**@@|
| 1013:66@O2  |  1488      :95@HH12        1486:95@NH1 |    53        2.807 ( 0.09)       37.27(10.83)        10.6(7.7)
         22      |@@*@x***@*o        |
| 1013:66@O2  |  1490      :95@HH21        1489:95@NH2 |    35.5      2.814 ( 0.09)       27.21 (12.21)       5.9(6.2)
         23      |         .*x*@@**@|
| 1013:66@O2  |  1491      :95@HH22        1489:95@NH2 |    28        2.804 ( 0.08)       46.25 ( 8.25)       1.8(0.9)
         5       |o-oxoox-x-.        |
| 1016:66@O3  |  1415      :91@HH          1414:91@OH  |    43.5      2.820 ( 0.11)       31.46 (11.54)       2.3(2.4)
         12      |-o-oxo*ox.o-o.  .*@|
| 1016:66@O3  |  1451      :93@HE21        1450:93@NE2 |    12        2.859 ( 0.08)       23.32 (13.57)       1.4(0.8)
         4       | -.  . . ...  ox   |
| 1006:66@OH  |  2289      :144@HH                  2288:144@OH |    27        2.877 ( 0.09)       20.57 (12.58)
         1.5(0.8)  4       |- ....--.o---o----@|
| 3599:231@O  |  1007      :66@HH          1006:66@OH  |    92        2.747 ( 0.11)       18.07 ( 8.36)       14.2(17.5)
         69      |o*@@@@@@***@*@*x@@@|
```

Apo

```
|  3500:221@OE2 | 996     :66@HG1            995:66@OG1 |    88.5    2.752 ( 0.12)    13.76    (-7.54)
         8.9(-7.8)  33      |**@*@x@@**x*x*****@|
|  3500:221@OE2 | 3222    :204@HG            3221:204@OG |   85      2.723 ( 0.12)    16.34    (-8.2)
         8.1(-5.4)  24      |*o******@*x***@*** |
|  3499:221@OE1 | 3632    :232@H1        3631:232@O  |    34      2.682 ( 0.11)    20.41    (-11.07)  1.7(-1)
         5          |o-o... .o-oo---ox.@|
|  3499:221@OE1 | 3635    :233@H1        3634:233@O  |    43      2.710 ( 0.12)    22.8(-13.09)      1.8(-1.2)
         6          |ox*o.--ox---.o-x--@|
|  3499:221@OE1 | 3629    :231@H1        3628:231@O  |    16.5    2.712 ( 0.11)    26.54(-12.68)     2.1(-2)
         8          | -.-*.ox          |
```

Holo

```
|  3500:221@OE2 | 996     :66@HG1            995:66@OG1 |    91.5    2.725 ( 0.12)    14.54 ( 7.20)
         11.4 (7.9)32       |@x@**@**@**x*@@**@@|
|  3500:221@OE2 | 3222    :204@HG            3221:204@OG |   98.5    2.647 ( 0.10)    13.32 ( 7.69)
         49.2 (38.2)        115       |@@*@@@@@@@@@@*@@*@@|
|  3499:221@OE1 | 3612    :235@H1        3611:235@O  |    40      2.698 ( 0.12)    23.40 (12.66)     1.8 (0.9)
         4          |xxox-oo--oo--..---@|
|  3499:221@OE1 | 3615    :236@H1        3614:236@O  |    52      2.683 ( 0.13)    21.90 (12.08)     2.1 (1.4)
         6          |oxoox*x-ox-.xo-xo- |
```

Apo

```
|  1049:68@O   |    1089    :71@HG         1088:71@OG  |    91      2.733 ( 0.12)    16.44(-9.64)      11.4(-
13.7)    53         |**x**@*@@@*@*@@*@x@|
|  1044:68@OE1 |    2900    :182@HE21      2899:182@NE2|    44      2.873 ( 0.08)    22.69    (-10.98)  1.8(-1.4)
         8          |-oxxxo-xo.-o-o.-o- |
|  3628:231@O  |    1047    :68@HE22       1045:68@NE2 |    40.5    2.870 ( 0.08)    20.27    (-11.23)  2.8(-1.7)
         7          |o .     xx*xoox*xx@|
```

Holo

```
|  1049:68@O   |    1089    :71@HG         1088:71@OG  |    82      2.744 ( 0.11)    17.83 (10.27)     7.1(8.3)
         30         |o*@@x*@xx-x*****@@@|
|  1049:68@O   |    3597    :230@H1        3596:230@O  |    13      2.829 ( 0.10)    29.53 (14.22)     2.6(1.5)
         6          |-.     -ox.  ...   |
|  1044:68@OE1 |    2900    :182@HE21      2899:182@NE2|    40      2.871 ( 0.08)    23.46 (10.62)     2.3(2.4)
         13         |oxx*oox---*--.     |
|  1044:68@OE1 |    1451    :93@HE21       1450:93@NE2 |    18.5    2.858 ( 0.10)    28.83 ( 9.70)     2.5(2.3)
         10         |.          .xoo x*@|
|  1044:68@OE1 |    1415    :91@HH         1414:91@OH  |    17.5    2.808 ( 0.13)    22.07 (11.00)     2.7(2.6)
         10         |           --oo*o  |
|  3608:234@O  |    1047    :68@HE22       1045:68@NE2 |    68.5    2.862 ( 0.08)    20.77 ( 9.88)     3.2(2.2)
         9          |xx***xx*xxxoxxox-o@|
```

Apo

```
|  3198:202@O  |    2326    :147@H         2325:147@N  |    44.5    2.888 ( 0.07)    20.5(-10.22)      2.2(-1.7)
         10         |.*xoxo-*-.-xoox-   |
|  2679:167@O  |    2337    :147@HE2       2336:147@NE2 |   17.5    2.855 ( 0.10)    31.98(-11.25)     1.5(-1.3)
         7          |x       ---o-.o.   |
|  2333:147@ND1 | 1007      :66@HH         1006:66@OH   |   41.5    2.806 ( 0.11)    40.69    (-13.11)  2.4(-2.3)
         10         |xx..--oxooxxxx.-   |
```

Holo

```
|  3198:202@O  |    2326    :147@H         2325:147@N  |    54.5    2.893 ( 0.06)    18.64 ( 8.00)     2.0(1.6)
         10         |ox-ooox-xoo-oxoox*@|
|  2679:167@O  |    2337    :147@HE2       2336:147@NE2 |   18      2.858 ( 0.08)    39.08 (12.95)     2.6(3.0)
         12         |xx*.    .  ......  |
|  2304:145@OD1 | 2337      :147@HE2       2336:147@NE2 |   48      2.819 ( 0.09)    34.15 (12.25)     2.7(1.8)
         7          |   .o*xxxxoxo--oxx@|
```

Apo

```
|  3198:202@O   |   2326     :147@H          2325:147@N   |   44.5    2.888 ( 0.07)    20.5(-10.22)        2.2(-1.7)
             10       |.*xoxo-*-.-xoox-   |
|  3195:202@OG1 | 3629      :231@H1         3628:231@O   |   10.5    2.857 ( 0.10)    18.08     (-9.79)   1.5(-0.8)
             4        |-        .....-..o |
|  3172:200@O   |   3196     :202@HG1        3195:202@OG1 |   19      2.880 ( 0.09)    21.45     (-9.84)   1.3(-0.5)
             3        |..-.....o.  . --o-@|
|  3172:200@O   |   3196     :202@HG1        3195:202@OG1 |   19      2.880 ( 0.09)    21.45     (-9.84)   1.3(-0.5)
             3        |..-.....o.  . --o-@|
```

Holo

```
|  3198:202@O   |   2326     :147@H          2325:147@N   |   54.5    2.893 ( 0.06)    18.64 ( 8.00)       2.0(1.6)
             10       |ox-ooox-xoo-oxoox*@|
|  3195:202@OG1 | 3609      :234@H1         3608:234@O   |   31      2.830 ( 0.11)    16.23 (11.26)       2.8(2.2)
             8        |xo xx.-o*x-      -@|
|  3172:200@O   |   3196     :202@HG1        3195:202@OG1 |   20.5    2.888 ( 0.08)    20.48 ( 7.77)       1.3(0.8)
             5        |----.xo.-.....  .  |
|  3172:200@O   |   3196     :202@HG1        3195:202@OG1 |   20.5    2.888 ( 0.08)    20.48 ( 7.77)       1.3(0.8)
             5        |----.xo.-.....  .  |
|  3198:202@O   |   3600     :231@H1         3599:231@O   |   43      2.754 ( 0.11)    17.63 (10.36)       1.8(1.1)
             6        |-o---oxxo-ooo--x-o |
```

Apo

```
|  3500:221@OE2 | 3222      :204@HG                3221:204@OG |   85      2.723 ( 0.12)    16.34     ( -8.2)
             8.1(-5.4)  24        |*o******@*x***@*** |
```

Holo

```
|  3500:221@OE2 | 3222      :204@HG                3221:204@OG |   98.5    2.647 ( 0.10)    13.32     ( 7.69)
             49.2( 38.2)        115       |@@*@@@@@@@@@@@*@@*@@|
```

Apo

```
|  3514:222@OE1 | 1110      :72@HH12        1108:72@NH1 |    39      2.788 ( 0.10)    23.4(-10.58)        3.7(-4.5)
             22       |  .x.-x*@o.ox - -x@|
|  3514:222@OE1 | 1113      :72@HH22        1111:72@NH2 |    27.5    2.824 ( 0.09)    31.1(-9.92)         2.6(-2.1)
             8        |    .--x*..oo.o .x |
|  3515:222@OE2 | 1113      :72@HH22        1111:72@NH2 |    20      2.824 ( 0.10)    28.58(-12.22)       2(-1.5)
             6        |  ..    .o-.xooo  |
|  3515:222@OE2 | 1110      :72@HH12        1108:72@NH1 |    32.5    2.803 ( 0.09)    23.17     (-10.24)  3.6(-4.2)
             17       |  -o .  ox--@-@x  |
|  3546:224@OE2 | 1106      :72@HE          1105:72@NE  |    38      2.820 ( 0.10)    27.49     (-9.28)   3.8(-4.7)
             21       | .x-  *    @**o-*o |
|  3546:224@OE2 | 1112      :72@HH21        1111:72@NH2 |    37.5    2.808 ( 0.10)    31.96     (-9.36)   3.4(-2.6)
             10       |  *--.x   .xo*--*x@|
|  3545:224@OE1 | 1112      :72@HH21        1111:72@NH2 |    29.5    2.808 ( 0.09)    27.9(-9.23)         2.5(-1.5)
             7        |  oo- xxo*   -x - |
|  3545:224@OE1 | 1106      :72@HE          1105:72@NE  |    29.5    2.830 ( 0.09)    28.36(-9.38)        3.7(-3.5)
             13       |  o.. ****   -o . |
|  2321:146@OE1 | 2677      :167@HH22       2675:167@NH2|    21      2.801 ( 0.09)    25.37     (-11.58)  3.5(-3.3)
             12       |       x*xox.-    |
|  2324:146@O   |   2674     :167@HH12       2672:167@NH1|    15.5    2.838 ( 0.09)    33.3      (-12.34)  1.5(-0.9)
             4        |.       ----oo-    |
|  2322:146@OE2 | 2677      :167@HH22       2675:167@NH2|    15.5    2.800 ( 0.11)    22.26     (-10.56)  2.4(-2.1)
             9        |       -.oo-x-    |
```

Holo

```
|  3514:222@OE1 | 1110      :72@HH12        1108:72@NH1 |    19      2.792 ( 0.10)    25.33 ( 7.92)       2.9(3.9)
             16       |        -o@o---   |
|  3514:222@OE1 | 1113      :72@HH22        1111:72@NH2 |    16      2.817 ( 0.09)    29.79 ( 8.79)       2.3(1.9)
             7        |        .ooo-o-   |
```

```
|  3546:224@OE2 | 1112        :72@HH21            1111:72@NH2 |    37.5         2.795 ( 0.09)          25.73 (10.01)          3.3(3.2)
               13           |xo-xxx**.x-.-      |
|  3545:224@OE1 | 1112        :72@HH21            1111:72@NH2 |    29           2.806 ( 0.08)          27.11 (11.72)          1.5(0.9)
               5            |-oo..-  o-oo.-o-.  |
|  3546:224@OE2 | 1106        :72@HE              1105:72@NE  |    16.5         2.817 ( 0.09)          29.19 ( 7.92)          1.6(1.0)
               5            |o- o.oo....        |
|  3545:224@OE1 | 1113        :72@HH22            1111:72@NH2 |    10.5         2.778 ( 0.07)          23.30 (10.38)          2.6(3.2)
               11           |           -..-.@ |
```

Appendix D Validation of Lys methylation using CaM

The Figure Appendix D.1 showed the dispersed peaks of dimethylated Lys. The calcium induced conformational change can be illustrated by the chemical shift change of the methyl groups. Two more peaks were observed in holo-CaM at pH 7.4, indicating the chemical environment and dynamics of Lys was different between apo and holo-CaM. Increasing pH from 7.4 to 10.0 resulted in the rearrangement of the peaks and there was one more peak was observed at pH 10.0.

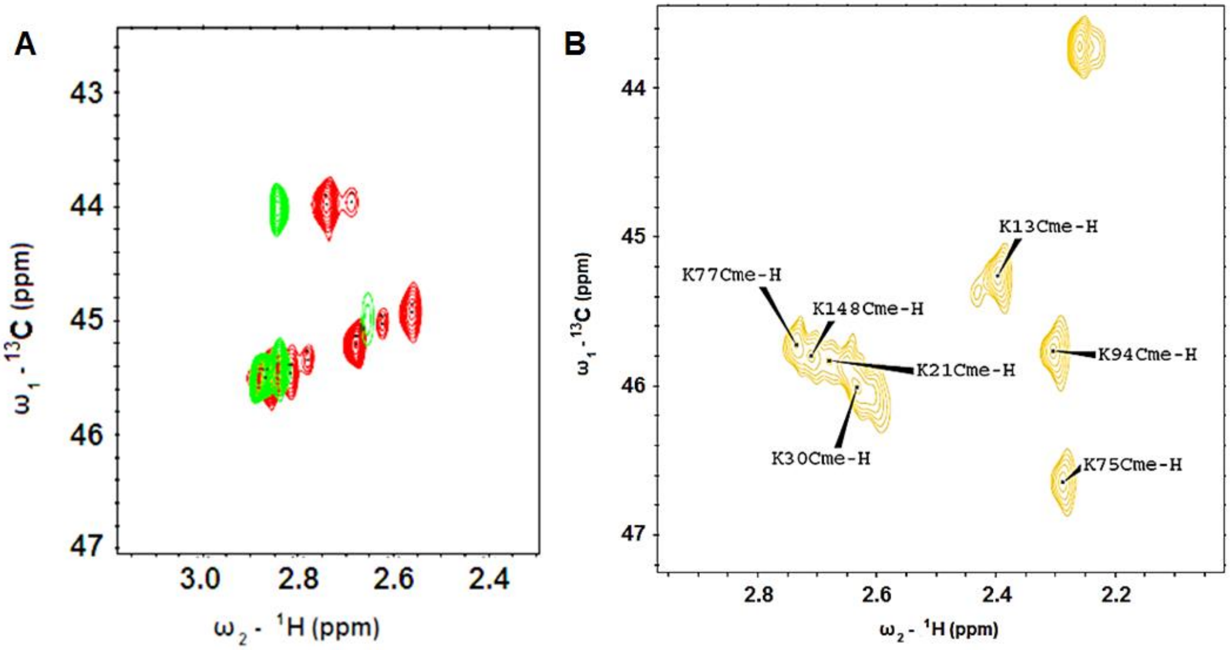

Figure Appendix D.1. ^{1}H-^{13}C HMQC of dimethylated [$^{13}CH_3$-Lys]-CaM. (A) The dimethylated Lys methyl signals of apo (green, 1 mM EGTA) and holo (red, 10 mM Ca^{2+}) CaM in 10 mM HEPES, pH 7.4, 100 mM KCl at 25 ℃. The CaM concentration was 100 μM. The ratio of H^{13}CHO: Lys was 5:1. And the ratio of H^{13}CHO:DMAB was 1:3. The reductive methylation was carried out at 4 ℃ for overnight. (B) The ^{1}H-^{13}C HMQC spectrum of [$^{13}CH_3$-Lys]-CaM in the presence of Ca^{2+} at pH 10.0. The assignment was made according to the literature published by Zhang and Vogel in 1993.

Appendix E Production of lentivirus

This protocol was provided by Dr. Guofu Fang from Emory University and modified by You Zhuo.

Maintain HEK 293FT in DMEM/10% FBS/1% penicillin-streptomycin medium in 10cm tissue culture dish. Culture the cell in a 37 ℃ incubator with a 5% CO_2, and split 1:4 to 1:6, three times per week.

Day 1: 293FT cell seeding

1. Passage HEK 293FT cells grown in DMEM supplemented with 10% FBS, 1% penicillin -streptomycin (pH 7.35).

2. Seed $1x10^7$ HEK 293FT cells in 15 cm dish and add 20 ml of DMEM supplemented with 10% FBS,1% penicillin-streptomycin . Swirl the cells thoroughly to obtain even distribution across the surface of the dish. Incubate the cells for 24 h at 37 ℃ with 5%CO_2

Day 2: Transfection

1. Observe the dishes. The cells should be approximately 70% confluent.

2. Transfection. Mix three DNA in a sterile 1.5ml tube (For 10 x150mm Dishes):

250 µg lentivirus transfer vector with insertion
187.5 µg pCMVΔR8.92
125 µg pVSVG

A. Add half of the DNA mixture to a sterile 50 ml conical tube, bring volume up to 6.25 ml with sterile distilled water. Repeat with second aliquot

B. Add 6.25 ml of 0.5M CaCl2 to each tube prepared in stepA, vortex for ~20-30 sec.

C. Add 12.5 ml of 2X HeBS (pH7.05) to a sterile 50 ml conical tube.

D. Use an automatic pipet aid and Pasteur pipette to bubble air through the HeBS tube prepared in step C, add DNA/CaCl2 solution in a dropwise fashion. After adding the DNA/CaCl2 solution, vortex for ~20-30 sec to form precipitates.

E. Leave the precipitates at RT for 20 min. Re-vortex for 20-30 sec.

F. Add 5 ml of the solution to each plate in a drop wise manner. Gently rock the plate back and forth during the addition.

G. Incubation under 3% CO_2 was recommended. However, incubation under 5% CO_2 does not cause any problem as transfection efficiency is not substantially influenced by medium pH when HEPES buffer is used for transfection. 3% may increase neuronal trophism.

3. Alternatively, the lipofentamin-2000 (Invitrogen) can be used for the transfection.

Day 3: change the media

Remove media, add 18 ml of pre-warmed to 37 ℃ fresh DMEM + 10% FBS/1% penicillin-streptomycin, and further incubate under 5% CO_2, 37 ℃ .

Day 5 and Day 6: Harvest and concentrate the viral particles

A. Transfer the culture media containing the virus from each plate to four sterile 50 ml conical tubes. Close the tubes, and spray them with 70% ethanol before taking them out of the hood.

B. Centrifuge at 1000 RPM for 5 min at 4 ºC, to pellet detached cells.

C. Filter the supernatant containing the virus through a 0.45 µm sterile filter unit.

D. Transfer the filtered medium into six 40ml Beckman ultracentrifuge tubes, place the tubes in a SW28 rotor.

E. Ultracentrifuge at 22,000 RPM (SW28) for 2 hrs at 4 ºC (or 28,000 RPM for Ti45).

F. Open the ultracentrifuge buckets in the hood. Use forceps to take the tubes carefully out of the buckets. Invert the tubes to transfer the supernatants to a flask containing bleach, wait 1 hour, and discard. Re-suspend the each virus pellet with 500µl to1 ml PBS by pipetting down and up a few times, avoid foaming.

G. Incubate on ice for 30 min.

H. Put six tubes resuspended virus together to 10ml Beckman ultracentrifuge tube, add 2ml 20% sucrose sterile solution on the bottom of centrifuge tube, ultracentrifuge at 28,000 RPM (SW41) for 2 hrs at 4 ºC

I. Re-suspend the virus pellet with 70-100 µl PBS.

J. Aliquot 5-10 µl each tube and Store viral stock at -80 ºC.

Materials:

HEK 293 FT cells
DMEM/10% FBS/1% penicillin-streptomycin
PBS
70% ethanol in a spray bottle
1.5ml sterile tube
10ml culture dish

15 cm culture dish
50 ml sterile PP conical tubes
250 ml 0.45 µm pore size filter apparatus with bottle
40 ml and 10 ml ultracentrifuge tubes (Beckman)

Solutions for Transfection:

50 ml 0.5 M $CaCl_2$

1.67 g $CaCl_2 \cdot 2H_2O$
50 ml H_2O
Filter sterilize with 0.45 µm pore size filter apparatus with bottle. Store at 4 °C

100 ml 2X HeBS (HEPES-Buffered Saline)

1.64 g NaCl
1.19 g HEPES free acid
0.04 g $Na_2HPO_4 \cdot 7H_2O$
80 ml H_2O
Adjust pH to 7.05 with 5N NaOH
Filter sterilize with 0.45 µm pore size filter apparatus with bottle. Store at 4 °C.

Infect cell with lentivirus:

Add virus with approximately 5-10 IU to the cell medium, change medium 4 -6 hours after infection. If virus titer are not sure, for virus not concentrated, add to cells with 2x dilution, (for example, 2ml virus with 2ml culture medium). For concentrated virus, 1ml medium add 5ul virus.